UC Berkeley
UC Berkeley Electronic Theses and Dissertations

Title

Towards More Predictive Models of Galactic Center Accretion

Permalink

https://escholarship.org/uc/item/31d79442

Author

Ressler, Sean Michael

Publication Date

2019

Peer reviewed|Thesis/dissertation

eScholarship.org Powered by the California Digital Library
University of California

Towards More Predictive Models of Galactic Center Accretion

By

Sean Michael Ressler

A dissertation submitted in partial satisfaction of the

requirements for the degree of

Doctor of Philosophy

in

Physics

in the

Graduate Division

of the

University of California, Berkeley

Committee in charge:

Professor Eliot Quataert, Chair
Professor Dan Kasen
Professor Joshua Bloom

Summer 2019

Towards More Predictive Models of Galactic Center Accretion

Copyright 2019
by
Sean Michael Ressler

Abstract

Towards More Predictive Models of Galactic Center Accretion

by

Sean Michael Ressler

Doctor of Philosophy in Physics

University of California, Berkeley

Professor Eliot Quataert, Chair

Sagittarius A* (Sgr A*), the roughly 4 million $M_\odot$ black hole at the center of our galaxy, is arguably the best natural test-bed for supermassive black hole accretion models. Its close proximity allows for detailed observations to be made across the electromagnetic spectrum that provide strong, multi-scale constraints on analytic and numerical calculations. These include exciting new event horizon scale results that directly probe the strong field regime for the first time. Spanning roughly 7 orders of magnitude in radius, the accretion system begins at $\sim$ parsec scales where a large population of Wolf-Rayet (WR) stars interact via powerful stellar winds. A fraction of the wind material accretes to the event horizon scales, heating up and radiating on the way down to provide the observed multi-wavelength emission. Detailed modeling of this process requires 3D numerical simulations spanning as large of a dynamical range as possible. The goal of this thesis has been to improve the predictive power of such simulations applied to Sgr A* by limiting the number of free parameters that they contain. This is done by incorporating more theoretical and observational knowledge into the calculations, for example, what collisionless physics tells us about how electrons/ions are heated in a turbulent medium and the properties of the winds of the WR stars. The resulting simulations have shown excellent agreement with a wide range of observational constraints and could have major implications for how the accretion flow around Sgr A* is modeled in the future. The techniques presented here are also applicable to other low luminosity AGN and X-ray binaries.

I dedicate this dissertation to my parents, Ron and Denise Ressler.

I hope this makes up for the time when I wrote about “Nintendo” as my hero in that infamous 3rd grade essay.

Contents

List of Figures

List of Tables

Acknowledgments

Often it is easier to express gratitude to those who perform small acts of kindness (like a stranger who holds open a door) than it is to express it to those who have a significantly more profound impact on one's life. So it is that many of the people in these acknowledgments have never heard me express how much they have actually meant to me during my graduate studies. Each contributed in some special way to make my experience at UC Berkeley one that was enjoyable, rewarding, and ultimately successful. Although simple words in the acknowledgement section of a thesis that only a handful of people will read cannot do justice to my gratitude towards those listed below, I would like them all to know that it is deep and heartfelt. Wherever the future takes me I will miss this department, this city, and most of all the people whom I have met along the way and come to call my friends and family.

First of all, I thank Eliot Quataert: I could not have hoped for a better advisor. He always gave me complete freedom to work in the way that I found myself the most productive, even when that meant keeping unorthodox hours and taking lots of long walks away from my desk. He was always there for sage advice both in research, career paths, communication, and even when I was stranded in NY without a passport and was supposed to be flying to Germany the next day. Not to mention that he provided a large fraction of our Friday Afternoon Cheese Time funding out of pocket.

I thank Stephen Reynolds, my undergraduate research advisor, for sparking my interest in astrophysics (particularly high energy astrophysics) and for his great help in navigating graduate school applications, wisely steering me towards accepting the offer from UC Berkeley.

I thank Sasha Tchekhovskoy whom I had the great fortune to work with on my first few projects in graduate school. From our first meeting together, he was always abounding in encouragement and was concerned about both my mental and physical well being. He also taught me essentially everything I know about data analysis.

I thank all the members of the Horizon Collaboration for their great ideas, numerical tools, and support. I especially thank Charles Gammie and Jim Stone for being my "advisors away from home."

I thank Mani Chandra and Ben Ryan for being close collaborators in my first few years of graduate school and providing a friendly welcome to their office and UIUC. I thank Elena Murchikova for also being a welcoming host on multiple occasions at Caltech and the IAS.

I thank Tanmoy Laskar for being an energetic, wise, and encouraging collaborator as he introduced me to the field of gamma-ray burst afterglows (and later, Renaissance polyphony).

I thank Mariska Kriek for hooding me in the place of Eliot and being a loyal accomplice in the great Drummond Fielding Exit Seminar Introduction Incident of May 2018.

I thank everyone who had the misfortune of sharing a cubicle space with me, including Drummond Fielding, Chris White, Kareem El-Badry, Hannah Klion, Phillip Kempski, and Daniel Lecoanet. Of these I especially thank Drummond Fielding, Chris White, and Kareem El-Badry. Drummond for being the first in the department to cross the line from colleague to friend, for always providing an open ear for my random musings, and for making me a nice cereal bowl that I unfortunately broke during the writing of this thesis. Chris for always being willing to selflessly drop whatever he was working on to help me make `Athena++` do what I needed and for creating the greatest regularly scheduled event known to astronomy: Friday Afternoon Cheese Time. Kareem for providing a memorable introduction to my exit seminar and for writing me a poem for Valentine's Day comparing me to Sagittarius A*.

I thank Drummond Fielding and Chris White for being my partners in cheese and Kareem El-Badry for admirably taking up the mantle of cheese-bearer when I leave. Wren Suess also deserves special thanks for continually offering her superb baking talents for the benefit of all.

I thank my good friends Daniel Wooten, Andrew Chirdon, Shalin Patel, and Greg Boheler (along with his parents, James and Jan) for always being there for laughs and deep conversation even after long periods of relatively little contact. I thank Daniel additionally for checking up on me every semester and for not giving up on inviting me to social events even after I declined a majority of the time.

I thank LaMon Johnson, Rob Pearson, Charles AKA "Blue Boy," Maria, and "Big Man" for always being friendly faces in the streets of Berkeley and having unwavering confidence in me. I thank Scott and Federica Debie for their encouraging interest in science and for welcoming me into their home for some wonderful dinners.

I thank my current and former roommates, Pim Dangkulwanich, Tay Nguyen, Vy Tran, Rachel Om, Sylvia Sanchez, Lisa Bergstrom, and Sam Ngo, for maintaining a relatively quiet and peaceful place to live while also providing a welcoming environment to come home to at the end of the day. Thanks to them also for tolerating all of my strange habits over the years, like my daily dinner/crossword ritual and my night-time refrigerator raids. Note: don't forget to take out the trash every week once I move out.

I thank The Cheeseboard Collective for introducing me to the wide world of gourmet cheese and bringing me under their wings as an informal disciple. This includes Linh, Igor, Matt, James, Anuja, Ursula, Art, Davy, Omri and several others who I know by face alone. Some of those names are probably misspelled. I especially thank Linh for volunteering to come give a talk in the department on her (former) role as a 'cheese buyer.'

I thank Iljin Cho for being a true friend and brother who I could always count on for wise advice. Likewise I thank Cara Farley as a sister and supporter (along with her parents Mark and Lynn).

I thank Steven Rhyse, master of Rhetoric with a capital 'R', for keeping me entertained in the RSF, serving as my loyal gaming partner every week, and being a constant source of advice even if I often ending up doing exactly the opposite of what he advised. Most of all for being there when I needed him after I didn't take his advice.

I thank Ploy Kongkapetch for cheering for me on several occasions and for a wonderful birth-

day mug that I will never use for fear of breaking (I learned my lesson after the cereal bowl incident...see above).

Speaking of small acts of kindness, I thank the employee of University Now Day Nursery (located in Princeton, New Jersey) who gave me a bottle of water after I stumbled into the building uninvited wearing raggedy clothes. I like to think that I was nearing dehydration and potentially heat exhaustion, but that is probably an exaggeration. In any case, I sure was sweaty and thirsty, so I really appreciated the drink even if it was toddler-sized.

I thank all the members of Covenant Presbyterian Church for adopting me into their community and providing constant spiritual support. This includes Wayne Forkner, Evelyn Fennell, The Roadifers, The Chungs, The Allens, Nancy Droppa, Jane Byer, You-Wei Cheah, Vivian Cheung, Diana Snodgrass, Yorkman Lowe, The Enases, The Verbys, The Wallings, The Harrises, The Tzens, Paul Hess, Sylvia Yee, Brian Blake, The Godinezes, Victoria Wang, Darren Hsiung, Josh Benjamins, Rachel Newman, Ezra Setiasabda, and Kweku Opoku-Agyemangs. I thank above all the great shepherd of the church, Jesus Christ, for not letting a lost sheep go astray.

I thank my parents for support in every possible way through their guidance, discipline, and love. I thank my siblings Devyn, Brad, Kirstyn, Michael, and Megan for loving me despite my oddities. I thank Kirstyn additionally for providing me with several drawings that I used in a series of talks for both humorous and informative purposes. I thank Megan additionally for flying all the way out to California to see me graduate and Michael for being there in spirit. I thank Alice Diaz for keeping my brother honest and for those Christmas mustaches. I thank my extended family as well for always having kind words of encouragement and support. These include my aunts Marion, Judy, Jackie, Cassie and Rosemary, my uncles Jon, Sonny, Joey, and (late) Ritchie, and my cousins Rosemary, Donna, Barbara, Chris M., Chris V., Anthony, Debbie, Jason and Jed, as well as the various offspring of those listed. Hopefully I didn't leave anyone out; our family is hard to keep track of sometimes. I thank also my late grandmothers Elizabeth Mitchell and Kathe Weidner; the latter unfortunately was right when she said in April 2018 that she would not make it to see me earn my PhD.

My graduate studies were supported in part by the NASA Earth and Space Science Fellowship, NSF grants AST 13–33612, AST 1715054, AST–1715277, Chandra theory grant TM7–18006X from the Smithsonian Institution, and by the NSF through XSEDE computational time allocation TG–AST090038 on SDSC Comet and TG–AST100040 on TACC Stampede. Finally, computing time granted by UCB on the Savio cluster was essential for all of my work.

This dissertation was typeset using the ucastrothesis LaTeX template.

Chapter 1

Introduction

1.1 Background

When my graduate studies began in 2013, the observational and theoretical communities were together hard at work preparing for the first light of two groundbreaking telescopes: The Event Horizon Telescope (EHT, Doeleman et al. 2009) and GRAVITY (Gillessen et al. 2010). These instruments promised for the first time to be able to directly probe the event horizon scale of Sagittarius A* (Sgr A*), the supermassive black hole in the centre of The Milky Way, testing the theory of general relativity (GR) and accretion models in the strong field regime. For the EHT, this meant spatially resolving the 230 GHz emission to capture the "shadow" of the black hole, that is, the distinct lack of emission caused by the presence of the event horizon. For GRAVITY, on the other hand, it meant performing high resolution astrometry on localized near infrared (NIR) emission, the ideal scenario being an orbitting "hot spot" that would test GR and provide information about the orientation of the accretion flow.

As my graduate studies now conclude in 2019, both collaborations have published their first results to much fanfare. In the middle of last year, Gravity Collaboration et al. (2018) reported that the ideal "hot spot" scenario had been found with the detection of several infrared flares in Sgr A* that displayed centroid motion at $\sim 10\ r_g$ consistent with a relatively face-on orbit. The polarization of the flares was also measured, with a periodicity that suggests predominantly vertical (parallel to the angular momentum vector) magnetic fields. This year, Event Horizon Telescope Collaboration et al. (2019a,b,c,d,e,f) unveiled the first 230 GHz image of the emission surrounding the supermassive black hole at the centre of M87, using the size of the black hole's "shadow" to precisely determine its mass and the asymmetry of the image to determine the orientation of its jet. Resolved polarization maps of this emission are currently being analysed and will provide a stronger constraint on the emitting plasma itself, particularly on the magnetic field as it determines the direction of polarization for synchrotron radiation. EHT results for Sgr A* are still forthcoming but are are expected relatively soon.

These exciting new constraints on the event-horizon scale accretion flow add to the wealth of multi-wavelength, time-variable observations of Sgr A*, arguably nature's best "laboratory" for supermassive black hole accretion. Numerous telescopes have taken data between $\sim 10^9$–10^{12} Hz, finding the emission of Sgr A* in this frequency range to be relatively stable with time but not without a small amount of variability (e.g., Falcke et al. 1998; An et al. 2005; Marrone et al. 2006; Bower et al. 2015a; Liu et al. 2016b,a). At low radio frequencies, the spectrum is nearly flat with frequency (in flux) and then turns over at the "sub-mm bump" just below ~ 230 GHz where (in the most common interpretation) the emission transitions from being optically thick to optically thin. Above 10^{12} Hz, Sgr A* is not a steady source of radiation. Instead, it displays frequent flaring behavior with large amplitude X-ray flares occurring roughly once per day (e.g., Neilsen et al. 2013) and Near-Infrared (NIR) flares occurring about four times as often (e.g., Genzel et al. 2003a; Schödel et al. 2011). All X-ray flares have been linked to a NIR counterpart but not all NIR flares have been linked to an X-ray counterpart. It is not known for certain whether these flares are synchroton emission, synchroton self-Compton emission, or a combination of both. Furthermore, the millimeter and sub-millimeter emission is observed to be $\sim$ a few percent polarized, with the fraction varying in time between ~ 1–10% (Aitken et al. 2000; Marrone et al. 2006). The rotation measure (RM) for this polarized emission was first measured to be $\approx -5.6 \times 10^5$ rad/m^2 (Marrone et al. 2007) and later found to vary by as much as a factor of 2 on $\lesssim$ month time scales[1](Bower et al. 2018).

Larger scale observations of Sgr A* can also provide key information regarding the properties of the gas that ultimately feeds the event horizon scale. Diffuse, spatially resolved X-ray emission is observed at 0.1–1 pc from the black hole (Baganoff et al. 2003) and is believed to be caused by shocks between winds of the ~ 30 Wolf-Rayet (WR) stars in the Galactic Centre. These observations can be used to infer a density and temperature that imply a spherical accretion rate orders of magnitude too large to account for the observed rotation measure, meaning that only a small fraction of this gas ultimately reaches the horizon. The rest either goes into outflow (e.g., Blandford & Begelman 1999) or is prevented from accreting, e.g., because it gets trapped in convective eddies (e.g., Quataert & Gruzinov 2000b) or it becomes magnetically frustrated (e.g., Pen et al. 2003; Pang et al. 2011). Determining which, if any, of these models is correct is important for constraining the accretion rate onto Sgr A* and horizon-scale models. Another potential probe of the gas at large radii is the rotation measure of the recently discovered magnetar, located ~ 0.1 pc in projected distance from the black hole (Eatough et al. 2013). The rotation measure is second in magnitude only to Sgr A* for our galaxy, and implies the presence of a relatively strong magnetic field, if indeed the RM is produced locally to the inner ~ 1 pc.

A comprehensive theoretical/numerical model of accretion onto Sgr A* must be able to account for all of these observational features. Ideally, starting from the $\sim$ pc scale where the winds of the WR stars provide the original accretion budget, it would describe how some fraction of this gas falls inward and ultimately reaches the event horizon. Though semi-analytic models more easily capture this large range in spatial scales ($\gtrsim 7$ orders of magnitude), they are not able to account for the turbulent nature of the flow, time-variability, the precise nature of how the winds feed the supply of gas, or other asymmetric features. Because of this, simulations are the most promising route forward, particularly those that include general relativity (GR) and magnetic fields. GR is needed

---

[1] The shorter term variability is uncertain because the variability of the RM is more difficult to disentangle from the variability of the intrinsic polarization angle. The time scale for the RM to vary by a factor of ~ 2 could be as short as hours.

in order to account for the effects of strong gravity near the black hole, while magnetic fields are required not only to accurately model synchrotron emission (the primary emission mechanism for the horizon-scale gas), but also because of their likely important role in the dynamics. Putting this all together results in General Relativistic Magnetohydrodynamic (GRMHD) simulations, which solve the equations of MHD in the Kerr metric appropriate for a rotating black hole. There are now a number of GRMHD codes in use and a recent code comparison paper concluded that they all essentially agree with one another when the resolution is sufficiently large (Porth et al. 2019). Thus we can have reasonable confidence that the conclusions drawn from these simulations are not dependent on numerical algorithms but on physical parameters.

Even the most ambitious 3D GRMHD simulations, however, can run for only a little more than 100,000 M[2], or ∼ a month for Sgr A* (e.g., Sądowski et al. 2013), while the free-fall time scale for the winds of the WR stars is on the order of 1000 yr. By current computational standards it is therefore impossible to run a GRMHD calculation long enough to accurately model the full dynamic range of accretion in a single simulation. Instead, assumptions must be made about how the gas at large radii (i.e., the Bondi radius) ultimately feeds small radii (i.e. 1–1000 M); these assumptions essentially correspond to initial and boundary conditions for GRMHD. The most common approach is to assume that by the time the gas reaches a few hundred M, it has been able to circularize into a disc of relatively high angular momentum gas and that some weak magnetic field is present. In practice, this means that the simulation starts with a torus in hydrodynamic equilibrium (e.g., Fishbone & Moncrief 1976; Penna et al. 2013) seeded with a magnetic field such that plasma β, the ratio between magnetic and thermal pressure, is $\gtrsim 100$. This configuration is unstable to the Magneto-Rotational Instability (MRI, Balbus & Hawley 1991a), a powerful instability that acts on differentially rotating gas that has an arbitrarily small magnetic field and an angular velocity that is decreasing with increasing radius. The MRI amplifies the initial magnetic field until it is strong enough to carry away a significant amount of angular momentum from the torus, driving accretion. As time progresses in the simulation, a roughly steady state is reached in which the midplane is highly turbulent while the polar regions are strongly magnetized, near vacuum jets. In the intervening regions there is a corona, generally outflowing, with a lower density than the midplane but large enough to potentially be a significant source of emission. This general picture describes simulations that fall under the Standard And Normal Evolution (SANE) description found in the literature. If the initial supply of coherent magnetic flux is large enough, however, after some time a new phase of accretion is reached, called a Magnetically Arrested disc (MAD, Narayan et al. 2003; Tchekhovskoy et al. 2011), where the magnetic flux threading the horizon of the black hole is large enough to forcefully "arrest" the inflowing gas. During this phase accretion occurs only along thin streams, the system is highly time variable, and the jets are much stronger than those found in SANE simulations. It is still an open debate whether the accretion flow in the Galactic Centre can be classified as a SANE disc, a MAD disc, or neither (e.g., accretion via low angular momentum gas). The question can only be answered by a combination of two things: 1) by more precisely modelling how the gas/magnetic fields at large radii accrete to the event horizon scale and 2) by comparing a wide range of simulations to observations. 1) is more *predictive*, basically amounting

---

[2] M is the mass of the black hole, which has dimensions of time in units such that $G = c = 1$.

to determining the "correct" initial/boundary conditions that are appropriate for simulating Sgr A* and involves accurately representing the accretion via the stellar winds of the WR stars. 2) is more *phenomenological* and often works by surveying a wide variety of initial/boundary conditions and then performing radiative transfer on each to see which class of simulation produces results most representative of the data.

Because of the strong gravitational effects of the black hole near the horizon (e.g., light bending and gravitational redshift) where much of the emission from Sgr A* originates, comparison of simulations to observations requires radiative transfer schemes that are fully general relativistic. Two commonly used methods exist, both of which have proven useful. Ray tracing methods integrate along geodesics as they pass through the plasma to the observer and are best suited for producing high resolution, monochromatic images (e.g.,Dexter 2016; Mościbrodzka & Gammie 2018; Zhu et al. 2015; Narayan et al. 2016). Monte-carlo based methods track the motion of photon packets as they are probabilistically absorbed, emitted, and scattered (e.g.,Dolence et al. 2009), and are best suited for computing multi-wavelength spectra. In addition to computing the total intensity/flux of the emission, some methods are also able to compute the other three Stokes parameters (e.g.,Dexter 2016; Mościbrodzka & Gammie 2018), quantities that will be measured and spatially resolved by the EHT. This is important because the polarization measurements may prove to be stronger constraints on accretion models than the total intensity (Jiménez-Rosales & Dexter 2018).

GRMHD and GR radiation transport alone, however, are not sufficient for emission modelling in the Galactic Genter. This is because the accretion rate onto Sgr A* is sufficiently low that the plasma is radiatively inefficient and unable to cool (Narayan et al. 1998), leading to a hot, low density environment where Coulomb collisions are exceedingly rare. On the surface, this would seem to indicate that a fluid model (e.g., GRMHD) would be completely inappropriate for describing the system and that our efforts should be focused on fully collisionless calculations (e.g.,particle-in-cell methods). A particle-in-cell (PIC) simulation of the accretion flow, however, would require resolving such a large range of spatial scales (roughly from a particle's gyroradius to the gravitational radius) that global PIC calculations are impossible in the foreseeable future. On the positive side, recent results have found that many of the properties of MRI in local hybrid-PIC simulations are strikingly similar to those in MHD (Kunz et al. 2016). The same conclusion was reached in weakly collisional calculations that extended fluid models to account for non-ideal effects such as anisotropic conduction or viscosity (Foucart et al. 2017; Kempski et al. 2019). The reason for this counter-intuitive result is that plasma microinstabilities, such as the firehose and mirror instabilities, regulate the degree to which the plasma departs from ideality. Physically, the instabilities create tangled magnetic fields that frequently scatter the charged particles in a way that mimics collisions. Each species of particles (i.e. electrons and ions) then behaves almost like an ideal fluid with its own temperature, though since the electron and ion fluid do not interact themselves these temperatures are not necessarily the same, resulting in a two-temperature fluid. A single-fluid GRMHD calculation can thus give a reasonable solution for the dynamics and the *total* temperature (electron plus ion), but it leaves the relationship between the electron and ion temperature undetermined. This is problematic because the electron temperature is of vital importance in determining the predicted emission from theoretical models.

To subvert this complication, the most common approach in the literature is to artificially assign an electron temperature to the simulation in post-processing using a phenomenological prescription. Sometimes this is as simple as setting a constant electron-to-ion temperature ratio everywhere (Mościbrodzka et al. 2009), but more often the models try to distinguish between the outflow and the disc proper by having different prescriptions for the electron temperature in each region (Mościbrodzka et al. 2014; Chan et al. 2015a). Generally, the models that have been the most successful in describing the observations of Sgr A* below 10^{13} Hz and in satisfying the NIR and X-ray quiescent upper limits have featured electrons that are relatively cold in the midplane but relatively hot in the outflow/corona. All of these models, however, generally fail to reproduce sufficiently large NIR and X-ray flares. This is likely because a purely thermal electron population is insufficient and that that a small population of nonthermal, accelerated electrons are necessary to account for the flares. In fact, such a population is expected to be provided by either magnetic reconnection (e.g., Sironi & Spitkovsky 2014), shocks (e.g.,Guo et al. 2014), or both in the accretion flow and outflow. While the field of modelling flares with nonthermal particles in GRMHD simulations is still young, a few pioneering works such as Mao et al. (2017) and Ball et al. (2016) have studied the observational consequences of adding a power law of electrons to the distribution function in the post-processing stage. Although Mao et al. (2017) did not study time variability, they did show that the high energy electrons can produce a diffuse halo in the 230 GHz images, altering its shape and size. Ball et al. (2016), on the other had, did apply their model to NIR/X-ray flares and found qualitative agreement with observations as well as good quantitative agreement with the observed power law index of the X-ray flux distribution. Still, however, their simulations did not show flares with large enough amplitude to account for the higher end of this distribution. Finally, Chael et al. (2017) presented a method for evolving the distribution of non-thermal electrons in GRMHD given some prescription for how the electrons are accelerated depending on local plasma properties. Applying this model to Sgr A* will likely provide valuable insight into the study of flares.

Though a large fraction of the work on modelling the emission from Sgr A* has focused on the horizon scale, several authors have performed much larger scale calculations to model, e.g., the $\lesssim$ parsec scale X-ray emission caused by the interactions of the WR stellar winds. Both the hydrodynamic properties of the winds (i.e. mass-loss rates and wind speeds, Martins et al. 2007) and the orbits of the stars themselves are reasonably well constrained (Paumard et al. 2006; Lu et al. 2009), so all that is needed is a mathematical prescription for how the winds source the accretion flow. 1D simulations can only do this in a simplified way, such as Quataert (2004), who treated the winds as a uniform annular source of mass and energy, or Shcherbakov & Baganoff (2010), who averaged individual wind sources over their orbits and over all angles. These calculations successfully reproduced the X-ray surface brightness profile while finding that only a small fraction of the total mass injection rate from the winds is accreted, chiefly because most of the gas at the Bondi scale is unbound outflow. This is qualitatively consistent with the polarization limits on horizon scale accretion. 3D simulations (e.g., Cuadra et al. 2005, 2006, 2008, 2015; Russell et al. 2017) can treat the winds more accurately by allowing the source terms to proceed along their individual orbits during the course of the simulation and are (in principle) able to model, e.g., disc formation (or lack thereof). Generally, the 3D simulations find that, similarly to the 1D calculations, the total X-ray luminosity of Sgr A* is easily reproduced in simulations with observationally motivated wind properties and that only a fraction of the total wind material accretes. Most of the 3D Galactic Centre wind accretion simulation literature, however, has not focused on studying how gas from large scales feeds the inner radii nor fully explored the implications of their calculations on horizon scale models.

1.2 Thesis Summary and Guide To Chapters

The majority of my thesis work can be broken down into two categories: 1) modelling the event horizon-scale accretion flow using two-temperature GMRHD simulations and 2) modelling the larger scale, wind-fed accretion onto Sgr A* and studying how it how it sources the innermost radii. Chapters 2 and 3 fall into Category 1, while Chapters 4, 5, and 6 fall into Category 2.

The plasma immediately surrounding the event horizon of Sgr A* is known to be an essentially collisionless plasma due to its high temperature and low density. However, because of the impossible (for today's computing standards) computational challenge of performing a fully collisionless simulation able to resolve global dynamics down to the scale of a particle's gyroradius, all early GRMHD models of Sgr A* were done under the assumption of an ideal fluid. Knowledge of the collisionless nature of the gas was only used as motivation for post processing radiative transfer methods that prescribed the electron temperature (a key parameter for determining the radiation) to be some function of the other variables. Though these models were fairly successful in modelling observations, they had many free parameters and lacked sufficient physical motivation. Seeking to improve the predictive power of simulations, my work described in Chapter 2 presented a new method for two-temperature GRMHD that self consistently evolves the electron temperature alongside the total gas dynamics. I applied this method to 2D simulations of Sgr A* and showed that using a subgrid model for electron heating appropriate for the conditions in the solar wind results in an electron temperature distribution near the black hole similar to that of best-fit phenomenological models of Sgr A*.

In the work described in Chapter 3, I applied this two-temperature GRMHD method to 3D simulations of Sgr A*, computing predictive spectra and images. The results from 3D confirmed my previous 2D results that a "disc-jet" structure (one in which the electrons in the corona/jet are relatively hot while the disc are relatively cold) can naturally arise from our particular choice of subgrid electron heating function. With essentially only one free parameter (the mass of the accretion disc) I found that the model successfully reproduced the higher frequency radio and mm emission of Sgr A* as well as the qualitative features of the temporal variability. This model, however, was not able to achieve a low frequency radio slope flat enough to explain observations, nor did it display any evidence for the significant X-ray flares that occur in the Galactic Centre roughly once per day. Most likely, this suggests that nonthermal particles are necessary to explain these observational features of Sgr A*, as often speculated in past work.

In Chapter 4, I describe hydrodynamic simulations performed on a much larger scale that studied how the winds of the ~ 30 WR stars in the Galactic Centre source the innermost accretion flow. Each wind was treated as a source term in mass, momentum, and energy as determined by the observationally constrained mass-loss rates and wind speeds. These source terms move on fixed

Keplerian orbits based on the observed proper motions of the WR stars. The simulations spanned the radial range of ~ 150 Schwarzschild radii ($\sim 2\times10^{-5}$ pc) to ~ 1 pc, encompassing a majority of the WR stars and allowing me to study self-consistently how the inner accretion flow is connected to the properties of the WR stars. I found that the accretion rate predicted by these simulations, when extrapolated to the event horizon, was entirely consistent with observational constraints and most previous model-dependent estimates despite the lack of magnetic fields to provide angular momentum transport. This is possible because the stellar winds provide a sufficiently large supply of low angular momentum gas that can accrete without the need for torques. Another key result was that, most of the time, the innermost accretion flow was generally aligned with the clockwise stellar disc containing roughly half of the WR stars.

Chapter 5 describes my implementation of *magnetized* stellar winds in my 3D simulations of wind accretion onto Sgr A*. I showed that a single simulation could explain the magnitude and variability of the rotation measures of both Sgr A* and the Galactic Centre magnetar in addition the variable component of the magnetar's dispersion measure. The simulations also predict that the magnetic flux ultimately threading the event horizon of the black hole would be significant but below the MAD limit, the point at which the field is strong enough to halt the inward flow of gas.

Finally, Chapter 6 presents a more detailed analysis of the inner accretion flow of the MHD wind accretion simulations of Sgr A*. I found that despite the magnetic field reaching near equipartition with the thermal energy, the time and angle averaged fluid quantities are not much different than those in purely hydrodynamic simulations, including the mass accretion rate. This is because the flow never circularizes but has large radial velocities at all radii, so that the radial ram pressure dominates over both the thermal and magnetic pressure in determining the dynamics. Such a flow structure differs from most GRMHD models applied to Sgr A*, which typically have gas slowly falling in as the magnetic field, amplified by the MRI, removes angular momentum from a circularized disc of gas. In contrast, in my simulations the MRI is not important and low angular momentum gas supplies the accretion. As in the hydrodynamic simulations, the angular momentum of the gas is roughly aligned with the clockwise stellar disc most of the time.

1.3 Applications To Other Systems

Though the techniques and models presented in this thesis were developed primarily with Sgr A* in mind, they are also relevant for other black hole accretion systems. The two-temperature GRMHD framework of Chapters 2 and 3 is appropriate for many other low-luminosity active galactic nuclei (AGN) and has already been applied to the one in the center of the galaxy M87 (e.g., Ryan et al. 2018; Chael et al. 2019), the first target of EHT. The methods for treating hydrodynamic and MHD stellar wind accretion presented in Chapters 4–6 could also be used to model other AGN where stellar winds contribute to the mass supply (e.g., NGC 3115, whose Bondi radius can be resolved, Wong et al. 2014) and high-mass, wind-fed X-ray binaries (e.g., Cygnus X-1).

1.4 Other Work

I published an additional first-author paper during graduate school with Tanmoy Laskar that calculated the spectra of gamma ray burst afterglows from a simple semi-analytic model that included emission from both thermal and nonthermal electrons (Ressler & Laskar 2017). This work was sufficiently different from the focus of my thesis that I do not include it here.

During my studies I was also involved in two published papers on which I was the second author and a third is in press. In Ryan et al. (2017, 2018), we presented simulations that used my two-temperature GRMHD model in a Monte Carlo radiation GR(adiation)RMHD code. This allowed us to study systems with higher accretion rates than Sgr A* where radiation becomes dynamically important. The first paper examined how the radiative efficiency of the accretion flow varies with accretion rate while the second modelled the emission from M87. In Anantua, Ressler, & Quataert 2019, we presented a suite of post-processing models of the electron temperature and studied how the images and spectra vary across these models for Sgr A*. The goal was to better better understand the effect that the large uncertainty electron heating physics could have on forthcoming EHT results.

Chapter 2

Electron Thermodynamics in GRMHD Simulations of Low-Luminosity Black Hole Accretion

An earlier version of this article was previously published as Ressler S. M., Tchekhovskoy A., Quataert E., Chandra M., and Gammie C. F., 2015, MNRAS, 454, 1848

2.1 Abstract

Simple assumptions made regarding electron thermodynamics often limit the extent to which general relativistic magnetohydrodynamic (GRMHD) simulations can be applied to observations of low-luminosity accreting black holes. We present, implement, and test a model that self-consistently evolves an entropy equation for the electrons and takes into account the effects of spatially varying electron heating and relativistic anisotropic thermal conduction along magnetic field lines. We neglect the back-reaction of electron pressure on the dynamics of the accretion flow. Our model is appropriate for systems accreting at $\ll 10^{-5}$ of the Eddington accretion rate, so radiative cooling by electrons can be neglected. It can be extended to higher accretion rates in the future by including electron cooling and proton-electron Coulomb collisions. We present a suite of tests showing that our method recovers the correct solution for electron heating under a range of circumstances, including strong shocks and driven turbulence. Our initial applications to axisymmetric simulations of accreting black holes show that (1) physically-motivated electron heating rates that depend on the local magnetic field strength yield electron temperature distributions significantly different from the constant electron to proton temperature ratios assumed in previous work, with higher electron temperatures concentrated in the coronal region between the disc and the jet; (2) electron thermal conduction significantly modifies the electron temperature in the inner regions of black hole accretion flows if the effective electron mean free path is larger than the local scale-height of the disc (at least for the initial conditions and magnetic field configurations we study). The methods developed in this chapter are important for producing more

realistic predictions for the emission from accreting black holes such as Sagittarius A* and M87; these applications will be explored in future work.

2.2 Introduction

A wide variety of low luminosity accreting black holes are currently interpreted in the context of a Radiatively Inefficient Accretion Flow (RIAF) model that describes a geometrically thick, optically thin disc with a low accretion rate and luminosity. In particular, this is true of the black hole at the center of our galaxy, Sagittarius A* (Narayan et al. 1998), the black hole at the center of Messier 87 (Reynolds et al. 1996), and other low luminosity Active Galactic Nuclei (AGN), as well as a number of X-ray binary systems (see Remillard & McClintock 2006 for a review). The gas densities in these systems are low enough that the time scale for electron-ion collisions is much longer than the time scale for accretion to occur, so a one-temperature model of the gas is no longer valid (as originally recognised by Shapiro et al. 1976, Ichimaru 1977, and Rees, Begelman, Blandford, & Phinney 1982). Instead, a better approximation is to treat the electrons and ions as two different fluids, each with its own temperature.

Calculating the emission from accreting plasma requires predicting the electron distribution function close to the black hole. To date, time dependent numerical models of RIAFs that attempt to directly connect to observations often assume a Maxwellian distribution with a constant electron to proton temperature ratio, T_e/T_p, and take the results of GRMHD simulations as the solution for the total gas temperature, $T_g = T_p + T_e$ (Dibi et al. 2012; Drappeau et al. 2013; Mościbrodzka et al. 2009). This neglects, however, several physical processes that have different effects on the electron and proton thermodynamics and that are currently only included in one-dimensional semi-analytic models. Such effects include electron thermal conduction (e.g., Johnson & Quataert 2007), electron cooling (e.g., Narayan & Yi 1995), and non-thermal particle acceleration and emission (e.g., Yuan et al. 2003). To date, extensions of the simple T_p/T_e = const. prescription have been limited to post-processing models that do not self-consistently evolve the electron thermodynamics over time. Examples include the prescription of Mościbrodzka et al. (2014) which takes T_p/T_e = const. in the disc proper but sets T_e = const. in the jet outflow region, as well as the model of Shcherbakov et al. (2012), who solve a 1-D radial equation for $T_p - T_e$ at a single time-slice in the midplane to obtain a functional relationship $T_p/T_e = f(T_g)$ that is then applied to the rest of the simulation. To enable a more robust connection between observations of accreting black holes and numerical models of black hole accretion, it is critical to extend the detailed thermodynamic treatment of electrons used in 1D calculations to multi-dimensional models. This is the goal of this chapter. In particular, we describe numerical methods for separately evolving an electron energy equation in GRMHD simulations. We focus on including heating and anisotropic thermal conduction in these models. Future work will include electron radiative cooling and Coulomb collisions between electrons and protons.

In a turbulent, magnetised plasma, electrons and ions are heated at different rates depending on the local plasma conditions (e.g., Quataert & Gruzinov 1999; Cranmer et al. 2009; Howes 2010; Sironi 2015). Furthermore, since the electron-to-proton mass ratio is small, electrons will both conduct and radiate their heat much more efficiently than the ions. The combination of these effects leads to the expectation that, in general, $T_e < T_p$. In the present paper, we thus neglect the effect of the electron thermodynamics on the overall dynamics of the accretion flow. This allows us to treat the simulation results as a fixed background solution on top of which we independently evolve the electrons. Even if we find that $T_e \sim T_p$ in some regions of the disc, this treatment may still be a reasonable first approximation given the uncertainties in the electron physics.

The neglect of electron cooling in the present chapter is reasonable for systems accreting at $\lesssim 10^{-5}$ of the Eddington rate, $\dot{M}_{\rm Edd}$, so that the synchrotron cooling time is much longer than the accretion time (Mahadevan & Quataert 1997). In particular, this likely includes Sagittarius A* in the galactic center. The application of our methodology to Sgr A* is particularly important given the wealth of multi-wavelength data (e.g., Serabyn et al. 1997, Zhao et al. 2003, Genzel et al. 2003a, Baganoff et al. 2003, Barrière et al. 2014) and current and forthcoming spatially resolved observations with the Event Horizon Telescope (Doeleman et al. 2008) and GRAVITY (Gillessen et al. 2010).[1]

The goal of this chapter is to present our formalism and methodology for evolving the electron thermodynamics and to apply the results to 2D (axisymmetric) GRMHD simulations of an accreting black hole. We show the range of possible electron temperature distributions in the inner region of the disc, which directly impacts the predicted emission. Future work will explore the impact that these results have on the emission, spectra, and images of Sagittarius A*.

The remainder of this chapter is organised as follows. §2.3 describes our theoretical model of electron heating and anisotropic electron conduction while §2.4 describes the numerical implementation of this model. §2.5 contains tests of the numerical implementation, §2.6 applies the model to a 2D simulation of an accretion disc around a rotating black hole, and §2.7 discusses the implications of this application and concludes. Boltzmann's constant, k_b, and proton mass, m_p, are taken to be 1 throughout. We use cgs units, with Lorentz-Heaviside units for the magnetic field (e.g., magnetic pressure is $b^2/2$), and a metric signature of $(-+++)$. We also assume that the gas is mostly hydrogen and ideal. Since we also assume $n_e \approx n_p \equiv n$, then $\rho = m_e n_e + m_p n_p \approx m_p n = n$ (setting $m_p = 1$), so we use ρ and n interchangeably.

2.3 Electron Thermodynamics

The accreting plasmas of interest are sufficiently low density that the electron-proton Coulomb collision time is much longer than the dynamical time and so a two-temperature structure can develop, with the protons and electrons having different temperatures (and, indeed, different distribution functions). Moreover, at the low accretion rates where radiative cooling can be neglected, the electron-electron and proton-proton Coulomb collision times are also much longer than the dynamical time (Mahadevan & Quataert 1997). However, the plasma densities are high enough

---

[1] This chapter was published in 2015, years before GRAVITY and EHT released their first results in 2018 (Gravity Collaboration et al.) and 2019 (Event Horizon Telescope Collaboration et al.), respectively. Note, however, that the first target of EHT was the black hole at the center of M87 and (as of the writing of this thesis) the EHT results for Sgr A* are still forthcoming.

that the plasma is nearly charge-neutral and so we assume that $n_e \approx n_p$. We further assume that the electron flow velocity is the same as that of the protons.[2] This need not strictly be true (e.g., in the solar wind the relative velocities of particle species can be of order the Alfven speed; e.g. Bourouaine et al. 2013), but is a reasonable first approximation. A similar approach is often used in modeling the global dynamics of the low-collisionality solar wind (e.g., Chandran et al. 2011).

Under these assumptions, the key difference in the electron and proton physics lies in their different thermodynamics: the protons and electrons have very different heating and cooling processes that need to be separately accounted for. Formally, because of the low collisionality conditions we should separately solve the electron and proton Vlasov equations. This is computationally extremely challenging, however, particularly in the global geometry required to predict the emission from accreting plasmas (even local shearing box calculations using the particle-in-cell technique to solve the Vlasov equation require an unphysical electron-proton mass ratio, thus making it difficult to reliably model the electron thermodynamics; e.g., Riquelme et al. 2012). As a result, we assume a fluid model in this paper. Our fluid approximation corresponds to taking moments of the Vlasov equation and applying closures on higher moments of the distribution function. As we shall describe, our closure corresponds to specific models for the conductive heat flux, the viscous momentum flux, and the turbulent heating rate of each particle species.

Our basic model is thus to take a single-fluid GRMHD solution (e.g., Komissarov 1999; Gammie et al. 2003; De Villiers & Hawley 2003) as an accurate description of the total fluid (composed of both the electron and proton gas) dynamics and thus the accretion flow density, magnetic field strength, and velocity field. We evolve the electrons as a second fluid on top of this background solution. The GRMHD solution may itself include viscosity and conduction as in Chandra et al. (2015b). Our assumption that the electrons do not back react on the flow dynamics is formally valid in the limit that $T_e \ll T_p$, but should be a reasonable approximation so long as $T_e \lesssim T_p$ in regions of large plasma $\beta \gtrsim 1$, i.e., where gas pressure forces are dynamically important. One advantage of not coupling the electron pressure to the GRMHD solution is that we can run multiple electron models in one simulation, allowing us to explore systematic uncertainties with a minimum of computational time.

In this paper, we focus on implementing electron heating and anisotropic conduction. Coulomb collisions are straightforward to include but are negligible for the low accretion rates at which electron cooling can be neglected. In future work, electron cooling will be self-consistently incorporated building on the BHlight code developed by Ryan et al. (2015).

2.3.1 Basic Model

The stress-energy tensors for the electron and proton fluids in our model take the form:

$$\begin{aligned} T_e^{\mu\nu} &= (\rho_e + u_e + P_e)\, u_e^\mu u_e^\nu + P_e g^{\mu\nu} + \tau_e^{\mu\nu} + q_e^\mu u_e^\nu + u_e^\mu q_e^\nu \\ T_p^{\mu\nu} &= \left(\rho_p + u_p + P_p\right) u_p^\mu u_p^\nu + P_p g^{\mu\nu} + \tau_p^{\mu\nu}, \end{aligned} \tag{2.1}$$

---

[2] More precisely, as in standard MHD, the relative velocity between electrons and protons required to produce currents that can maintain magnetic fields near $\beta \sim 1$ is orders of magnitude less than the mean sound speed.

where ρ_k, u_k, and P_k are the fluid frame density, internal energy, and pressure, respectively, u_k^μ is the fluid four-velocity in the coordinate frame, $\tau_k^{\mu\nu}$ is a general stress tensor that accounts for viscous effects, and q_e^μ is the heat flux carried by the electrons. The subscript k denotes p or e (and will also denote the total gas quantities labeled by g below). We leave $\tau_k^{\mu\nu}$ as a general tensor that will be model-specific. For each species, ignoring electron-electron, electron-ion, and ion-ion collisions, one can take the zeroth and first moment of the Vlasov equation to show that

$$\nabla_\mu \left(\rho_k u_k^\mu\right) = 0 \tag{2.2}$$

and

$$\begin{aligned} \nabla_\mu T_e^{\mu\nu} &= -enu_e^\mu F_\mu^{\ \nu} \\ \nabla_\mu T_p^{\mu\nu} &= enu_p^\mu F_\mu^{\ \nu}, \end{aligned} \tag{2.3}$$

where $F^{\mu\nu}$ is the electromagnetic field tensor. In ideal, single-fluid GRMHD in the absence of shocks, the conservation of entropy equation, $\rho T_g u^\mu \partial_\mu s_g = 0$, where s_g is the entropy per particle, follows directly from the conservation of particle number and the stress-energy (see page 563 in Misner et al. 1973). To derive entropy equations for the electron and proton fluid used in our model, we perform the same series of manipulations; namely, contracting both equations (2.3) with u^ν (the total fluid velocity, which we take to be $\approx u_p^\mu \approx u_e^\mu$) and invoking equation (2.2), which give us:

$$\rho T_e u^\mu \partial_\mu s_p = Q_p, \tag{2.4}$$

and

$$\rho T_e u^\mu \partial_\mu s_e = Q_e - \nabla_\mu q_e^\mu - a_\mu q_e^\mu, \tag{2.5}$$

where we have defined the heating rate per unit volume for each species as a sum of viscous and Ohmic resistance terms, $Q_e \equiv u_\nu \nabla_\mu \tau_e^{\mu\nu} + enu_e^\mu u^\nu F_\mu^{\ \nu}$ and $Q_p \equiv u_\nu \nabla_\mu \tau_p^{\mu\nu} - enu_p^\mu u^\nu F_\mu^{\ \nu}$, and where $a^\mu \equiv u^\nu \nabla_\nu u^\mu$ is the four-acceleration, which accounts for gravitational redshifting of the temperature by the metric. We can write the heating rates in terms of the electric field four-vector, $e^\mu \equiv u_\nu F^{\nu\mu}$, and the four-currents, $J_e^\mu \equiv -neu_e^\mu$, $J_p^\mu \equiv neu_p^\mu$ as[3]:

$$\begin{aligned} Q_e &= u_\nu \nabla_\mu \tau_e^{\mu\nu} + J_e^\mu e_\mu \\ Q_p &= u_\nu \nabla_\mu \tau_p^{\mu\nu} + J_p^\mu e_\mu. \end{aligned} \tag{2.6}$$

The intuitive understanding of the Ohmic heating terms on the right-hand side of equation (2.6) is that they are $\sim \vec{J}_k \cdot E$ evaluated in the rest frame of the total fluid. To derive the entropy equation for the total fluid, we first define several total fluid variables as a sum of electron and proton terms: $\rho = \rho_p + \rho_e \approx n$, $u_g = u_p + u_e$, $P_g = P_p + P_e$, $T_g = T_p + T_e$, $J^\mu = J_p^\mu + J_e^\mu = en(u_p^\mu - u_e^\mu)$ and $\tau_g^{\mu\nu} = \tau_e^{\mu\nu} +$

---

[3] We have kept the subscripts e and p for the four-currents (and thus four-velocities) in equation (2.6) because the details of the Ohmic heating depend on the small but non-zero velocity difference between the proton and electron fluids (or equivalently the velocity difference between the electron/proton fluid and the total fluid). An explicit expression for these terms would require a detailed kinetic theory calculation beyond the scope of the present work (i.e., some form of "generalized Ohm's Law," as in, e.g., Koide 2010). In our model, as described in the text, numerical resistivity provides the Ohmic heating that is then distributed to electrons and protons according to a closure model obtained from previous work in kinetic theory.

$\tau_e^{\mu\nu}$, denoting total gas mass density, internal energy, pressure, temperature, current, and viscous stress. Then, using the thermodynamic identity, $\rho T_k u^\mu \partial_\mu s_k = u^\mu \partial_\mu u_k - (u_k + P_k)\, u^\mu \partial_\mu \log(\rho)$, we find that the entropy per particle of the total gas, s_g, satisfies the relation $\rho T_g u^\mu \partial_\mu s_g = \rho T_p u^\mu \partial_\mu s_p + \rho T_e u^\mu \partial_\mu s_e$, resulting in

$$\rho T_g u^\mu \partial_\mu s_g = Q - \nabla_\mu q_e^\mu - a_\mu q_e^\mu, \tag{2.7}$$

with the total heating rate per unit volume:

$$Q = Q_p + Q_e = u_\nu \nabla_\mu \tau_g^{\mu\nu} + J^\mu e_\mu. \tag{2.8}$$

In practice, we use the electron entropy equation (2.5) to evolve the electron thermodynamics. To determine the overall dynamics of the electron + proton gas, we use Maxwell's equations in addition to a standard, single-fluid GRMHD evolution representing the total gas. The equations for the latter are obtained by separately summing the electron and proton parts of equation (2.2) and equation (2.3), resulting in a mass conservation equation,

$$\nabla_\mu (\rho u^\mu) = 0, \tag{2.9}$$

and an energy-momentum equation,

$$\nabla_\mu \left(T_g^{\mu\nu} + T_{EM}^{\mu\nu} \right) = -\nabla_\mu \tau_g^{\mu\nu}, \tag{2.10}$$

with the total gas stress-energy tensor,

$$T_g^{\mu\nu} = \left(\rho + u_g + P_g \right) u^\mu u^\nu + P_g g^{\mu\nu}, \tag{2.11}$$

and the electromagnetic stress energy tensor[4], $T_{EM}^{\mu\nu} = F^{\mu\alpha} F_\alpha^{\ \nu} - g^{\mu\nu} F_{\alpha\beta} F^{\alpha\beta}/4$. We have used the identity $\nabla_\mu T_{EM}^{\mu\nu} = -J^\mu F_\mu^{\ \nu}$ in equation (2.10), the assumption that $u_e^\mu \approx u_p^\mu \approx u^\mu$ in equation (2.11), and the charge-neutrality assumption $n_e = n_p = n$ throughout. Furthermore, we have dropped the electron thermal conduction terms in the evolution of the total gas properties, though we keep them in the evolution of the electron entropy (equation 2.5). This is consistent if $T_e \lesssim T_p$ since electron conduction will then affect the electron thermodynamics but not the overall stress-energy of the fluid. Finally, we take $T_{EM}^{\mu\nu}$ to be given by the ideal MHD limit (i.e., $e^\mu \to 0$):

$$T_{EM}^{\mu\nu} = b^2 u^\mu u^\nu + \frac{b^2}{2} g^{\mu\nu} - b^\mu b^\nu, \tag{2.12}$$

where $b^\mu \equiv \epsilon^{\mu\nu\kappa\lambda} u_\nu F_{\lambda\kappa}/2$ is the magnetic field four-vector defined in terms of the Levi-Civita tensor, $\epsilon^{\mu\nu\kappa\lambda}$, and $b^2 \equiv b^\mu b_\mu$ is twice the magnetic pressure. With these assumptions, equations (2.9), (2.10), and Maxwell's equations are simply the standard single-fluid equations of ideal GRMHD except with an explicit viscosity tensor. In standard conservative GRMHD codes (including the one used in this work), this viscosity tensor is not included explicitly but implicitly generated numerically by the Riemann solver. Furthermore, the Riemann solver also introduces a finite

---

[4] Here we have chosen to absorb a factor of $(4\pi)^{-1/2}$ into the definition of $F^{\mu\nu}$.

numerical resistivity into Maxwell's equations, allowing for a nonzero e^μ (and thus nonzero Ohmic heating). For further discussion of these points, see § 2.4.1.

To summarise, we take a standard single fluid GRMHD evolution of u^μ, ρ, u_g, and P_g as a reasonable estimate of the total gas properties. This corresponds to assuming that electron conduction has a negligible contribution to the dynamics of the total gas and that the adiabatic index is independent of the electron thermodynamic quantities (e.g.; $P_g/u_g \equiv [P_p+P_e]/[u_e+u_p] \equiv \gamma-1 \approx$ some function of total gas quantities only). Formally, this assumption requires that the electron internal energy is small compared to the proton internal energy. From this, we can calculate the heating directly from equation (2.7) (dropping the conduction terms) without requiring an analytic expression for Q. Finally, we use knowledge of the nature of heating in a collisionless plasma obtained from kinetic theory (described in §2.6.1) to relate the heating rate per unit volume of the electrons, Q_e, to that of the total fluid, Q, and directly add it to the electron entropy equation (equation 2.5), as described in §2.3.2. This completes our model.

For simplicity, we assume that the adiabatic indices of the electron, γ_e, proton, γ_p, and total gas, γ, are constants, where $P_k = (\gamma_k - 1)u_k$ for $k = e, p$, or g. This simplifies the numerical implementation of the model, as it allows us to write the entropy per particle in a simple form, $s_k = (\gamma_k - 1)^{-1}\log(P_k\rho^{-\gamma_k})$, and avoids the complication of having to evaluate T_p/T_e when updating the total fluid variables. This can be seen by noting that

$$\frac{P_g}{u_g} \equiv \frac{P_e + P_p}{u_e + u_p} = (\gamma_e - 1)(\gamma_p - 1)\frac{1 + T_p/T_e}{(\gamma_p - 1) + (\gamma_e - 1)T_p/T_e}, \tag{2.13}$$

which is only constant in the limits that $T_e \ll T_p$ or $T_p \ll T_e$. From this, we see that this simplification of $\gamma =$ const. is formally inconsistent if $\gamma_e \neq \gamma_p$, which is generally the case in the accreting systems of interest, where the electrons are typically relativistically hot ($\gamma_e \approx 4/3$) but the protons are nonrelativistic ($\gamma_p \approx 5/3$). However, since equation (2.13) is bounded between 1/3 and 2/3 and we expect $T_e \lesssim T_p \Rightarrow \gamma \approx \gamma_p$, we do not anticipate that this approximation will affect our results significantly.

2.3.2 Electron Heating

We parameterise the heating term, Q_e in equation (2.6) by writing $Q_e = f_e Q$, where $f_e(\beta, T_e, T_p, ...) \equiv Q_e/Q$ is the fraction of the total dissipation, Q, received by the electrons. This function, in general, depends on the local plasma environment and our model is not limited to any particular choice of f_e. As knowledge in the field develops we can readily incorporate different assumptions about electron heating. A more detailed discussion of one physically-motivated prescription for f_e is given in §2.6.1. Given a GRMHD solution, the total heating rate of a fluid element moving with four-velocity u^μ in the coordinate frame can be computed (from equation 2.7, dropping the conduction terms):

$$Q = \rho T_g u^\mu \partial_\mu s_g, \tag{2.14}$$

where s_g is the entropy per particle. We can rewrite equation (2.14) in terms of $\kappa_g \equiv P_g\rho^{-\gamma}$, where $s_g = (\gamma - 1)^{-1}\log(\kappa_g)$, as $Q = \rho^\gamma(\gamma - 1)^{-1}u^\mu\partial_\mu\kappa_g$. We use κ_g to avoid the undesirable numerical properties of logarithms as the argument goes to 0. Likewise, we will often use κ_e in place of s_e in equation (2.5).

2.3.3 Anisotropic Electron Conduction

Some care must be taken when generalising the theory of anisotropic conduction along magnetic field lines to a relativistic and covariant formulation. In particular, the theory must be consistent with causality in that the heat flux should not respond instantly to temperature gradients. Our formulation of anisotropic electron conduction draws heavily on the treatment of Chandra et al. (2015b), who consider a single fluid model in which the heat flux is coupled to the dynamics via the stress-energy tensor. We give a brief summary of our approach here, highlighting those aspects of our electron-only treatment that differ from the formulation in Chandra et al. (2015b).

One can derive a perturbation solution for the heat flux, q_e^μ, by expanding the entropy current in powers of q_e^μ and imposing the second law of thermodynamics. The most straightforward relativistic generalisation of the classical, isotropic heat flux first written down by Eckart (1940) is first order in this expansion and was later shown by Hiscock & Lindblom (1985) to be unconditionally unstable, precisely because it violated causality (Chandra et al. 2015b showed the same for anisotropic conduction). Israel & Stewart (1979) derived a second order solution for q_e^μ which was later shown to be conditionally stable (Hiscock & Lindblom 1985; Chandra et al. 2015b). Here we use a first order reduction of that second order model that has been shown to be both stable and self-consistent (Andersson & Lopez-Monsalvo 2011). We refer the reader to Chandra et al. (2015b) for more details.

We parameterise the heat flux as

$$q_e^\mu = \phi \hat{b}^\mu, \tag{2.15}$$

where $\hat{b}^\mu$ is a unit vector ($\hat{b}^\mu \hat{b}_\mu = 1$) along the magnetic field four-vector, b^μ, and the scalar ϕ is given by the following evolution equation:

$$\nabla_\mu \left(\phi \rho u^\mu\right) = \frac{1}{\sqrt{-g}} \partial_\mu \left(\sqrt{-g} \phi \rho u^\mu \right) = -\rho \left[\frac{\phi - \phi^{\rm eq}}{\tau} \right], \tag{2.16}$$

where g is the determinant of the metric, and we used an identity, $\nabla_\mu A^\mu = \partial_\mu(\sqrt{-g} A^\mu)/\sqrt{-g}$, to convert covariant derivatives into partial ones (eq. 86.9 in Landau & Lifshitz 1975). Here $\phi^{\rm eq}$ is the equilibrium value of the heat flux given by

$$\phi^{\rm eq} = -\rho \chi_e \left(\hat{b}^\mu \partial_\mu T_e + \hat{b}^\mu a_\mu T_e \right). \tag{2.17}$$

where χ_e is the thermal diffusion coefficient of the electrons and τ is the relaxation time scale for the heat flux over which it responds to temperature gradients. Note that equation (2.16) is a relaxation equation in which the heat flux relaxes on a timescale τ to the equilibrium value.

The equilibrium heat flux in equation (2.17) is the natural relativistic extension of anisotropic conduction along the magnetic field (analogous to the isotropic heat flux of Eckart 1940). The heat flux, q_e^μ, then contributes to the electron energy equation as in equation (2.5). Physically motivated prescriptions for the parameters χ_e and τ are all that are required to complete the model. We discuss one choice of these in §2.6.1.

Stability of Anisotropic Electron Conduction Theory

In our formalism, we assume that the fluid velocity, u^μ, and the electron number density, $n_e = \rho/m_p$, are independent of the electron thermodynamics. Thus, in order to do a perturbative analysis we need only perturb the electron temperature, T_e, and the heat flux, ϕ, in equations (2.5) and (2.16). Doing this in the fluid rest frame in Minkowski space, where $u^\mu = (1, 0, 0, 0)$, and writing the perturbations in Fourier space as $\propto \exp(\lambda t + i\vec{k} \cdot \vec{x})$, we find the dispersion relation:

$$\lambda^2 + \frac{\lambda}{\tau} + (\gamma_e - 1)\frac{\chi_e}{\tau}(\hat{b} \cdot \vec{k})^2 = 0 \tag{2.18}$$

with the solutions:

$$\lambda = \frac{1}{2\tau}\left(-1 \pm \sqrt{1 - 4(\gamma_e - 1)\chi_e \tau(\hat{b} \cdot \vec{k})^2}\right). \tag{2.19}$$

The theory is unstable if $\mathrm{Re}(\lambda) > 0$, which can only occur if the term under the square root is both real and greater than unity. However, this is impossible for any value of k when $\gamma_e \geq 1$, so we conclude that equations (2.5) and (2.16) are unconditionally stable. This is in contrast to the case where equations (2.5) and (2.16) are coupled to the ideal MHD equations, which is unstable to small perturbations unless the relaxation time is larger than a critical value (Hiscock & Lindblom 1985; Chandra et al. 2015b).

2.4 Numerical Implementation of Electron Heating and Conduction

The method outlined above can, in general, be applied to any GRMHD "background" simulation. For the rest of this work, however, we will consider only conservative codes, as the equations of ideal MHD can be naturally written in that form. Because of this, in what follows we will seek to put all of our evolution equations in a conservative form, namely:

$$\frac{\partial U}{\partial t} + \frac{\partial F^i}{\partial x^i} = S, \tag{2.20}$$

where U is a "conserved" variable, F^i is the corresponding flux in the ith direction, and S is the source, which in general includes the contribution from the connection coefficients. Equation (2.20) can then be approximated in one spatial dimension by the following discretisation:

$$\begin{aligned} U^{n+1} &= U^n \\ &\quad - \Delta t\left(\frac{F^{n+1/2}_{j+1/2} - F^{n+1/2}_{j-1/2}}{\Delta x} - S^{n+1/2}\right), \end{aligned} \tag{2.21}$$

where the fluxes are evaluated at face centres using the chosen Riemann solver. The generalisation to higher dimensions is straightforward.

With that in mind, we can rewrite equation (2.5):

$$\partial_\mu \left(\sqrt{-g}\rho u^\mu \kappa_e \right) = \frac{\sqrt{-g}(\gamma_e - 1)}{\rho^{\gamma_e - 1}} \left[f_e Q - \nabla_\mu q_e^\mu - a_\mu q_e^\mu \right], \tag{2.22}$$

where we have used the definition $\kappa_e \equiv \exp[(\gamma_e - 1)s_e]$. Note that equation (2.22) is a quasi-conservative equation with $U_{\kappa_e} = \sqrt{-g}\rho u^t \kappa_e$ and $F^i_{\kappa_e} = \sqrt{-g}\rho u^i \kappa_e$ ('quasi' conservative because the standard definition of conservative equations excludes source terms with derivatives). To solve equation (2.22), we use operator splitting in the following sequence of steps:

1. Solve the conservative equation with $S_{\kappa_e} = 0$.
2. Explicitly update κ_e with the heating term (the first term in the brackets in eq. 2.22).
3. Implicitly solve a matrix equation to include the conduction source terms (the rest of the terms in square brackets in eq. 2.22).

Steps 2 and 3 are described in detail in §2.4.3 and §2.4.4, respectively, while step 1 will be specific to the choice of the background numerical scheme.

2.4.1 Heating in Conservative Codes

Formally, the equations of ideal MHD used by conservative GRMHD simulations imply that the heating rate per unit volume, Q, in equation (2.8) is identically zero. However, conservative codes implicitly add numerical viscosity and resistivity terms to the stress-energy tensor and Maxwell's equations, respectively. The former implies that the numerically evolved stress tensor is in fact $T^{\mu\nu}_{g,\mathrm{num}} = T^{\mu\nu}_g + \tau^{\mu\nu}_g = T^{\mu\nu}_{MHD} + \mathcal{O}$ (truncation error) for some numerical viscosity tensor $\tau^{\mu\nu}_g$, while the latter implies $J_\mu e^\mu = 0 + \mathcal{O}$ (truncation error). The numerical resistivity can be thought of as implicitly introducing a form of Ohm's law that allows for a nonzero electric field four-vector, e^μ. Thus, even though the energy implied by $T^{\mu\nu}_{MHD,\mathrm{num}} = T^{\mu\nu}_{g,\mathrm{num}} + T^{\mu\nu}_{EM,\mathrm{num}}$ is conserved to machine precision (see below for details), $T^{\mu\nu}_{MHD}$ experiences truncation-level heating. This manifests itself as entropy generation: truncation errors lead to dissipation of magnetic and kinetic energy close to the grid scale that is captured as internal energy. We use this change in entropy to directly calculate the heating rate per unit volume of the gas, Q.

Although $T^{\mu\nu}_{MHD,\mathrm{num}}$ is conserved to machine precision, the second law of thermodynamics is satisfied only to truncation error. Thus there can be locally regions with $Q < 0$. In particular, the truncation error can be positive or negative, so in places with small actual change in entropy or large truncation error the change in entropy can be negative. This is the case even in test problems in which our methods of calculating the heating give the correct, converged, answer for the fluid variables (see § 2.5). Thus, while Q may be instantaneously or locally negative, when integrated over a sufficient length of time and/or space in the fluid frame it will satisfy the second law of thermodynamics.

We choose this method of calculating the heating rate as opposed to introducing an explicit functional form for Q because it seems reasonable to assume that for several applications, the grid-scale dissipation in conservative codes is a well-defined quantity determined by the converged large-scale physics of the problem. Turbulence, for example, takes kinetic and/or magnetic energy at the largest scales and cascades it down to a small dissipative scale where it is converted into internal energy. For a numerical scheme with no explicit viscosity, the scale at which dissipation occurs depends entirely on the resolution of the simulation, but we expect the heating rate itself will be fixed (in an averaged sense; see, e.g., Davis et al. 2010). We expect the same for forced reconnection at high β values, as in the disc midplane, where the large-scale dynamics sets the rate at which the field lines of opposite sign are brought together.

The above argument relies on the conservation of energy. In an arbitrary space-time, however, conservation of energy is only well-defined if the metric is stationary (time-independent) and therefore possesses a time-like Killing vector, K^μ. If such a vector exists (as it does for the Kerr metric of interest in this work), we can construct a conserved current from the stress-energy tensor via $J^\mu \equiv -K^\mu T^\nu_\mu$, where this current satisfies $\nabla_\mu J^\mu = 0$. This allows us to define a conserved energy in a coordinate basis:

$$E = \int J^t \sqrt{-g} dx^1 dx^2 dx^3, \tag{2.23}$$

where the integral is over all space (i.e. the space orthogonal to the time coordinate). Often, the Killing vector takes the form $K = \partial_t$, which simplifies equation (2.23) to

$$E = \int -T^t_t \sqrt{-g} dx^1 dx^2 dx^3. \tag{2.24}$$

Thus, $-T^t_t$ can be thought of as the conserved energy per unit volume for a particular choice of coordinates. The total energy, E, is conserved to machine precision, modulo fluxes of energy through the boundaries, so entropy can only be generated by conversion of one form of energy to another.

2.4.2 Calculating the Total Heating Rate

To calculate the heating generated at each time step, we introduce an entropy-conserving equation as a reference to compare with the energy conservation equation. The entropy-conserving equation is simply a conservation equation like equation (2.20) with $U_{\kappa_g} = \sqrt{-g}\rho u^t \kappa_g$, $F^i_{\kappa_g} = \sqrt{-g}\rho u^i \kappa_g$, and $S_{\kappa_g} = 0$. If we call the solution to this equation $\hat{\kappa}_g$ (the $\hat{}$ denotes the solution corresponding to entropy conservation), then we show in Appendix 2.B.1 that the total heating rate of the fluid (measured in the fluid rest frame) incurred over an interval Δt (measured in the coordinate frame),

$$Q = \left(\frac{\rho^{\gamma-1}}{\gamma-1}\right)^{n+1/2} \left[\frac{\rho u^t (\kappa_g - \hat{\kappa}_g)}{\Delta t}\right]^{n+1}, \tag{2.25}$$

where u^t accounts for the transformation of Δt from the coordinate frame to the fluid rest frame, n and $n+1$ denote the values at the beginning and the end of the time step, respectively, so that $t_{n+1} = t_n + \Delta t$, and $n+1/2$ denotes the values when calculating the fluxes. To compute the dissipation rate via eq. (2.25), we set $\hat{\kappa}^n_g = \kappa^n_g$ at the beginning of each time step and use $\hat{\kappa}^{n+1/2}_g = \kappa^{n+1/2}_g$ when calculating the fluxes. Physically, equation (2.25) means that the Lagrangian heating rate is set by the difference between the entropy implied by the total energy conserving solution (κ_g) and the entropy implied by the entropy conserving solution ($\hat{\kappa}_g$).

2.4.3 Electron Heating Update

Let us call $\hat{\kappa}_e$ the solution to equation (2.22) without any source terms. On top of this adiabatic evolution, electrons receive a fraction, f_e, of the heating of the gas, $Q_e = f_e Q$. In discrete form, this can be written as follows,

$$\frac{(\rho^{\gamma_e})^{n+1/2}}{\gamma_e - 1}(\kappa_e - \hat{\kappa}_e)^{n+1} = f_e^{n+1/2}\frac{(\rho^{\gamma})^{n+1/2}}{\gamma - 1}(\kappa_g - \hat{\kappa}_g)^{n+1}. \tag{2.26}$$

Therefore, the heating update to the electrons, $\hat{\kappa}_e^{n+1} \to \kappa_e^{n+1}$, takes the following form:

$$\kappa_e^{n+1} = \hat{\kappa}_e^{n+1} + \frac{\gamma_e - 1}{\gamma - 1}\left(\rho^{\gamma-\gamma_e} f_e\right)^{n+1/2}(\kappa_g - \hat{\kappa}_g)^{n+1}. \tag{2.27}$$

2.4.4 Electron Conduction Update

We note that the evolution equation for the heat flux ϕ (equation 2.16) is already in a quasi-conservative form if we define $U_\phi = \sqrt{-g}\rho u^\mu \phi$ and $F^i_\phi = \sqrt{-g}\rho u^i \phi$. We treat the evolution of ϕ in an operator split way similar to the evolution of κ_e with the following series of steps:

1 Solve the conservative equation with $S_\phi = 0$.

2 Implicitly solve a matrix equation to include the source terms.

The source terms in the electron entropy and ϕ equation due to conduction are given by:

$$\begin{aligned} S_{\kappa_e,\mathrm{cond}} &= \sqrt{-g}(\gamma_e - 1)\rho^{1-\gamma_e}\left(-\nabla_\mu q_e^\mu - a_\mu q_e^\mu\right) \\ S_\phi &= -\rho\sqrt{-g}\left[\frac{\phi + \rho\chi_e\left(\hat{b}^\mu\partial_\mu T_e + T_e\hat{b}^\mu a_\mu\right)}{\tau}\right], \end{aligned} \tag{2.28}$$

which are discretised in space by using slope-limited derivatives across three grid cells and discretised in time by centring the time derivatives at $t_{n+1/2}$. The latter discretisation gives us an implicit equation for the variables κ_e and ϕ at time t_{n+1}. If we call $\hat{\phi}^{n+1}$ the heat flux after being updated by step 1, and $\kappa_{e,\mathrm{H}}$ the electron entropy after being updated by heating, then this matrix equation takes the form:

$$\begin{pmatrix} a_{11} & a_{12} \\ a_{21} & a_{22} \end{pmatrix}\begin{pmatrix} \kappa_e^{n+1} \\ \phi^{n+1} \end{pmatrix} = \begin{pmatrix} b_1 \\ b_2 \end{pmatrix}, \tag{2.29}$$

with components

$$
\begin{aligned}
a_{11} &= \left(\frac{\sqrt{-g}\rho u^t}{\Delta t} \right)^{n+1} \\
a_{12} &= \left[\sqrt{-g}(\gamma_e - 1)\rho^{1-\gamma_e} \right]^{n+1/2} \left[\frac{\hat{b}^t}{\Delta t} \right]^{n+1} \\
a_{21} &= \left[\frac{\sqrt{-g}\rho^2 \hat{b}^t \chi_e}{\tau} \right]^{n+1/2} \left[\frac{\rho^{\gamma_e - 1}}{\Delta t} \right]^{n+1} \\
a_{22} &= \left(\frac{\sqrt{-g}\rho u^t}{\Delta t} \right)^{n+1}
\end{aligned}
\tag{2.30}
$$

and

$$
\begin{aligned}
b_1 =& \left(\frac{\sqrt{-g}\kappa_{e,\mathrm{H}}\rho u^t}{\Delta t} \right)^{n+1} + \left[(\gamma_e - 1)\rho^{1-\gamma_e} \right]^{n+1/2} \\
& \times \left[\sqrt{-g} \left(\frac{q_e^t}{\Delta t} \right)^n - \left(\partial_i \left(\sqrt{-g} q_e^i \right) - \sqrt{-g} q_e^\mu a_\mu \right)^{n+1/2} \right] \\
b_2 =& \left(\frac{\sqrt{-g}\hat{\phi}\rho u^t}{\Delta t} \right)^{n+1} - \sqrt{-g} \left(\frac{\rho\phi}{\tau} \right)^{n+1/2} \\
& + \sqrt{-g} \left(\frac{\rho^2 \chi_e}{\tau} \right)^{n+1/2} \\
& \times \left[\left(\hat{b}^t \right)^{n+1/2} \left(\frac{T_e}{\Delta t} \right)^n - \left(\hat{b}^\mu \partial_\mu T_e + \hat{b}^\mu a_\mu T_e \right)^{n+1/2} \right].
\end{aligned}
\tag{2.31}
$$

The system of equations has a straightforward solution,

$$
\begin{pmatrix} \kappa_e^{n+1} \\ \phi^{n+1} \end{pmatrix} = \frac{1}{a_{11}a_{22} - a_{21}a_{12}} \begin{pmatrix} b_2 a_{11} - b_1 a_{21} \\ b_1 a_{22} - b_2 a_{12} \end{pmatrix}. \tag{2.32}
$$

To ensure that the heat flux, ϕ, does not reach unphysically large values, we apply a limiting scheme to keep $|\phi| \lesssim \left(u_e + \rho_e c^2 \right) v_{t,e} \equiv \phi_{\max}$, where $\rho_e = \rho m_e / m_p$ and $v_{t,e}$ is the electron thermal speed. Since we are considering physical systems in which the electrons are always at least mildly relativistic, this limit effectively reduces to $|\phi| \lesssim u_e c / \sqrt{3}$, which corresponds to a 'saturated' heat flux in which the heat is redistributed at the electron thermal speed. The numerical implementation of this limit is to replace the values of the thermal diffusivity, χ_e, and the relaxation time-scale, τ, with 'effective' values (Chandra et al. 2015b):

$$
\chi_{\mathrm{eff}} = \chi_e f \left(\frac{|\phi|}{\phi_{\max}} \right), \tag{2.33}
$$

and

$$
\tau_{\mathrm{eff}} = \tau f \left(\frac{|\phi|}{\phi_{\max}} \right), \tag{2.34}
$$

where

$$f(x) = 1 - \frac{1}{1 + \exp\left(-\frac{x-1}{0.1}\right)} + \epsilon, \tag{2.35}$$

which sharply transitions from $1 \to \epsilon$ for some small ϵ as $|\phi| \to \phi_{\rm max}$. Thus, according to equation (2.16), when $|\phi| > \phi_{\rm max}$, $|\phi|$ decays exponentially on a timescale $\sim \epsilon\tau$ until it drops below $\phi_{\rm max}$. The parameter ϵ is chosen such that the criterion for numerical stability is always satisfied (see §2.4.4 and Appendix 2.B.3).

Numerical Stability of Electron Conduction

A detailed derivation of the criteria for numerical stability is in Appendix 2.B.3. The basic result is that for a Courant-Friedrichs-Lewy (CFL) number, C, reasonably chosen between 0 and 1, the relaxation time, τ, must satisfy

$$\tau > f(C)\left(\frac{\Delta t}{\Delta x}\right)^2 \chi_e, \tag{2.36}$$

where $f(C)$ is a function of the CFL number. This can be understood as a requirement that the relaxation time τ (which we are free to choose as arbitrarily large, though which should correspond to a physical time scale), must be larger than the time step Δt (which is limited by computational expense) by the ratio between Δt and the standard Courant limit for a diffusive process $\Delta t_{\rm diff} = \Delta x^2/\chi_e$.

2.4.5 Treatment of the Floors

Conservative codes deal poorly with vacua of internal energy and density. Because of this, many schemes employ floors on internal energy and density to ensure that the errors in solving for the primitive variables from the conservative variables do not produce unphysically small or negative values. The nature of the model outlined above requires special care to be taken when these floors are activated, as they introduce artificial changes in internal energy, which act as a source of heat, and density, which change the conversion between entropy and internal energy.

Electron Energy Floors

Though the second law of thermodynamics states that the heating term $u^\mu \partial_\mu \kappa_g$ should be positive definite, numerically we find that $u^\mu \partial_\mu \kappa_g$ can be locally negative because of truncation errors. This introduces the possibility of the electron internal energy going to zero (or even becoming negative) due to truncation error fluctuations in our heating term. To correct for this, we implement a floor on the electron internal energy that is 1% of the floor on the total gas internal energy. That is, if u_e drops below $0.01u_g$, we reset u_e to $0.01u_g$.

Total Gas Internal Energy Floors

When the floor on internal energy of the total gas is activated, there is an artificial increase in u_g which then shows up in our heating term. We treat this addition of energy as if it were a physical, isochoric addition to the energy of the gas and add it to the electrons as described above. We emphasise that the internal energy floor does not affect the system dynamics in any significant way because it is only activated in magnetically-dominated regions where the value of the internal energy is dynamically irrelevant.

Density Floors

When the floor on density is activated, the total gas internal energy remains unchanged. However, the value of $\hat{u}_g \equiv \hat{\kappa}_g \rho^\gamma/(\gamma - 1)$ increases by a factor of $(\rho_{\rm floor}/\rho_{\rm init})^\gamma$, where $\rho_{\rm init}$ is the pre-floor density. To correct for this, we require conservation of the evolved gas entropy when the density floor is activated by decreasing $\hat{\kappa}_g$ by a factor of $(\rho_{\rm floor}/\rho_{\rm init})^\gamma$. Furthermore, we enforce that the evolved electron entropy remains unchanged by the density floor in the same manner by decreasing κ_e by a factor of $(\rho_{\rm floor}/\rho_{\rm init})^{\gamma_e}$. Similar to the internal energy floors, the density floors do not affect the dynamics of the system.

2.5 Tests of Numerical implementation

In this section we describe a series of tests that demonstrate the robustness and accuracy of our method of evolving the electron internal energy. We implemented the model described in §2.3 and §2.4 into the conservative GRMHD code, HARM2D (High-Accuracy Relativistic Magnetohydrodynamics; Gammie et al. 2003; Noble et al. 2006). To speed up the computations, we parallelised the code using OpenMP and MPI via domain decomposition.

2.5.1 Tests of Electron Heating

In what follows we demonstrate the validity and convergence of our implementation of electron heating using a number of tests. The 2nd order convergence of HARM in smooth flows and 1st order convergence in discontinuous flows is well documented in Gammie et al. (2003) and we will not reproduce it here.

Explicit Heating in a Hubble-Type Flow

To test whether our discretizations of the heating is correctly time centred, i.e., converges at the expected 2nd order in time, we focus here on solving the electron equation when we introduce an explicit heating term to the total energy equation. We do this in an unmagnetised, 1D Hubble-type flow with $v \propto x$ (restricting ourselves to non-relativistic velocities). In the local rest frame of a fluid element, this velocity field gives an outflow in both directions that is homogenous and isotropic, causing the density to uniformly decrease with time as matter leaves the computational domain.

The velocity profile also scales with time to satisfy the momentum equation ($\partial v/\partial t + v\partial v/\partial x = 0$). In the absence of heating, the internal energy and pressure evolve according to entropy conservation ($P \propto \rho^{\gamma}$), so that the solution at later times is given by (Tchekhovskoy et al. 2007):

$$\begin{aligned} v &= \frac{v_0 x}{1+v_0 t} \\ u_g &= \frac{u_{g,0}}{(1+v_0 t)^{\gamma}} \\ \rho &= \frac{\rho_0}{1+v_0 t}. \end{aligned} \tag{2.37}$$

If we now add a cooling term to the energy equation, of the form:

$$Q = -\frac{u_{g,0} v_0 (\gamma - 2)}{(1+v_0 t)^3}, \tag{2.38}$$

the internal energy should evolve as

$$u_g = \frac{u_{g,0}}{(1+v_0 t)^2}. \tag{2.39}$$

Plugging these solutions in the electron entropy equation (2.22) for $f_e = 1$ and $u_e(t=0) = u_0$, we obtain:

$$\kappa_e = \frac{(\gamma - 2)(\gamma_e - 1)}{\gamma_e - 2} \frac{u_0}{\rho_0^{\gamma_e}} \frac{1}{(1+v_0 t)^{2-\gamma_e}}. \tag{2.40}$$

For the numerical test, we set these analytic solutions as the boundary and initial conditions in a one-dimensional grid and check if we maintain this solution after a dynamical time of $L/\max[v(t=0)]$. We set $\gamma = 5/3$, $\gamma_e = 4/3$, $\max(v_0 x) = 10^{-3}c$, and $\max(\rho v_0 x/u_g) = 1$, on a computational domain of $0 \leq x \leq 1$. Formally, since $\Theta_e \equiv kT_e/m_e c^2 \ll 1$, the choice of $\gamma_e = 4/3$ is unphysical. However the motivation for this choice stems from the fact that our primary application is to the inner regions of an accretion disc around a black hole, where we expect $\gamma_e \approx 4/3 \neq \gamma \approx 5/3$. We find that our calculation converges at second order (see Figure 2.1), up until the point at which the errors in the analytic solution due to relativistic effects become important (which, for $\max(v_0 x) = 10^{-3}$ is $\delta\kappa_e/\kappa_e \sim v^2/c^2 \sim 10^{-6}$).

1D (Noh) Shock Test

In Appendix 2.B.4, we show that for a high Mach number shock in which the electrons are assumed to receive a constant fraction f_e of the 'viscous' heating in the shock, the post shock electron internal energy u_e is given by:

$$\frac{u_e^f}{u_g^f} = \frac{f_e}{2}\left[\left(\frac{\gamma+1}{\gamma-1}\right)^{\gamma_e}\left(1-\frac{\gamma}{\gamma_e}\right) + 1 + \frac{\gamma}{\gamma_e}\right]\frac{\gamma^2-1}{\gamma_e^2-1}, \tag{2.41}$$

where u_g^f and γ are the post-shock internal energy and the adiabatic index of the fluid. Equation (2.41) assumes that the electrons do not back react on the shock structure, consistent with the

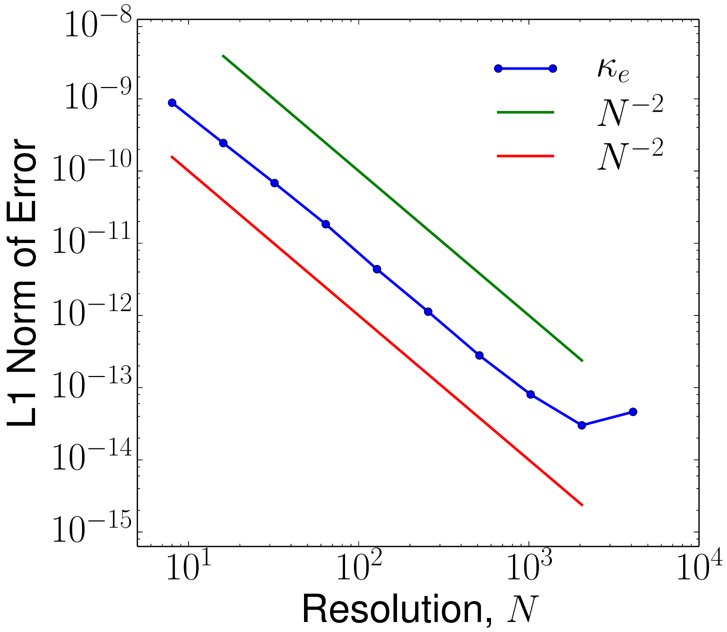

Figure 2.1: L1 norm of the error in the electron entropy for heating in a 1D Hubble-type flow (see §2.5.1). Above a resolution of ∼ 1000 the relativistic errors in the analytic result are comparable to the numerical truncation errors, so convergence is no longer seen.

model developed in this paper. When $\gamma = \gamma_e$, equation (2.41) is equal to f_e, while for $\gamma = 5/3$ and $\gamma_e = 4/3$ it is $\sim 0.76 f_e$. Here we check whether our numerical implementation of electron heating is consistent with this result.

The initial conditions for this test are an unmagnetised, non-relativistic ($\gamma = 5/3$), uniform density and internal energy fluid. The velocity profile is discontinuous at the center of the grid, with a left and a right state given by $v_l = -v_r = \text{constant} > 0$. The resulting solution is two shocks propagating outwards with a static region in between. We focus on a non-relativistic ($|v| = 10^{-3}c$) flow of initially cold gas so that the Mach number of the flow satisfies $M \gg 1$. For this test we fix $f_e = 0.5$ and show the results for both $\gamma_e = 4/3$ and $\gamma_e = 5/3$.

Figure 2.2 shows the density and electron internal energy as a function of position for a shock with $M \sim 49$ at $t = 0.6L/|v_l|$, where L is the size of the computational domain. Figure 2.3 shows that our simulation converges at 1st order to the analytic result for the post-shock electron internal energy when $\gamma = \gamma_e$ but to a value differing from the expected result by $\sim 3\%$ when $\gamma_e \neq \gamma$ (Figure 2.2). This difference is smaller at lower Mach number, as shown explicitly in Figure 2.4. The modest discrepancy between the analytic post-shock electron temperature and the HARM solution is because an accurate, converged calculation of the heating term requires a well-resolved shock structure that gets better resolved at higher resolution. This is not the case for modern shock capturing techniques, for which the numerical width of the shock is always a few grid points and our heating calculation is never able to resolve the shock. This is not an issue when $\gamma = \gamma_e$ because the factors of density in equation (2.27) cancel, removing the dependence on the shock structure. We show in Appendix 2.C that introducing an explicit bulk viscosity leads to convergence to the analytical result at 2nd order for $\gamma \neq \gamma_e$. However, the $\lesssim 3\%$ error as seen in Figures 2.2 and 2.4 is sufficient for our purposes so we do not include a bulk viscosity in our calculations.

2D Forced MHD Turbulence Test

Another test problem with a known, converged heating rate is driven turbulence in a periodic box. If we inject the fluid with a constant energy input rate of $\dot{E}_{\rm in}$ at large-scales, we should find that $\int Q dV = \dot{E}_{\rm in}$ after saturation of kinetic and magnetic energies has been reached. Thus, for the electron heating model outlined above, after this saturation point the electrons should receive a fraction f_e of $\dot{E}_{\rm in}$. Furthermore, if we have a periodic box in which the particle number is fixed, then the total internal energy change from adiabatic expansion/compression will sum to zero. Thus the analytic result we expect for our model of electron heating is that $\int \rho T_e \dot{s}_e dV = f_e \int Q dV = f_e \dot{E}_{\rm in}$. This test checks whether our model satisfies this result numerically.

We start with a static, uniform density fluid with $\beta = 6$ and sound speed $c_{s,0} = 8.6 \times 10^{-4} c$ in a 2D periodic box. The initial magnetic field is uniform: the magnetic field lines are straight and lie in the plane of the simulation. Then, at each time step, we give Gaussian random kicks to the velocity such that the wave number satisfies $\vec{k} \cdot \delta\vec{v} = 0$ (i.e. the driving is incompressible), and $\sigma_v^2 \propto k^6 \exp(-8k/k_{\rm peak})$ (compare to Lemaster & Stone 2009). The normalisation is fixed such that the rate of energy injection is equal to $\dot{E}_{\rm in} = 0.5\bar{\rho}c_{s,0}^3$. This leads to a rms turbulent velocity that is $\sim 0.8 c_{s,0} \sim 1.8 v_A$, so that the turbulence is subsonic and roughly Alfvénic. The peak driving wave number is set to half the box size: $k_{\rm peak} = 4\pi/L$. Furthermore, we ensure that no net momentum is added to the box by subtracting off (from the kicks) any average velocity that would have been generated by the kicks. For this test we fix $f_e = 0.5$, $\gamma = 5/3$ and $\gamma_e = 4/3$.

Figure 2.5 shows our results for the electron and total internal energies as a function of time in the box at 512^2. We see that once approximate saturation of the turbulence is reached at $t \sim L/c_{s,0}$ (or $\widetilde{t} \sim 0$ in the figure), the internal energies are in very good agreement with a linear fit, as expected given the constant rate of energy injection. For a parameterization of $\int u_e dV = g_e t + b_e$ and $\int u_g dV = g_g t + b_g$, g_e and g_g represent the electron and total heating rates, respectively. These can be compared to the energy injection rate, $\dot{E}_{in}$, which is a fixed constant of $0.5\bar{\rho}c_{s,0}^3$. At a resolution of 512^2, we find the total heating rate differs from $\dot{E}_{in}$ by $\sim 4\%$, while the electron heating rate differs from $f_e\dot{E}_{in}$ by $\sim 2\%$. Unfortunately, a rigorous convergence study of these quantities is not possible because of the nature of turbulence in 2D. Due to the inverse energy cascade, the kinetic and magnetic energies never truly saturate and convergence of *any* of the fluid variables is never achieved. This can be seen from Table 2.1, where the values of g_e and g_g are quoted at various resolutions, neither of which display significant convergence to the expected $0.5\dot{E}_{in}$ and $\dot{E}_{in}$, respectively. Nevertheless, we find the percent level error found at all resolutions to be sufficiently small to satisfy our error tolerance in the full accretion disc simulation.

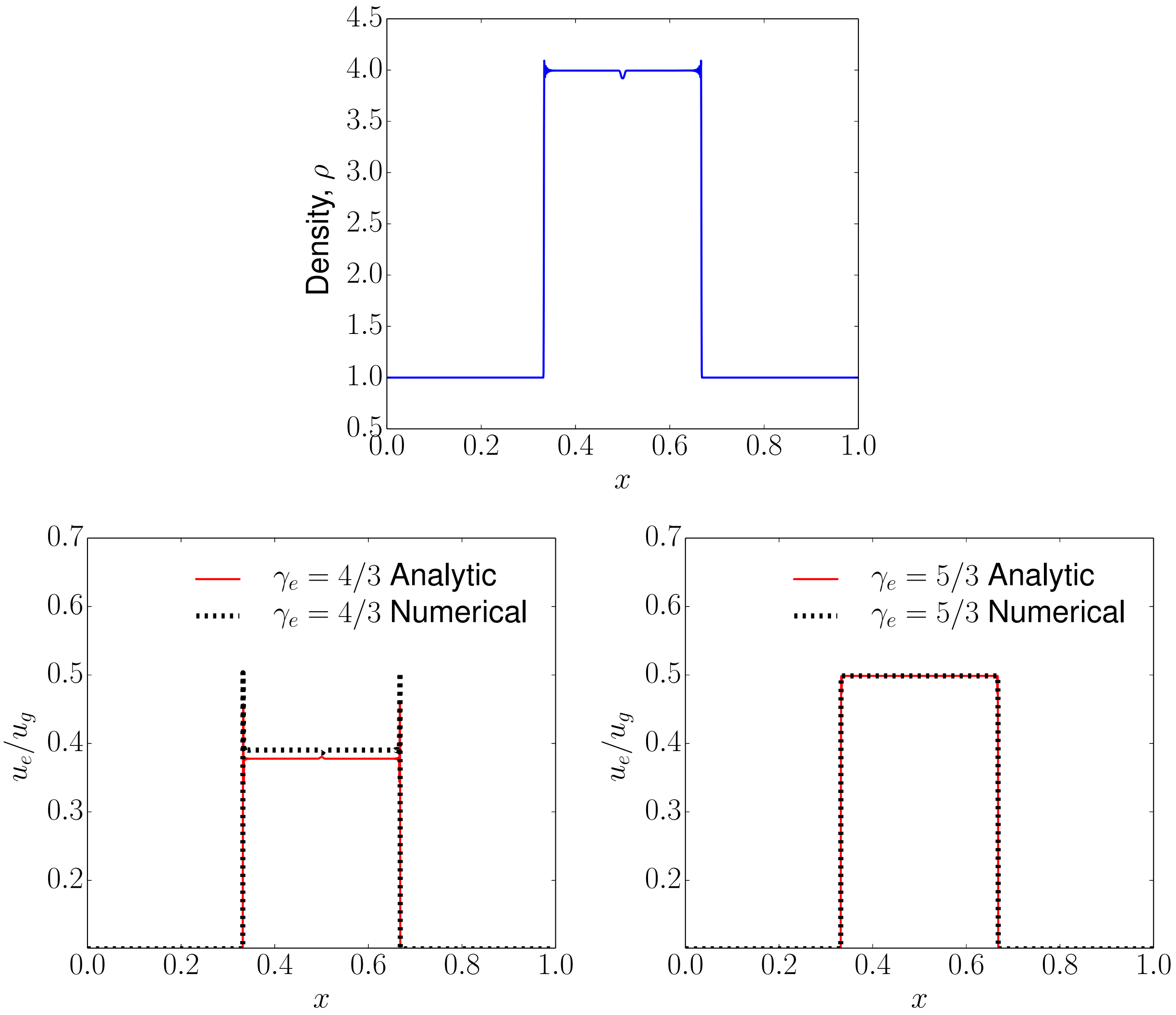

Figure 2.2: High Mach number shock results for an electron heating fraction $f_e = 0.5$ at a resolution of 2000 cells. Top: solid blue line shows the fluid density in a numerical simulation. Density undergoes a jump of $\rho_2/\rho_1 = (\gamma + 1)/(\gamma - 1) = 4$ at the two shocks, located at $x \approx 0.35$ and $x = 0.65$. Left: electron internal energy relative to total fluid internal energy for $\gamma_e = 4/3$. The analytic solution is shown with the solid red line and the numerical solution with the dotted black line. Right: the same for $\gamma_e = 5/3$. The analytic solution uses the functional form for $u_e/u_g(\rho)$ (see Appendices 2.B.4 and 2.C for details) and applies it to the density returned by the simulation. At this resolution all the fluid variables are essentially converged. The $\gamma_e = 5/3$ electrons show convergence to the expected result of $u_e = f_e u_g$ (the numerical and analytical lines are essentially on top of each other) while the $\gamma_e = 4/3$ electrons converge to a value that is greater than the analytic result ($u_e = 0.379 u_g$ for $f_e = 0.5$; equation 2.41) by $\sim 3\%$. This is because the internal shock structure is never well resolved without an explicit bulk viscosity (see §2.5.1 and Appendix 2.C for details).

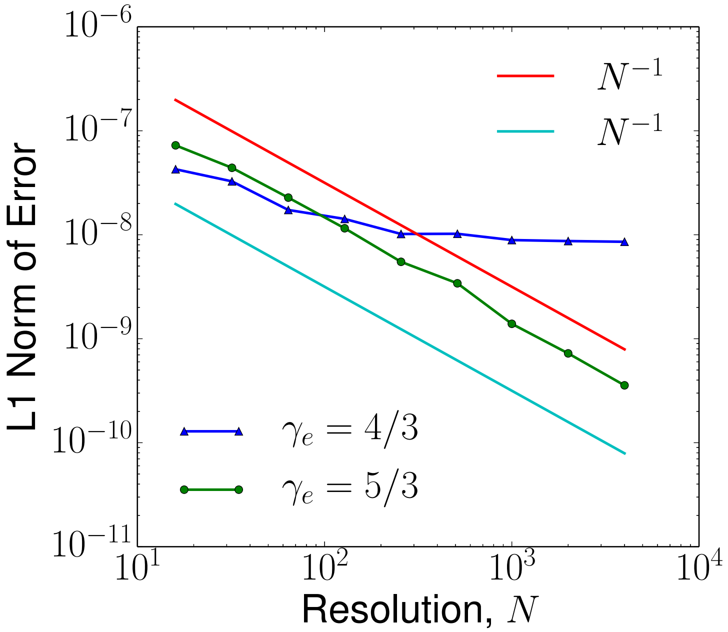

Figure 2.3: Convergence of the post-shock electron internal energy in the 1D shock test to the analytic solution (equation 2.41). The shock's Mach number is ~ 49 (see Sec. 2.5.1). The $\gamma_e = \gamma = 5/3$ electrons converge at 1st order, as expected, but the $\gamma_e = 4/3$ electrons do not converge to the correct solution to better than ~ 3% (see Figure 2.2). This is because our calculation of the heating requires a well-resolved shock structure, which is not the case for modern shock-capturing conservative codes (see §2.5.1 for details). Introducing an explicit bulk viscosity to resolve the shock structure leads to convergence for $\gamma_e \neq \gamma$ (see Appendix 2.C). For $\gamma_e = \gamma$, a convenient cancellation makes the evolution of the electron entropy independent of the shock structure.

Table 2.1: Turbulence Test Linear Fits (§2.5.1)

Resolution:	128	256	512
$g_e/\dot{E}_{in} - 0.5$[a]	0.0027	0.0042	0.0024
$g_g/\dot{E}_{in} - 1$[b]	−0.00017	0.0012	−0.0016

[a] Fractional error in the electron heating rate relative to the analytic solution.

[b] Fractional error in the total heating rate relative to the analytic solution.

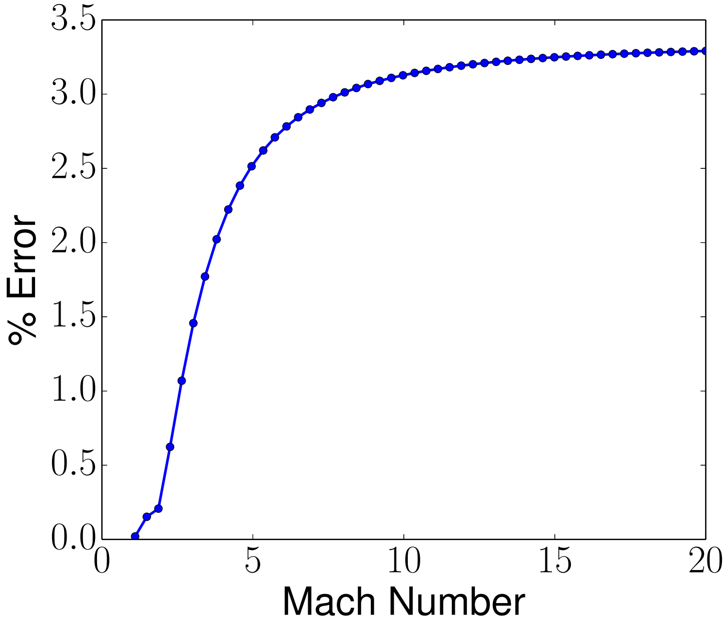

Figure 2.4: Percent error in the post-shock electron internal energy for $\gamma_e = 4/3$ and $\gamma = 5/3$ as a function of Mach number in the 1D shock test as computed by HARM at a resolution of 2000 for a fractional heat given to the electrons of $f_e = 1/2$ and an initial $u_e/u_g = 0.1$. The analytic solution is given by equation (2.84). The final time was fixed such that the two shocks were located at $x = 0.25$ and $x = 0.75$ in a $0 \leq x \leq 1$ domain. Note that the fractional errors are always $\lesssim 3.3\%$. The change in the percent error as Mach number goes to 1 is because the flow becomes increasingly smooth and the electron internal energy is no longer converged at a resolution of 2000.

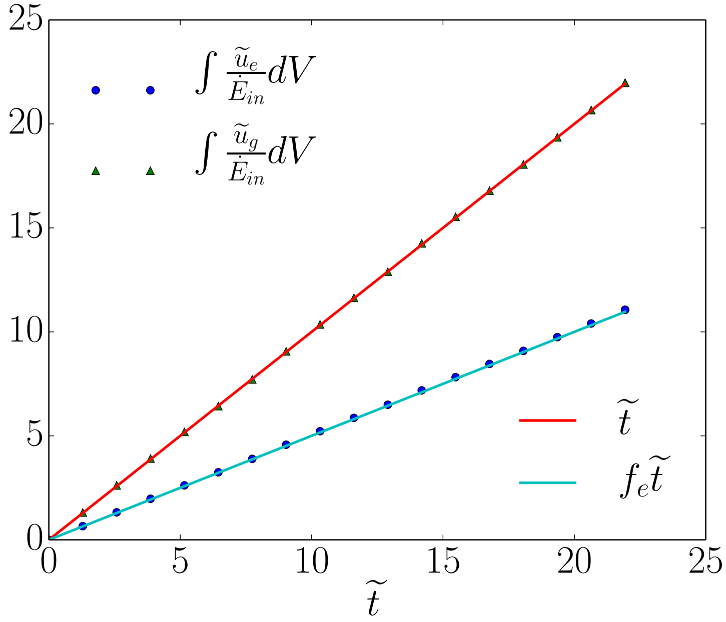

Figure 2.5: Electron and total gas internal energies summed over the grid as a function of time at a resolution of 512^2 for the forced subsonic MHD turbulence simulation with an assumed electron heating fraction of $f_e = 0.5$ and initial $\beta = 10$. We define $\widetilde{t} = (t - t_i)c_{s,0}/L$ and $\widetilde{u}_{g,(e)} = u_{g,(e)} - u_{g,(e)}(t = t_i)$, where $t_i \sim 4L/c_{s,0}$ is the time at which kinetic and magnetic energy roughly saturate. We normalised the integrated internal energy by the energy injection rate, $\dot{E}_{\rm in} = 0.5\rho c_{s,0,}^3$, so that the y-axis has dimensions of time which we measure in units of $L/c_{s,0}$. In these variables, the analytic solutions for the total gas and electron internal energies are lines with slopes of 1 and $f_e = 0.5$, which are plotted as solid lines, to be compared to the simulation results which are represented by points. We find that the electron heating rate is 0.5 of the total heating rate, consistent with the analytic solution given the input value of $f_e = 0.5$. For a numerical comparison at different resolutions, see Table 2.1, which shows the results of applying a linear regression fit to the internal energies.

Shadow Solution

For our two-temperature model, we can seek a solution in which the electron fluid simply 'shadows' the total gas, in that $u_e \propto u_g$. Such a solution is found by setting $u_e(t = 0) = f_e u_g(t = 0)$ at some initial time, since we can solve the first law of thermodynamics for the electrons with $u_e = f_e u_g$ for all time, assuming that $\gamma_e = \gamma$ and f_e is a constant. This can be seen from the first law:

$$u^\mu \partial_\mu u_e = f_e \rho T_g u^\mu \partial_\mu s_g - \frac{u_e + P_e}{\rho} u^\mu \partial_\mu \rho, \tag{2.42}$$

because the electrons will always get a fraction, f_e of the entropy-generated heat (the first term on the RHS of equation 2.42), while the compression term is directly proportional to $u_e \propto f_e u_g$. This solution is valid regardless of the details of the overall fluid evolution, so we can apply it to an arbitrarily complicated system.

For this test, we evolve the electron internal energy in the full accretion disc simulation around a rotating black hole as outlined in §2.6. We initially apply small ($\delta u_e/u_e \sim 0.04$) perturbations to the electron internal energy about the average value of $u_{g,e,0} = 0.5 u_{g,0}$, and set $f_e = 0.5$ and $\gamma_e = \gamma = 5/3$. For this test alone, we set the floor on electron internal energy to be a fraction f_e of the floor on the total fluid (as opposed to our usual choice of 1%). If this latter step were neglected, the floors would cause the polar regions to differ significantly from the expected result, though leaving the disc and corona unaffected (i.e. they still satisfy the analytic result). The test is whether or not our simulation can maintain this result over the run time of $2000M$.

Running this test at a resolution of 512^2 gives an average fractional error of

$$\frac{1}{N^2} \sum_{j=0}^{N-1} \sum_{i=0}^{N-1} \left| \frac{\left(\left[u_e/u_g \right]_{ij} - f_e \right)}{f_e} \right| \sim 0.8\%, \tag{2.43}$$

which is smaller than our initial perturbations and shows that our numerical solution correctly evolves equation (2.42) even in a complex problem with MHD turbulence, weak shocks, and other heating processes in the presence of a curved metric.

2.5.2 Tests of Electron Conduction

Our model and testing suite for conduction closely resembles that of Chandra et al. (2015a), so we leave the details to Appendix 2.A. In summary, we have found second order convergence for linear modes, for a static, 1D atmosphere in the Schwarzschild metric, and for a relativistic, spherically symmetric Bondi accretion flow. We also show that the electrons properly conduct along field lines in a 2D test.

2.6 Application to an Accreting Black Hole in 2D GRMHD Simulations

We apply the new methods discussed in §2.3 and the numerical implementation described in §2.4 to the astrophysical environment of an accretion disc surrounding a spinning black hole as described by the Kerr Metric with a spin parameter of $a = 0.9375$. For this spin the last stable circular orbit is $\approx 2.04 r_g$ and the thin disc radiative efficiency is ≈ 0.18 (Novikov & Thorne 1973). We use the conservative code HARM (Gammie et al. 2003) as our background GRMHD solution. Our initial conditions for the total fluid are the Fishbone & Moncrief (1976) equilibrium torus solution (see Appendix 2.D) with inner radius $r_{\rm in} = 6 r_g$ and with the maximum density of the disc occurring at $r_{\rm max} = 12 r_g$. Note that here and throughout r and θ refer to the Boyer-Lindquist coordinates. This equilibrium solution has a temperature maximum of $\approx 7.5 \times 10^{10} K$ and a thickness[5] of $h/r \sim 0.18$ at $r_{\rm max}$. We normalise the torus density distribution such that the maximum value of density in the torus is $\rho_{\rm max} c^2 = 1$ and perturb the internal energy of the gas with random kicks on the order of $\delta u_g / u_g \sim 0.04$ to provide the perturbations for the magnetorotational instability (MRI, Balbus & Hawley 1991a) to develop.[6] We overlay this equilibrium solution with an initial magnetic field with $2P_{\rm max}/b^2_{\rm max} = 100$ (where max refers to the maximum value inside the torus), defined by the scalar vector potential:

$$A_\varphi \propto (\rho/\rho_{\rm max} - 0.2) \cos\theta, \tag{2.44}$$

if $\rho > 0.2 \rho_{\rm max}$ and 0 otherwise. This vector potential defines two meridional loops contained in the torus that are antisymmetric about the equator. This choice ensures that the field lines are not along constant density. Since constant density implies constant temperature when entropy is constant, field lines along constant density would be isothermal in the initial condition (as would happen if we dropped the factor of $\cos\theta$ in eq. 2.44). 2D MHD torus simulations are unable to reach a statistical steady state in which the initial conditions are forgotten, so initially isothermal field lines could artificially suppress electron conduction even at later times. We choose the 2-loop initial condition to avoid this.

For the electrons, we start with $u_e/u_g = 0.1$, and run two different models for f_e, described below. For conduction runs, we set the initial heat flux to zero.

Our conduction runs are all in 256^2 grids with a physical size of the domain in spherical polar coordinates of $(R_{\rm in}, R_{\rm out}) \times (\theta_{\rm in}, \theta_{\rm out}) = (0.8 r_{\rm H}, 1000 r_g) \times (0, \pi)$, where $r_{\rm H} = r_g(1 + \sqrt{1 - a^2})$ is the black hole event horizon radius. For $a = 0.9375$, $r_{\rm H} \approx 1.35 r_g$. In the regions with $r < 50 r_g$, the code uses modified Kerr-Schild coordinates (t, x^1, x^2, and φ) of Gammie et al. (2003), so that the regions with the highest resolution are near the mid-plane close to the horizon. For $r > 50 r_g$, we use hyper-exponential coordinates to move out the outer radial boundary $r = R_{\rm out}$ and limit

---

[5] Here we define $h/r \equiv \iint \rho u^t |\theta - \pi/2| \sqrt{-g} {\rm d}\theta {\rm d}\phi \Big/ \iint \rho u^t \sqrt{-g} {\rm d}\theta {\rm d}\phi$.

[6] In addition to the electron specific floor described in §2.4.5, there are also floors on the density and internal energy of the HARM single fluid GRMHD solution. These are $\rho_{\rm floor} c^2 = \max\left[b^2/50, 10^{-4} (r/r_g)^{-3/2} \rho_{\rm max} c^2\right]$ and $u_{\rm floor} = \max\left[b^2/250, 10^{-6} (r/r_g)^{-5/2} \rho_{\rm max} c^2\right]$. Note that the unit choice for the background "atmosphere" is such that the initial torus maximum density is $\rho_{\rm max} c^2 = 1$ and the initial torus internal energy is $u_{\rm max} \approx 0.01$.

unphysical reflection effects by defining the internal code coordinate x^1 implicitly by the equation (Tchekhovskoy et al. 2011):

$$r/r_g = \begin{cases} \exp(x^1) & : \quad r \leq 50 r_g \\ \exp\left\{x^1 + [x^1 - x^1(r = 50 r_g)]^4\right\} & : \quad r > 50 r_g. \end{cases}$$

The electron heating-only (i.e. without conduction) runs have the same parameters but a higher resolution of 512^2. At the inner and outer radial boundaries we apply the standard outflow (copy) boundary conditions, at the polar boundaries we apply the standard antisymmetric boundary conditions (with all quantities symmetric across the polar axis except u^θ and B^θ, whose signs are reversed).

Figure 2.6 shows the background HARM solution for the density, magnetic field, temperature, plasma $\beta \equiv 2P_g/b^2$, and the heating rate per unit volume in the coordinate frame, $-Qu_t$, averaged over the time interval 900−1100 r_g/c, as well as the initial field configuration. After $\sim 1200 r_g/c$ the turbulence starts to decay, an artefact of 2D simulations in which MRI turbulence is not sustainable.

As noted in §2.4.1, we find locally that $Q < 0$ (violating the second law of thermodynamics) in many regions due to truncation errors. This is because HARM satisfies the total energy equation to machine precision but only satisfies the second law of thermodynamics to truncation error. However, while Q may be instantaneously or locally negative, when integrated over a sufficient length of time and/or space in the fluid frame it will satisfy the second law of thermodynamics. In our torus simulation, for instance, Figure 2.7 shows that when averaged over θ and time (900 − 1100 r_g/c), the heating rate is entirely positive definite within the region of interest. Furthermore, when integrated over the volume enclosed between the event horizon, r_H, and $r = 6r_g$ (roughly the radius at which the accretion time $\sim$ 1000 r_g/c), we find

$$\int_0^{2\pi}\int_0^{\pi}\int_{r_H}^{6r_g} -u_t Q (r^2 + a^2\cos^2\theta)\sin\theta \,\mathrm{d}r\,\mathrm{d}\theta\,\mathrm{d}\varphi \approx 0.17\dot{M}c^2, \tag{2.45}$$

where the factor of $-u_t$ converts Q to the coordinate frame. In equation (2.45), $\dot{M}$ is the accretion rate of the black hole in terms of coordinate time (corresponding to time measured by a distant observer) at the event horizon radius, $r = r_{\rm H}$,

$$\dot{M} = \int_{r=r_{\rm in}} \rho u^r (r^2 + a^2\cos^2\theta)\sin\theta\,\mathrm{d}\theta\,\mathrm{d}\varphi. \tag{2.46}$$

The heating rate in equation (2.45) is in excellent agreement with that expected for a rapidly spinning black hole (e.g., the Novikov & Thorne 1973 model predicts a radiative efficiency of ≈ 0.18 for $a = 0.9375$).

In this work, all mass-weighted averages are computed using the weighting function: $\rho u^t\sqrt{-g}$, which represents the conserved mass per unit coordinate volume. For example, a radial average of a function $f(x^1, x^2, x^3, t)$ is computed as:

$$\frac{\int_{x^1_{\min}}^{x^1_{\max}} f(x^1, x^2, x^3, t)\rho u^t \sqrt{-g} dx^1}{\int_{x^1_{\min}}^{x^1_{\max}} \rho u^t \sqrt{-g} dx^1}. \tag{2.47}$$

2.6.1 Electron Parameter Choices

Here we describe physically motivated estimates of the electron heating fraction, f_e, and the electron thermal diffusivity, χ_e, appropriate for low-collisionality accretion flows such as that of Sagittarius A*. A more comprehensive exploration of physical models will be explored in future work.

We consider two simple models for the electron heating fraction f_e. The first sets $f_e = 1/8$, a constant. Because the electron adiabatic index is not the same as the proton (total) adiabatic index, and the heating is not spatially uniform, a constant f_e model does *not* necessarily lead to a constant T_p/T_e. The second, more physical model, sets f_e based on theoretical models of the dissipation of MHD turbulence in low-collisionality plasmas. These generically predict that electrons receive most of the turbulent heating at low β while protons receive most of the turbulent heating at high β. This is true both for reconnection (Numata & Loureiro 2015) and collisionless damping of turbulent fluctuations (Quataert & Gruzinov 1999). This dependence on β is the key qualitative feature of our chosen model of f_e. For concreteness, we use the specific calculations of Howes (2010) who provided a simple fitting function for the electron to proton heating rate as a function of plasma parameters in calculations of the collisionless damping of turbulent fluctuations in weakly compressible MHD turbulence like that expected in accretion discs. These models do a reasonable job of explaining the measured proton and electron heating rates in the near-Earth solar wind (Howes 2011). The functional form of f_e is derived from the relations:

$$\frac{Q_p}{Q_e} = c_1 \frac{c_2^2 + \beta_p^{2-0.2\log_{10}(T_p/T_e)}}{c_3^2 + \beta_p^{2-0.2\log_{10}(T_p/T_e)}} \sqrt{\frac{m_p T_p}{m_e T_e}} e^{-1/\beta_p}, \tag{2.48}$$

with $c_1 = 0.92$, $c_2 = 1.6/(T_p/T_e)$, and $c_3 = 18 + 5\log_{10}(T_p/T_e)$ for $T_p/T_e > 1$, while $c_2 = 1.2/(T_p/T_e)$ and $c_3 = 18$ for $T_p/T_e < 1$. The corresponding result for f_e is simply

$$f_e \equiv \frac{Q_e}{Q_p + Q_e} = \frac{1}{1 + Q_p/Q_e}. \tag{2.49}$$

The critical assumption used in deriving equation (2.48) is that the turbulent fluctuations on the scale of the proton Larmor radius have frequencies much lower than the proton cyclotron frequency. This is believed to be well-satisfied for weakly compressible MHD turbulence in accretion disks (e.g., Quataert 1998). For concreteness, we note that for $T_p/T_e = 1$ and $\beta_p = (0.1, 0.3, 1, 10)$,

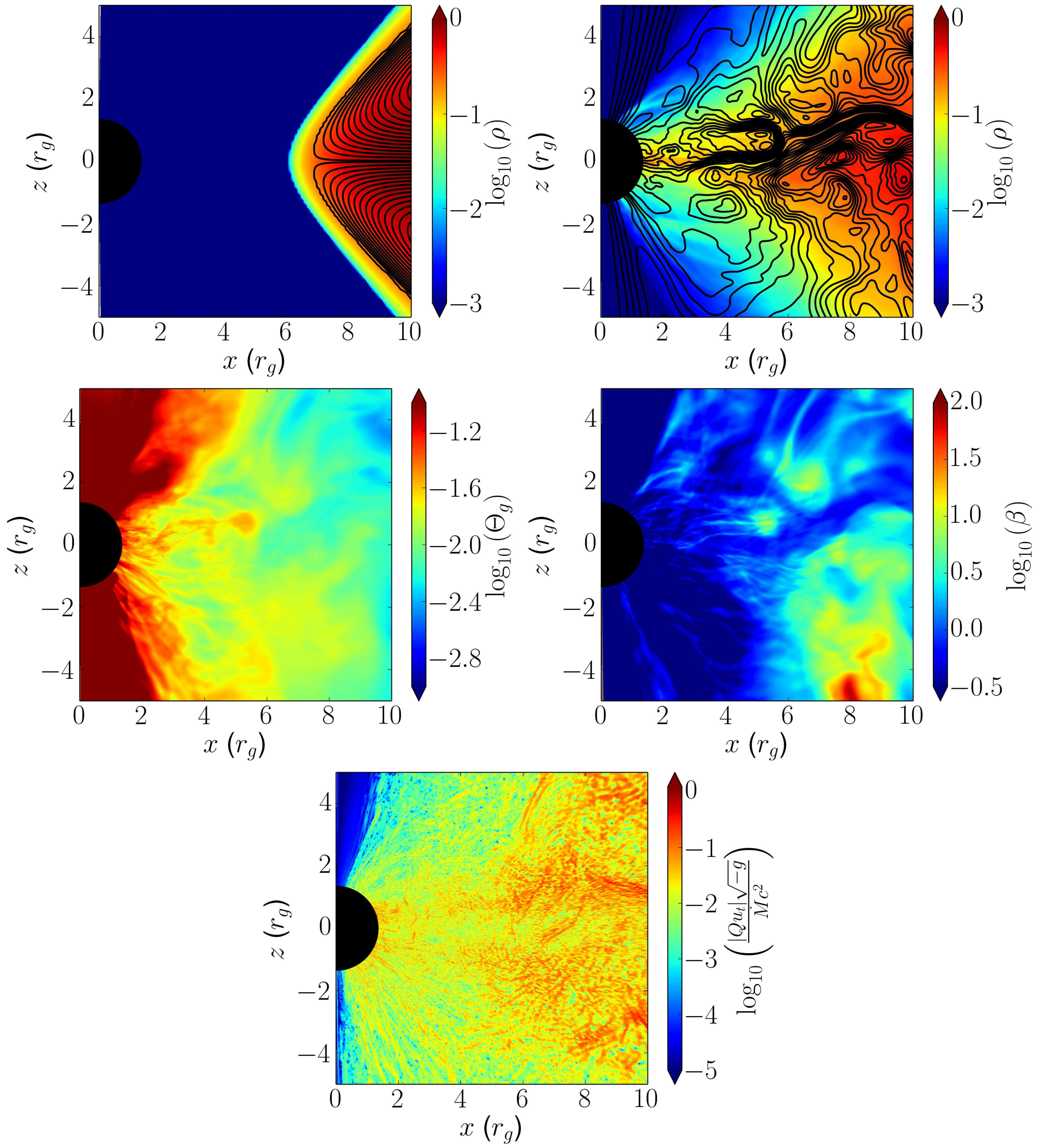

Figure 2.6: Properties of our 2D black hole accretion simulations. The top panel shows the density overplotted with magnetic field lines in the initial conditions (left) and averaged over $900 - 1100\ r_g/c$ (right). The remaining panels are the total gas temperature in units of $m_p c^2$ (middle left), the plasma parameter, $\beta \equiv 2P_g/b^2$ (middle right), and the absolute value of the heating rate per unit volume in the coordinate frame, $|Qu_t|$, in units of $\dot{M}c^2/(\sqrt{-g})$ (bottom), all averaged over time in the interval $900 - 1100\ r_g/c$. Note that for calculating the average β, we use $2\langle P_g\rangle/\langle b^2\rangle$, where $\langle\rangle$ denotes an average over time. These plots represent the background GRMHD solution on top of which we separately solve the electron entropy equation.

we have $Q_p/Q_e = (0, 0.01, 0.16, 8.6)$, while for $T_p/T_e = 10$ and $\beta_p = (0.1, 0.3, 1, 10)$, $Q_p/Q_e = (0, 0.001, 0.09, 12)$, respectively. This demonstrates the strong transition from predominantly electron to predominantly proton heating with increasing β_p, with the transition happening at a value of β_p that depends weakly on the proton to electron temperature ratio. This implies that we expect strong electron heating in the corona and jet regions but suppressed electron heating in the bulk of the disc.

We reiterate that the key feature of equation (2.48) is not the precise value of the predicted Q_p/Q_e, but rather the transition from $Q_p \gtrsim Q_e$ for $\beta_p \gg 1$ to $Q_p \ll Q_e$ for $\beta_e \ll 1$. This qualitative transition is much more robust than the specific functional form in equation (2.48) (e.g., Quataert & Gruzinov 1999; Numata & Loureiro 2015).

For the electron thermal diffusion parameters, since χ_e is a diffusion coefficient, we assume that it has the form

$$\chi_e = \alpha_e c r, \tag{2.50}$$

where α_e is a dimensionless thermal diffusivity, and r is the radial distance from the center of the black hole, which is comparable to the density scale height of the disc, H. Since we are interested in fairly relativistic electrons, we choose the relevant velocity to be c in our diffusivity estimate. In what follows, we consider a range of dimensionless diffusivities, $\alpha_e \sim 0.1 - 10$. A typical value of $\alpha_e \sim 1$ is motivated by the idea that particles scatter roughly after moving a distance comparable to the length-scale over which the magnetic field strength, density, etc. change. In fact, for high beta plasmas, the mean free path due to wave-particle scattering can be significantly lower, reducing the thermal diffusivity significantly. In Appendix 2.B.2 we discuss the specific limits imposed by electron temperature anisotropy instabilities present in a turbulent plasma. In particular, the whistler and firehose instabilities lead to limits on $\Delta T_e/T_e$ (eq. 2.66) and thus the electron viscosity and thermal diffusivity, where the temperature anisotropy is defined with respect to the local magnetic field. In terms of the electron thermal diffusivity, this becomes $\chi_e = \min(\alpha_e r c, \chi_{\max})$, where $\chi_{\max}$ is set by velocity space instabilities and is estimated in Appendix 2.B.2. Finally, we choose the relaxation time scale, τ to be given by the thermal time scale:

$$\tau \sim \frac{\chi_e}{v_{th}^2} \sim \frac{\chi_e}{c^2}. \tag{2.51}$$

Comparing this to the stability condition given by equation (2.36), we see that stability is ensured if

$$v_{th} \lesssim \frac{\Delta x}{\Delta t}. \tag{2.52}$$

Since we have a non-uniform grid, the time step Δt is essentially set by the light crossing time of the smallest grid cell (i.e. that nearest the horizon), meaning that $\Delta t \lesssim c\Delta x$ near the horizon and $\Delta t \ll c\Delta x$ further from the horizon. For a reasonable choice of a CFL number of 0.5, we find that equation (2.52) is satisfied everywhere and is not a limiting factor in our simulation. Moreover, we find that the exact value of τ is not critical as long as it satisfies numerical stability and is not too long (e.g. is less than a local dynamical time).

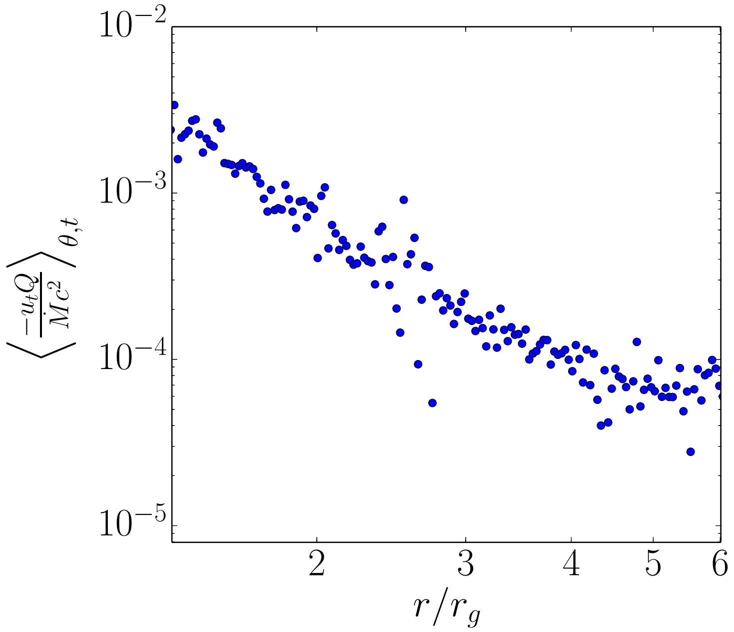

Figure 2.7: Mass-weighted average (see eq. 2.47) of the heating rate per unit volume in the coordinate frame, averaged over time in the interval 900 − 1100 r_g/c and over θ from 0 to π. Note that for our metric sign convention, $u_t \leq 0$. The total volume integrating heating out to $\sim 6r_g$ is $\sim 0.17\dot{M}c^2$ (equation 2.45), comparable to the Novikov & Thorne (1973) heating rate for this black hole spin.

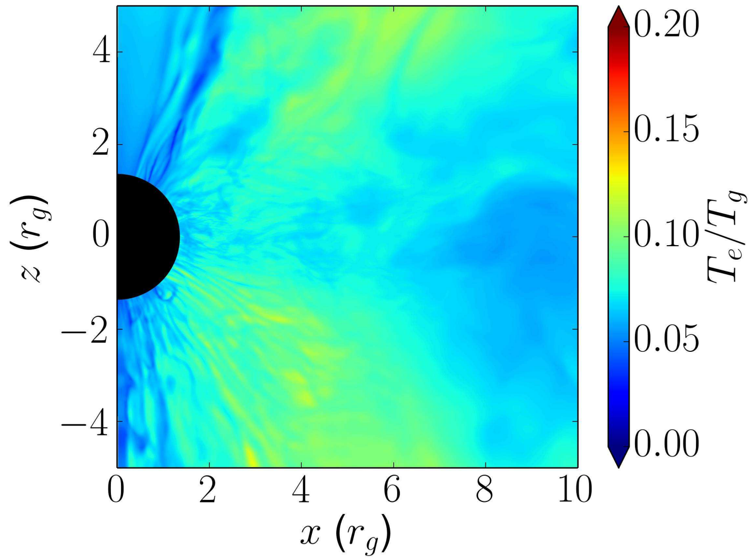

Figure 2.8: Ratio of $\langle T_e \rangle / \langle T_g \rangle$ in our black hole accretion simulation, where $\langle \rangle$ denotes an average over time in the interval $900 - 1100\ r_g/c$ (where T_g is the temperature of the single fluid GRMHD simulations and T_e is the electron temperature). These results assume a constant fraction of dissipated heat is given to the electrons ($f_e = 1/8$). Compare with the more physical β-dependent heating results in Figure 2.9.

2.6.2 Electron Heating Only

In this section we focus solely on the effects of separately evolving the electron internal energy equation without conduction in our black hole torus simulation and compare the results for different electron heating models.

Constant Electron Heating Fraction

Figure 2.8 shows the temperature ratio, T_e/T_g, averaged over the interval $900 - 1100 r_g/c$ for $f_e = 1/8$. We reiterate that T_g here is the temperature inferred from the underlying single fluid GRMHD solution (approximately the proton temperature in our model) while T_e is the electron temperature determined from our separate electron entropy equation. We include this constant f_e result primarily because it is conceptually similar (although quantitatively different) to the constant T_p/T_e assumption often used in the literature. Notice that the resulting T_e/T_g ratio, seen in Fig. 2.8, is non-uniform despite the constant f_e. Also note that due to the fact that MHD turbulence is unsustainable in 2D simulations, the heating dies off after $\sim 1200 r_g/c$ of evolution and prevents the outer $r \gtrsim 10 r_g$ region of the disc from ever being heated substantially. However, as we will see later, conduction can occur at a much faster (electron thermal) speed along the magnetic field lines and can affect the solution at somewhat larger radii.

β-Dependent Electron Heating

Figure 2.9 shows the temperature ratio, T_e/T_g, the electron temperature itself, Θ_e, and the electron heating fraction, f_e, averaged over the interval $900 - 1100\ r_g/c$ for the β-dependent heating model of equation (2.48), which we regard as a more physical electron heating model than $f_e =$ const. We note that this leads to hot electrons being strongly concentrated in the corona of the torus in between the disc and the jet, where β is the smallest (and $f_e \sim 1$ from equation 2.48). This is also clear from the 1D profiles of electron temperature as a function of polar angle in Figure 2.10.

Figure 2.10 shows the mass-weighted average over radius ($r = 5{-}7 r_g$) of the electron and gas temperatures, plotted versus the polar angle, θ. The $f_e = 1/8$ electrons and total gas temperatures have mild variation in T with θ, while the $f_e = f_e(\beta)$ electrons have significantly higher temperatures in the polar regions. This demonstrates that the non-uniformity of the electron temperature in the $f_e(\beta)$ model is primarily caused by the strong β-dependence of our model of f_e as opposed to any non-uniformity of the heating rate itself (Figure 2.6).

2.6.3 Conduction and Electron Heating

We now consider the effects of electron conduction on the electron temperature structure of black hole accretion discs. We focus on the more physical model of β−dependent heating described in §2.6.1. In all of our calculations, we include the velocity space instability limit on the electron thermal conductivity (Appendix 2.B.2), although runs without this limit produce similar results because β is modest ($\lesssim 1 - 10$) in the inner regions of these simulations (Figure 2.6). Figure 2.11 shows the electron temperature as a function of radius at the mid-plane in the simulations with and without conduction. Figure 2.12 shows the effects of conduction more quantitatively via the fractional change in temperature between the electron temperature solution with conduction and that without.

To summarise Figures 2.11 and 2.12, conduction has little effect on the electron temperature for $\alpha_e \lesssim 1$. However, for $\alpha_e \gtrsim 1$, conduction leads to a significant radial redistribution of heat such that the electron temperature is factors of a few larger at large radii. Even for $\alpha_e > 1$, however, the angular redistribution of heat is much less efficient, as seen in the radially and time-averaged electron temperatures in Figure 2.10 for $\alpha_e = 10$. This is primarily because of the structure of the magnetic field, as can be seen by noting that the regions where conduction modifies the temperature in Figure 2.12 largely follow magnetic field contours which do not efficiently connect the polar and equatorial regions. To aid the interpretation of these results, Figure 2.13 shows the heat flux ϕ normalised to the maximum value $\phi_{\max} = (u_e + \rho_e c^2)v_{t,e}$; even for $\alpha_e = 10$ the heat flux is still well below the saturated value in significant parts of the domain. We now summarise and interpret these results in more detail.

For $\alpha_e \lesssim 1$ we find conduction to have only a small effect on the electron thermodynamics in the accretion disc, despite the relatively high conductivity. We can understand this result as being due to the suppression of the isotropic heat flux by being projected along field lines, quantified by

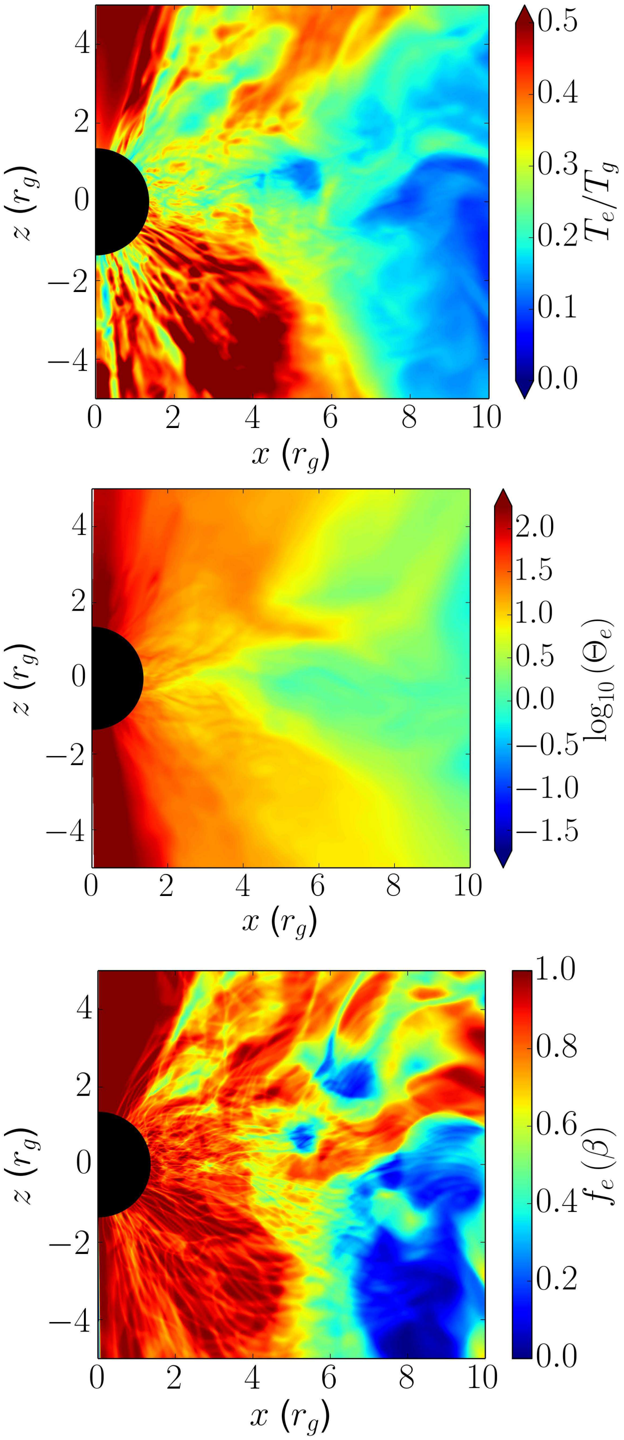

Figure 2.9: Ratio of $\langle T_e \rangle / \langle T_g \rangle$ (top), electron temperature, $\langle T_e \rangle$, in units of $m_e c^2$ (middle), and electron heating fraction, $\langle f_e \rangle$ (bottom), where $\langle\rangle$ denotes an average over time in the interval $900 - 1100\ r_g/c$. These results are for β-dependent heating (see §2.6.2). Compare to Figure 2.8 for a constant electron to proton heating ratio. The highly non-uniform distribution of β (see Figure 2.6) and the strong β dependence of the electron-to-total heating ratio (equation 2.48) lead to a strong angular dependence of T_e/T_g.

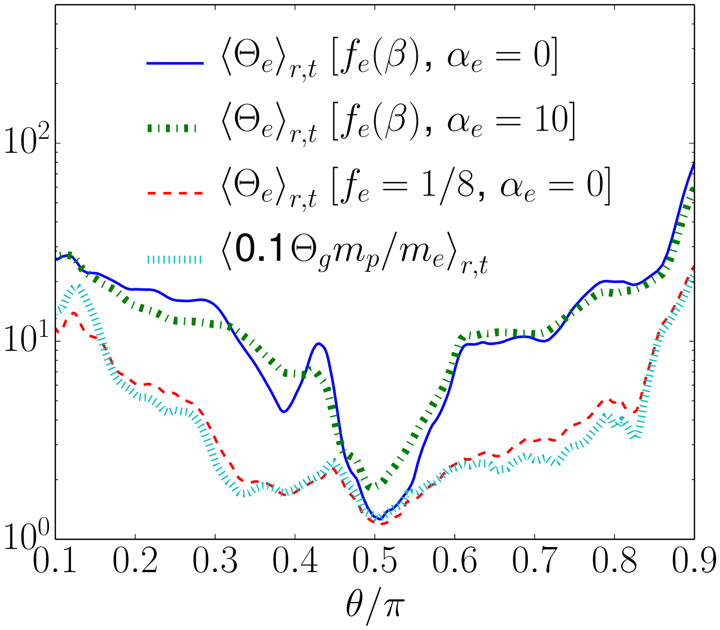

Figure 2.10: Mass-weighted average of total gas and electron temperature (in units of $m_e c^2$) as a function of the polar angle, θ. We show the electron temperature with and without conduction for a β-dependent electron heating fraction, f_e, as well as without conduction for a constant electron heating fraction $f_e = 1/8$. The results are averaged over time from $900-1100$ r_g/c and averaged over r from $5-7$ r_g. Note that the total gas temperature has been multiplied by a constant fraction to more clearly compare to the electron temperatures. The electron temperature with β-dependent heating displays much stronger θ variation because the electron heating fraction itself varies with θ (see Figure 2.9). Conduction has only a modest effect on redistributing heat in θ due to the geometry of the field.

the ratio,

$$\epsilon^2 \equiv \frac{\left(q_\mu q^\mu\right)_{\rm aniso}}{\left(q_\mu q^\mu\right)_{\rm iso}}, \tag{2.53}$$

where $q^\mu_{\rm iso}$ and $q^\mu_{\rm aniso}$ are evaluated using the electron temperature as evolved *without* conduction and which we now define. For this diagnostic, we use

$$q^\nu_{\rm iso} = -\rho\chi_e h^{\mu\nu}\left(\partial_\mu T_e + T_e a_\mu\right), \tag{2.54}$$

where $h^{\mu\nu} = u^\mu u^\nu + g^{\mu\nu}$ is the projection tensor that projects along a space-like direction perpendicular to the fluid velocity u^μ. This projection ensures that the heat flux in the fluid frame has a zero time-component. Likewise, for $q^\nu_{\rm aniso}$, we use the first order anisotropic heat flux: $q^\nu_{\rm aniso} = \left(\hat{b}^\mu q^{\rm iso}_\mu\right)\hat{b}^\nu$. Note that in equation (2.53), ϵ is always ≤ 1 because both heat fluxes are mutually orthogonal to u^μ. Figure 2.14 shows $|q_{\rm aniso}| \,/\, |q_{\rm iso}|$ in our torus simulation, where we find the suppression of the isotropic heat flux to be around $\epsilon \sim 0.2$. The simplest explanation for this small number is that the field is predominantly in the φ direction, where the temperature gradient is identically 0 in 2D simulations. For instance, in local shearing box calculations, Guan et al. (2009) found that the typical angle between $\vec{B}$ and $\hat{\varphi}$ was $\sim 10 - 15°$, corresponding to a suppression of the heat flux with $\epsilon \sim 0.25$.

Contrary to the $\alpha_e < 1$ cases, setting $\alpha_e \geq 1$ causes conduction to have a significant effect by redistributing the electron heat from the coronal regions to the bulk of the torus at larger radii. This redistribution of heat causes the electron temperature to actually exceed the total gas temperature in certain regions, which formally violates our assumption that $T_e \ll T_p$.

While the calculation with $\alpha_e = 10$, or with $\chi_e = 10rc$, might seem to use an unphysically large conductivity, roughly corresponding to a length scale for conduction of $\sim 10H$, where H is the disc density scale height, the heat flux in these calculations is limited to be smaller than the value set by the physically motivated whistler criterion in equation (2.67) and to be less than the saturated heat flux $\sim u_e c$. As Figure 2.13 shows, the heat flux is saturated in only part of the domain. Furthermore, the appropriate length scale for conduction should be the scale height *along field lines*, which could be significantly greater than the overall density scale height if the field has a large toroidal component. For these reasons, we believe that the larger α_e solutions may in fact be physical because they correspond to a heat flux closer to the saturated value $\sim u_e c$ expected in low-collisionality plasmas.

2.7 Conclusions

We have presented a method for evolving a separate electron entropy equation in parallel to the standard equations of ideal General Relativistic MHD. Our motivation is the study of two-temperature radiatively inefficient accretion flows (RIAFs) onto black holes, in which the electron-proton Coulomb collision time is sufficiently long that the proton and electron thermodynamics decouple (e.g., Rees et al. 1982). Understanding the electron temperature distribution close to

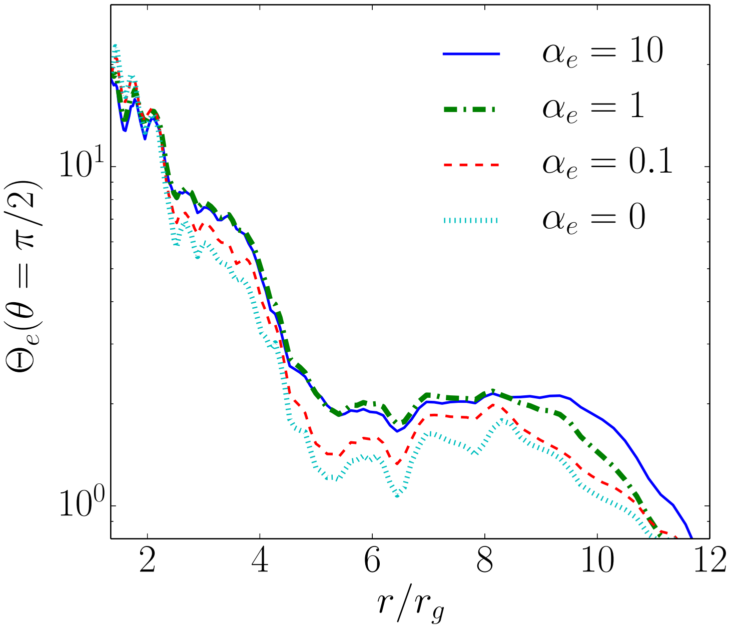

Figure 2.11: Electron temperature in the mid-plane ($\theta = \pi/2$) in units of $m_e c^2$ for black hole accretion simulations with β-dependent heating and for electron conduction with dimensionless conductivity $\alpha_e = 0, 0.1, 1, 10$ (where the electron thermal diffusivity is $\chi_e = \alpha_e r c$; see §2.6.1). The results are time averaged over the interval $900 - 1100 r_g/c$. For $\alpha_e \gtrsim 1$, conduction redistributes energy from small to large radii, increasing the electron temperature at larger radii. Compare to Figure 2.10, which shows that redistribution of heat in the polar direction is less efficient.

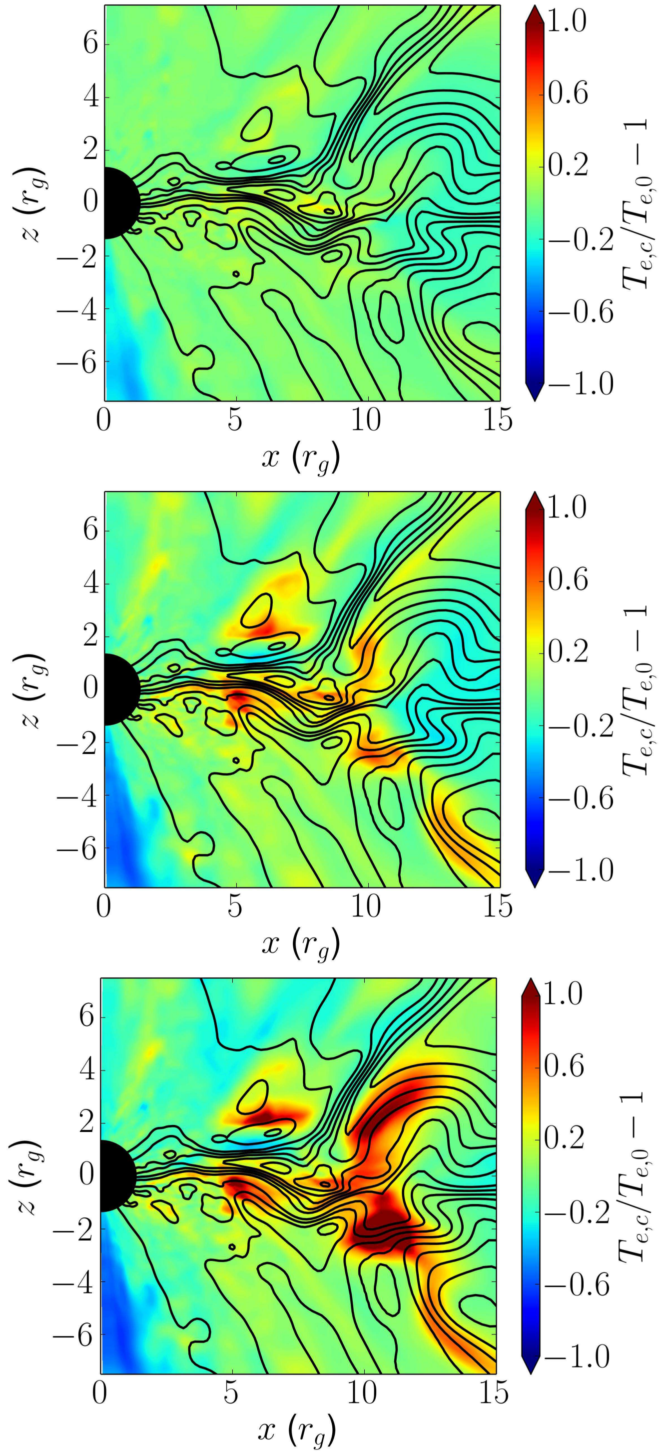

Figure 2.12: Fractional difference in electron temperature between solutions with and without electron conduction shown in colour (see colour bar for details) over-plotted with magnetic field lines shown as solid black lines. The fractional difference is calculated as $\langle T_{e,c} \rangle / \langle T_{e,0} \rangle - 1$, where $\langle \rangle$ denotes an average over time from $900 - 1100\ r_g/c$. The results include β-dependent electron heating for $\alpha_e = 0.1$ (top), $\alpha_e = 1$ (middle), and $\alpha_e = 10$ (bottom panel), where the electron thermal diffusivity is $\chi_e = \alpha_e rc$ (§2.6.1). Higher α_e allows more heat to flow from the inner regions to larger radii. For $\alpha_e = 0.1$ conduction has a negligible effect on the electron temperature, while for $\alpha_e \gtrsim 1$ conduction leads to order unity changes in T_e.

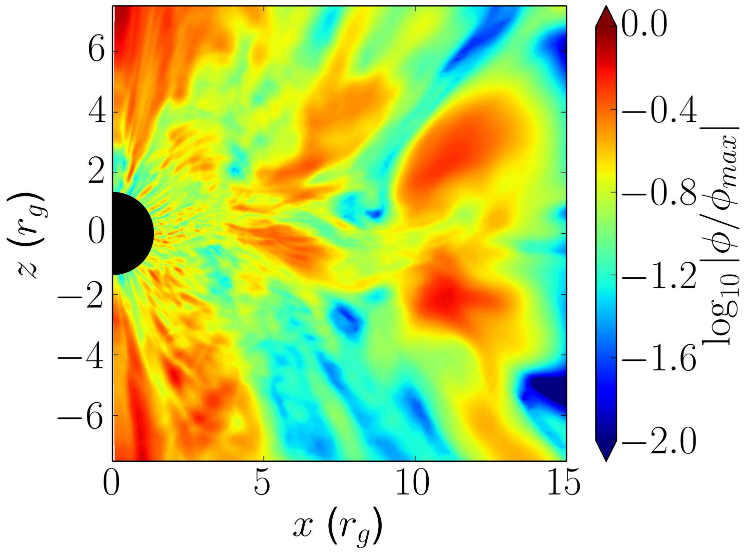

Figure 2.13: $\langle|\phi|\rangle/\langle\phi_{\rm max}\rangle$, the ratio of the electron heat flux to the maximum value $\phi_{\rm max} = (u_e + \rho_e c^2)v_{t,e}$, where $\langle\rangle$ denotes an average over time from $900 - 1100\ r_g/c$. This is calculated based on the results of a black hole accretion simulation with β-dependent electron heating and a dimensionless electron thermal conductivity of $\alpha_e = 10$ (where the electron thermal diffusivity is $\chi_e = \alpha_e rc$; see §2.6.1). Comparison with Figure 2.12 shows that conduction has a significant effect on redistributing heat only in the regions where the heat flux is saturated or nearly saturated. However, even for a high electron thermal conductivity of $\alpha_e = 10$, the heat flux is still well below the saturated value over much of the domain.

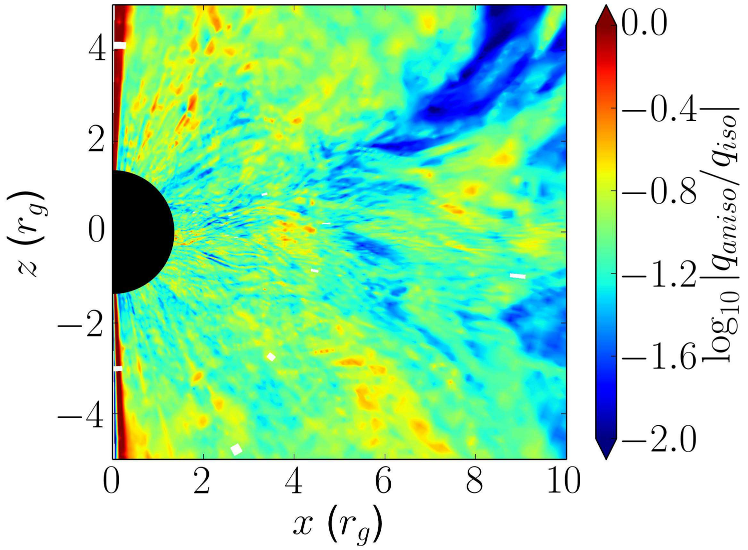

Figure 2.14: $\langle|q_{\rm aniso}|\rangle/\langle|q_{\rm iso}|\rangle$, the ratio of the anisotropic (field-aligned) heat flux to the isotropic heat flux , where $\langle\rangle$ denotes an average over time from $900 - 1100\ r_g/c$. This is calculated based on the results of a black hole accretion simulation with β-dependent electron heating but without conduction. The factor of $\sim 5 - 10$ suppression of the field aligned heat flux is roughly consistent with that expected from local shearing box calculations of MRI turbulence, where $\vec{B}$ is aligned with the $\hat{\varphi}$ direction (e.g. Guan et al. 2009).

the black hole is necessary for robustly predicting the radiation from the numerical simulations of black hole accretion (and outflows) in the sub-Eddington regime.

The long-term goal of the present work is to incorporate the key processes that influence the electron thermodynamics in RIAFs into GRMHD simulations: heating, thermal conduction, radiative cooling, and electron-proton Coulomb collisions. In the present chapter we have focused on the first two of these processes. Specifically, we have developed, implemented, and tested a model that quantifies the rate of heating in a conservative GRMHD simulation (§2.3). We then assign a fraction f_e of this heating to the electrons based on a microphysical model of the key heating processes (e.g., turbulence, reconnection, shocks; see, e.g., §2.6.1). In addition, we have implemented and tested a model of relativistic anisotropic conduction of heat (by electrons) along magnetic field lines, based on the Chandra et al. (2015b) formulation of anisotropic relativistic conduction (§2.3.3). The electron thermal diffusivity is a free parameter in this calculation. For the black hole accretion disc applications of interest, we advocate a 'saturated' heat flux in which the thermal diffusivity is $\sim rc$, subject to additional constraints imposed by velocity space instabilities and scattering by wave-particle interactions (Appendix 2.B.2).

We implemented our electron energy model in a conservative GRMHD code HARM2D (Gammie et al. 2003), though the model we have developed can be applied to any underlying GRMHD scheme. For simplicity, the implementation in this chapter neglects the back reaction of the electron pressure on the dynamics of the accretion flow. We believe that this is a reasonable first approximation given some of the uncertainties in the electron physics. Formally, this approximation is is valid only when $T_e \ll T_p$ though we expect it to be a reasonable first approximation when $T_e \lesssim T_p$ in regions with plasma $\beta \gtrsim 1$, i.e., in the regions where gas thermal pressure forces are dynamically important.

We have demonstrated that our implementations of electron heating and conduction are accurate and second order convergent in several smooth test problems (§2.5 and Appendix 2.A). For shocks, the heating converges at first order but to a post shock temperature that differs from the analytic solution by $\lesssim 3\%$ when the electron adiabatic index differs from the adiabatic index of the fluid in the GRMHD solution (e.g., Figure 2.2). This discrepancy arises because standard Riemann solvers 'resolve' the shock structure with only a few grid points. Including an explicit bulk viscosity to broaden and resolve the shock leads to a converged numerical solution for the post-shock electron energy that agrees with the analytic solution (Appendix 2.C). In practice, the $\lesssim 3\%$ discrepancy between the numerical and analytic solutions for standard Riemann solvers is sufficiently accurate given other uncertainties in the electron physics. For this reason, we do not use bulk viscosity in our calculations. Moreover, strong shocks are rare and account for a negligible fraction of the dissipation in accretion disc simulations with aligned black hole and accretion disc angular momentum.

In addition to formulating and testing our electron energy equation model, we have also presented a preliminary application of these new methods to simulations of black hole accretion. Specifically, we have studied the impact of realistic electron heating and electron thermal conduction on the spatial distribution of the electron temperature in 2D (axisymmetric) simulations of black hole accretion onto a rotating black hole. We find that the resulting electron temperatures differ significantly from the assumption of a constant electron to proton temperature ratio used in previous work to predict the emission from GRMHD simulations (Mościbrodzka et al. 2009; Dibi et al. 2012; Drappeau et al. 2013); see, e.g. Figures 2.9-2.11. This is due to the strong β-dependence of the electron heating fraction, f_e, described in §2.6.1: electrons are preferentially heated in regions of lower β, causing T_e/T_p to be larger in the coronal regions compared to the midplane. In addition, we find that the effect of thermal conduction on the electron temperatures is suppressed by the fact that the heat flux must travel along field lines, which are predominantly toroidal and thus not aligned with the temperature gradient. Specifically, we find that electron conduction modifies the temperature distribution only if the effective electron mean free path along the magnetic field is $\gtrsim$ the local radius in the flow (see Figure 2.12). In this case, there is a net transfer of heat from the corona to the bulk of the disc. This increases the electron temperature at larger radii by a factor of ~ 2.

It is important to stress that the unsustainability of MHD turbulence in 2D simulations (e.g., Guan & Gammie 2008) limits how thoroughly we can interpret the accretion disc results presented in this paper. Since a steady state is never truly reached, the bulk of the disc retains memory of the initial conditions and only the innermost regions ($r \lesssim 10r_g$) develop significant turbulence. This could artificially limit the effects of electron conduction because the thermal time for relativistic electrons is $\sim r/c$ and is thus substantially shorter than the local dynamical time only at large radii. Future work will use the methods developed here in 3D simulations.

It is also important to stress that, as in previous work, our results for both the gas and electron temperature are not reliable when $b^2 \gg \rho c^2$. In these regions the ratios of $b^2/\rho c^2$ and b^2/u_g are so large that the evolution of the density and internal energy are dominated by truncation errors in the magnetic field, to which they are nonlinearly coupled by the total energy equation. This requires the use of density and internal energy floors. Because our calculation of the electron heating rate relies on quantifying the entropy changes in the underlying GRMHD solution, our predicted electron temperatures also become unreliable when $b^2 \gg \rho c^2$. In the accretion disc simulations, this only affects the regions close to the pole where there is very little matter, not the evolution of the electrons in the bulk of the accretion disc or corona. We have specifically tested several treatments of the internal energy and density floors which produce dramatically different results in the poles but are all consistent in the higher density regions for both the fluid variables and the electron temperature.

Future applications of the methods developed in this chapter will center on using our electron temperature calculations to predict the emission from accreting black holes. In particular, we hope to produce more accurate images of the radio and IR emission of Sagittarius A* (and M87) that can be used to interpret the forthcoming spatially resolved observations by the Event Horizon Telescope (Doeleman et al. 2009) and Gravity (Gillessen et al. 2010).

Acknowledgements

We thank F. Foucart for useful discussions, as well as all the members of the horizon collaboration, horizon.astro.illinois.edu, for their advice and encouragement. We also thank Dmitri Uzdensky for a useful and thorough referee report. This chapter was supported by NSF grant AST 13-33612 and NASA grant NNX10AD03G, and a Romano Professorial Scholar appointment to CFG. EQ is supported in part by a Simons Investigator Award from the Simons Foundation and the David and Lucile Packard Foundation. MC is supported by the Illinois Distinguished Fellowship from the University of Illinois. Support for AT was provided by NASA through Einstein Postdoctoral Fellowship grant number PF3-140131 awarded by the Chandra X-ray Center, which is operated by the Smithsonian Astrophysical Observatory for NASA under contract NAS8-03060, and by NSF through an XSEDE computational time allocation TG-AST100040 on TACC Stampede. This chapter was made possible by computing time granted by UCB on the Savio cluster.

Appendix

2.A Tests of Electron Conduction

This Appendix outlines tests of our numerical implementation of electron conduction that demonstrate that our calculations are robust and second-order accurate. The tests are taken directly from Chandra et al. (2015a), to which we refer the reader for more details.

2.A.1 Conduction Along Field Lines

This test is simply to check whether the electrons conduct heat along field lines properly. The initial conditions are a 2D, periodic box of physical size 1 × 1 with uniform pressure and a small, density variation (and hence temperature variation) of the form:

$$\rho = \rho_0 \left(1 - e^{-\frac{(x-0.5)^2+(y-0.5)^2}{0.005}} \right). \tag{2.55}$$

The field lines are sinusoidal and given by

$$\begin{aligned} B_x &= B_0 \\ B_y &= B_0 \sin(8\pi x), \end{aligned} \tag{2.56}$$

derived from a scalar potential of

$$A_z = B_0 \left(y + \frac{1}{8\pi} \cos(8\pi x) \right). \tag{2.57}$$

For the conduction parameters, we choose $\chi_e = 0.5/\rho$ and $\tau = 1$ and run the simulation for 10τ.

Figure 2.A.1 shows that the final state of the fluid is that of isothermal field lines, exactly as expected, with heat flux equilibrating the temperature along the magnetic field lines. This shows that our implementation of conduction properly limits the heat flux to be parallel to the magnetic field.

2.A.2 Linear Modes Test

This test checks whether our implementation of conduction gives the correct eigenmodes corresponding to Equation (2.19). Writing $\lambda = -\alpha \pm i\omega$, we initialise perturbations in an otherwise

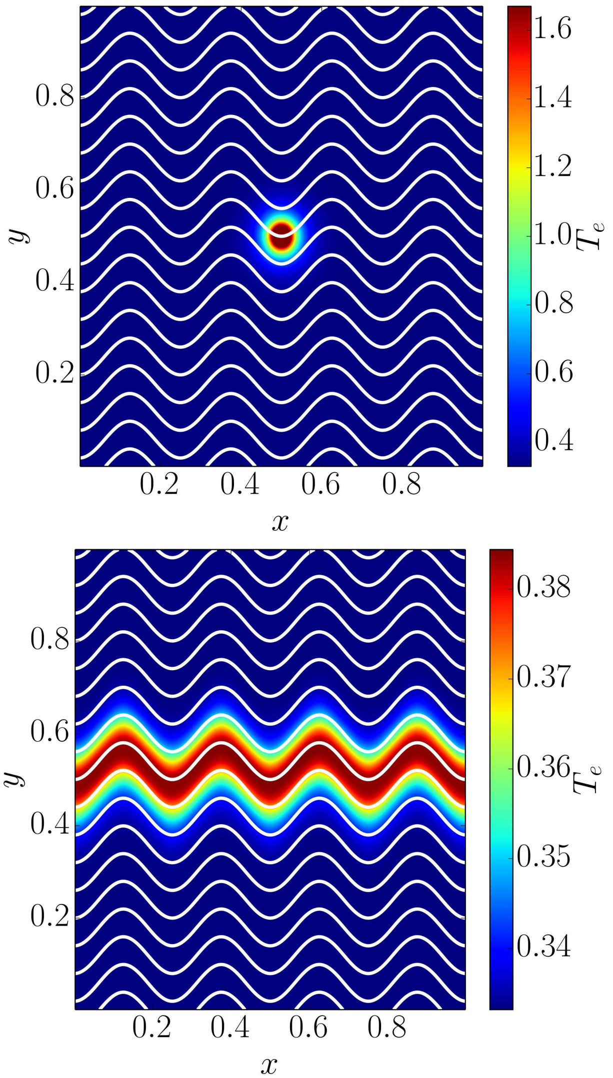

Figure 2.A.1: Temperature profiles over-plotted with magnetic field lines in the 2D anisotropic conduction test from Chandra et al. (2015a), adapted for electron conduction (see §2.A.1). The top panel is at the initial time while the bottom panel is at the end of the run ($t = 10\tau$). The field lines become isothermal, consistent with heat conduction only along the magnetic field.

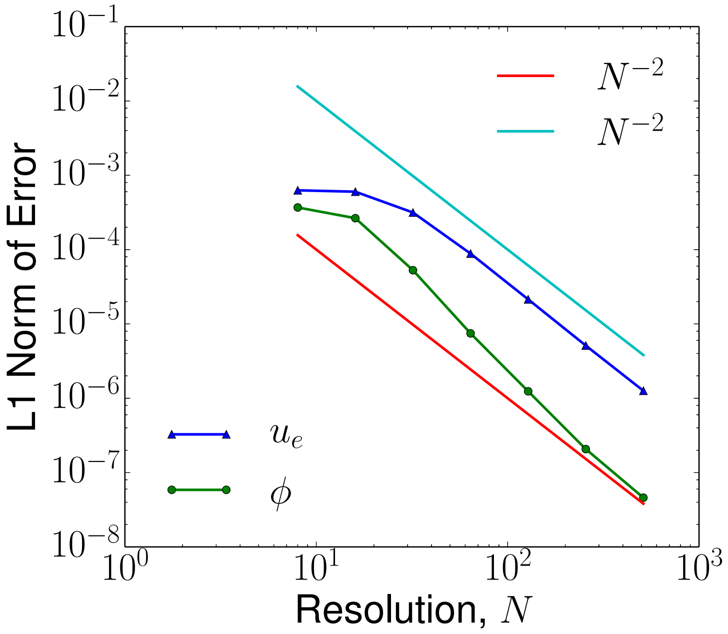

Figure 2.A.2: L1 Norm of errors in the 2D linear modes test after one period as computed from the eigenfrequencies given in equation (2.19). See §2.A.2.

uniform box about the equilibrium solution with wave number $k = 2\sqrt{2}\pi$ and run the simulation for one period: $t = 2\pi/\omega$. The analytic solution is that the perturbations, δ, should obey $\delta(t = 2\pi/\omega) = \delta(t = 0)e^{-2\pi\alpha/\omega}$. We choose $\hat{b} = 1/\sqrt{3}\hat{x} + \sqrt{2}/\sqrt{3}\hat{y}$ and $\vec{k} = 2\pi\hat{x} + 2\pi\hat{y}$. We find that both ϕ and u_e converge at second order to the analytical solution as shown in Figure 2.A.2.

2.A.3 1D Atmosphere in a Schwarzschild Metric

This test checks whether our implementation of the electron conduction gives the correct analytic result in a non-trivial space-time. In the Schwarzschild metric, the solution for a fluid in hydro-static equilibrium reduces to a system of two ordinary differential equations, which can be solved for any given temperature profile (see Chandra et al. 2015a for details). For this test, we initialise the temperature and heat flux of the electrons to be this equilibrium solution for a purely radial field and see if the code can maintain it over a time of 100 r_g/c in a computational domain of $1.4r_g \leq r \leq 90r_g$. To compute the error, we again use the L1 norm and find 2nd order convergence for both ϕ and u_e, as shown in Figure 2.A.3.

2.A.4 Relativistic Bondi Accretion

This test checks whether our implementation of the electron conduction gives the correct analytic result in a fluid with $u^i \neq 0$, which activates terms that were not present in the 1D atmosphere

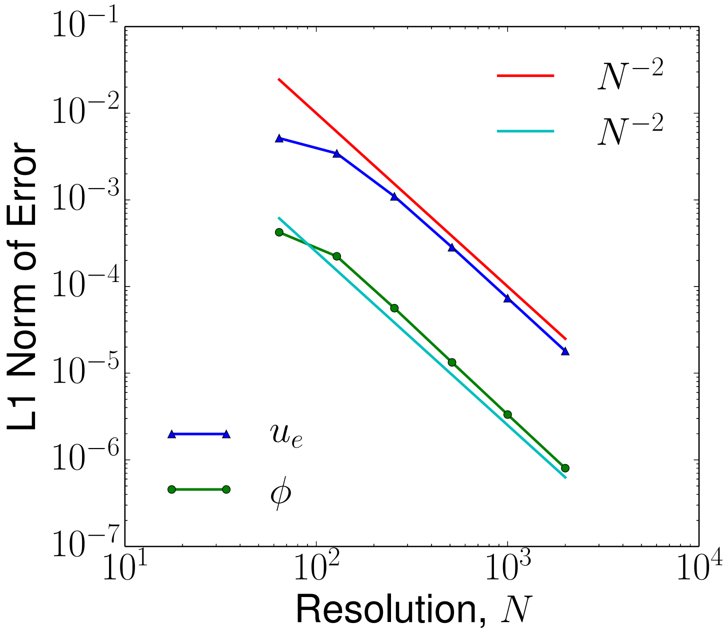

Figure 2.A.3: L1 norms of the error in both the heat flux and electron internal energy for the 1D atmosphere test in the Schwarzschild metric (§2.A.3).

test. For the standard, spherically symmetric, steady-state Bondi solution for an accreting black hole (Hawley et al. 1984), we can solve equation (2.16) by numerical integration if we assume that the heat flux does not back-react on the electron temperature. For this test, we set the initial condition of the fluid variables to be the Bondi solution and the initial conditions of ϕ to be given by the solution to equation (2.16) with Dirichlet boundary conditions. We choose the sonic point to occur at $r_c = 20M$ and fix the outer boundary at a spherical radius of $R_{\rm out} = 40M$ to have $\phi(r = 40M) = 0$. The inner radius of the grid is inside the event horizon at $r = 1.6M$. The test is whether or not the code can maintain this state over a period of $t = 200M$. We find second order convergence of the heat flux to the analytical solution, as shown in Figure 2.A.4.

2.B Derivations

2.B.1 Total Heating Rate

This section derives the result quoted in equation (2.25).

First, we introduce the variable $\hat{\kappa}_g$, which is equivalent to $\kappa_g \equiv P_g \rho^{-\gamma}$ at the beginning of the time step and at the $n + 1/2$ "predictor" step, but which is evolved over a time step according to:

$$\partial_\mu(\sqrt{-g}\rho\hat{\kappa}_g u^\mu) = 0. \tag{2.58}$$

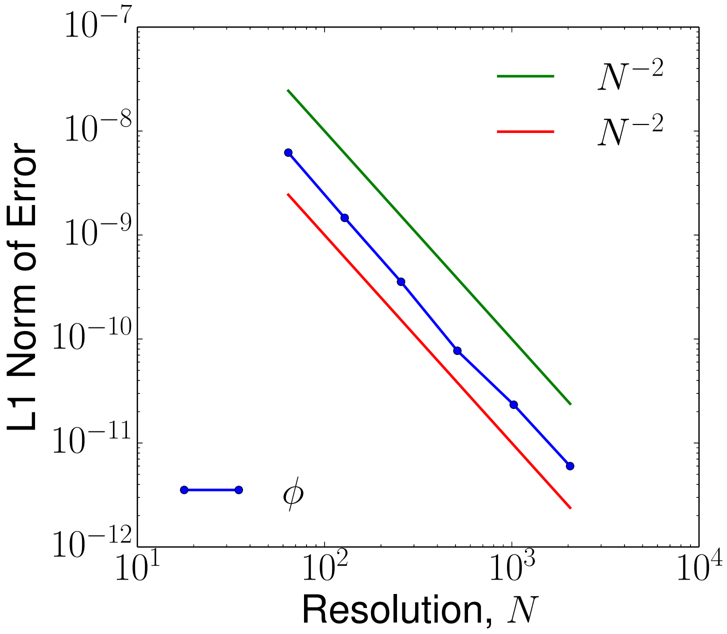

Figure 2.A.4: L1 norms of the error in the magnitude of the heat flux for the relativistic Bondi accretion test (§2.A.4).

We discretise equation (2.58) in a standard way (i.e. equation 2.21):

$$\begin{aligned}&\frac{\left(\sqrt{-g}\rho\hat{\kappa}_g u^t\right)^{n+1}-\left(\sqrt{-g}\rho\kappa_g u^t\right)^{n}}{\Delta t}\\&+\frac{[\sqrt{-g}\rho\kappa_g u^x]_{i+1}^{n+1/2}-[\sqrt{-g}\rho\kappa_g u^x]_{i}^{n+1/2}}{\Delta x}=0,\end{aligned} \tag{2.59}$$

where the square brackets indicate fluxes computed via the Riemann solver at cell interfaces and the generalisations to higher dimensions is straightforward. Note that we have dropped the ˆ in the $n+1/2$ and n terms because $\hat{\kappa}_g=\kappa_g$ at the beginning of the time step and at the $n+1/2$ step. We obtain the new value of entropy, $\hat{\kappa}_g^{n+1}$, at $t_{n+1}\equiv t_n+\Delta t$ via solving equation (2.59). We emphasise that $\hat{\kappa}_g$ is not the true entropy at t^{n+1} but the entropy evolved according to equation (2.58) [or its discretised equivalent equation 2.59] and thus does *not* include any heating.

At the end of the time step (i.e. at $t=t_{n+1}$), we compute the "true" value of the entropy due to the full GRMHD evolution, according to the definition of κ_g:

$$\kappa_g^{n+1}=\left(\frac{P_g}{\rho^{\gamma}}\right)^{n+1}. \tag{2.60}$$

Unlike $\hat{\kappa}_g^{n+1}$, which does not include any heating, κ_g^{n+1} accounts for the heating as implied by the conservative evolution of the underlying GRMHD scheme. The difference $(\kappa_g-\hat{\kappa}_g)^{n+1}$ is related to the heating incurred during time step n, and we will use it below.

To compute the heating rate we evaluate the quantity:

$$
\begin{aligned}
Q \equiv \rho T u^\mu \partial_\mu s_g &= \frac{\rho^\gamma}{\gamma - 1} u^\mu \partial_\mu \kappa_g \\
&\equiv \frac{\rho^{\gamma-1}}{\gamma - 1} (\rho \kappa_g u^\mu)_{;\mu} \\
&\equiv \frac{1}{\gamma - 1} \frac{\rho^{\gamma-1}}{\sqrt{-g}} \partial_\mu \left(\sqrt{-g} \rho \kappa_g u^\mu \right),
\end{aligned}
\tag{2.61}
$$

where the third equality holds because

$$
\begin{aligned}
(\rho \kappa_g u^\mu)_{;\mu} &= \partial_\mu (\sqrt{-g} \rho \kappa_g u^\mu) / \sqrt{-g} \\
&\equiv \kappa_g \partial_\mu (\sqrt{-g} \rho u^\mu) / \sqrt{-g} + \rho u^\mu \partial_\mu \kappa_g
\end{aligned}
$$

and the first term vanishes due to conservation of mass. We evaluate eq. (2.61) at the $n + 1/2$ time step in a discretised form by centring the time derivatives at $n + 1/2$ but evaluating the prefactor at the $n + 1$ time step:

$$
\begin{aligned}
Q^{n+1/2} = & \left(\frac{1}{\gamma - 1} \frac{\rho^{\gamma-1}}{\sqrt{-g}} \right)^{n+1/2} \\
& \times \left\{ \frac{(\sqrt{-g} \rho \kappa_g u^t)^{n+1} - (\sqrt{-g} \rho \kappa_g u^t)^n}{\Delta t} \right. \\
& + \left. \frac{[\sqrt{-g} \rho \kappa_g u^x]_{i+1}^{n+1/2} - [\sqrt{-g} \rho \kappa_g u^x]_{i}^{n+1/2}}{\Delta x} \right\}.
\end{aligned}
\tag{2.62}
$$

Now, multiplying eq. (2.59) by $\left(\frac{1}{\gamma-1} \rho^{\gamma-1} / \sqrt{-g} \right)^{n+1/2}$ and adding the result to eq. (2.62), we obtain equation (2.25) of the main text:

$$
Q^{n+1/2} = \left(\frac{\rho^{\gamma-1}}{\gamma - 1} \right)^{n+1/2} \frac{\{ \rho u^t (\kappa_g - \hat{\kappa}_g) \}^{n+1}}{\Delta t}. \tag{2.63}
$$

2.B.2 Whistler Instability Limit on Conduction

We assume that the electrons are relativistic with $\Theta_e = kT_e / m_e c^2 \gtrsim 1$. If the electrons relax to thermal equilibrium with a scattering rate ν_e, relativistic kinetic theory implies that the electron viscosity η_e and thermal diffusivity χ_e satisfy (Anderson & Witting 1974)

$$
\eta_e \simeq \Theta_e \frac{c^2}{\nu_e} \qquad \chi_e \simeq 1.6 \frac{c^2}{\nu_e} \tag{2.64}
$$

Velocity space instabilities set an upper limit on the electron thermal conductivity in a turbulent plasma. Physically, as the magnetic field in the accretion disc fluctuates in time, this generates pressure anisotropy, which is resisted by velocity space instabilities that isotropise the distribution function and thus limit the magnitude of the thermal diffusivity. Chandra et al. (2015b) show that the theory of relativistic anisotropic viscosity implies that the pressure anisotropy and scattering rate are related by

$$\nu_e \frac{\Delta P_e}{P_e} \simeq u^\mu \partial_\mu \ln\left[\frac{B^3}{\rho^2}\right]. \tag{2.65}$$

where $\Delta P_e = P_\perp - P_\parallel$ and we have neglected some general relativistic terms for simplicity.

Electrons satisfy limits on pressure anisotropy of

$$\frac{\Delta P_e}{P_e} \gtrsim -\frac{1.3}{\beta_e} \qquad \frac{\Delta P_e}{P_e} \lesssim \frac{0.25}{\beta_e^{0.8}} \tag{2.66}$$

The second term on the right hand side of equation (2.66) is a fit to the whistler instability threshold for relativistically hot electrons (based on numerical solutions of the dispersion relation derived in Gladd 1983). The coefficient in the numerator technically depends weakly on Θ_e, varying from $\simeq 0.125$ for non-relativistic electrons to $\simeq 0.25$ for $\Theta_e \simeq 10$ (Lynn 2014). Note that the slope of the β_e term for the whistler instability in equation (2.66) is a fit for $\beta_e \simeq 0.1 - 30$. Gary & Wang (1996) and Sharma et al. (2007) found a somewhat shallower slope $\propto \beta_e^{-1/2}$ in non-relativistic calculations but this is not a good fit over the large dynamic range of β_e considered here. The first limit in equation (2.66) is the electron firehose instability which is an electron-scale resonant analogue of the fluid firehose instability (Gary & Nishimura 2003). This limit is based on non-relativistic calculations and should to be extended to the relativistic limit in future work. However, based on our whistler calculations this is unlikely to be a significant effect.

Sharma et al. (2007) found that the typical pressure anisotropy satisfied $\Delta P/P \geq 0$ in simulations that explicitly evolved a pressure tensor. Physically, this sign of the pressure anisotropy corresponds to outward angular momentum transport. Assuming that the RHS of equation (2.65) is $\sim \Omega$, the whistler instability limit in equation (2.66) thus implies $\chi_e \sim c r_g (r/r_g)^{3/2}(4\beta_e)^{-0.8}$. This is not a significant constraint on the conductivity relative to the saturated value ($\chi_e \sim c r_g$), for $\beta_e \lesssim 1$, which can occur either in the corona/outflow or because $T_e \ll T_p$. However, this estimate does suggest that the electron conductivity may be modest in the bulk of the disc at $\sim 10 r_g$ if $\beta_e \gg 1$.

Equation (2.66) can be implemented by calculating $\Delta P_e/P_e$ using equation (2.65) given an assumed χ_e (and using equation (2.64) to relate ν_e and χ_e). If equation (2.66) is violated, ν_e should be increased and χ_e decreased such that equation (2.66) is satisfied. Alternatively, an even simpler first approximation would be to simply limit

$$\chi_e \lesssim c r_g (r/r_g)^{3/2}(4\beta_e)^{-0.8} \equiv \chi_{\rm max} \tag{2.67}$$

motivated by the estimate in the preceding paragraph for the whistler instability. This is the limit we have used in the accretion disc simulations in §2.6 of the main text.

2.B.3 Electron Conduction Numerical Stability

Non-relativistically, an explicit implementation of thermal conduction is stable only if the time step, Δt, satisfies the condition $\Delta t \lesssim \Delta x^2/\chi$, where Δx is the grid spacing in 1-dimension and χ is the thermal diffusivity. The relativistic theory outlined in §2.3.3, however, where the heat flux ϕ is evolved according to equation (2.16), differs from the non-relativistic case in that it is no longer diffusive. This alters the criterion for stability to be a condition on the relaxation time, τ, given by equation (2.36), which we derive here.

To check the numerical stability of our conduction theory we assume that we are in Minkowski space in the rest frame of the fluid, and further simplify our analysis to one dimension in which $\hat{b} = \hat{\imath}$.

Under these assumptions, a Von Neumann stability analysis on equations (2.16) and (2.5) leads to a quadratic equation for the amplification factor, G, with the following solutions:

$$\begin{aligned} G = {} & 1 - C\,[1 - \cos(k)] \\ & - \frac{1}{2}\frac{\Delta t}{\tau}\left(1 \pm \sqrt{1 - 4(\gamma_e - 1)\frac{\chi_e \tau}{\Delta x^2}\sin{(k)}^2}\right), \end{aligned} \tag{2.68}$$

with the condition for stability being that $|G| \leq 1$. Here, as before, C denotes the Courant factor. To analyse equation (2.68), we consider two cases: 1) when the square root term is real, and 2) when the square root term is imaginary.

When the square root term is real, the condition for stability becomes:

$$\tau \geq \Delta t \left[\frac{2 - C\,[1 - \cos(k)] - (\gamma_e - 1)\frac{\chi_e \Delta t}{\Delta x^2}\sin{(k)}^2}{(2 - C[1 - \cos(k)])^2}\right] \tag{2.69}$$

The right hand side is a maximum for $k = \pi$ modes, which gives, simply:

$$\tau \geq \frac{\Delta t}{2(1 - C)}. \tag{2.70}$$

The more interesting case is when the square root term in Equation (2.68) is imaginary, where the criterion for stability becomes:

$$\tau \geq \Delta t \left[\frac{(\gamma_e - 1)\frac{\chi_e \Delta t}{\Delta x^2}\sin{(k)}^2 + C\,[1 - \cos(k)] - 1}{C\,(2 - C[1 - \cos(k)])\,[1 - \cos(k)]}\right], \tag{2.71}$$

which, defining $K \equiv (\gamma_e - 1)\Delta t \chi_e / \Delta x^2$, has a maximum at

$$\cos(k) = 1 - \frac{C - \sqrt{4K(1 - C) - C^2}}{a^2 - 2K(1 - C)} \tag{2.72}$$

if

$$\begin{aligned} \Delta t > {} & \frac{\Delta x^2}{(\gamma_e - 1)\chi_e}\,\frac{1 - 4C(1 - C) + \sqrt{1 - 4C(2C - 1)}}{8(1 - C)} \\ \equiv {} & \Delta t_{crit}, \end{aligned} \tag{2.73}$$

and a maximum at $k = \pi$ otherwise. So if $\Delta t < \Delta t_{crit}$, our criterion becomes:

$$\tau \geq \Delta t \left[\frac{2C - 1}{4C\,(1 - C)}\right] \equiv \tau_{max,1}. \tag{2.74}$$

Finally, if $\Delta t > \Delta t_{crit}$, then we have

$$\begin{aligned} &\tau \geq \\ &\Delta t \times \left[\frac{2K\left(C^2 - 4C(1-C)\right)}{4KC(1-C)\left(\sqrt{4K(1-C)-C^2} - 2C\right) + 2C^4} \right. \\ &\left. + \frac{\left(4K^2(1-C) + 4KC(1-C) - C^3\right)\sqrt{4K(1-C)-C^2}}{4KC(1-C)\left(\sqrt{4K(1-C)-C^2} - 2C\right) + 2C^4} \right] \\ &\equiv \tau_{max,2}. \end{aligned} \tag{2.75}$$

The general behaviour of Equation (2.75) is complicated, but the result is roughly consistent with

$$\tau \gtrsim (\gamma_e - 1)\left(\frac{\Delta t}{\Delta x}\right)^2 \chi_e. \tag{2.76}$$

for most reasonable choices of the Courant factor. This is the result quoted in equation (2.36) of the main text.

To summarise, our scheme is stable when:

$$\tau \geq \begin{cases} \max\left[\dfrac{\Delta t}{2(1-C)}, \tau_{max,1}\right] & : \Delta t < \Delta t_{crit} \\ \max\left[\dfrac{\Delta t}{2(1-C)}, \tau_{max,2}\right] & : \Delta t \geq \Delta t_{crit}, \end{cases}$$

for Δt_{crit}, $\tau_{max,1}$, and $\tau_{max,2}$ as defined in equations (2.73), (2.74), and (2.75), respectively.

2.B.4 Electron Heating in a 1D Shock

Formally, for an ideal shock in a zero-viscosity fluid there is no unique path in (P, ρ) space that connects the pre and post-shock values given by the Rankine-Hugoniot conditions, meaning that the dissipation per unit volume, $\int \rho T ds$, is not a well-defined quantity. However, by introducing *any* non-zero viscosity, the degeneracy is broken and there exists a unique path in (P, ρ) space and hence a well-defined dissipation. To see this, we take the 1D Rankine-Hugoniot relations for a static shock, given some prescription for the viscous stress, $\tau \equiv 4/3\mu\vec{\nabla} \cdot v$ (μ is the dynamic viscosity coefficient, and can be an arbitrary function of plasma parameters),

$$\begin{aligned} \dot{m} &= \rho v \\ \dot{p} &= \rho v^2 + P + \tau \\ \dot{E} &= \frac{1}{2}\rho v^3 + \frac{\gamma}{\gamma - 1} P v + \tau v, \end{aligned} \tag{2.77}$$

where $\dot{m}$, $\dot{p}$, and $\dot{E}$ are constants representing the mass, momentum, and energy flux across the shock. Absent τ, we could combine these three equations in several different ways to get a relationship of the form $P = P(\rho)$. With non-zero viscosity, however, there is only one unique way to do this, namely, by taking $\dot{p}v - \dot{E}$ and solving for $\dot{m}$, which gives:

$$P(\rho) = (\gamma - 1)\left(\frac{1}{2}\frac{\dot{m}^2}{\rho} - \dot{p} + \frac{\dot{E}}{\dot{m}}\rho\right), \tag{2.78}$$

or, in terms of $\kappa \equiv P\rho^{-\gamma}$,

$$\kappa_g(\rho) = (\gamma - 1)\left(\frac{1}{2}\frac{\dot{m}^2}{\rho^{\gamma+1}} - \frac{\dot{p}}{\rho^{\gamma}} + \frac{\dot{E}}{\dot{m}\rho^{\gamma-1}}\right). \tag{2.79}$$

We assume that the electrons receive a constant fraction of the total heat:

$$\begin{aligned} &\rho T_e u^\mu \partial_\mu s_e = f_e \rho T_g u^\mu \partial_\mu s_g \\ &\Rightarrow \frac{\rho^{\gamma_e}}{\gamma_e - 1} u^\mu \partial_\mu \kappa_e = f_e \frac{\rho^{\gamma}}{\gamma - 1} u^\mu \partial_\mu \kappa_g, \end{aligned} \tag{2.80}$$

or in quasi-conservative form (using the mass continuity equation and assuming a flat space metric):

$$\frac{\partial}{\partial x^\mu}\left(\rho u^\mu \kappa_e\right) = f_e \frac{\gamma_e - 1}{\gamma - 1}\rho^{\gamma - \gamma_e}\frac{\partial}{\partial x^\mu}\left(\rho u^\mu \kappa_g\right). \tag{2.81}$$

The final electron entropy is given by integrating this equation from the initial to the final density, which, for a 1D shock reduces to

$$\int_{-\infty}^{\infty} \frac{\partial}{\partial x}\left(\dot{m}\kappa_e\right) = f_e \frac{\gamma_e - 1}{\gamma - 1}\int_{\rho_i}^{\rho_f} \rho^{\gamma - \gamma_e}\dot{m}\frac{\partial \kappa}{\partial \rho} d\rho, \tag{2.82}$$

giving:

$$\begin{aligned} u_e^f = {} & u_e^i \left(\frac{\rho_f}{\rho_i}\right)^{\gamma_e} \\ & + \frac{f_e}{\gamma - 1}\left(\frac{\dot{m}}{2\rho_f}\frac{\gamma + 1}{\gamma_e + 1} - \dot{p}\frac{\gamma}{\gamma_e} + \frac{\dot{E}\rho_f}{\dot{m}}\frac{\gamma - 1}{\gamma_e - 1}\right) \\ & - \frac{f_e}{\gamma - 1}\left(\frac{\rho_f}{\rho_i}\right)^{\gamma_e}\left(\frac{\dot{m}}{2\rho_i}\frac{\gamma + 1}{\gamma_e + 1} - \dot{p}\frac{\gamma}{\gamma_e} + \frac{\dot{E}\rho_i}{\dot{m}}\frac{\gamma - 1}{\gamma_e - 1}\right), \end{aligned} \tag{2.83}$$

where ρ_f is determined from the Rankine-Hugoniot conditions. For a strong shock with Mach number $\gg 1$, this simplifies to

$$u_e^f = \dot{m}v_i \frac{f_e}{\gamma_e^2 - 1}\left[\left(\frac{\gamma + 1}{\gamma - 1}\right)^{\gamma_e}\left(1 - \frac{\gamma}{\gamma_e}\right) + 1 + \frac{\gamma}{\gamma_e}\right], \tag{2.84}$$

where v_i is the pre-shock fluid velocity in the shock's rest frame. Dividing by $u_g^f = 2\dot{m}v_i\left(\gamma^2 - 1\right)^{-1}$ yields equation 2.41.

2.C Electron Heating in a Viscous Shock

In this appendix we show that by introducing an explicit bulk viscosity to the non-relativistic hydrodynamic equations, our electron heating calculation outlined in §2.4.3 give an electron internal energy that converges to the analytic result derived in Appendix 2.B.4 for electron heating at a shock.

We treat viscosity by explicitly adding the 1D viscous energy and momentum fluxes to the ideal MHD fluxes for a constant kinematic viscosity, ν:

$$\begin{aligned} F_{E,visc} &= -\frac{4\nu}{3}\rho v\frac{\mathrm{d}v}{\mathrm{d}x} \\ F_{p,visc} &= -\frac{4\nu}{3}\rho\frac{\mathrm{d}v}{\mathrm{d}x}. \end{aligned} \tag{2.85}$$

Note that these are non-relativistic fluxes which are formally inconsistent with the relativistic code in which they are used. However, our goal here is simply to show that with a resolved shock structure the electron heating calculation converges to the correct answer. The non-relativistic limit is fine for this purpose. The fluxes in equation (2.85) smooth out discontinuities to a continuous profile of finite width, determined by ν and the velocity scale. The solution for the profile of a viscous shock, now defined as a smooth transition from an initial to final state as opposed to a discontinuity, can be computed analytically for a constant kinematic viscosity, ν. In the shock frame, taking $x \rightarrow -\infty$ as the initial state, this solution takes the form:

$$v(x) = \frac{\left(\gamma + \frac{2}{M} - 1\right) + \exp\left[-\frac{3(x-x_0)v_i}{4\nu}\left(1 - \frac{1}{M}\right)\right]}{\exp\left[-\frac{3(x-x_0)v_i}{4\nu}\left(1 - \frac{1}{M}\right)\right] + (\gamma + 1)}, \tag{2.86}$$

where M is the pre-shock Mach number, v_i is the pre-shock speed at $x \rightarrow -\infty$, and x_0 is a constant determining the location of the shock. For a pre-shock density ρ_i, the density profile is obtained from the mass conservation equation: $\rho_i v_i / v(x)$, which determines the pressure profile from equation (2.78). Similarly, the profile for the internal energy of the electrons in terms of $\rho(x)$ is given by equation (2.83) with the substitution $\rho_f \rightarrow \rho(x)$.

For our numerical test, we do not use the standard Noh test as outlined in §2.5.1 due to the problems noted by the original paper (Noh 1987). For any numerical scheme that gives the shock a finite width, the formation of the shock from the converging flow undershoots the density at the center of the grid by a finite amount that does not disappear at higher resolution. Given this difficulty, our numerical test is instead to set the initial and boundary conditions of both the fluid and electron variables equal to the analytic solution for a stationary shock (e.g., equation 2.86) and evolve for a dynamical time of L/v_i, where L is the grid size. We choose $\gamma = 5/3$, $v_i = 10^{-2}c$, $M \sim 49$, and $\nu = 0.01 v_i L$. Figure 2.C.1 shows both the density profile and the ratio of the electron internal energy to the total internal energy for both $\gamma_e = 4/3$ and $\gamma_e = 5/3$ electrons at the end of the run as compared to the analytic solution (equation 2.83). We find good agreement with the analytic solution and second order convergence (Figure 2.C.2) up to the resolution at which relativistic errors in the analytic solution become important ($\delta u_g / u_g \sim (v/c)^2 \sim 10^{-4}$).

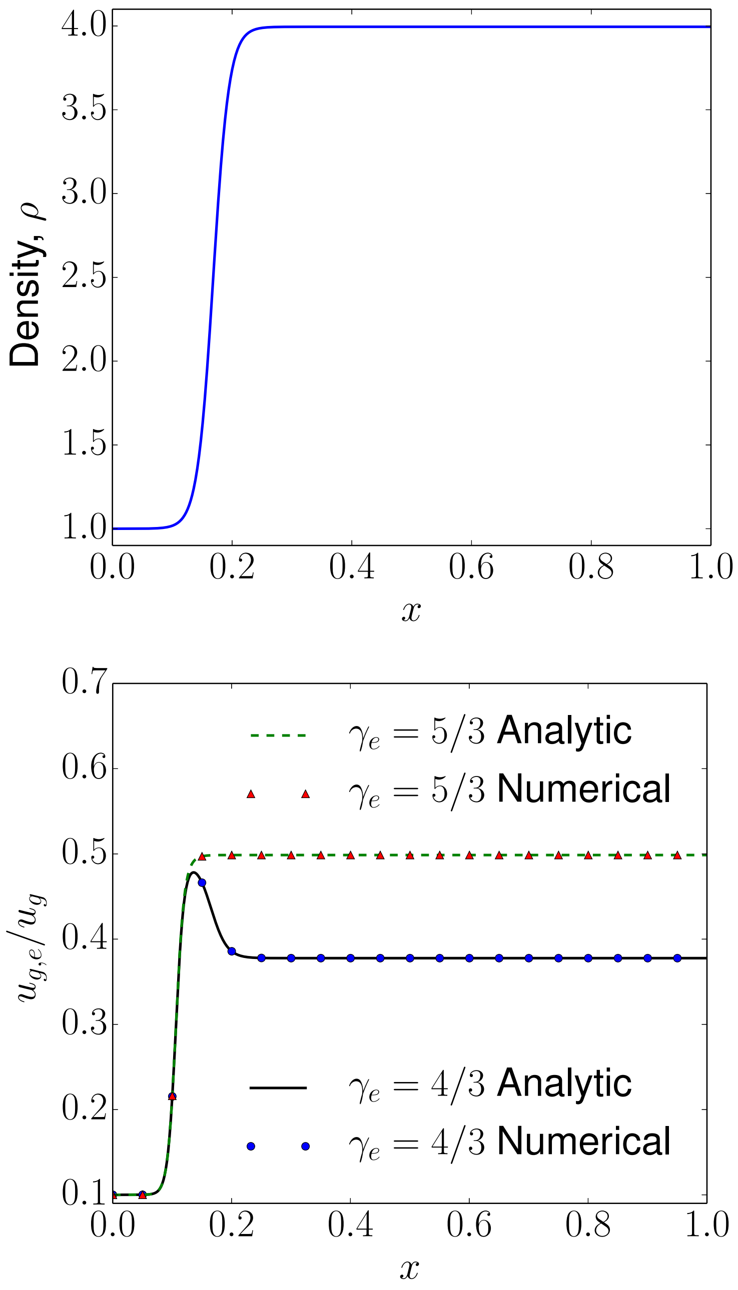

Figure 2.C.1: High Mach number ($\sim$ 49), stationary, viscous shock results for an electron heating fraction $f_e = 0.5$ at a resolution of 2000 cells. Top: fluid density. Bottom: electron internal energy relative to total fluid internal energy. Both the $\gamma_e = 4/3$ and $\gamma_e = 5/3$ electrons display good agreement with the analytic solution, converging at 2nd order (see Figure 2.C.2). This is in contrast to the formulation without explicit viscosity used in §2.5.1, in which the shock structure is always just a few grid points. An accurate calculation of the shock heating requires a well-resolved shock structure (i.e., a shock with a finite width), which is provided by adding explicit bulk viscosity to the fluid equations. Given that the error incurred by our numerical scheme without explicit viscosity ($\sim$ 3%) is acceptable for our purposes, we do not use explicit viscosity in our calculations.

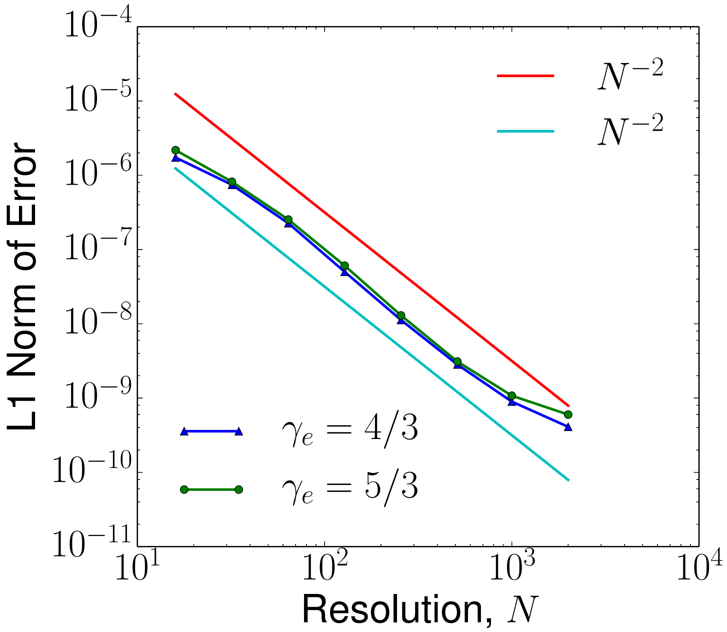

Figure 2.C.2: Convergence results for the electron internal energy in a steady-state, 1D, high Mach number, viscous shock as compared to the analytic solution (see Appendix 2.C). Both the $\gamma_e = 5/3$ and $\gamma_e = 4/3$ electrons converge at 2nd order, as opposed to the non-viscous shock of §2.5.1 where only the $\gamma_e = 5/3$ electrons converged to the analytic solution. Second order convergence is achieved in this test problem because the shock profile is well-resolved and continuous. This shows that our method correctly captures the dissipation in strong shocks when the shock profile can be resolved. At the highest resolution, relativistic corrections to the (non-relativistic) analytic solution become important so the error no longer converges at second order.

2.D Torus Initial Conditions

In this appendix we describe in more detail the initial configuration of the torus in our simulations of an accreting black hole. In all expressions that follow we measure radii in units of the gravitational radius $r_g \equiv GM/c^2$ (or equivalently set $G = M = c = 1$).

Fishbone & Moncrief (1976) derived an equilibrium solution (their equation 3.6) of the general relativistic hydrodynamic equations in the Kerr metric in terms of the relativistic enthalpy, $h \equiv (\rho + P_g + u_g)/\rho$, and the constant angular momentum per unit mass, $l \equiv u_\varphi u^t$. We use their equation 3.6 exactly as presented when $r > r_{in}$ and when the right-hand side is positive, otherwise we set $\rho = P = 0$. Additionally, we assume an adiabatic equation of state, $P = \kappa_0 \rho^\gamma$, for some choice of κ_0, and fix l such that the density maximum occurs at $r_{\max}$:

$$\begin{aligned} l = &\left\{ \frac{\left[a^2 - 2a\sqrt{r_{\max}} + r_{\max}^2\right]\left[-2ar_{\max}\left(a^2 - 2a\sqrt{r_{\max}} + r_{\max}^2\right)\right]}{\sqrt{2a\sqrt{r_{\max}} + r_{\max}^2 - 3r_{\max}}} \right. \\ &\left. + \frac{\left(a + \sqrt{r_{\max}}(r_{\max} - 2)\right)\left(r_{\max}^3 + a^2(r_{\max} + 2)\right)}{(a^2 + r_{\max}^2 - 2r_{\max})\sqrt{1 + 2ar_{\max}^{-3/2} - 3/r_{\max}}} \right\} \\ &\times \frac{1}{r_{\max}^3\sqrt{2a\sqrt{r_{\max}} + r_{\max}^2 - 3r_{\max}}}, \end{aligned} \tag{2.87}$$

where a is the dimensionless spin parameter of the black hole. This expression for l is equivalent to the Keplerian value at $r = r_{\max}$.

Chapter 3

The Disc-Jet Symbiosis Emerges: Modeling the Emission of Sagittarius A* with Electron Thermodynamics

An earlier version of this article was previously published as Ressler S. M., Tchekhovskoy A., Quataert E., and Gammie C. F., 2017, MNRAS, 467, 3604

3.1 Abstract

We calculate the radiative properties of Sagittarius A* – spectral energy distribution, variability, and radio-infrared images – using the first 3D, physically motivated black hole accretion models that directly evolve the electron thermodynamics in general relativistic MHD simulations. These models reproduce the coupled disc-jet structure for the emission favored by previous phenomenological analytic and numerical works. More specifically, we find that the low frequency radio emission is dominated by emission from a polar outflow while the emission above 100 GHz is dominated by the inner region of the accretion disc. The latter produces time variable near infrared (NIR) and X-ray emission, with frequent flaring events (including IR flares without corresponding X-ray flares and IR flares with weak X-ray flares). The photon ring is clearly visible at 230 GHz and 2 microns, which is encouraging for future horizon-scale observations. We also show that anisotropic electron thermal conduction along magnetic field lines has a negligible effect on the radiative properties of our model. We conclude by noting limitations of our current generation of first-principles models, particularly that the outflow is closer to adiabatic than isothermal and thus underpredicts the low frequency radio emission.

3.2 Introduction

Sagittarius A* (Sgr A*), the supermassive black hole at the center of our galaxy, is a prime candidate for directly comparing general relativistic magnetohydrodynamic (GRMHD) simulations of accretion discs to observations. Not only is there a wealth of observational data in the radio-millimetre (Falcke et al. 1998; An et al. 2005; Doeleman et al. 2008; Bower et al. 2015a), near-infrared (Genzel et al. 2003a; Do et al. 2009; Schödel et al. 2011), and X-ray (Baganoff et al. 2003; Neilsen et al. 2013) bands, but the Event Horizon Telescope (Doeleman et al. 2008) and GRAVITY (Gillessen et al. 2010) will soon be able to spatially resolve the structure of the innermost region of the disc near the event horizon. [1]

The accretion rate in Sgr A* is orders of magnitude less than the Eddington limit, putting it in the Radiatively Inefficient Accretion Flow (RIAF) regime, characterised by a geometrically thick, optically thin disc (Ichimaru 1977; Rees et al. 1982; Narayan & Yi 1994; Quataert 2001; Yuan & Narayan 2014). This particular class of accretion discs in some ways lends itself well to numerical simulation, given the dynamical unimportance of radiation and the large scale height of the disc that can be more easily resolved. Over the past few decades, several numerical methods to simulate single-fluid RIAFs around rotating black holes in full general relativity have been developed (e.g. Komissarov 1999; De Villiers & Hawley 2003; Gammie et al. 2003; Tchekhovskoy et al. 2007; White et al. 2016).

On the other hand, the low densities typical of RIAFs imply that the electron-ion Coulomb collision time is much longer than an accretion time, so a single fluid model of the thermodynamics is not applicable. However, in the limit that the electrons are colder than the protons, $T_e \lesssim T_p$, which is generally expected for RIAFs, these single-fluid simulations should provide a reasonable description for the total gas properties. Thus, to first approximation, the accretion dynamics, magnetic field evolution, and ion thermodynamics are known but the electron temperature is undetermined. Previous approaches to modelling the emission from single-fluid RIAF simulations have attempted to overcome this limitation by adopting simplified prescriptions for the electron thermodynamics, such as taking $T_e/T_p = \text{const.}$ (e.g. Mościbrodzka et al. 2009), splitting the simulation into jet and disc regions with different electron temperatures in each (e.g. Mościbrodzka et al. 2014; Chan et al. 2015b), or by solving a 1D, time-independent electron entropy equation in the midplane and interpolating to the rest of the grid (e.g. Shcherbakov et al. 2012). Recently, however, we have developed a model which allows for the self-consistent evolution of the electron entropy alongside the rest of the GRMHD evolution, including the effects of electron heating and electron thermal conduction along magnetic field lines (Ressler et al. 2015, Chapter 2). This model has been further extended by Sadowski et al. (2016) to include the dynamical effects of radiation and Coulomb Collisions on the fluid (while neglecting electron conduction), where they demonstrate that these effects are negligible for the accretion rate of Sgr A*; thus we neglect them here.

Here we present the observational application of that electron model to Sgr A* using 3D GRMHD simulations. Throughout we focus on emission by thermal electrons. The aim of this chapter is to elucidate the basic properties of a fiducial model that is representative of simulations that include our electron entropy evolution. We do not provide an exhaustive study of parameter

---

[1] This chapter was published in 2017, before GRAVITY and EHT released their first results in 2018 (Gravity Collaboration et al.) and 2019 (Event Horizon Telescope Collaboration et al.), respectively. Note, however, that the first target of EHT was the black hole at the center of M87 and (as of the writing of this thesis) the EHT results for Sgr A* are still forthcoming.

space in order to find a "best-fit" model. This is in part because we believe that the theoretical problem in its present state is too degenerate and uncertain to warrant such inferences. We do, however, compare and contrast our results to observations of Sgr A* and previous models.

The literature has used various terms to distinguish between types of outflow in black hole accretion disc systems. Most notable are the labels"jet," "disc-jet," and "wind," (see section 3.3 in Yuan & Narayan 2014 for a review). "Jet" typically refers to the Blandford & Znajek (1977a) model, which describes an electromagnetically dominated, relativisitic outflow powered by the spin of the black hole. In GRMHD simulations, the thermodynamics are unreliable in this region due to its high magnetization. Thus we do not attempt to model the emission from the jet but exclude it from the domain when calculating the spectra (see §3.4 for details). The "disc-jet" is the label typically given to the more mildly relativistic outflow sourced by the accretion disc (e.g., the Blandford & Payne 1982 or Lynden-Bell 2003 models, see Yuan et al. 2015 for the distinction), while the term "wind" generally refers to non-relativistic outflow that occupies a larger solid angle. The thermodynamics of these regions are more reliably captured by GRMHD simulations since they are not as extremely magnetized. In the present chapter we do not make a precise distinction between the labels"disc-jet" and the "wind," but will generally use the term "outflow" and "disc-jet" to refer to the disc-jet and wind regions.

The chapter is organized as follows. §3.3 describes our GRMHD method for electron entropy evolution, §3.4 describes how we construct spectra and images of Sgr A*, §3.5 describes the basic parameters and initial conditions of our fiducial model, §3.6 presents the results, §3.7 discusses the thermodynamics of the outflowing polar regions, §3.8 compares our model to the phenomenological disc-jet models in the literature, and §3.9 concludes.

For convenience, we absorb a factor of $\sqrt{4\pi}$ into the definition of the magnetic field 4-vector, b^μ, so that the magnetic pressure is $P_m = b^2/2$. Furthermore, we set $GM = c = 1$ throughout, where G is the gravitational constant, M is the black hole mass, and c is the speed of light.

3.3 Fluid Model and Electron Thermodynamics

Using the assumption that $T_e \lesssim T_p$ we take the solution of the single-fluid, ideal GRMHD equations to be a good approximation for the total fluid number density, n, pressure, P_g, magnetic field four-vector, b^μ, and four-velocity, u^μ. We solve these equations using a version of the numerical code `HARM` (Gammie et al. 2003) that we parallelized using message passing interface (MPI), extended to 3D, and made freely available online as the `HARMPI` code.[2] For the electron variables, we use the charge neutrality assumption to constrain the electron number density and four-velocity to be the same as that of the ions (i.e.; $n_e = n_i = n, u_e^\mu = u_i^\mu = u^\mu$) but evolve a separate entropy equation to solve for the electron temperature:

$$\rho T_e u^\mu \partial_\mu s_e = f_e Q - \nabla_\mu q_e^\mu - a_\mu q_e^\mu \tag{3.1}$$

where f_e is a function of the local plasma parameters determining the fraction of the total heating rate per unit volume (Q) given to the electrons, $q_e^\mu = \phi \hat{b}^\mu$ is the anisotropic thermal heat flux

---

[2] `https://github.com/atchekho/harmpi`

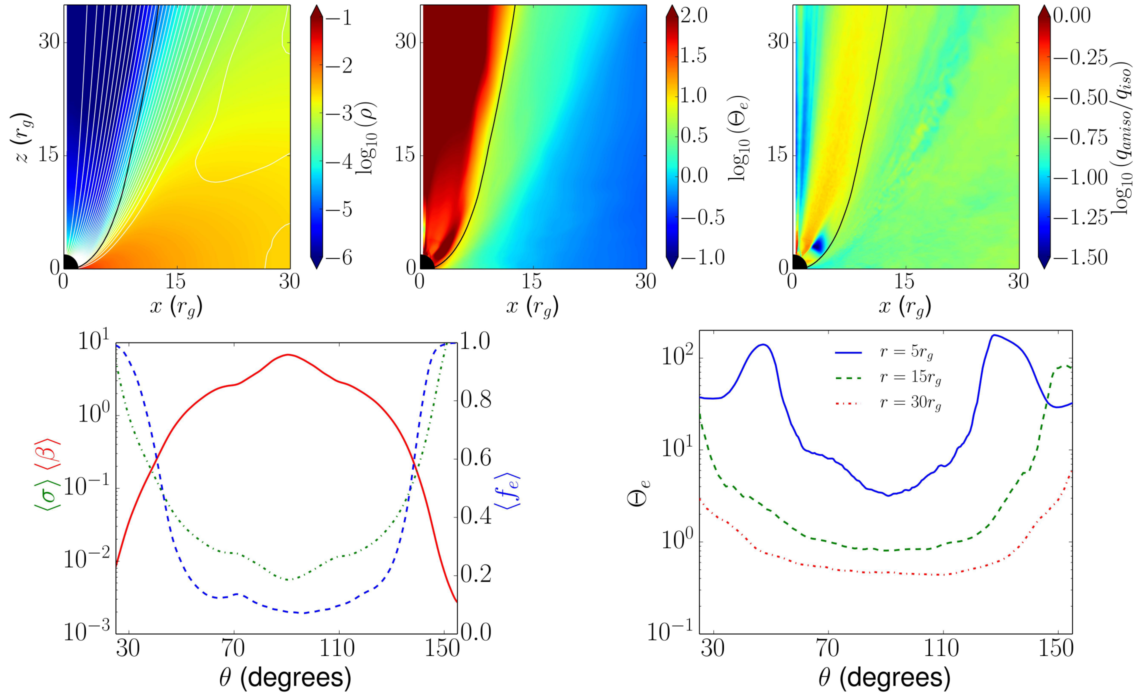

Figure 3.1: Properties of our 3D black hole accretion simulations. The top left panel shows the density over-plotted with white magnetic field lines, the top middle panel shows the time- and φ-average electron temperature in units of $m_e c^2$, and the top right panel shows the ratio of the anisotropic (field-aligned) heat flux to the isotropic heat flux (both computed from a simulation without electron conduction). All quantities in the top panel have been folded across the equator, and black lines denote the $b^2/\rho = 1$ contour. The bottom left panel shows the angular variation of the plasma parameter, $\beta \equiv 2P_g/b^2$, the magnetization parameter, $\sigma \equiv b^2/\rho$, and the electron heating fraction, f_e, averaged over r from the event horizon to $25r_g$, while the bottom right panel shows the angular variation of the electron temperature at 5, 15, and 30 r_g. All quantities have been averaged over φ and time from $15,000-19,000\ r_g/c$. Note how the relativistic electron temperatures important for synchrotron emission are strongly concentrated in the coronal and outflowing regions where $\beta \lesssim 1$. This is a consequence of the strong β-dependence of our electron heating fraction, f_e (see §3.3).

along field lines, $\hat{b}^\mu$ is a unit vector along b^μ, and $a^\mu = u^\nu \nabla_\nu u^\mu$ is the four acceleration. The latter properly accounts for gravitional redshift of the heat flux (Chandra et al. 2015b). To calculate Q, we directly compare the internal energy obtained from solving an entropy conserving equation to the total internal energy of the gas as described in Ressler et al. (2015). As in all conservative GRMHD codes, the heating is provided by grid-scale dissipation that is a proxy for of magnetic reconnection, shock heating, Ohmic heating, and turbulent damping. In this work, we determine f_e via equations (48) and (49) in Ressler et al. (2015), which were obtained from a fit to plasma heating calculations (Howes 2010) and are reasonably accurate at modelling particle heating in the solar wind (Howes 2011). The key qualitative feature of this prescription for f_e is that it depends on the plasma β-parameter, $\beta \equiv P_g/P_m$, the ratio between the fluid and magnetic pressures: electrons (ions) are predominantly heated for $\beta \lesssim 1$ ($\beta \gtrsim 1$), which is a general result predicted by linearizing the Vlasov equation and calculating the fractional heating rates of the two species due to MHD turbulence (Quataert & Gruzinov 1999).

Thus, for a magnetized accretion disc, we expect to have hot electrons primarily concentrated in the coronal and outflowing regions characterized by $\beta \lesssim 1$. Note that although the quantitative formula we use is only strictly valid for heating due to dissipation at the smallest scales of the MHD turbulent cascade and not magnetic reconnection, heating due to the latter has a qualitatively similar dependence on β (Numata & Loureiro 2015). To calculate the total heating rate per unit volume, $Q \equiv \rho T_g u^\mu \partial_\mu s_g$, we use the model detailed and tested in Ressler et al. (2015), which self-consistently captures the numerical heating provided by the ideal conservative GRMHD evolution. Ressler et al. (2015) show that this method accurately calculates the heating rate in several test problems, including strong shocks and forced MHD turbulence. Finally, we evolve the conductive flux identically to Ressler et al. (2015) using the model of Chandra et al. (2015b), where we parametrize the electron thermal conductivity with a dimensionless number α_e, related to the conductivity, χ_e via

$$\chi_e = \alpha_e c r. \tag{3.2}$$

For the present work, we focus on $\alpha_e = 10$ and $\alpha_e = 0$. The former essentially saturates the heat flux at its maximum value of $u_e v_{t,e}$, where u_e is the electron internal energy per unit volume and $v_{t,e}$ is the electron thermal speed, while $\alpha_e = 0$ corresponds to zero heat flux.

The only free parameter in our electron model is the dimensionless electron conductivity, α_e, since we have fixed the electron heating model as described above. Note that there are, however, significant uncertainties introduced by the uncertainty in the poorly constrained macroscopic parameters of the system (e.g., magnetic flux and black hole spin).

3.4 Radiation Transport

To calculate model spectral energy distributions (SEDs), we use the Monte Carlo radiation code `GRMONTY` (Dolence et al. 2009) adapted to use our evolved electron temperature to calculate the emissivity and scattering/absorption cross-sections. We include synchrotron emission/absorption and inverse Compton scattering. The emission is calculated in post-processing and does not affect the flow dynamics. Furthermore, we also generate radio and infrared images using the ray-tracing code `iBOTHROS` (Noble et al. 2007) which includes synchrotron emission/absorption.

When calculating the spectrum, we average the emission over azimuthal observing angle in order to reduce noise. This does not qualitatively affect the time-averaged spectrum and only very modestly reduces temporal variability (as we have determined using a subset of the simulation outputs). Furthermore, we also make the "fast light" approximation, meaning that we compute a single spectrum by propagating photons on a fixed time slice of fluid quantities. This amounts to assuming that the light propagation time across the domain is small compared to the dynamical time and should not be a dominant source of error.

While the GRMHD simulation is scale free, the radiation transport depends on the physical mass scale of the accretion disc. This dependence can be represented by a single free parameter, namely, the mass unit, $M_{\rm unit}$, which is a number in grams that converts the simulation density to a physical density (and thereby fixes the physical accretion rate). We set this free parameter by normalizing the time-averaged flux at 230 GHz to the observational value of 2.4 Jy (Doeleman et al. 2008).

Finally, in order to limit the emission to regions of the simulation in which we can reasonably trust the fluid thermodynamics, we impose a limit on the flow magnetization $\sigma = b^2/\rho c^2$. That is, we only consider emission that originates or scatters from regions of $\sigma < 1$. The thermodynamics in regions with larger σ become uncertain in conservative codes because small errors in the total energy (which is dominated by magnetic energy) lead to large errors in the internal energy. Note that this is true for both the underlying GRMHD entropy and temperature and not just the electron temperature. The motivation for our particular maximum value of σ and the effects of varying this parameter are described in Appendix 3.C.

3.5 Accretion Disc Model

We initialise the simulation with the now "standard" Fishbone & Moncrief (1976) equilibrium torus solution with a dimensionless spin, $a = 0.5$ (note the change from $a = 0.9375$ used in Chapter 2), inner radius, $r_{\rm in} = 6r_g$, and with the maximum density of the disc occurring at $r_{\rm max} = 13r_g$ (see Appendix 3.B for more details). Here $r_g = GM/c^2$ is the black hole gravitational radius. The adiabatic index of the gas is taken to be $\gamma = 5/3$, appropriate for ions with sub-relativistic temperatures. We initialize the torus with a single magnetic field loop in the (r, θ) plane, as we discuss in Appendix 3.B.

We take the adiabatic index of the electron fluid to be $\gamma_e = 4/3$, appropriate for relativistically hot electrons, and initially set $u_e = 0.1u_g$ and the electron heat flux to zero. We apply the floors on internal energy (both for the total gas and electrons) and density in the drift frame of the plasma as described in Appendix 3.B. Here we use the same floor prescription for the electrons as in Ressler et al. (2015). We run the simulation for a time of $19,000\ M$, which is long enough for the inner $r \lesssim 25r_g$ portion of the disc to be in inflow equilibrium. The outflow, however, travels at higher velocities so that it takes $\lesssim 1000\ M$ for the flow to reach $100r_g$.

Note that we have assumed a constant value for both the electron and total gas adiabatic indices.

Sadowski et al. (2016) implemented temperature-dependent adiabatic indexes and showed that while γ_e was always $\approx 4/3$ in the domain of interest, the total adiabatic index varied from $5/3$ in the midplane to $4/3$ in the polar regions, meaning that assuming $\gamma = 5/3$ (as we do here) overestimates the gas temperature by about a factor of 2. However, their resulting electron temperatures were qualitatively very similar to those in the constant adiabatic index model (see their Figure 5), so we do not expect this approximation to have a significant effect on our results.

Figure 3.B.1 shows our computational grid, which is uniformly discretized in "cylindrified" and "hyper-exponential" modified Kerr-Schild (MKS) coordinates as described in Appendix 3.B. The grid extends from an inner radius of $r_{\rm in} = 0.8(1 + \sqrt{1 - a^2})\ r_g$ ($\approx 1.62 r_g$ for $a = 0.5$) to an outer radius of $r_{\rm out} = 10^5 r_g$. In contrast to the cylindrified and hyper-exponentiated coordinates we use in `HARMPI`, we use standard MKS coordinates in `iBOTHROS` and `GRMONTY`. As photons propagate between grid points, the radiation transport algorithms require frequent evaluation of the connection coefficients which are analytic in MKS but require multiple numerical derivatives in the cylindrified coordinates. The latter greatly increases the computational cost of these methods, which is not an issue for `HARMPI` because after it evaluates the connection values once at the beginning of the simulation at each grid point, it stores them for future use. To read in data from `HARMPI`, we first use the Jacobian of the coordinate transformation to convert all 4-vectors and then interpolate onto the grids of `iBOTHROS` and `GRMONTY`.

3.6 Results

3.6.1 Basic Flow Properties

Figure 3.1 shows the time and azimuthally averaged electron temperature, density, and heat flux relative to the field-free value, as well as 1D angular profiles of the plasma beta parameter, β, magnetization, $\sigma = b^2/\rho$, electron heating fraction, f_e, and dimensionless electron temperature, $\Theta_e \equiv k_B T_e/m_e c^2$. The 1D profiles are additionally averaged over radius from the horizon to $25 r_g$. Our 3D simulations reproduce the general qualitative result of Ressler et al. (2015)'s 2D simulation: the hottest electrons are concentrated in the lower density coronal and funnel wall regions, while the midplane of the disc remains relatively cold. Furthermore, we find that the anisotropic heat flux is suppressed by a factor of $\sim 5 - 10$ relative to the isotropic heat flux, roughly equivalent to the 2D result. This is because the magnetic field is, on average, primarily toroidal, while the temperature gradients are primarily poloidal. We note that the total heating rate integrated over the volume with $\sigma < 1$ between the event horizon and the inflow equilibrium radius[3] ($\sim 25 r_g$) is $\sim 0.39\%$ of $|\dot{M}c^2|$, well below the efficiency predicted by the Novikov & Thorne (1973) (NT) model for a disc extending out to $25 r_g$ with a spin of $a = 0.5$ (6.3%). This result is not necessarily surprising; the thin disc efficiency assumes that all of the gravitational binding energy of the disc must be dissipated and radiated away and that outflow is negligible. RIAF discs, on the other hand, are typically characterized by significant outflow in the form of Poynting and turbulent energy flux

---

[3] The integrated heating rate is calculated as $\int_{r_H}^{25 r_g} -Q u_t \sqrt{-g} dx^1 dx^2 dx^3$, where r_H is the radius of the event horizon.

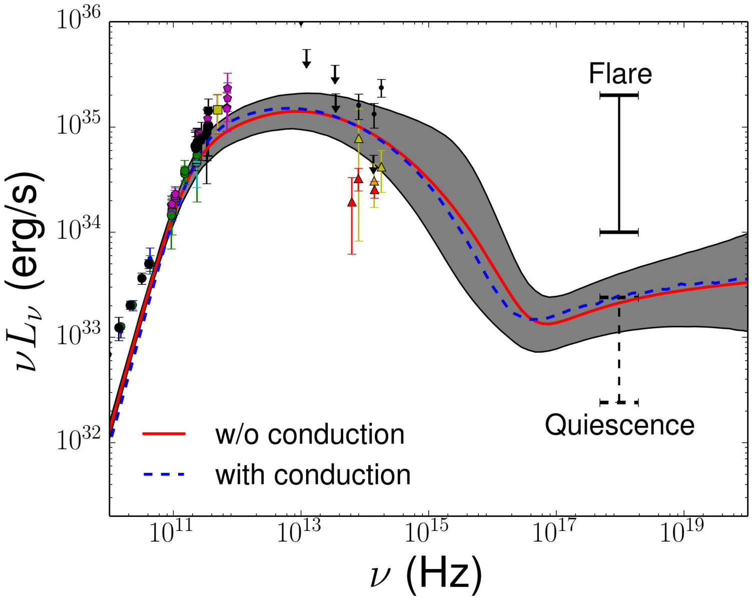

Figure 3.2: Spectral Energy Distribution (SED) for our fiducial model averaged over $15,000 - 19,000\ r_g/c$ (about 1 day for Sgr A*), as observed at an inclination angle of 45° with respect to the spin axis of the black hole. We show results with and without anisotropic electron conduction (with the dashed blue and solid red lines, respectively). The shaded grey region represents the 1σ time-variability of the SED over this time interval without conduction (the time variability with conduction is indistinguishable, so it is not plotted here). Data points represent various observations and upper limits (see Appendix 3.A). The solid vertical line in the X-rays roughly represents the range of observed flares in Sgr A* (Neilsen et al. 2013), while the dashed vertical line represents "quiescent" emission (i.e. between 10 -100% of the total total quiescent emission observed from Sgr A*; Baganoff et al. 2003). The SED is normalized to match the observed 230 GHz flux.

so that the energy going into dissipation can be much less (though the latter is typically only a small fraction of $\dot{M}c^2$, e.g. Yuan et al. 2012, the former can be significant, e.g. McKinney & Gammie 2004). However, we find that our calculation of the total heating rate has significant contribution from the negative heating in the polar regions (discussed in §3.7) which is a consequence of numerical diffusion. If we focus exclusively on the disc, excluding negative heating rates in the polar regions, the heating rate in the same volume totals $\sim 4.6\%$ of $|\dot{M}c^2|$, much higher, of order the NT efficiency.

The simulation has a significant amount of magnetic flux threading the black hole, with a time averaged value of $\Phi_{BH} \approx 40\ (\dot{M}c)^{1/2} r_g$, which can be compared to the typical saturation value of a Magnetically Arrested Disc, $\approx 50\ (\dot{M}c)^{1/2} r_g$ (MAD, Narayan et al. 2003; Tchekhovskoy et al. 2011), at which the excess flux impedes the inflowing matter. Interestingly, in a few test runs varying the magnetic flux, we have found that as long as the magnetic flux is below this saturation value, the qualitative features of the spectrum are not strongly dependent on the flux threading the black hole. Note that this is true only when normalising the spectrum to the 230 GHz flux by varying the accretion rate. Higher (lower) magnetic flux values tend to require smaller (higher) accretion rates. If instead we increased Φ at a fixed accretion rate we would expect significant differences in the spectrum (e.g., higher flux, higher peak frequency, etc).

3.6.2 Spectra and Images

Figure 3.2 shows the SED of our model averaged from $15,000 - 19,000\ r_g/c$ (a time of about 1 day for Sgr A*), at an inclination angle of 45° with and without thermal conduction and with time-variability shown by the shaded region. To normalize the 230 GHz flux, the simulation required a time-averaged accretion rate of $1.1 \times 10^{-8} M_\odot\,\mathrm{yr}^{-1}$, or $\sim 1.2 \times 10^{-7}\ \dot{M}_{\mathrm{Edd}}$ for Sgr A*. This is in reasonable agreement with the estimate of $6 \times 10^{-8} M_\odot\,\mathrm{yr}^{-1}$ provided by the inflow-outflow model of Shcherbakov & Baganoff (2010) and falls within the constraints set by radio polarization measurements (Marrone et al. 2007). Interestingly, this accretion rate is about two orders of magnitude less than the accretion rate at the Bondi radius inferred from X-ray observations (Baganoff et al. 2003), suggesting the existence of a strong, large scale outflow.

It is convenient to interpret the spectrum using the luminosity-weighted fluid quantities at the last scattering surface (this is simply the location of the emitting regions for photons optically thin to scattering). These are shown as a function of frequency in Figure 3.3. The spectrum can be decomposed into three distinct regions:

1. Below about ~ 230 GHz the emission is optically thick synchrotron and originates at larger radii ($\sim 10 - 200 r_g$) in the outflow ($v^r \sim 0.01 - 0.1c$) of the corona/funnel ($|\theta - \pi/2| \sim 20° - 60°$).

2. Between ~ 230 GHz and $\sim 10^{17}$ Hz $\simeq 0.5$ keV the emission is optically thin synchrotron from radii close to the horizon ($\lesssim 10 r_g$) and closer to the midplane ($|\theta - \pi/2| \sim 10° - 30°$). On average, the emitting regions are inflowing.

3. Above $\sim 10^{17}$ Hz $\simeq 0.5$ keV the luminosity-weighted number of scatterings sharply transitions from ~ 0 to ~ 1, indicating that the X-ray emission is dominated by inverse Compton scattering. More precisely, by computing the luminosity-weighted photon energy gain per scattering and the luminosity-weighted pre-scattering frequency, we find that the X-ray emission is dominated by infrared photons ($\sim 10^{13} - 10^{15}$ Hz) scattered by electrons emitting synchrotron radiation in the IR. The latter point can also be seen in the correspondence between the luminosity-weighted fluid quantities at the point of origin for the IR and X-ray photons in Figure 3.3.

Figure 3.2 shows that the spectra of models with and without anisotropic electron thermal conduction are nearly indistinguishable from each other. We have found this to be a robust result for the Standard and Normal Evolution (SANE) accretion flows (Narayan et al. 2012) without dynamically-important magnetic flux over a wide variety of initial conditions, black hole spin, and magnetic flux (that is, for fluxes less than the MAD saturation limit).

We find that our model produces significant X-ray and NIR variability, which qualitatively agrees with the observed flaring behaviour of Sgr A* (see §3.6.3), though for this particular model we do not see strong X-ray flaring events ($\gtrsim$ 10 times quiescence) and the quiescent X-ray flux may be moderately overpredicted. We also find that our fiducial model has a spectral slope near 230 GHz that agrees well with observations, but at $\lesssim 10^{11}$ Hz the slope becomes steeper than that observed, $d\log(F_\nu)/d\log\nu \approx 0$, resulting in an underprediction of the low frequency emission (see § 3.7.1 for more details).

Figure 3.4 shows time-averaged 30 GHz, 230 GHz, and 2 μm images without electron thermal conduction at 12°, 45° and 90° (images with electron conduction look nearly identical). In generating these images we used `iBOTHROS` and neglected Inverse Compton scattering, as appropriate for such low frequencies. The photon ring is clearly visible at both 230 GHz and 2 μm. This bright circle of emission surrounding the shadow of the black hole is the observational signature of the effects of the circular photon orbit and strong lensing on the small emitting region in the simulations. A primary goal of the Event Horizon Telescope is to measure the size of this ring in order to probe the strong field limit of general relativity. The lower frequency images are dominated by disc-jet emission from larger radii while the higher frequency emission is dominated by disc emission close to the black hole.

An important property of our results is that they self-consistently produce the "disc-jet" structure appealed to in previous phenomenological models (e.g.; Falcke & Biermann 1995; Yuan et al. 2002; Mościbrodzka & Falcke 2013; Mościbrodzka et al. 2014; Chan et al. 2015b). This is clear in the luminosity-weighted fluid quantities in Figure 3.3 which show a transition from emission dominated by inflowing equatorial material above 10^{11} Hz to emission dominated by outflowing polar material at lower frequency. The disc-jet structure is particularly clear in the images in Figure 3.4, which show that the outflow dominates at lower frequency while the very compact emitting disc dominates at higher frequencies. This type of structure naturally occurs in our model because of the strong β dependence of the electron heating fraction, f_e, which suppresses electron heating in the midplane in favour of the polar regions.

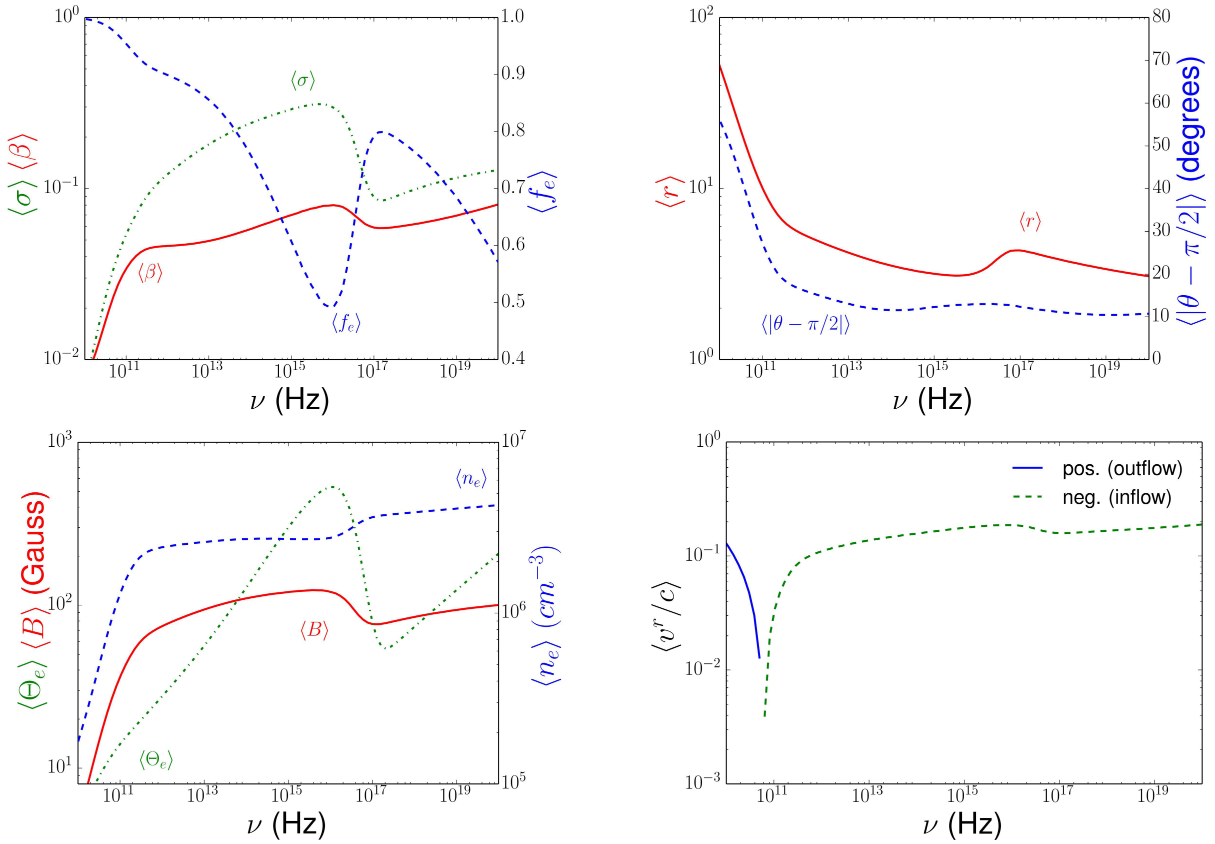

Figure 3.3: Fluid quantities at the point of origin averaged over individual photons as a function of observed photon frequency for the spectrum shown in Figure 3.2. Plotted are the magnetization, $\langle\sigma\rangle = \langle b^2\rangle/\langle\rho\rangle$, the plasma $\langle\beta\rangle = \langle P_g\rangle/\langle P_m\rangle$, the electron heating fraction, $\langle f_e\rangle$, the Boyer-Lindquist (BL) radial coordinate, $\langle r\rangle$, the deviation of the BL polar angle from the midplane, $\langle|\theta-\pi/2|\rangle$, the magnitude of the fluid-frame magnetic field, $\langle B\rangle = \langle\sqrt{b^\mu b_\mu}\rangle$, the electron number density, $\langle n_e\rangle$, and the dimensionless electron temperature in units of the electron rest mass, $\langle\Theta_e\rangle = \langle k_B T_e/m_e c^2\rangle$, as well as the radial velocity, $v^r = \sqrt{g_{11}}\langle u^{x1}/u^t\rangle$. The optically thick low frequency synchrotron emission (below $\sim$ 230 GHz) comes from larger radii in the outflow away from the midplane where β is smallest and hence the electron heating fraction, f_e, is largest. It is interesting to note that despite the larger f_e in these regions that the electron temperatures are quite modest ($\Theta_e \lesssim 10$) (see Section 3.7.1 for more details). The higher frequency emission (above $\sim$ 230 GHz) is emitted and/or scattered from smaller radii close to both the horizon and the midplane. In these regions, the temperatures are much larger (reaching $\Theta_e \sim 100$ and above), due to the increased turbulent heating in the disc fuelled by the deeper gravitational potential. Between 230 GHz and about 10^{17} Hz the emission is predominantly optically thin synchrotron, while above 10^{17} Hz the emission is predominantly inverse Compton scattering of IR photons by IR-emitting electrons. This explains the transitions in the average fluid quantities at about 10^{17} Hz.

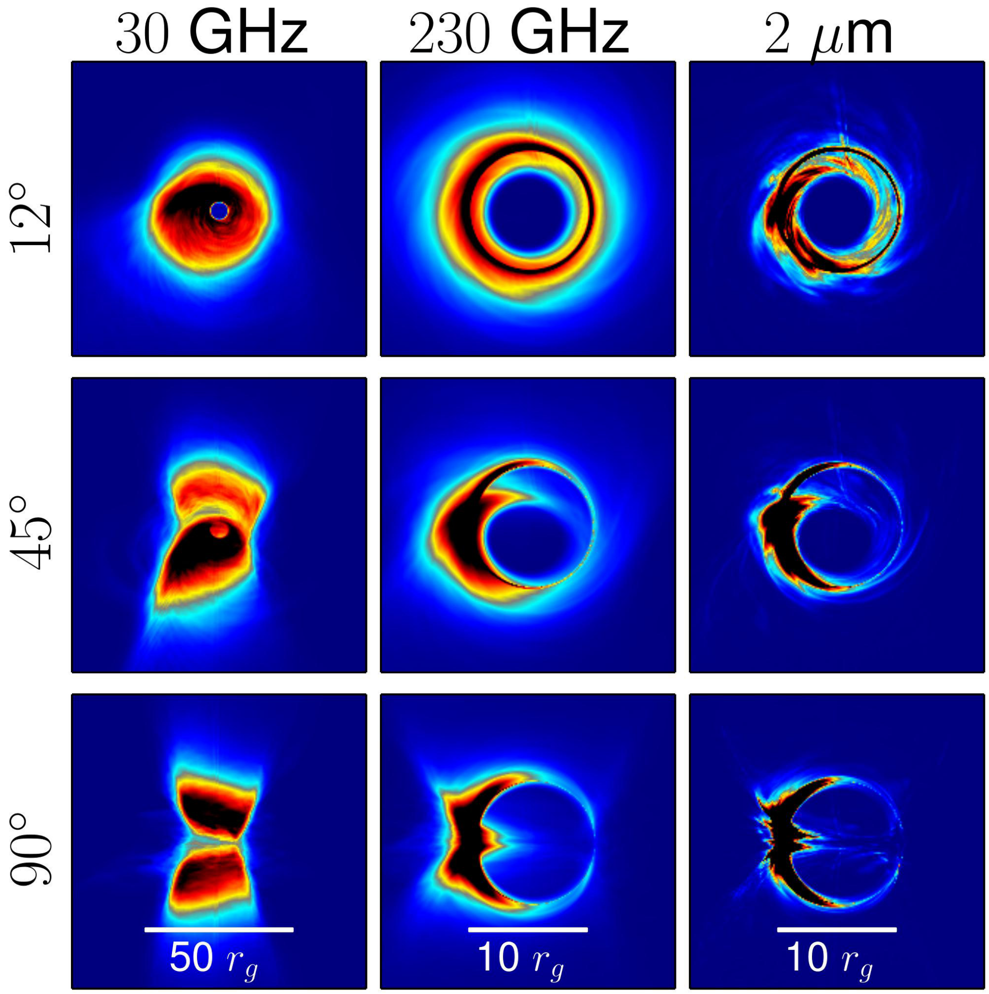

Figure 3.4: Linear intensity maps for our fiducial model of Sgr A* without electron thermal conduction (the effect of conduction on the images is negligible) at 30 GHz (left column), 230 GHz (middle column), and 2 μm (right column) for inclination angles of 12° (top row), 45° (middle row) and 90° (bottom row). The inclination of 90° is edge-on while 12° is nearly face-on. Images are averaged over time from $15,000 - 19,000\ r_g/c$ and normalized such that the 230 GHz flux is 2.4 Jy (Doeleman et al. 2009). The physical size of the 30 GHz images is 100 r_g × 100 r_g while the physical size of the 230 GHz and 2 μm images is 25 r_g × 25 r_g. For all inclination angles, the photon ring is clearly visible at 230 GHz, the frequency at which the Event Horizon Telescope will be able to spatially resolve Sgr A* (Doeleman et al. 2008), and is also clearly visible at 2 μm, the wavelength of interest to GRAVITY (Gillessen et al. 2010). The low frequency radio emission is dominated by the outflow at large radii, consistent with previous phenomenological models of Sgr A* (e.g. Falcke & Biermann 1995; Yuan et al. 2002; Mościbrodzka & Falcke 2013; Mościbrodzka et al. 2014; Chan et al. 2015b).

3.6.3 Time Variability

Figure 3.5 shows the light curves of our fiducial model in the mm, NIR, and X-ray frequencies compared to the accretion rate of the disc over the same time interval. Our simulations show significant and correlated time variability in the NIR and X-ray bands while the mm emission is significantly less variable.

The general correspondence between the NIR and X-ray light curves is due to the fact that the flares are caused by localized hot spots of low β that emit high levels of NIR synchrotron emission, a fraction of which is then additionally upscattered to the X-rays. Each large spike in X-rays is accompanied by a comparably large spike in the NIR emission (e.g. the X-ray peak labeled “A”), in agreement with observations of Sgr A* that find that all X-ray flares have NIR counterparts (see, e.g., Table 3 in Eckart et al. 2012 for a recent summary). On the other hand, there are a few large spikes in the NIR emission that are accompanied by only relatively small increase in the X-ray flux (e.g. the NIR peak labeled “B”). Since we have not tuned our model to precisely match the time-averaged quiescent X-ray flux, the key feature here is the significant increase in IR luminosity without a corresponding increase in X-ray luminosity (and not necessarily whether the X-ray luminosity is above the quiescent threshold). Therefore, these particular NIR flares are consistent with lacking a strong X-ray counterpart, which are are also observed in Sgr A* (e.g., Hornstein et al. 2007, Trap et al. 2011). Furthermore, we find that the X-ray emission in our model in fact has no well defined “quiescent state” but is rather constantly flaring. This has been suggested for Sgr A*, where the observed “quiescent state” could be a collection of undetectable flares (Neilsen et al. 2013).

The X-ray “flares” in our model shown in Figure 3.5 are relatively weak in magnitude, with luminosities peaking at factors of only a few times the quiescent level. During this time interval, we find no evidence for the strong X-ray flares observed in Sgr A* which range from ~ 10 to $\gtrsim 100$ times the quiescent level (e.g.; Trap et al. 2011 and references therein; Neilsen et al. 2013). While this could point to the need for nonthermal particles (see, e.g. Ball et al. 2016), it could also be a consequence of the limited time interval considered here ($\sim$ one day, while Sgr A* has major flares only $\sim$ once per day) or the particular parameters used in our model (e.g., spin and magnetic flux). This will be investigated in future work.

3.6.4 Dependence of Observables on Disc Parameters

Here we briefly describe the qualitative effects of varying several parameters of our fiducial model. These effects are not unique to our electron model but are more general properties of radiative GRMHD models of low $\dot{M}$ discs as seen in previous parameter studies (e.g. Mościbrodzka et al. 2009; Chan et al. 2015b)

Spin: Larger black hole spin tends to increase both NIR and X-ray emission. This is because high spin black holes have inner-most stable circular orbits (ISCOs) that are closer to the event horizon, which means that the accretion disc will extend to smaller radii where the temperatures are generally higher due to the deeper gravitational potential. These higher temperature regions emit at higher frequencies.

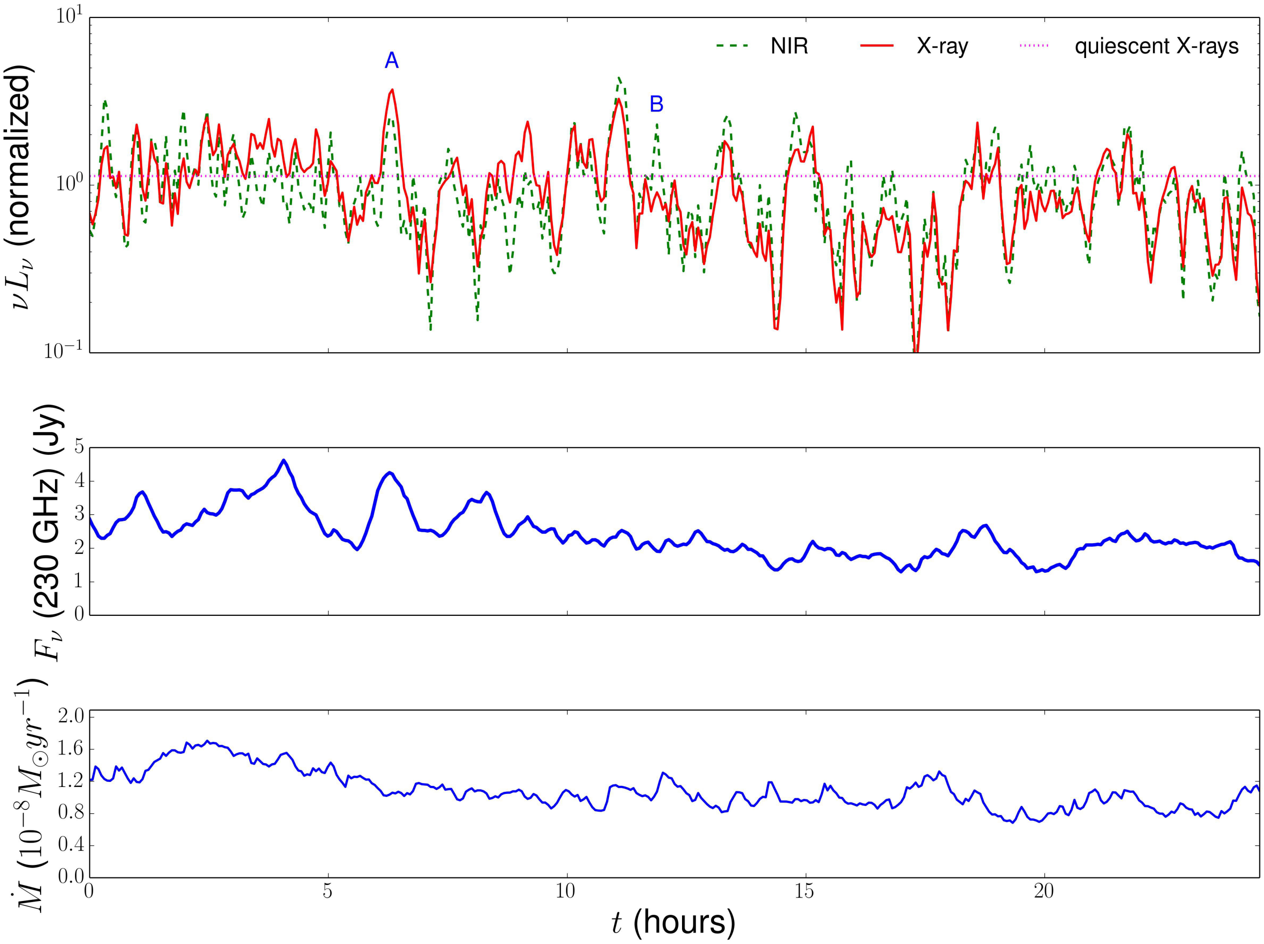

Figure 3.5: *Top Panel*: νL_ν as a function of time at an inclination angle of 45° for NIR (2.18 microns) and X-ray (2-8 keV) bands during the time interval $15,000 - 19,000\ r_g/c$ or $\sim$ 1 day for Sgr A*. Each light-curve is normalized to the mean value of νL_ν over the entire interval. Also plotted is the total quiescent X-ray flux as observed by *Chandra* (Neilsen et al. 2013), with the same normalization as our model's X-ray light curve. Though only $\sim$ 10% of this quiescent emission is believed to originate from the inner accretion flow, the total quiescent flux is the relevant threshold for X-ray flares. Both the X-ray and NIR emission show order of magnitude variability on time-scales of $\sim$ 0.5 hours and are strongly correlated. Note that, as observed in Sgr A*, each X-ray flare is associated with a NIR flare (e.g. the peak labeled "A"), but there are also a few candidates for NIR flares without X-ray counterparts (e.g. the peak labeled "B"), which are also observed in Sgr A*. *Middle Panel*: 230 GHz flux in Jy as a function of time at an inclination angle of 45°. Compared to the NIR and X-ray flux, the mm flux varies only weakly over this time interval (note the linear scale), consistent with observations. *Bottom Panel*: Accretion rate in units of 10^{-8} solar masses per year. The variability in $\dot{M}$ has roughly the same time scale as the variability in NIR and X-ray emission because the latter originate close to the horizon. However, in detail the emission is not well-correlated with fluctuations in $\dot{M}$.

Inclination Angle: Inclination angles closer to 90° (edge-on), tend to have larger NIR and X-ray emission (relative to the mm emission) than inclination angles closer to 0° (face-on). This is primarily due to Doppler boosting caused by rotation of the disc. When looking edge-on, Doppler beaming leads to the observed emission being dominated from the side of the disc that is moving towards us, which will also be Doppler blue-shifted from the fluid frame frequency. This increases the relative NIR and X-ray emission compared to the mm emission. On the other hand, when looking face-on, the motion of the disc is perpendicular to the line of sight and Doppler effects are minimized (though there can still be Doppler effects from the outflow).

3.6.5 Convergence of Spectra

In order to test whether our results are converged, we restarted the fiducial model described in Section 3.5 at double the resolution in each direction (namely, $640 \times 512 \times 128$). We did this by copying the fluid quantities at a particular time in each cell on the lower resolution grid into 8 cells on the higher resolution grid and using this as an initial condition. To prevent magnetic monopoles from being generated by the numerical interpolation, we operated on the magnetic vector potential instead of the magnetic field directly. We then ran for 2000 M, computed the time-averaged spectra, and compared to the lower resolution spectra that had also run for an additional 2000 M. Since 2000 M is roughly enough time for the inner $\sim 15r_g$ of the disc to accrete and for the outflow to reach beyond $100r_g$, we are reasonably confident that the simulation has had enough time to evolve dynamically from the initial restart. Figure 3.6 shows that the time averaged spectra are qualitatively the same. Quantitatively, the differences are minor, though interestingly the low frequency slope in the higher resolution simulation is slightly closer to observations. Unfortunately, doubling the resolution even further to see if this trend continues is too computationally expensive with our current resources; in fact, even running the $640 \times 512 \times 128$ simulation for much longer is pushing the limit of what we can afford for the present work. With that said, the fact that the differences between the spectra at these two different resolutions are almost negligible is encouraging and provides some assurance that the observational features of our model are not strongly dependent on resolution.

3.7 Thermodynamics in the Polar Outflow

The low frequency radio emission in our simulation generally originates within or near to what has in past work been described as the jet “sheath” (e.g. Mościbrodzka & Falcke 2013), which is the portion of the outflow that contains enough mass to produce emission, typically with $\sigma \lesssim 1$. This region is characterized by a strong gradient in mass density and entropy, corresponding to a nearly stationary contact discontinuity. The local Lax-Friedrichs (LLF) Riemann solver employed in `HARM` is known to have poor performance in such flows. When the gradient is not well resolved, artificial numerical diffusion affects the solution. In our calculations, the e-folding length of the entropy is only ~ 0.15 cells, i.e., very poorly resolved. This leads to a largely negative time and φ-averaged heating rate close to the contact discontinuity, seen in Figure 3.7 as the white regions.

Since the entropy equation is only being solved to truncation error while the conservation of energy equation is satisfied to machine precision, it is fine for the *instantaneous* heating rate to be locally negative. However, it is a concern that the time and spatially integrated heating rate is negative. This still would not be a concern if the negative heating was negligible in magnitude. However, when integrated over the volume between the black hole event horizon and the inflow equilibrium radius (and limiting the integration domain to $\sigma < 1$), the heating totals $\sim -4.2\%$ of $|\dot{M}c^2|$, roughly the same magnitude as the positive heating ($\sim 4.6\%$ of $|\dot{M}c^2|$). In Appendix 3.D we discuss this issue in detail using a simple 1D test of advection of a contact discontinuity. This test shows explicitly that large, unresolved gradients in entropy lead to negative heating rates such as those seen in Figure 3.7. This is a manifestation of the diffusion of contact discontinuities inherent in finite-volume codes made more extreme by the use of the LLF Riemann solver. These errors do converge to 0 if the contact "discontinuity" is actually a smooth but steep transition, but the jet-sheath interface layer is not well-resolved at the current resolution. It is important to stress that in addition to affecting the heating rate inference, related concerns apply to the thermodynamics of the `HARM` solution as well, which are significantly less accurate in regions of steep (poorly resolved) gradients.

More sophisticated Riemann solvers are known to be significantly less diffusive near contact discontinuities and are particularly well-suited for those with small perpendicular velocity components (as we have here). It is possible that including one of these solvers (e.g., the Harten-Lax-van-Leer-Discontinuities solver) might reduce or remove this negative heating and affect the thermodynamics of the polar outflow. This in turn might affect the low frequency emission from the simulations. However, it is not straightforward to implement these more advanced Riemann solvers in a general relativistic framework and thus it has only been done by a handful of groups (e.g., Komissarov 2004; Antón et al. 2006; White et al. 2016). We will explore the impact of these more sophisticated Riemann solvers in future work.

3.7.1 Low Frequency Radio Slope

A simple analytic argument can predict the low frequency radio slope for emission from an outflowing plasma (Blandford & Königl 1979; Falcke & Biermann 1995; Mościbrodzka & Falcke 2013). Assuming that the magnetic field, mass density, and electron temperature follow power laws in radius of the form:

$$
\begin{aligned}
B &\propto r^{m_B} \\
\rho &\propto r^{m_\rho} \\
\Theta_e &\propto r^{m_\Theta},
\end{aligned}
$$

it follows that

$$
F_\nu \propto \nu^2 \left[\Theta_e A\right](r_{\rm peak}) \propto \left[\Theta_e^5 B^2 A\right](r_{\rm peak}), \tag{3.3}
$$

where $A(r)$ is the cross-sectional area of the outflow at radius r and $r_{\rm peak}$ is the radius at the location of peak emissivity, given by the solution to $\nu \propto [\Theta_e^2 B](r_{\rm peak})$. Equation (3.3) is simply the black body emission at $r_{\rm peak}(\nu)$ where the optical depth drops to ~ 1. If magnetic flux is conserved,

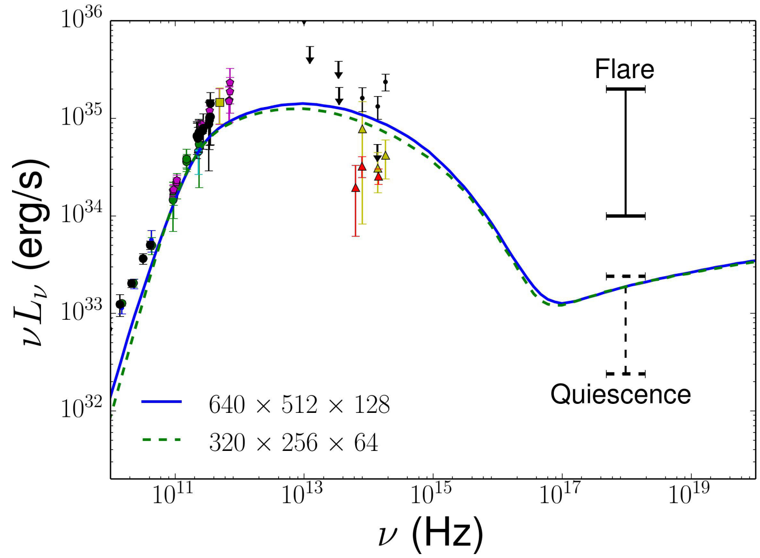

Figure 3.6: Spectral Energy Distribution (SED) for our fiducial model averaged over $11,800 - 12,300\ r_g/c$ at an inclination angle of 45° at two different resolutions (please see the legend). The higher resolution simulation was initialized with the results of the low resolution simulation at $10,000\ r_g/c$ and run for an additional $2,300\ r_g/c$. The spectra only display minor differences below $\sim 10^{11}$ Hz and above $\sim 10^{14}$ Hz.

then $B_r A$ = const. and $B_\varphi \sqrt{A}$ = const., meaning that if $A(r)$ is an increasing function of radius (as it is in conical or parabolic outflows) then $B \approx B_\varphi \propto 1/\sqrt{A}$ at large distances. Thus we have $F_\nu \propto \Theta_e^5(r_{\rm peak})$.

Clearly, if the outflow is isothermal, $F_\nu \propto \nu^0$ and the spectrum is flat, matching observations of Sgr A* and other jet sources. On the other hand, if the outflow is adiabatic, i.e. $\Theta_e \propto \rho^{\gamma_e - 1}$, then

$$F_\nu \propto \nu^{\frac{10(\gamma_e-1)}{4\gamma_e-3}}, \tag{3.4}$$

where we have assumed mass conservation: ρA = const. For $\gamma_e = 4/3$, this gives $F_\nu \propto \nu^{10/7}$. Note that this is independent of the jet shape as long as $A(r)$ increases with radius.

We find that our simulation generally has an adiabatic outflow (at least in the regions that primarily contribute to the low frequency radio emission) and the low frequency radio slope agrees roughly with $\nu^{10/7}$, under-predicting the observations. This suggests that our simulations are either missing some important heating mechanism in the outflow or that nonthermal particles (which we do not include) may play a crucial role.

3.8 Comparison to Previous Models of Sgr A*

We have shown that our model naturally and self-consistently produces the "coupled disc-jet" phenomenological model adopted in previous work to explain observations of Sgr A* (Falcke & Biermann 1995; Yuan et al. 2002; Mościbrodzka & Falcke 2013; Mościbrodzka et al. 2014; Chan et al. 2015b). The polar outflow dominates the low frequency radio emission while the accretion disc dominates the higher frequency emission. Our work thus provides strong theoretical support for some of the assumptions used by previous phenomenological models. However, we also find some important differences which we now highlight for a few representative cases.

Yuan et al. (2002) used a self-consistent analytical model that coupled an ADAF disc to a shocked outflow. In order to fit the spectrum of Sgr A* they required an electron heating fraction in the disc of $f_e = 10^{-3}$, corresponding to a maximum disc temperature of $\Theta_e \approx 1$ and resulting in $\Theta_e \approx 35$ at the base of the jet. As a result, the jet dominates the emission at all frequencies except for a narrow region around 230 GHz and a narrow region around 10^{15} Hz. In our model we find that outflow accounts only for the emission below about 10^{11} Hz while the disc dominates the emission above 10^{11} Hz (see Figure 3.3). The reason for this difference is that although our disc has, on average, $T_e \ll T_g$, there are localized hot-spots of low β that contribute significantly to the emission. These hot spots are natural in a turbulent 3D simulation but cannot be captured easily in 1D temperature profiles.

Disc-jet models in 3D GRMHD simulations have typically assigned a constant relativistic electron temperature, T_e, to the "jet" and a relatively large constant proton-to-electron temperature ratio, T_p/T_e, to the "disc". Two notable examples are Mościbrodzka et al. (2014), who defined the "jet" as regions with $-\rho h u_t > 1.02$, where h is the specific relativistic enthalpy, and Chan et al. (2015b), who defined the "jet" as regions with $\beta < 0.2$. Here "jet" and "disc" are in quotation marks because both the criterion $\beta < 0.2$ and the criterion $-\rho h u_t > 1.02$ occasionally include localized regions close to the horizon in the disc proper (i.e. inflowing material near the midplane). These small regions in the disc are then assigned relativistic electron temperatures and become a dominant source of higher frequency emission ($\gtrsim$ 230 GHz). Thus, in contrast to the 1D analytic models, only the low frequency emission ($\lesssim$ 230 GHz) is provided by the outflow while the rest of the emission is provided by the turbulent inflow.

Despite having similar emitting regions, Mościbrodzka et al. (2014) and Chan et al. (2015b) differ substantially in the amount of NIR emission they predict. This difference is due to the different choices of electron temperatures for the "jet" regions. Mościbrodzka et al. (2014) used relatively small electron temperatures ($\Theta_e \sim 10-20$), while Chan et al. (2015b) used relatively large electron temperatures ($\Theta_e \sim 30-60$ in their SANE models). The former choice leads to a low level of NIR emission and a dearth of flaring events, contrary to what we find (see Figures 3.2 and 3.5). The latter choice, on the other hand, is closer to the temperatures of the hot-spots in our model ($\Theta_e \sim 100$; see Figure 3.3) and leads to significant NIR emission via frequent flares (Chan et al. 2015a), similar to what we find.

We note, however, that our X-ray emission and X-ray time variability differ substantially from Chan et al. (2015b) and Chan et al. (2015a) due to the different emission processes considered. Their work neglects Compton scattering and the X-rays in their model are entirely produced by bremsstrahlung at large radii. On the other hand, our calculations include Compton scattering and focus on the inner portion of the disc where bremsstrahlung is negligible. We have shown that this Compton component is not only large enough to account for the "quiescent" emission but is also a source of weak X-ray flaring. Thus it is crucial to include it for any comparison to X-ray data of Sgr A*.

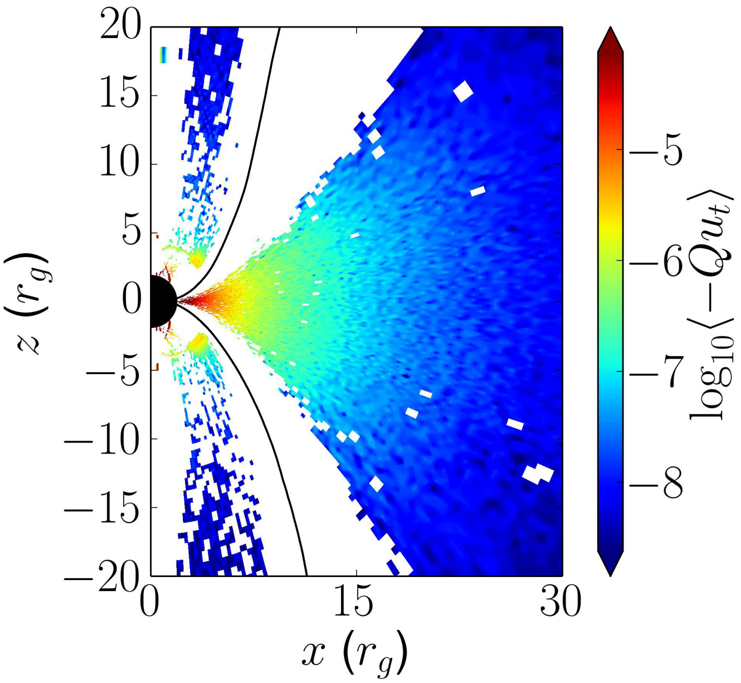

Figure 3.7: Time and φ-averaged heating rate per unit volume, with the black lines denoting the $b^2/(\rho c^2) = 1$ contour. The white regions represent negative heating rates, which are unphysical and are a consequence of the LLF Riemann solver's poor treatment of contact discontinuities (the strong density gradient in the polar region; see Figure 3.1; see §3.7 and Appendix 3.D). Better Riemann solvers should reduce this diffusion and could modify the thermodynamics in the polar region that dominates the low frequency radio emission in our models of Sgr A*.

Our model under-predicts the radio emission of Sgr A* below $\sim 10^{11}$ Hz. This is, by contrast, well fit by the phenomenological models. This is because we find the outflow to be roughly adiabatic and not isothermal, leading to a much steeper spectral slope (see Section 3.7.1). Electron thermal conduction would seem a natural way for the outflow to be closer to isothermal, but we have shown that it has a negligible effect even with a large thermal conductivity. This implies that our simulations are either failing to capture enough heating in the outflow or are missing additional physics (e.g., nonthermal particles, heating due to pressure anisotropy, etc.). Our calculation of the heating in the outflow may also be limited by numerical diffusion (see §3.7 and Appendix 3.D). Future work with improved numerical methods and physical models will help to distinguish among these possibilities.

3.9 Conclusions

We have presented the first results of applying a self-consistent treatment of electron thermodynamics in GRMHD simulations to observations of Sgr A*. Our goal is not to fit the observations in detail but to qualitatively determine the basic predictions of our model in which the electron entropy is self-consistently evolved including electron heating and anisotropic electron thermal conduction. In our calculation, the electron heating fraction, f_e, is not a free parameter adjusted to match observations but is fixed by a first principles calculation (§3.3). We have only modeled the emission by thermal electrons, deferring models of non-thermal particle acceleration and emission to future work

Despite the lack of any free parameters tuned to match observations, we find encouraging agreement between some properties of our predicted spectra and variability and observations of Sgr A*. This agreement includes the spectral slope near 230 GHz and the approximate magnitude of the time-averaged NIR and X-ray emission (Figure 3.2), as well as many of the qualitative features of the time variability (Figure 3.5). The images produced by our model at 230 GHz and 2 μm (Figure 3.4) display the characteristic "Einstein ring" at all inclination angles. This is encouraging for upcoming horizon-scale observations at these frequencies.

Our model reproduces the disc-jet structure of the accretion flow appealed to in the literature to explain the emission from Sgr A* (Yuan et al. 2002; Mościbrodzka et al. 2014; Chan et al. 2015b). The polar outflow dominates the low frequency radio emission and the turbulent inflow dominates the emission at frequencies above $\sim$ 230 GHz. This can be seen directly using the properties of the emitting regions as a function of frequency in Figure 3.3, and the 30 GHz, 230 GHz, and 2 μm images in Figure 3.4. Our results thus provide physical justification for many of the phenomenological prescriptions used in the past to model Sgr A* and can help motivate more sophisticated variants of these models in the future.

We find that anisotropic electron thermal conduction along magnetic field lines has little effect on our model spectra and images (see Figure 3.2 for the SEDs; images including conduction are not shown here because they are nearly identical to those without conduction in Figure 3.4). This is because the field lines in our simulation are primarily toroidal while the temperature gradients are primarily poloidal. Foucart et al. (2016) came to a similar conclusion for the effect of ion conduction on the fluid dynamics when including it in the total fluid stress-energy tensor. The small effect of electron conduction in our model suggests that future modelling of electron thermodynamics can probably neglect electron conduction, greatly simplifying the numerics and reducing the computational expense by a factor of $\sim$ 4. This needs, however, to be confirmed for Magnetically Arrested Discs (MADs, Narayan et al. 2003) or any other disc which differs significantly from the structure in our model.

The variability in our simulations is qualitatively similar to that seen in Sgr A* (Figure 3.5): 1) we find frequent X-ray and NIR flaring events 2) those flares are correlated 3) mm emission displays less variability 4) all X-ray flares have NIR counterparts, but we also find evidence for NIR flares without X-ray counterparts. The X-ray flares, however, are much weaker in magnitude than the strong flaring events observed in Sgr A*. This could be a result of our relatively small sample size in time ($\sim$ 1 day) or it could imply the need for nonthermal particles (e.g. Özel et al.

2000; Yuan et al. 2003; Ball et al. 2016). Given the wealth of time-dependent observational data on Sgr A* and the uncertainties that remain in its underlying physics, it is of great interest to study the statistical properties of the model's time variability in more detail. This will be a focus of future work.

Finally, like all numerical calculations, our model is not without its potential failure modes. In our disc models, numerical diffusion of poorly resolved entropy gradients affects the thermodynamics of both the electrons and the total fluid in the polar regions. This may affect the low frequency ($\lesssim 10^{11}$ Hz) emission in our model. On the other hand, all emission above $\sim 10^{11}$ Hz is unaffected by this issue. Moreover, we find that doubling the resolution of our simulation does not affect our predicted spectra (see Figure 3.6), but somewhat improves the agreement of the low-frequency slope with the observations.

Acknowledgments

We thank B. Ryan, J. Neilsen, A. Sadowski, and R. Narayan for useful discussions, as well as all the members of the horizon collaboration, http://horizon.astro.illinois.edu, for their advice and encouragement. We also thank the referee, F. Yuan, for useful comments on the manuscript. This chapter was supported by NSF grant AST 13-33612, and a Romano Professorial Scholar appointment to CFG. SMR is supported in part by the NASA Earth and Space Science Fellowship. EQ is supported in part by a Simons Investigator Award from the Simons Foundation and the David and Lucile Packard Foundation. Support for AT was provided by NASA through Einstein Postdoctoral Fellowship grant number PF3-140131 awarded by the Chandra X-ray Center, which is operated by the Smithsonian Astrophysical Observatory for NASA under contract NAS8-03060, the TAC fellowship, and by NSF through an XSEDE computational time allocation TG-AST100040 on TACC Stampede. This chapter was made possible by computing time granted by UCB on the Savio cluster.

Appendix

3.A Observational Data

The radio and millimetre data we use are taken from the mean spectra of Sagittarius A* as calculated by Falcke et al. (1998), combining the Very Large Array (VLA), the Institut de Radioastronomie Millimetrique (IRAM), the Nobeyama 45 m, and the Berkeley-Illinois-Maryland Array (BIMA) observational results over the frequency interval 1.46 - 235.6 GHz, An et al. (2005) combining VLA and Giant Metrewave Radio Telescope (GMRT) observational results over the frequency interval 0.33 - 42.9 GHz, Doeleman et al. (2008) using the Event Horizon Telescope (EHT) at 230 GHz, Bower et al. (2015a), combining VLA, the Atacama Large Millimetre/submillimetre Array (ALMA), and the Submillimetre Array (SMA) observational results over the frequency interval 1.6 - 352.6 GHz, and finally, Liu et al. (2016a) and Liu et al. (2016b) using ALMA over the frequency interval 92.996 - 708.860 GHz and at 492 GHz, respectively. Infrared upper limits are taken from Telesco et al. (1996) at 30 μm, Cotera et al. (1999) at 24.5 μm and 8.81 μm, Genzel & Eckart (1999) at 2.2 μm, and Schödel et al. (2007) at 8.6 μm, while infrared data points for both the quiescent and flare states are taken from Genzel et al. (2003a) and Schödel et al. (2011). Finally, we use the range of 2-10 keV X-ray flare luminosities seen in Sgr A* during the year 2012 (Neilsen et al. 2013) and the quiescent level of 2.4 $\times 10^{33}$ erg s^{-1} (Baganoff et al. 2003). Note that the inner accretion flow is believed to contribute only $\sim$ 10% of this quiescent flux (Neilsen et al. 2013), but we use the total quiescent emission to define the luminosity that "flares" must exceed in our model.

3.B Initial conditions, Coordinate System and Floors

In this appendix we describe our specific choice of initial conditions, coordinates, and numerical floors.

3.B.1 Initial Conditions

One approach for initial conditions is to overlay the torus with a weak magnetic field with field lines along contours of density, $A_\varphi \propto \rho - \rho_0$ (Gammie et al. 2003). This results in a single magnetic field loop in the (r, θ) plane. The centre of the loop is at the density maximum, and the loop is fully contained within the torus. However, we found that by about $t \sim 10^4 r_g/c$ such a loop gets

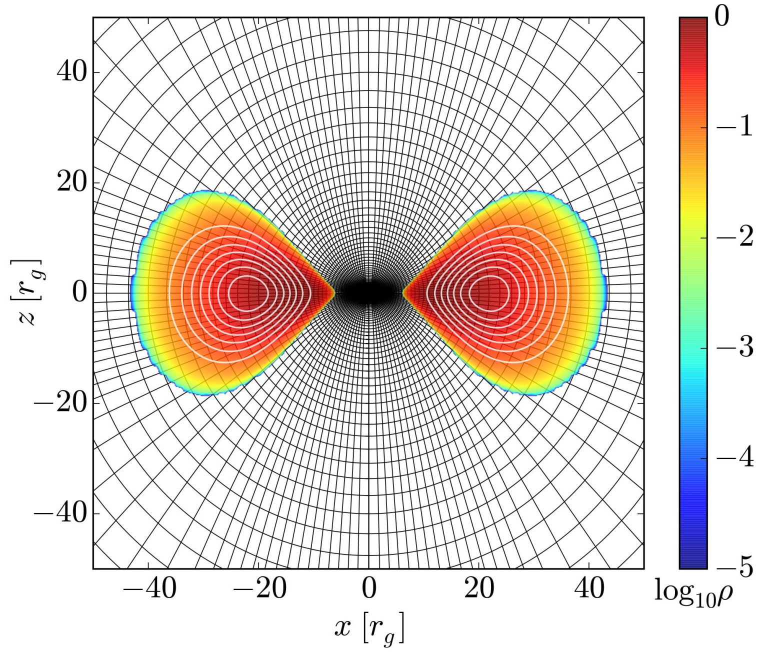

Figure 3.B.1: Our simulations use a grid adapted for the disc-jet problem. The grid lines, shown with black lines (every 4th cell interface is shown for our fiducial model at the resolution of 320×256×64), concentrate resolution both toward the equatorial plane to resolve the disc turbulence and toward the polar regions to resolve the twin polar jets. Colours show the initial density distribution on a logarithmic scale (red shows high, blue low values, please see the colour bar). White lines show initial poloidal magnetic field lines.

nearly fully consumed by the black hole. To avoid this, we opt for a larger loop that survives for a longer time. We choose magnetic vector potential $A_\varphi \propto r^4\rho^2$. Figure 3.B.1 shows that the radial pre-factor shifts the loop to larger radii and increases its size: the centre of the loop shifts from $r = 13r_g$ to $\sim 22r_g$. This leads to a stronger initial magnetic field at larger radii and makes it easier to resolve the magnetorotational instability (MRI, Balbus & Hawley 1991b) throughout the torus. We normalize the magnetic field strength such that the ratio of maximum gas to maximum magnetic pressure equals 100.

3.B.2 Coordinate System

We use a variant of 3D modified Kerr-Schild (MKS) coordinates (Gammie et al. 2003). `HARM` discretizes the equations of motion on a uniform grid in the internal code coordinates, $t, x^{(1)}, x^{(2)}, x^{(3)}$. Figure 3.B.1 displays this grid in Boyer-Lindquist coordinates with the initial conditions overplotted on top of it.

Radial grid. The original MKS coordinates used an exponential mapping of the internal radial coordinate $x^{(1)}$ into radius r: $r = \exp[x^{(1)}]$. In this work, we instead use a "hyper-exponential" mapping (Tchekhovskoy et al. 2011), as described in previous work (Tchekhovskoy et al. 2009, 2011; Ressler et al. 2015). Outside a break radius, $r_{\rm br} \equiv \exp(x_{\rm br})$, the radial grid becomes highly unresolved and spans very a large distance in just a few cells: $r = \exp[x^{(1)} + 4(x^{(1)} - x_{\rm br})^4]$. Inside $r_{\rm br}$, this radial mapping is equivalent to the MKS coordinates. The advantage of this grid is that it prevents unphysical reflections off the outer radial grid boundary by moving the boundary out of causal contact with the disc, outflows, and the jets. Here we take $r_{\rm br} = 400M$, which guarantees that the regions of interest $r \lesssim r_{\rm br}$ are well-resolved.

Angular grid. The original MKS coordinates used non-collimating grid lines that followed lines of $\theta = \text{const}$. Since we are interested in the physics of the jet sheath, which collimates into small opening angles, we adopt a grid that focuses substantial resolution into the polar regions of interest. The grid consists of disc and jet angular patches that are smoothly stitched together using a transition function,

$$\Theta_s(x, x_a, x_b, y_a, y_b) = y_a + (y_b - y_a)\,\tilde{\Theta}_s[2(x - x_a)/(x_b - x_a) - 1], \tag{3.5}$$

where $\tilde{\Theta}_s(x)$ is a dimensionless smooth step-function:

$$\tilde{\Theta}_s(x) = \begin{cases} 0, & \text{for } x < -1, \\ [70\sin(\pi x/2) + 5\sin(3\pi x/2) - \sin(5\pi x/2) + 64]/128, & \\ & \text{for } -1 \le x < 1, \\ 1, & \text{for } x \ge 1. \end{cases} \tag{3.6}$$

We also introduce its integral, $\tilde{\Psi}_s(x) \equiv \int_{-1}^{x} \tilde{\Theta}_s(x')\mathrm{d}x'$,

$$\tilde{\Psi}_s(x) = \begin{cases} 0, & x < -1 \\ [-35\cos(\pi x/2) - 5\cos(3\pi x/2)/6 + \cos(5\pi x/2)/10]/32\pi & \\ \qquad +(x+1)/2, & -1 \le x < 1, \\ x, & x \ge 1. \end{cases} \tag{3.7}$$

We use eqs (3.6) and (3.7) to define smooth versions of the min and max functions,

$$\min_s(f_1, f_2, \mathrm{d}f) = f_2 - \tilde{\Psi}_s\left(\frac{f_2 - f_1}{\mathrm{d}f}\right)\mathrm{d}f \tag{3.8}$$

$$\max_s(f_1, f_2, \mathrm{d}f) = -\min_s(-f_1, -f_2, \mathrm{d}f). \tag{3.9}$$

These functions are useful for introducing smooth radial breaks.

We now use the machinery developed above to construct the mapping from the internal coordinates, $x^{(1)}, x^{(2)} \in [-1, 1], x^{(3)} \in [0, 2\pi]$, to the physical coordinates, $r \in [r_{\rm in}, r_{\rm out}], \theta \in [0, \pi], \varphi \in [0, 2\pi]$. Quantitatively, we describe the grid as follows, and we give a qualitative explanation below:

$$r_{1,\#} = \min_s\left[r, r_{\rm decoll,\#}, 0.5 r_{\rm decoll,\#}\right]/r_{\rm uniform}, \tag{3.10}$$

$$r_{2,\#} = \min_s\left[r/(r_{1,\#}r_{\rm uniform}), g_\#, 0.5 g_\#\right], \tag{3.11}$$

$$\theta_\# = \pi/2 + \tan^{-1}\left[r_{1,\#}^{\alpha_{1,\#}} r_{2,\#}^{\alpha_{2,\#}} \tan(x^{(2)}\pi/2)\right], \tag{3.12}$$

where “#” stands for either “disk” or “jet” and $g_\# = r_{\rm coll,\#}/r_{\rm decoll,\#}$. We now define a “jet weight”, $w_{\rm jet} = \Theta_s\left(|x^{(2)}|, f_{\rm disk}, f_{\rm jet}, 0, 1\right)$, that controls the contribution of the jet grid patch for a given value of $x^{(2)}$. The values of $f_{\rm disk}$ and $f_{\rm jet}$ control the fractions of the grid devoted to resolving the disk and jet regions. We obtain the net polar angle as a function of $x^{(i)}$ via

$$\theta = w_{\rm jet}\theta_{\rm jet} + (1 - w_{\rm jet})\theta_{\rm disk}. \tag{3.13}$$

We direct about 25% of the resolution into the disk regions, $f_{\rm disk} = 0.25$, and about 40% of resolution into the jet regions, $f_{\rm jet} = 0.4$; the rest 35% resolves the disk outflow sandwiched between the disk and the jet. At $r = r_{\rm uniform}$, the angular grid is uniform. We take this radius to be equal to the inner radius of the grid, $R_{\rm in}$: uniform angular grid at the inner boundary maximizes the simulation time step and reduces time to solution.

The value of α controls the collimation of the grid: in the polar regions, $\sin\theta \propto r^{-\alpha}$, and in the equatorial regions, $\cos\theta \propto r^{\alpha}$. Therefore, $\alpha > 0$ leads to collimation (toward the poles) of the radial grid lines. Very close to the black hole, we choose a negative α value for both disk and jet regions, $\alpha_{1,\rm disk} = \alpha_{1,\rm jet} = -1$, which leads to a mildly decollimating grid that follows $r\cos\theta = z =$ constant in the equatorial region and focuses the resolution on the turbulent accretion disk. (Another possible approach to focus the resolution on the equatorial plane could be to reduce the value of $r_{\rm uniform}$, but this would make the grid non-uniform at $R_{\rm in}$, reduce the time step, and increase the simulation cost.) At larger radii, at $r \gtrsim r_{\rm decoll,disk} = r_{\rm decoll,jet} = 2R_{\rm in}$, we choose $\alpha = \alpha_{2,\rm disk} = \alpha_{2,\rm jet} = 3/8$. This leads to a collimating grid near the poles, as seen in Fig. 3.B.1. At $r \gtrsim r_{\rm coll,disk} = 5R_{\rm in}$ the grid becomes radial in the disk region, as seen in Fig. 3.B.1. The grid becomes radial in the polar regions at much larger radii, $r \gtrsim r_{\rm coll,jet} = 10^3 r_g$, well outside of Fig. 3.B.1.

Cylindrification. In standard 3D MKS coordinates, hyper-exponential MKS coordinates, and in general for all spherical-type 3D coordinate systems, the small physical extent of the cells closest to the poles introduces a severe constraint on the time-step via the Courant-Friedrichs-Lewy condition (roughly $\Delta t \lesssim \min[\Delta x]/c$, where the minimum is taken over the entire grid and in each spatial direction). To avoid this, we use the technique of "cylindrification" (Tchekhovskoy et al. 2011), which takes the polar cell closest to the poles and expands it laterally below a certain radius. This effectively makes the polar regions more closely resemble cylindrical coordinates than spherical. This causes the row of cells closest to the pole to be wider than the rest at $r \lesssim 10r_g$, as seen in Figure 3.B.1. Because this grid deformation is concentrated at small r and θ values, where the jets carry very little energy flux (enclosed jet energy flux scales as $\sin^4\theta$) and the radial velocity is directed into the black hole, this does not noticeably affect the simulations. However, it substantially – by an order of magnitude – speeds up the simulations.

3.B.3 Density Floors

Black hole magnetospheres naturally develop highly magnetized polar regions: gas drains off the magnetic field lines into the black hole due to gravity or is flung out to infinity due to magnetic forces. Eventually, vacuum regions would develop, which would pose numerical difficulties with grid-based MHD codes. Because of this, all such codes employ numerical floors that prevent density and internal energy from becoming too low. When the fluid density or total internal energy dip below the floor limits, $\rho_{\rm floor} = \max[b^2/50, 10^{-6}(r/r_g)^{-2}]$ or $u_{\rm floor} = \max[b^2/2500, 10^{-8}(r/r_g)^{-2\gamma}]$, we add mass or energy in the drift frame, respectively. This contrasts with the more standard approaches of adding gas in the fluid frame (Gammie et al. 2003) or in the zero angular momentum observer (ZAMO) frame (McKinney et al. 2012). By preserving the component of the fluid momentum along the magnetic field, our drift frame floor approach (i) prevents the parallel (to the magnetic field) velocity from running away, which happens in the fluid frame floor approach (this problem becomes especially severe in 3D), (ii) avoids artificial drag on the magnetic field lines, which happens in the ZAMO frame floor approach.

Although both the ZAMO and drift frame floors result in stable numerical evolution, there are several practical advantages of the drift floor. The ZAMO floor approach is not analytic and requires an additional inversion of conserved to primitive quantities per cell per Runge-Kutta substep. We found that this adversely affects the speed and parallel scaling of the code: most of the floor activations occur near the black hole and thus disproportionately affect only a few MPI processes; this slows down the entire code, especially at late times in the evolution when the region affected by the floors grows in size. Second, the drift frame floors add just the right amount of mass, energy and momentum to get $\rho = \rho_{\rm floor}$ and $u_g = u_{\rm floor}$. This is not guaranteed by the ZAMO floors because of their iterative nature.

We define the normal observer frame by $\eta_\mu = (-\alpha, 0, 0, 0)$ where $\alpha = (-g^{tt})^{-1/2}$ is the lapse. The conserved fluid momentum in the normal observer frame is $Q_\mu \equiv -(T_g)^\nu_\mu \eta_\nu/\alpha = w_g u^t u_\mu + \delta^t_\mu P_g$, where $w_g = \rho + u_g + P_g$ is the gas enthalpy (see also Noble et al. 2006). We define the normal observer frame magnetic field 4-vector, $B^\mu = -{}^*F^{\mu\nu}\eta_\nu/\alpha$ and its covariant component $B_\mu = g_{\mu\nu}B^\nu$ and magnitude $B = (B^\mu B_\mu)^{1/2}$. Note that by definition, $B^t = 0$. We demand that the projection of the momentum along the magnetic field remains constant as we apply the floors:

$$\text{constant} = B^\mu Q_\mu \equiv B^i Q_i = (B^\mu v_\mu) w_g (u^t)^2 = B v_\| w_g (u^t)^2, \tag{3.14}$$

where i runs through the spatial components only ($i = 1, 2, 3$), $v^\mu \equiv u^\mu/u^t$ is the 3-velocity four-vector, and $v_\| = B^\mu v_\mu/B$ is the parallel velocity component. From eq. (3.14) we see that because the floors increase the enthalpy, w_g, in order to preserve the parallel momentum, we need to decrease the parallel velocity, $v_\|$. For convenience, we decompose v^μ into the sum of the drift and parallel velocity components,

$$v^\mu = v^\mu_{\rm dr} + v_\| B^\mu/B, \tag{3.15}$$

where the drift velocity is perpendicular to the magnetic field,

$$B_\mu v^\mu_{\rm dr} = 0. \tag{3.16}$$

Equations (3.15) and (3.16) define the drift velocity and the parallel velocity. By requiring that the gas velocity is physical, $u^\mu u_\mu = -1$, and making use of eq. (3.16), we can express u^t in terms of the parallel velocity:

$$(u^t)^2 = \frac{1}{(u^t_{\rm dr})^{-2} - v_\|^2}. \tag{3.17}$$

Plugging this into eq. (3.14) and solving a quadratic equation for $v_\|$ gives:

$$v_\| = \frac{x}{1 + (1 - x^2)^{1/2}} \times \frac{1}{u^t_{\rm dr}}, \tag{3.18}$$

where $x = 2B^\mu Q_\mu/(B w_g u^t_{\rm dr})$. After applying the floors on ρ and u_g, we update w_g and recompute x. Then, using eq. (3.18), we recompute the value of $v_\|$ and, using eq. (3.15), the fluid velocity. As discussed above, this reduces $v_\|$, and leads to enhanced stability of the method.

Floor test. In order to verify the performance of the floor, we have simulated a monopole magnetosphere of a spinning black hole. We chose the same spin $a = 0.5$ as in our fiducial simulation and adopted a resolution of $768 \times 512 \times 1$. We used a uniform angular grid and a logarithmic radial grid with $R_{\rm in} = 0.7 r_{\rm H}$ and $R_{\rm out} = 10^3 r_g$. We set density and internal energy floors as $\rho_{\rm floor} = b^2/50$ and $u_{\rm floor} = b^2/2500$. Based on simulations of force-free (infinitely magnetized, $\rho, u_g \to 0$ limit) magnetospheres we expect our solution to approach $\Omega_{\rm F} = 0.5\Omega_{\rm H}$ if the floors were absent (Tchekhovskoy et al. 2010). For finite floors, however, we expect the gas inertia effects to have an effect of order $\rho_{\rm floor}/b^2 = 0.02$.

To verify this, we ran our simulation until $t = 1.7 \times 10^3 r_g/c$, which is sufficiently long for the near black hole solution to reach a steady state and yet be unaffected by potential reflection from the outer radial grid boundary. Figure 3.B.2 shows the ratio of the angular rotational frequency

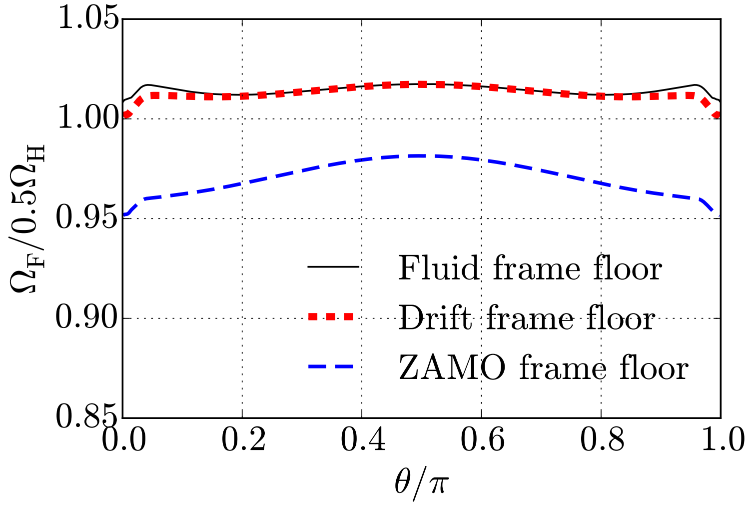

Figure 3.B.2: Angular rotational frequency $\Omega_{\rm F}$ of magnetic field lines in units of the force-free expectation, $\Omega = 0.5\Omega_{\rm H} = ac/4r_{\rm H}$, versus the polar angle for the monopolar magnetosphere test. The measurements are performed at the black hole event horizon. We expect that gas inertia makes a difference on the order of $\rho c^2/b^2 = 2\%$. The simulations with the fluid frame floor (thin solid black line) and drift frame floor (thick red short-dashed line) are within 2% of the analytic expectation, in line with what we expect for the small but finite gas inertia effects. For the simulation with the ZAMO frame floor (blue long-dashed line), the deviation from the analytic expectation is a bit higher, about 5%, with the difference especially pronounced near the poles. A larger deviation might be expected because, unlike fluid and drift frame floors, the ZAMO floors add transverse (to the magnetic field lines) momentum and therefore apply a drag to magnetic field lines.

of the magnetic field to that expected in an infinitely magnetized magnetosphere (Tchekhovskoy et al. 2010), evaluated at the event horizon. The results of the drift frame floor simulation, shown with the short dashed red line, and the fluid frame floor simulation, shown with the thin black solid line, are in line with the expectation, within 2% of the force-free result. The angular frequency in the ZAMO frame floor simulation shows a larger deviation, ≃ 5%, relative to the force-free value. A larger deviation might be expected because, unlike fluid and drift frame floors, the ZAMO floors add transverse (to the magnetic field lines) momentum and therefore apply a drag to magnetic field lines. This effect might contribute to the lower values of $\Omega_{\rm F} < 0.5\Omega_{\rm H}$ in the polar regions reported by McKinney et al. (2012).

3.C Motivation For the Choice of Magnetization Cut-off

In all of the radiative calculations shown in this work, we have limited the emitting domain of the simulation to include only the regions of the flow with $\sigma = b^2/(\rho c^2) < 1$. The motivation for this restriction is to exclude regions which are known to have larger errors in the thermodynamics in conservative codes. This is because as σ approaches ~ 1 and above, the total energy of the fluid (which is conserved to machine precision) becomes dominated by magnetic energy, so that small errors in the magnetic field evolution lead to large errors in the internal energy of the gas. Thus, we limit the radiative domain to regions with $\sigma < \sigma_{\rm max}$ with $\sigma_{\rm max} = 1$, which is a somewhat arbitrary but conservative value chosen to minimize the effect of errors at high σ on our results. Figure 3.C.1 demonstrates how the particular choice of $\sigma_{\rm max}$ affects our results. Over a factor of 10 in $\sigma_{\rm max}$, there is only a factor of few change in the higher frequency flux, which is encouraging for the qualitative results in this paper. Ultimately more accurate methods will be required to model the polar region thermodynamics (where $\sigma \gtrsim 1$) more accurately.

3.D Steep Entropy Wave Test

In the main text we argued that numerical diffusion of entropy at steep entropy gradients is the cause of the unphysically negative heating rate near the funnel wall shown in Figure 3.7. Here we present a simple 1D test that shows that contact discontinuities and unresolved gradients do indeed produce negative heating, as computed with our prescription for Q using the local Lax-Friedrichs Riemann (LLF) solver in `HARM`. We stress that this is simply another manifestation of the unavoidable diffusion of contact discontinuities in finite-volume codes. This diffusion may be amplified by the LLF Riemann solver, which is known to be significantly more diffusive than other Riemann solvers (see, e.g., Chapters 5 and 6 in Toro 2009).

We initialize the unmagnetized fluid with a constant velocity, v, and pressure, p, as well as either a discontinuous, square density profile, $\rho_{dis}(x)$, or a continuous profile, $\rho_{cont}(x)$, defined as:

$$\rho_{dis}(x) = \begin{cases} \rho_{\rm min} & x \leq 0.4L \\ \rho_{\rm max} & 0.4L < x < 0.6L \\ \rho_{\rm min} & 0.6L \leq x \end{cases}$$

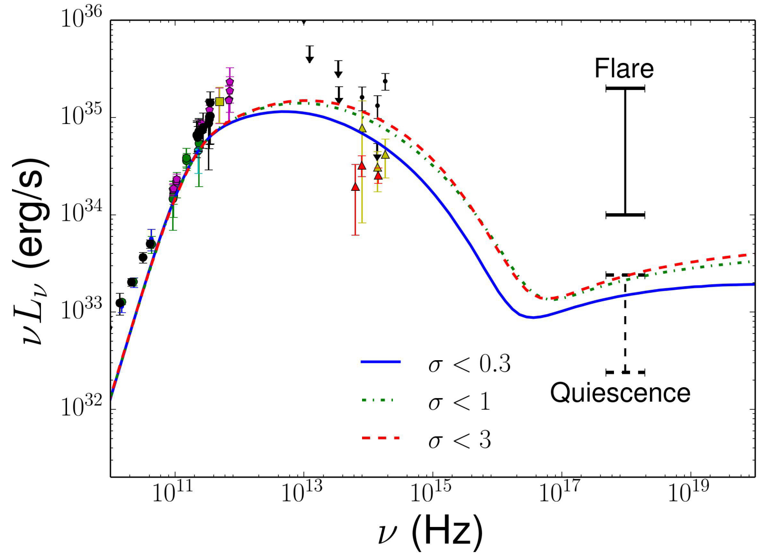

Figure 3.C.1: Time-averaged SED for different limits on the magnetization parameter, $\sigma \equiv b^2/(\rho c^2)$, where regions with $\sigma < \sigma_{\rm max}$ have been excluded from the spectral calculation. The choice of $\sigma_{\rm max}$ has no effect on the radio and millimetre emission but directly affects the NIR and X-ray emission. More restrictive cuts have reduced high frequency emission, while less restrictive cuts have increased high frequency emission. The change in the predicted luminosity is only a factor of few for this range of $\sigma_{\rm max}$, which demonstrates that our results do not strongly depend on the choice of $\sigma_{\rm max}$. All of the results presented in the main text use $\sigma_{\rm max} = 1$, which excludes the regions with the most uncertain thermodynamics.

and

$$\rho_{cont}(x) = \left(\frac{\exp\left[(x-0.4L)/w\right]}{\exp\left[(x-0.4L)/w\right]+1} - \frac{\exp\left[(x-0.6L)/w\right]}{\exp\left[(x-0.6L)/w\right]+1}\right) \times(\rho_{\max}-\rho_{\min})+\rho_{\min},$$

where $\rho_{\max} = 10^3\rho_{\min}$, $w = 0.01L$, and L is the size of the 1D computational domain. ρ_{cont} is simply a smooth approximation to a square wave that transitions from $\rho_{\min}$ to $\rho_{\max}$ and vice-versa over a region of length $\sim w$. The velocity is chosen to be $10^{-3}c$, which is ≈ 0.2 of the minimum sound speed. The pressure is chosen to be $0.012\rho_{\min}c^2$, making the sound speed $\ll c$. The electron entropy is initialized such that the electron internal energy is equal to the gas internal energy and the electron heating fraction, f_e, is set to either 0 or 1 to isolate the effect of the heating rate on the electron evolution. Furthermore, the adiabatic index of the gas is 5/3 while the adiabatic index of the electrons is 4/3. No floors are used on the electron variables to allow the electron entropy variable to become negative. The simulation is performed in a periodic box and run for a single advection time, L/v. The analytic solution is that the final state should be identical to the initial state and the heating rate should be 0. We define a resolution parameter, RP, as the approximate number of cells per order unity change in $\kappa_g = p/\rho^\gamma$: $RP \equiv \kappa/\Delta\kappa_g$, where $\Delta\kappa_g$ is the change in κ_g across one cell. $RP \gg 1$ indicates a well resolved gradient, while $RP \lesssim 1$ represents a poorly resolved gradient.

This set-up is chosen to mirror the typical angular entropy profiles seen in our global accretion disc simulations. These generally have a near discontinuity in entropy (and density) close to the disc-jet boundary (Figure 3.1). The sharp gradient is nearly, though not perfectly, perpendicular to the grid, and the flow does have a small velocity component misaligned with the gradient. The fact that these velocities are small (compared to the local fast magnetosonic speed used in determining the CFL condition) means that diffusion errors can be significant. We performed a more complicated test of a contact discontinuity slightly misaligned with the grid in 2D with a thermal pressure gradient balancing a magnetic pressure gradient but found similar results to the simpler 1D hydrodynamic test; thus we focus on the latter here.

Figure 3.D.1 shows the initial entropy for this test compared with a typical angular profile of the entropy in our accretion disc simulations, along with the resulting time averaged heating rates and total gas/electron entropy after one advection time. Note that the 1D coordinate x corresponds to θ/π in the global disc simulation. Large gradients in entropy clearly lead to negative heating rates (caused by excessive numerical diffusion), which appear on the low entropy side of the gradient. In the disc simulation this is the side closest to the disc where synchroton emissivities might be significant. Figure 3.D.1 (bottom panel) shows that the negative heating rates cause the electron entropy to become largely negative in regions surrounding the entropy gradient, while the total gas entropy diffuses but is reasonably well behaved. This shows that the diffusion errors more strongly affect the electrons than the total gas. This is because small diffusive errors in the total gas entropy can lead to large errors in the calculation of Q which then acts as a source term in the electron entropy evolution. It is also clear that the smooth profile has less artificial heating at this resolution; this discrepancy only increases with resolution.

Figure 3.D.2 shows the integrated error in the electron entropy at the end of the simulation

normalized to the total entropy in the box as a function of resolution for the two different profiles. The artificial heating converges to 0 at second order for the smooth profile but the artificial heating does not converge to 0 for the discontinuous profile. The reason for this is the nature of numerical diffusion. The square wave will always be diffused over a small number of cells that is roughly independent of resolution, so the derivatives needed in the heating calculation will never be able to better resolve the gradient. This is exactly analogous to the non-converging errors in the heating rate seen in the strong shock test of Ressler et al. (2015). We note that though the magnitude of the errors in Figure 3.D.2 are relatively small at the highest resolution (with a maximum of $\sim 10\%$ for the discontinuous wave with $f_e = 1$), this depends on the chosen magnitude of the advection velocity relative to the sound speed and the duration of the 1D simulation. The errors are larger if advection velocities perpendicular to the gradient are $\ll$ the fast magnetosonic speed.

For the smooth entropy wave test used here, the minimum resolution parameter is $RP \approx 0.42(N/128)$, which represents the number of grid cells per order unity change in κ_g at the steepest part of the gradient. From Figure 3.D.2, we see that this means that when $RP \approx 1$, the artificial heating rate will start converging and quickly become insignificant for a smooth flow. Two questions then arise pertaining to the accretion disc simulation: 1) How well is the gradient resolved at the fiducial resolution? and 2) Is the gradient a true discontinuity or a smooth profile that is under-resolved? If it is in fact a true discontinuity then we have no hope of better resolving it and the negative heating will be present at all resolutions with the LLF Riemann solver. On the other hand, if the gradient is, in fact, smooth, then higher resolution simulations will reduce the negative heating.

To attempt to answer these questions, we can directly compute the minimum resolution parameter for the entropy profile in the accretion disc simulation. At a resolution of $320 \times 256 \times 64$ we find that the minimum resolution parameter is a mere $\sim$0.15, though at the same radius in the $640 \times 512 \times 128$ simulation the minimum resolution parameter approximately doubles to ~ 0.32. This suggests that the gradient is smooth and that we are better resolving it with finer grids. On the other hand, we are still under-resolving the gradient even at the very expensive resolution of $640 \times 512 \times 128$, meaning that it would take an unreasonably high resolution by today's computational standards to suppress the negative heating. Better Riemann solvers are known to reduce the artificial numerical diffusion that we have shown leads to these negative heating rates. Future work will explore their impact in detail.

Finally, it is important to stress that spectrum generated by our global accretion disc simulation is reasonably well converged (Figure 3.6), so it is unclear whether the excess numerical diffusion and associated negative heating strongly affect the observable quantities of interest in this paper.

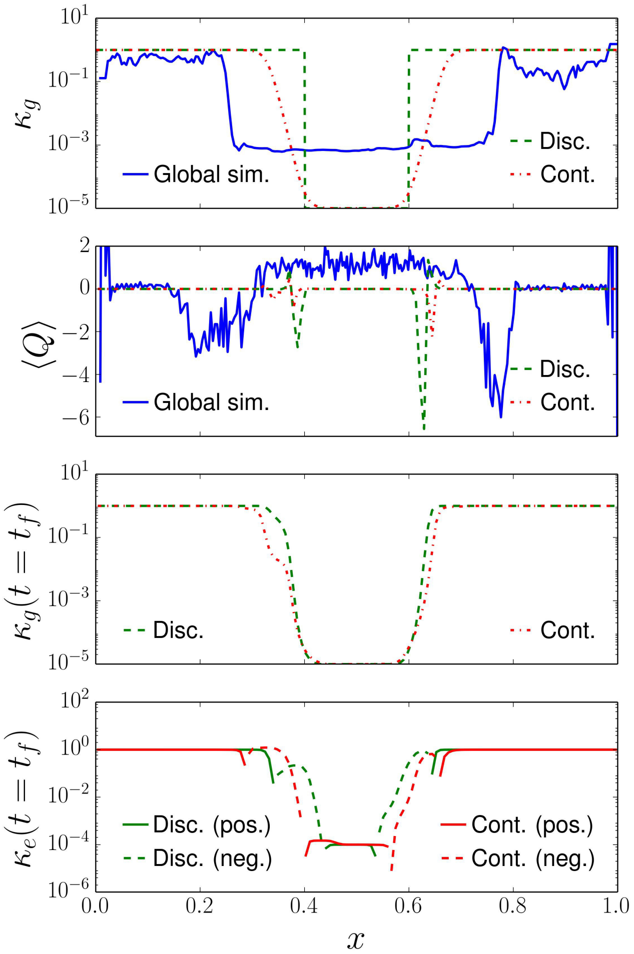

Figure 3.D.1: *Top Panel*: Gas entropy in our global accretion disc simulation as a function of polar angle at $r \approx 15r_g$ at a snapshot in time and slice in φ compared to the gas entropy initial conditions for both the discontinuous and continuous steep entropy wave test. The entropies have been scaled for ease of comparison. *Second panel*: Time averaged Lagrangian heating rates per unit volume for both the discontinuous and continuous steep entropy wave test at a resolution of $N = 128$ as well as the time and φ averaged heating rate per unit volume in our global accretion disc simulation at $r \approx 15r_g$ (for the global simulation, $x = \theta/\pi$). The test problem heating rates are plotted in units of $5 \times 10^{-6}\rho_{\max}c^3/L$, while the global disc simulation heating rate has been arbitrarily scaled for ease of qualitative comparison. From these plots, it is clear that diffusion of large gradients in entropy leads to negative "heating" rates on the side of the gradient with lower entropy (corresponding to the disc side of the boundary in the accretion disc simulation). Note that since the accretion disc simulation has been averaged over time and φ in an Eulerian and not Lagrangian sense, motion of the disc-jet boundary increases the angular extent of the negative heating. *Third and Fourth Panels*: Total gas and electron entropy at the end of the 1D entropy wave test. All entropies have been scaled such that $\kappa_i(x = 0) = 1$. For the electrons, the magnitude of the entropy is plotted, with solid lines representing regions with positive entropy and dashed lines representing regions with negative entropy. The electron entropy becomes significantly negative in the cells surrounding the sharp gradient while the total gas entropy is comparatively well behaved. This shows that the effects of numerical diffusion are amplified for the electrons via the dependence on the heating rate, Q.

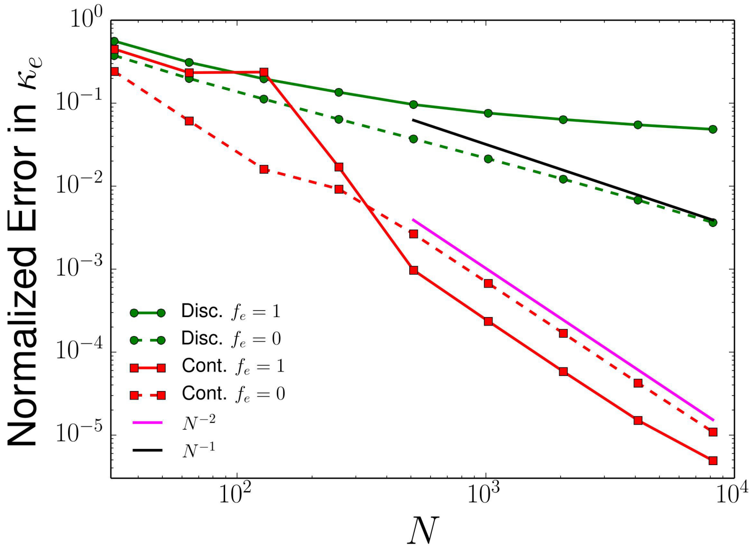

Figure 3.D.2: Error in the electron entropy after a single advection time for the steep entropy wave test, defined as $\sum |\kappa_e(t = L/v) - \kappa_e(t = 0)| / \sum \kappa_e(t = 0)$. We plot both the error in electron entropies evolved with a heating fraction of $f_e = 1$ (i.e. the electrons receive all of the heat) and those evolved with a heating fraction of $f_e = 0$ (i.e. the electrons are simply adiabatically advected with the flow). As expected, when $f_e = 0$, the electron entropy converges at roughly the expected order (1st and 2nd, respectively) for the the discontinuous and continuous profiles. On the other hand, when $f_e = 1$ only the continuous profile converges to the correct result. This is because discontinuities in the flow lead to non-converging errors in the calculation of the heating rate. Better Riemann solvers will reduce the magnitude of this error but will not improve convergence.

Chapter 4

Hydrodynamic Simulations of the Inner Accretion Flow of Sagittarius A* Fueled By Stellar Winds

An earlier version of this article was previously published as Ressler S. M., Quataert E., and Stone J. M., 2018, MNRAS, 478, 3544

4.1 Abstract

We present `Athena++` grid-based, hydrodynamic simulations of accretion onto Sagittarius A* via the stellar winds of the ~ 30 Wolf-Rayet stars within the central parsec of the galactic center. These simulations span ~ 4 orders of magnitude in radius, reaching all the way down to 300 gravitational radii of the black hole, ~ 32 times further in than in previous work. We reproduce reasonably well the diffuse thermal X-ray emission observed by *Chandra* in the central parsec. The resulting accretion flow at small radii is a superposition of two components: 1) a moderately unbound, sub-Keplerian, thick, pressure-supported disc that is at most (but not all) times aligned with the clockwise stellar disc, and 2) a bound, low-angular momentum inflow that proceeds primarily along the southern pole of the disc. We interpret this structure as a natural consequence of a few of the innermost stellar winds dominating accretion, which produces a flow with a broad distribution of angular momentum. Including the star S2 in the simulation has a negligible effect on the flow structure. Extrapolating our results from simulations with different inner radii, we find an accretion rate of ~ a few $\times 10^{-8} M_{\odot}$/yr at the horizon scale, consistent with constraints based on modeling the observed emission of Sgr A*. The flow structure found here can be used as more realistic initial conditions for horizon scale simulations of Sgr A*.

4.2 Introduction

Both the Event Horizon Telescope (EHT, Doeleman et al. 2008) and GRAVITY (Gillessen et al. 2010) will soon reach resolution comparable to the event horizon scale of the supermassive black hole at the center of our own galaxy, Sagittarius A* (Sgr A*), at 230 GHz and in the infrared, respectively.[1] The primary source of emission in Sgr A* is believed to be a combination of thermal and nonthermal particles in either an accretion disc or the strongly magnetized outflow fed by a disc. The properties of the plasma immediately surrounding the black hole are then coupled with the properties of the black hole itself in determining what we will actually observe. In order to properly interpret current and forthcoming observations and to be able to infer physical parameters from the data, it is of paramount importance to have theoretical and computational models of the inner accretion flow.

Because the luminosity of Sgr A* is well below the Eddington limit, it is classified as a Radiatively Inefficient Accretion Flow (RIAF). RIAFs are well suited for numerical simulation because they are geometrically thick, meaning that they can more easily be resolved than their thin-disc counterparts. To date, a number of groups have simulated RIAFs around rotating black holes in the Kerr metric using general relativistic magneto-hydrodynamic simulations (GRMHD,Komissarov 1999; De Villiers & Hawley 2003; Gammie et al. 2003; White et al. 2016). However, due to the large temperatures and low densities inherent in RIAFs, a variety of collisionless effects not captured in the standard ideal MHD framework may be dynamically important. Recent work has made great strides in this respect by incorporating increasingly sophisticated physics into simulations. This includes considering the plasma as a two-temperature fluid (Ressler et al. 2015; Sądowski et al. 2017; Ressler et al. 2017; Chael et al. 2018), fully coupling radiation to the MHD equations (Sądowski et al. 2013; Ryan et al. 2015; Sądowski et al. 2017; Ryan et al. 2017; Chael et al. 2018), injecting nonthermal particles into the fluid (Ball et al. 2016; Chael et al. 2017), as well as adding the effects of anisotropic electron conduction (Ressler et al. 2015, 2017), anisotropic ion conduction, and anisotropic viscosity (Foucart et al. 2016, 2017).

These simulations, however, predominantly use a fairly standard set of initial conditions. An equilibrium, constant angular momentum torus (e.g., Fishbone & Moncrief 1976, though see also Penna et al. 2013, Witzany & Jefremov 2017), surrounded by empty space is seeded with a magnetic field, a configuration which is unstable to the magneto-rotational instability (MRI). As the instability grows, enough angular momentum is transported outward so that the torus is able to accrete and eventually reach an approximate steady state in which the magnetic energy is comparable to the thermal energy of the disc. The flow structure can, however, depend strongly on the initial conditions. For instance, if there is a net vertical magnetic flux in the equilibrium torus, an entirely different evolution is seen in which the flux threading the black hole eventually becomes large enough to halt accretion, leading to a violently time-variable, magnetically arrested disc (MAD, Narayan et al. 2003; Tchekhovskoy et al. 2011). In contrast to the growing body of

---

[1] This chapter was published in August 2018, before GRAVITY and EHT released their first results in October 2018 (Gravity Collaboration et al.) and April 2019 (Event Horizon Telescope Collaboration et al.), respectively. Note, however, that the first target of EHT was the black hole at the center of M87 and (as of the writing of this thesis) the EHT results for Sgr A* are still forthcoming.

work on plasma microphysics, there has been much less work done studying the effect of varying the initial conditions on GRMHD simulation results; much of what has been done has focused in the possibility that the angular momentum vector of the disc is misaligned with the spin of the black hole (Fragile & Anninos 2005; Liska et al. 2017).

In general, not much is known about the feeding of black holes in galactic nuclei. For the case of the galactic center in particular, however, we have a unique opportunity to actually determine a proper set of initial conditions, as the source of accretion is believed to be known. This source is the stellar winds of the ≈ 30 Wolf-Rayet (WR) stars orbiting within ~ 1 pc of the black hole. Though there are over a million other stars in the central nuclear star cluster (Feldmeier-Krause et al. 2017), including the well known "S-stars" whose orbits have been used to significantly improve estimates of the mass of Sgr A* (Ghez et al. 2008; Gillessen et al. 2009), these stars are generally fainter and less massive, with mass loss rates orders of magnitude smaller than the WR stars (see e.g. Vink et al. 2001; Habibi et al. 2017). Since the mass loss rates and wind velocities (Martins et al. 2007; Yusef-Zadeh et al. 2015a), as well as the positions and orbital velocities (Paumard et al. 2006; Lu et al. 2009) of the WR stars have been well constrained by both infrared and radio observations, this problem is well posed. Moreover, both simple 1D calculations (Quataert 2004; Shcherbakov & Baganoff 2010) and 3D smoothed particle hydrodynamic (SPH) simulations (Rockefeller et al. 2004; Cuadra et al. 2008) have shown that the observed stars provide more than enough mass to explain the observed accretion rate onto Sgr A* and the diffuse X-ray emission in the galactic center observed by *Chandra* (Baganoff et al. 2003).

In this work we seek to better inform initial conditions of GRMHD simulations of Sgr A* by directly simulating the accretion flow produced by the winds of the WR stars in the galactic center. Though this calculation is similar to the work of Cuadra et al. (2008) (see also, Rockefeller et al. 2004; Cuadra et al. 2015; Russell et al. 2017), we use completely different numerical methods, probe even smaller radii, and focus especially on the properties of the innermost accretion flow, which has not been a primary focus of previous work.

To do this, we employ three dimensional hydrodynamic simulations with $\sim$30 independent orbiting stars as sources of mass, momentum, and energy. While it is almost certainly true that on scales comparable to the event horizon of Sgr A* magnetic fields play an important role in the transport of angular momentum, and thus, in determining the structure of the accreting plasma, here we focus on a purely hydrodynamic calculation. This is primarily because, even if magnetic fields are important for the gas near the horizon, the properties of the flow at larger radii may be set by strictly hydrodynamic considerations. Furthermore, in order to properly evaluate the effects of magnetic fields in the future, we must first understand the detailed properties of the hydrodynamic simulation, meaning that this work will serve as a basis for comparison to subsequent calculations. In addition, both the direction and the magnitude of the magnetic fields in the WR stellar winds are unconstrained observationally, so that a full treatment will require a larger exploration of parameter space than is needed in the purely hydrodynamic case.

The chapter is organized as follows. §4.3 describes the physical model and numerical methods, §4.4 describes two tests of our implementation of the subgrid stellar wind model, §4.5 details the properties of the full 3D simulation of stellar wind accretion onto Sgr A*, §4.6 compares the X-ray luminosity of our simulation to *Chandra* observations, §4.7 discusses the implication of these results for GRMHD simulations, §4.8 compares our results to previous work, and §4.9 concludes.

4.3 Model and Computational Methods

4.3.1 Equations Solved

We perform our simulations with `Athena++`, a 3 dimensional grid-based scheme that solves the equations of conservative hydrodynamics. `Athena++` is a complete rewrite of the widely used `Athena` code (Stone et al. 2008) optimized for the c++ coding language. We use a point source gravitational potential for the central black hole. The code is 2nd order in space and time and adopts piece-wise linear reconstruction with the Harten-Lax-van Leer-Contact (HLLC) Riemann solver.

In addition to the basic equations of hydrodynamics, we include the effect of the stellar winds emitted by stars orbiting the black hole by adding source terms in mass, energy, and momentum. Each star is assumed to orbit in a Keplerian orbit as described in §4.5.1. The wind of each star is given an effective radius of $r_{wind} \approx 2$ cells centered on the position of the star's orbit (more precisely, twice the length of the diagonal of a cell determined by the local level of mesh refinement). Inside this radius the wind is assumed to supply a constant source of mass that is determined by the observed mass loss rate, $\dot{M}_{wind}$: $\dot{\rho}_{wind} = \dot{M}_{wind}/V_{wind}$, where $V_{wind} = 4\pi/3\ r^3_{wind}$. Furthermore, the wind is assumed to have a constant radial velocity in the frame of the star, v_{wind}, and a negligible pressure. To calculate the net source terms for the finite volume, conservative equations solved by `Athena++` we break each cell that intersects a stellar wind into a $5 \times 5 \times 5$ subgrid and integrate over the whole cell. For a wind which occupies a fractional volume f of a cell, this amounts to source terms in mass, momentum, and energy of $f\dot{\rho}_{wind}$, $f\dot{\rho}_{wind}\langle \mathbf{v}_{wind,net}\rangle$, and $1/2 f\dot{\rho}_{wind}\langle|\mathbf{v}_{wind,net}|^2\rangle$, respectively, where $\mathbf{v}_{wind,net}$ is the wind velocity in the fixed frame of the grid and $\langle\rangle$ denotes an average over the volume of the star contained in the cell. Though similar in purpose, we note that this model differs from Lemaster et al. (2007) in that the stellar winds are treated as source terms as opposed to "masked regions," within which the fluid quantities are over-written by an analytic solution. The benefit of treating the winds as source terms is that we can accommodate scenarios where multiple stellar winds overlap.

As the stellar winds interact and shock-heat, radiative losses due to optically thin bremsstrahlung and line cooling are expected to become significant. To account for this, we use the optically thin cooling routine described in Townsend (2009), which analytically integrates the energy equation over a single time step using a piece-wise power law approximation to the cooling curve. This avoids any limitation on the accuracy or time step when the cooling time is short compared to the dynamical time of the fluid. The piece-wise power law approximation to the cooling curve is obtained from a tabulated version of the exact collisional ionization equilibrium cooling function (as is appropriate for the hot $\sim 10^7$ K gas in the Galactic Center; see the next section for details).

To summarize, the equations we solve are the equations of conservation of mass, momentum, and energy, with source terms to account for the gravity of the supermassive black hole, optically thin radiative cooling, and the stellar winds of the orbiting stars:

$$\begin{aligned}
\frac{\partial \rho}{\partial t} + \nabla \cdot (\rho \mathbf{v}) &= f \dot{\rho}_{wind} \\
\frac{\partial (\rho \mathbf{v})}{\partial t} + \nabla \cdot (P\mathbf{I} + \rho \mathbf{v}\mathbf{v}) &= -\frac{\rho G M_{BH}}{r^2}\hat{r} \\
&\quad + f \dot{\rho}_{wind} \langle \mathbf{v}_{wind,net} \rangle \\
\frac{\partial (E)}{\partial t} + \nabla \cdot [(E + P)\mathbf{v}] &= -\frac{\rho G M_{BH}}{r}\mathbf{v} \cdot \hat{r} \\
&\quad + \frac{1}{2} f \dot{\rho}_{wind} \langle |\mathbf{v}_{wind,net}|^2 \rangle - Q_{-},
\end{aligned} \tag{4.1}$$

where ρ is the mass density, P is the pressure, $\mathbf{v}$ is the fluid velocity, $E = 1/2\rho v^2 + P/(\gamma - 1)$, $\gamma = 5/3$ is the adiabatic index of the gas, and Q_{-} is the cooling rate per unit volume. The calculation of Q_{-} is described in the next section. Note that in equation (4.1), we have neglected the effect of the central nuclear star cluster on the gravitational potential. For the galactic center, the gravitational contribution from these stars is negligible for $r \lesssim 5'' \approx 0.2$ pc but is non-negligible ($\sim 25\%$) for $r \gtrsim 10'' \approx 0.4$ pc (Genzel et al. 2003b). In the innermost regions of the domain that are the primary focus of this work, neglecting the stellar contribution to gravity is a good approximation.

4.3.2 Calculating The Cooling Function

We define the cooling function, Λ, such that the cooling rate per unit volume is $Q_{-} = n_e \frac{\rho}{m_p} \Lambda$, where $n_e = \rho/\mu_e$, m_p is the mass of a proton, and μ_e is the mean molecular weight per electron. For the conditions in the galactic center, the dominant cooling mechanisms are line emission in collisional ionization equilibrium and thermal bremsstrahlung. The cooling function is thus a function not only of temperature but also of the relative abundances of the elements. To calculate Λ for a given set of hydrogen, helium, and metal mass fractions (X, Y and Z, respectively), we first calculate the cooling curve for the photospheric solar abundances presented in Lodders (2003), that is, $X_{\odot} = 0.7491$, $Y_{\odot} = 0.2377$,and $Z_{\odot} = 0.0133$. We do this using the spectral analysis code `SPEX` (Kaastra et al. 1996) in the manner of Schure et al. (2009), and calculate separately the contributions from H, $\Lambda_{H,\odot}$, He, $\Lambda_{He,\odot}$, and metals, $\Lambda_{Z,\odot}$. Then we can write the cooling curve for arbitrary abundances as a linear combination of these solar quantities as

$$\Lambda = \frac{X}{X_{\odot}} \Lambda_{H,\odot} + \frac{Y}{Y_{\odot}} \Lambda_{He,\odot} + \frac{Z}{Z_{\odot}} \Lambda_{Z,\odot}. \tag{4.2}$$

The mean molecular weight per electron, μ_e, and the mean molecular weight per particle, μ, are directly related to X and Z by (Townsend 2009)

$$\begin{aligned}
\mu_e &= \frac{2m_p}{1 + X} \\
\mu &= \frac{m_p}{2X + 3(1 - X - Z)/4 + Z/2},
\end{aligned} \tag{4.3}$$

where we have made the approximation that the majority of the mass in metals is provided by oxygen, and that the mean molecular weights are constant. The former is a good approximation assuming that the relative abundance of metals are roughly solar, while the latter is a good approximation for $T \gtrsim$ a few $\times 10^4$ K for a gas composed of mostly hydrogen or $T \gtrsim 10^5$ K for a gas composed of mostly helium. At lower temperatures, where hydrogen/helium become less ionized, the approximation breaks down. This introduces an error in the cooling curve at lower temperatures, but this error only increases the sharpness at which $\Lambda \to 0$ and is thus limited to a small range in temperatures. Furthermore, most of the gas in our simulation is above 10^5 K, so this approximation does not significantly affect our results.

Once we have calculated the cooling curve, we then approximate it as a piece-wise power law composed of 12 carefully chosen segments over the range 10^4 and 10^9 K. Above 10^9 K we use a single power law, which is reasonable because at such high temperatures Λ is dominated by thermal bremsstrahlung of electrons with either H or He.

The values of X and Z in the stellar winds is somewhat uncertain. However, WR stars are typically bereft of Hydrogen, having ejected their outer hydrogen envelopes in earlier stages of stellar evolution. We would thus expect their stellar winds to be composed of very little hydrogen and a higher fraction of metals. Indeed, by fitting the spectra, Martins et al. (2007) find that the H/He ratio is small in most of the stars and suggest that higher values of Z might be appropriate. Therefore, for this work we adopt $X = 0$ and $Z = 3Z_\odot$. Note that this is also the metallicity assumed in several previous works (e.g., Cuadra et al. 2008, Calderón et al. 2016). The resulting cooling curve is plotted in Figure 4.1 along with the piece-wise power law approximation that we employ in our simulation. The agreement is excellent. Also plotted in Figure 4.1 is the ratio between the number of free electrons and ρ/m_p, which shows that the approximation of $\mu_e \approx$ const. is good for $T \gtrsim 10^5$ K. For lower temperatures, Helium becomes mostly neutral and that approximation breaks down. However, the cooling curve also rapidly decreases below 10^5 K so this is not a significant source of error.

4.3.3 Computational Grid and Boundary/Initial Conditions

Our simulations are performed on a Cartesian grid to avoid the severe time step restriction inherent in 3D spherical-polar coordinates caused by the limited azimuthal extent of the cells near the pole. In addition, there is not necessarily an a priori symmetry axis in our problem, limiting the utility of spherical-polar coordinates. To effectively resolve the smaller spatial scales of interest, we utilize nested levels of static mesh refinement (SMR) to resemble logarithmic spacing in radius. Furthermore, to avoid an unphysical build-up of material in the cells near the origin, we remove a sphere of radius r_{in} equal to twice the width of the smallest grid cell, replacing it with a region of negligible pressure, negligible density, and zero velocity. This allows material to flow into the "black hole" while limiting unphysical boundary effects to only a few cells outside of r_{in}. Tests demonstrate that this effective inner boundary condition correctly reproduces the Bondi accretion solution. The outer boundary condition is outflow in all directions.

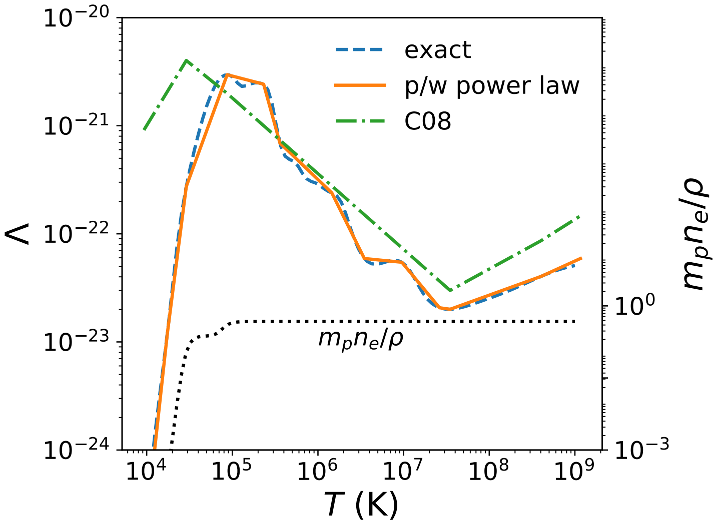

Figure 4.1: Piece-wise power law approximation used in this work (solid) compared to the full cooling curve calculated by `SPEX` (dashed, see §4.3.2) and the cooling curve used by Cuadra et al. (2008) (C08, dot-dashed). Our cooling curve is for hydrogen free, $Z = 3Z_\odot$ gas appropriate for the Wolf-Rayet star winds near Sgr A*. Also plotted is the number of free electrons relative to ρ/m_p. This shows that 1) the piece-wise power law does an excellent job capturing the shape of the full cooling curve, and 2) the simplification that $\mu_e \approx$ const. is well motivated for all temperatures in which the cooling curve is non-negligible. The main difference between our cooling function and that of C08 is our choice to use $X = 0$, which reduces the high temperature bremsstrahlung tail and moves the cut-off at low temperatures to slightly higher temperatures.

4.3.4 Floors and Ceilings

Since `Athena++` evolves the conservative variables of mass density, momentum density, and total energy density, occasionally the primitive variables of ρ and P can reach unphysical (i.e., negative) values. When this occurs, to prevent code failure, we utilize floors on the density and pressure such that if $\rho < \rho_{\rm floor}$, we set $\rho = \rho_{\rm floor}$, and if $P < P_{\rm floor}$ we set $P = P_{\rm floor}$. In particular, we adopt the values of $\rho_{\rm floor} = 10^{-7} M_\odot {\rm pc}^{-3}$ and $P_{\rm floor} = 10^{-10} M_\odot {\rm pc}^{-1}{\rm kyr}^{-2}$. In runs with radiative cooling, we impose a minimum temperature of 10^4 K which acts as an additional, density-dependent floor on pressure. The aforementioned floors are activated sufficiently rarely that they do not affect our results.

Additionally, unphysically large temperatures or velocities that occur in a handful of problematic cells can severely limit the time step of the simulation, which is set by the Courant–Friedrichs–Lewy number multiplied by the maximum wave speed over all cells in the domain. To limit the effect of these isolated cells, we impose a ceiling on both the sound speed and the velocity that is equal to 10 times the free-fall velocity at the inner boundary. If the sound speed of a cell exceeds this value, we reduce the pressure in that cell such that the new sound speed is equal to the ceiling. When the magnitude of one of the components of the velocity exceeds the ceiling, we reduce the magnitude to the ceiling while keeping the sign fixed. In practice, we find that these ceilings are only necessary during the first time step of our simulations for cells located within the stellar wind source term. This is because the initial time step, which is set by the initial conditions of a cold, low density gas, is large compared to the wind crossing time in these cells. The time step is appropriately reduced after the first time step and the ceilings are no longer needed.

4.4 Tests of Implementation

In this section we describe two hydrodynamic simulations to both test and demonstrate the implementation of the model described above.

4.4.1 Stationary Stellar Wind

In order to test that our subgrid model for the stellar winds produces the desired effect, we place a single, stationary star with $v_{wind} = 1$ pc/kyr $\approx$ 1000 km/s and $\dot{M}_{wind} = 10^{-5}\ M_\odot/yr$ at the center of a uniform, low density, low pressure medium. The grid is a cube of 128^3 cells with three levels of mesh refinement, so that the box size is $\approx 300 r_{wind}$. We run the test for $\approx$ 2 times the wind crossing time of the box. Absent gravity, as time evolves a steady state should be reached where the star drives a global wind with $\mathbf{v} = v_{wind}\hat{r}$ and $\rho = \dot{M}_{wind}/(4\pi v_{wind} r^2)$.

Our simulation shows excellent agreement with the analytic solution, as shown in the left panel of Figure 4.2, where the angle averaged density, outflow rate, and radial velocity are all essentially equal to the expected values for $r > r_{wind}$. In principle, the temperature of the wind should be ≈ 0, but in practice there is a finite amount of thermal pressure added by the model described in §4.3 due to the difference between $|\langle \mathbf{v}_{wind,net}\rangle|^2$ and $\langle|\mathbf{v}_{wind,net}|^2\rangle$ caused by the averaging of a purely radial velocity over a Cartesian grid cell. This effect, however, is sufficiently small for our purposes, as

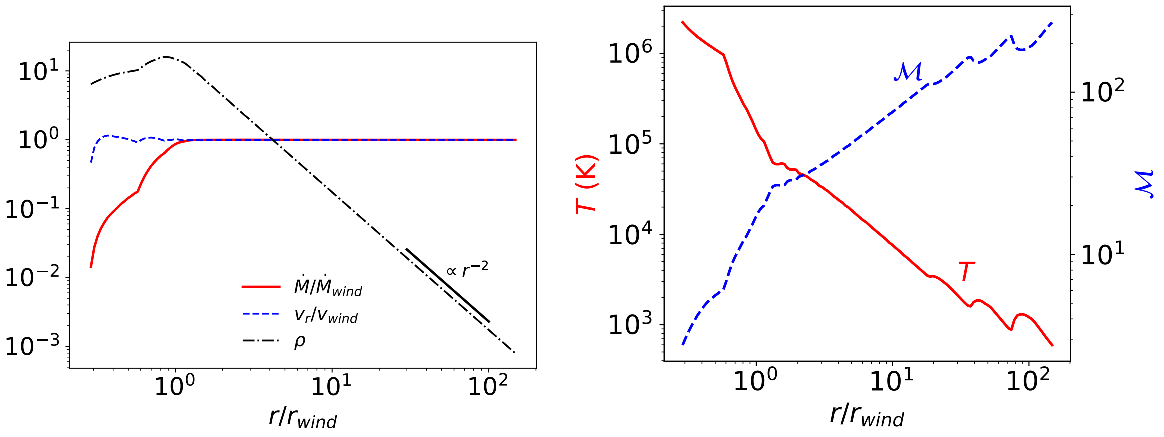

Figure 4.2: Left: Angle averaged outflow rate, radial velocity, and mass density profiles for a single, stationary stellar wind at the center of a uniform, low pressure medium (§4.4.1). The wind is sourced in a sphere of radius $r_{wind} \approx 2$ cells. Right: Temperature profile and mach number, $\mathcal{M} \equiv v_r/c_s$, in the same test. For $r > r_{wind}$, the angle-averaged $\dot{M}$, v_r, and ρ match nearly perfectly with the desired solution. As desired, the wind is also cold, with the Mach number at the base of the wind of ≈ 30 and rising with increasing distance from the base. Note that the bumps in the temperature profile for $r/r_{wind} \gtrsim 20$ (directly corresponding to the bumps in Mach number) are caused by truncation error as the internal energy of the gas drops to the level of the numerical precision of the total energy.

shown in the right panel of Figure 4.2. At the base of the wind, the radial Mach number of the flow is ≈ 30 and increases due to adiabatic cooling as $\sim (r/r_{wind})^{2/3}$, showing that the thermal pressure is a negligible contribution to the wind dynamics. For this particular choice of v_{wind} and $\dot{M}_{wind}$, which are typical of the values of the stars contributing to accretion onto Sgr A*, this corresponds to a base wind temperature of $\approx 2 \times 10^4$ K that decreases as $\sim (r/r_{wind})^{-4/3}$. Furthermore, despite the Cartesian nature of the grid, the generated wind is still approximately spherically symmetric, as seen by the relatively small deviations ($< 10\%$) from spherical symmetry shown in Figure 4.3.

4.4.2 Isotropic Stars on Circular Orbits

In order to test our implementation of the stellar winds in a more complicated and dynamic problem, we seek to reproduce the results of Quataert (2004), in which the winds of the stars orbiting Sgr A* were modeled in spherical symmetry using a smooth source term in mass and energy. To do this, we place 720 stars in circular orbits in a point source gravitational potential, roughly uniformly distributed in solid angle and uniformly spaced in radius between 2″ (0.08 pc) and 10″ (0.4 pc). Each star has the same stellar wind velocity, namely, 1000 km/s, and mass loss rate determined by requiring the total mass loss rate to be 10^{-3} $M_\odot$/yr. Furthermore, we neglect radiative cooling. In the limit of an infinite number of stars, this should be equivalent to a smooth source term between 2″ (0.08 pc) and 10″ (0.4 pc) that depends only on radius and supplies a net addition of mass and energy without adding momentum (corresponding to $\eta = 2$ in

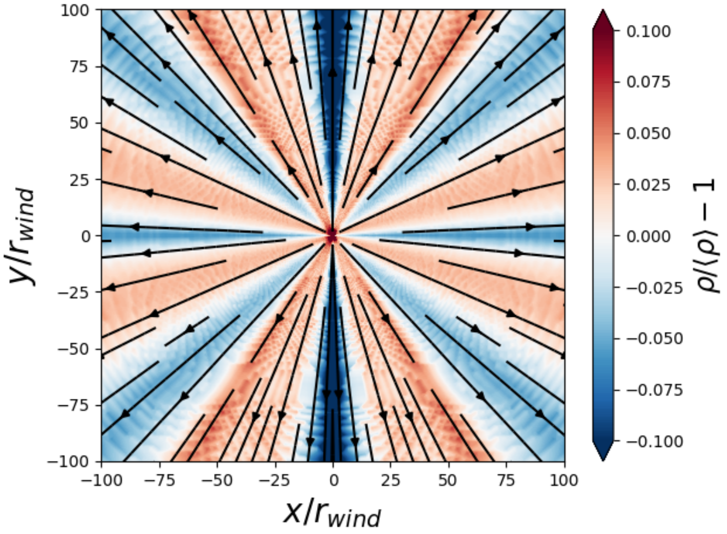

Figure 4.3: Deviation of the φ-averaged density from spherical symmetry for the stationary stellar wind test (see §4.4.1, Figure 4.2), over-plotted with velocity streamlines. These deviations caused by the Cartesian grid are acceptably small, $< 10\%$ everywhere.

the notation of Quataert 2004). Since we consider orbiting and not stationary stars, in order to make a proper comparison we add an additional source term to Quataert (2004)'s spherically symmetric calculation to account for the extra kinetic energy in the injected gas due to orbital motion: $1/2$ $q(r)$ GM_{BH}/r where $q(r)$ is the stellar mass loss rate per unit volume and $M_{BH} \approx 4 \times 10^6 M_\odot$. The 3D simulation is run for 7 kyr, and performed with a base resolution of 128^3 with 6 levels of nested mesh refinement on a 5^3 pc^3 Cartesian grid, resulting in an inner boundary of $r_{in} \approx 2.4 \times 10^{-3}$ pc.

The angle-averaged results for the density, temperature, and radial velocity in this test are shown in Figure 4.4, over-plotted with the results of a high resolution 1D calculation using the smooth source term described in the preceding paragraph. We find excellent agreement between the two calculations. The small differences are (i) small variations in the region where mass is injected due to the finite number of stars and (ii) small differences in the few cells closest to the absorbing inner boundary. We have verified that by moving the inner boundary to smaller radii, the agreement improves. These results verify that 1) our subgrid model for the stars effectively drives stellar winds with the desired accretion rate and wind speed and 2) the effects of the inner boundary condition are limited to only a few cells and do not affect the rate at which mass is captured by the black hole or the flow structure in the majority of the computational domain.

4.5 3D Simulation of Accreting Stellar Winds Onto Sgr A*

In this section we focus on the problem of accretion onto Sgr A* as fed by the stellar winds of the 30 Wolf-Rayet stars and describe in detail the resulting flow properties.

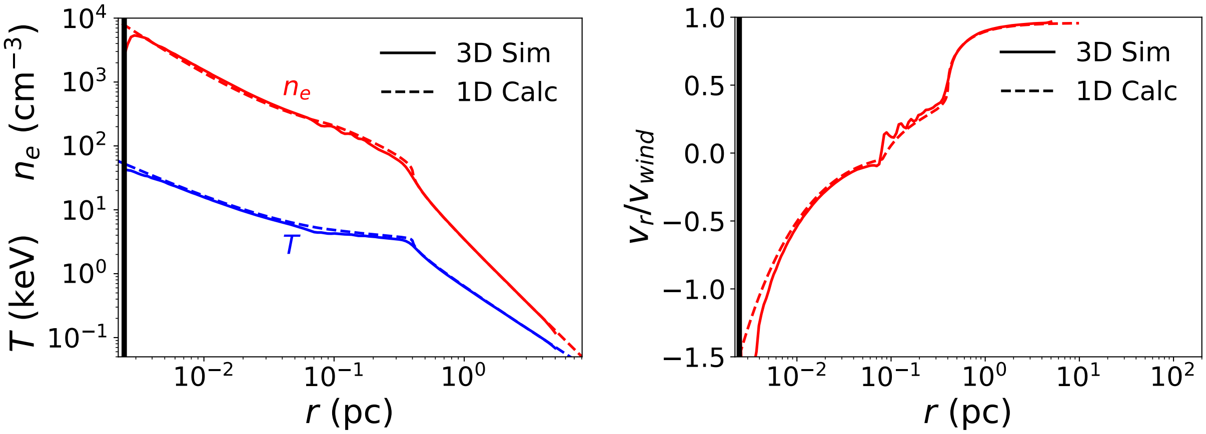

Figure 4.4: Electron number density, n_e, temperature, T, (left) and radial velocity normalized to the stellar wind velocity, v_r/v_{wind}, (right), all averaged over solid angle for the isotropic circular orbits test described in §4.4.2. Dashed lines represent the high resolution spherically symmetric solution with a smooth radial source of mass and energy, while solid lines represent a full 3D simulation of 720 stars in circular orbits uniformly spaced in solid angle and radius between 0.08-0.4 pc ($2-10''$). The black vertical line is the location of the inner boundary, r_{in}, for the 3D simulation. We find excellent agreement between the two calculations, which verifies that our model for injecting stellar winds (§4.3) produces the desired results. The small differences we find are due to both the finite number of stars and minor effects of the absorbing inner boundary condition.

4.5.1 Stellar Winds and Orbits

Before describing the simulation itself, we first briefly summarize the stellar wind parameters and orbits of the stars that we include as sources of mass, momentum, and energy.

Of the hundreds of stars orbiting Sgr A* at distances less than about a parsec, we include in our simulation only the $\approx$ 30 Wolf-Rayet stars identified in Martins et al. (2007) as strong wind emitters. The wind speeds and mass loss rates that we set for each star are taken directly from Table 1 of Cuadra et al. (2008), which summarizes Martins et al. (2007). The locations of the stars are determined by solving Kepler's equation at each time step for the set of orbital elements corresponding to the present day location and velocities with respect to Sgr A*. Unfortunately, while the proper motions, radial velocities, and positions in the plane of the sky for the stars are precisely measured (Paumard et al. 2006; Lu et al. 2009), their location in the plane of the sky (i.e. the z direction) is undetermined because the acceleration measurements for nearly all of stars are consistent with 0 (Lu et al. 2009). It was noted by Levin & Beloborodov (2003) (and later confirmed by Beloborodov et al. 2006; Lu et al. 2009; Bartko et al. 2009), however, that the velocities of some of the stars lie within a thin planar structure, which allowed them to perform a likelihood analysis to precisely determine the z-coordinates of the disc-stars. Some have proposed the existence of a second stellar disc (e.g. Paumard et al. 2006), but this disc remains uncertain (Beloborodov et al. 2006; Lu et al. 2009). Thus, in order to determine the orbits of the remaining, non-disc-stars, we require a prescription for their z-coordinates. For simplicity and ease of comparison to previous calculations, we adopt the "1-disc" model of Cuadra et al. (2008)[2], where the z-coordinate of the stars outside the stellar disc are determined by minimizing the eccentricity of the implied stellar orbit.

In summation, for each disc-star as identified by Beloborodov et al. (2006), we use the velocities and three dimensional positions as listed in Table 2 of Paumard et al. (2006) to determine the stellar orbits, while for the remaining stars we use the velocities and two dimensional positions from Table 2 of Paumard et al. (2006) with z-coordinate determined by minimizing the eccentricity. The single exception to this is the star S97 (aka E23), whose orbit has a short enough period to have been precisely determined (e.g., Gillessen et al. 2009, 2017). For this star we use the orbital elements listed in Table 3 of Gillessen et al. (2017).

In addition to the winds of the WR stars, we also perform one simulation that includes the stellar wind of the star S2. For this star we use the orbit given by Gillessen et al. (2017) and theoretical estimates of its mass-loss rate and stellar wind speed. This is described in more detail in §4.5.3.

The radii of the resulting stellar orbits (not including S2) as a function of time as well as their height and cylindrical radius defined with respect to the stellar disc at the present day are shown in Figure 4.5 for the inner few arc seconds (inner few $\sim$ 0.1 pc). Here and throughout we define $t = 0$ as December 2017. We expect the handful of stars in the inner few arc-seconds region to be the dominant source of accretion, as their stellar winds are more gravitationally bound to the black hole than the winds of the stars orbiting at larger radii. From Figure 4.5, note first that,

---

[2] Note, however, that in this work we assume a black hole mass of 4.3 $\times 10^6$ $M_\odot$, resulting in orbits that are not quite identical to those in Cuadra et al. (2008), who assumed a black hole mass of 3.6 $\times 10^6$ $M_\odot$.

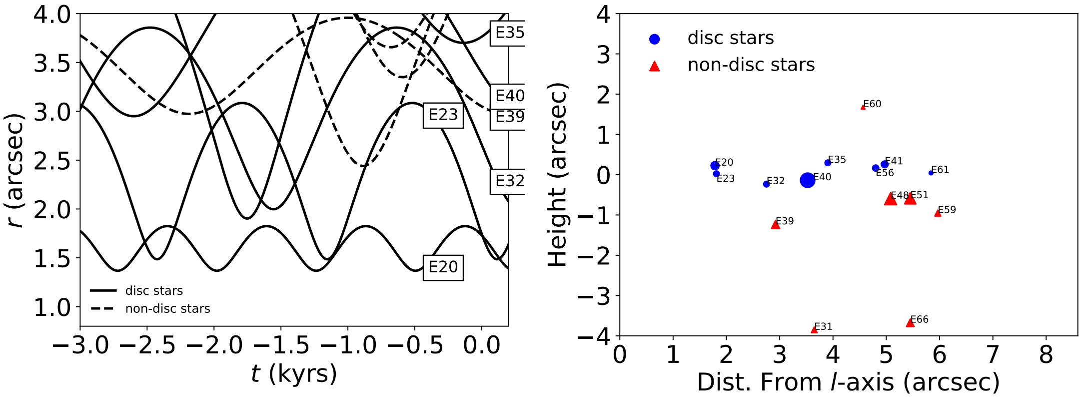

Figure 4.5: Left: Radial distance from the black hole for the innermost stars in our simulation. Right: Present day height and cylindrical radius of the innermost stars defined with respect to the anuglar momentum axis of the clockwise stellar disc described by Beloborodov et al. (2006), where the sizes of the circles/triangles are linearly proportional to the mass-loss rate of the stars. Each star is labeled using the 'E' notation of Paumard et al. (2006). Solid lines (blue circles) denote stars identified with the stellar disc, while dashed lines (red triangles) denote stars outside the disc that fall into a more isotropic distribution of angular momentum. The line-of-sight position for the latter stars are chosen by minimizing the eccentricity of the orbit, as in Cuadra et al. (2008). At the present day, five out of the six stars in the inner 4″ are disc-stars, which suggests that the angular momentum of the inner accretion flow might preferentially be aligned with the angular momentum of the stellar disc. Moreover, within the central 6″, at the present day, five of the six non-disc stars are located below the midplane of the stellar disc, which further suggests that the accretion flow structure might be asymmetric in polar angle (defined with respect to the angular momentum vector of the stellar disc). Indeed, we find both of these to be true in our simulations, as discussed in §4.5.3.

at the present day, a majority of the innermost stars are disc-stars, which is encouraging for the robustness of our calculation of the inner accretion flow as these orbits are better constrained than the orbits of non-disc stars. Furthermore, this predominance of disc stars in the inner region will provide the accretion flow with a preferred angular momentum direction and thus encourage a coherent formation of a disc, as we will show in §4.5.3. Secondly, note that a majority of the innermost non-disc stars are located below the plane of the stellar disc. This introduces an inherent asymmetry about the midplane of the disc. This asymmetry shows up in the accretion flow structure outlined in §4.5.3.

4.5.2 Parameters and Initialization

We perform our simulation on a base grid with physical size of 1 pc^3 that is covered with 128^3 cells. Additionally, to further resolve the innermost region, we use 9 levels of nested SMR, resulting in an inner boundary of $r_{in} \approx 6.0 \times 10^{-5}$pc $\approx 1.6 \times 10^{-3}$ ″ $\approx 300 r_G$, where $r_G \equiv GM_{BH}/c^2$ is the gravitational radius of the black hole. To study the dependence of our results on r_{in}, we also carry out simulations for $r_{in} \approx 3.0 \times 10^{-5}$pc, 1.2×10^{-4}pc, and $\approx 2.4 \times 10^{-4}$pc (see §4.5.3).

Since we are interested in the accretion flow at the present day, we start the simulation at an initial time of $t_0 = -1.1$ kyr, that is, 1100 years in the past, starting with zero velocity and the floor values of pressure and density. 1100 years corresponds to an orbital period at $r \approx 0.3$ pc $\approx 7''$. Since we are interested in the flow properties at radii much smaller than this, such a run time is sufficient for our purposes (as we have also checked by running larger r_{in} simulations for longer times).

Finally, we adopt the recent estimates of $M_{BH} = 4.3 \times 10^6 M_\odot$ and $d_{BH} = 8.3$ kpc (Gillessen et al. 2017), where d_{BH} is the distance to Sgr A*. For these parameters, $1'' \approx 0.04$ pc $\approx 2 \times 10^5$ r_g, where $r_g \equiv \mathrm{G}M_{BH}/\mathrm{c}^2$, G is the gravitational constant, and c is the speed of light.

4.5.3 Results

Figure 4.6 shows a volume rendering of our simulation for the outer ~ 0.5 pc ($\sim 13''$) of the galactic center at the present day, while Figure 4.7 shows two-dimensional plane-of-the-sky slices of electron number density and temperature at the same time and spatial scale. The stellar winds of the "stars" in our simulation (which appear in the figure as dense, cool circular point-like objects) strongly interact and produce a myriad of bow shocks, heating the gas to temperatures as high as $\sim 2 \times 10^8$ K. These point-like sources and shocks also light up in X-rays, as shown in the X-ray surface brightness profile of Figure 4.8 (see caption and §4.6 for details of this calculation), which is overall in good agreement with the observed brightness profile seen by *Chandra* (also shown in Figure 4.8). The largest differences (not including the pulsar wind nebula at ΔRA, ΔDec $\approx -4'', 8.5''$ that appears in the observations) occur a few arcseconds to the left of Sgr A* in the plane of the sky (ΔRA offset from Sgr A* of $\sim 3''$), where our simulations show a point-like source of emission not seen in the observational data, and around the star IRS 13E at (ΔRA, ΔDec) $\approx (-4'', -2'')$, which is significantly brighter than the observations. Since both of these differences were also seen by Russell et al. (2017), who simulated the same problem[3] with a similar orbital configuration, mass-loss rates, and stellar wind speeds (see §4.8), they can likely be interpreted as additional constraints on the properties of the stellar winds. For a more detailed discussion, we refer the reader to Russell et al. (2017).

As we will show, much of the material at the scale pictured in Figures 4.6-4.8 is unbound outflow; only a small fraction actually reaches the inner domain. Furthermore, by the present day, the total amount of mass in the simulation contained within $r \lesssim 0.5$ pc has saturated at a constant value of $\sim 0.2 M_\odot$. This implies that the mass-feeding rate of the stellar winds is approximately balanced by the rate at which mass leaves the computational domain. Figure 4.9 focuses closer in to the black hole, again showing plane-of-the-sky slices of mass-density and temperature but only in the inner 0.04 pc ($\sim 1''$). By the time the gas has reached this scale, the shocks formed by the colliding winds have mostly dissipated, resulting in a hot, smooth flow combined with a few cooler ($T \lesssim 2 \times 10^7$ K), dense clumps. The gas at this scale consists of roughly equal proportions of inflow and outflow (see below).

---

[3] Russell et al. (2017) also included various subgrid models of feedback from Sgr A*, but the two features discussed here are seen in all of their mock X-ray images, including the "control run" with no feedback.

Figure 4.10 shows the mass accretion rate through the inner boundary and the angular momentum direction vector of the inner 0.03 pc ($\sim 0.8''$) of the simulation as a function of time. The accretion rate varies between $\sim 2.0 \times 10^{-7} \dot{M}_\odot$/yr to $\sim 1.75 \times 10^{-6} \dot{M}_\odot$/yr on time scales as short as 10s of years. The angular momentum vector of the flow, on average, oscillates around the normal vector of the stellar disc in which most of the innermost stars lie. The largest deviation occurred during a period of $\sim$ 300 yrs that began $\sim$ 500 yrs ago when there was a rapid change from clockwise to counter-clockwise rotation with respect to the line of sight. This event was associated with the largest spike in accretion rate that we see at $\sim$ 200 yrs ago. This was likely caused by one or two of the non-disc stars briefly providing a large source of accretion as they approached pericenter (see Figure 4.5) which then temporarily disrupted whatever coherent disc may have formed. By the present day, however, the gas has settled back down to once again be aligned with the stellar disc and the flow enters a brief "quiescent" phase with a relatively low accretion rate that lasts for the next ~200 years. One should not read too much into the latter result beyond the fact that the accretion rate could have been higher by factors of $\lesssim$7 within the recent hundreds of years. This is because we find that our simulations are highly stochastic, and thus the exact behavior of the accretion rate as function of time can vary even with the smallest perturbation.

With that said, to study the flow properties in more detail it is useful to study averaged fluid quantities to account for this stochastic time variability. We define the time and angle average of a fluid quantity A as

$$\langle A \rangle \equiv \frac{1}{4\pi(t_{max} - t_{min})} \int\limits_{t_{min}}^{t_{max}} \int\limits_{0}^{2\pi} \int\limits_{0}^{\pi} A \sin(\theta) d\theta d\varphi dt, \tag{4.4}$$

and the w-weighted time and angle average as

$$\langle A \rangle_w = \frac{\langle Aw \rangle}{\langle w \rangle}, \tag{4.5}$$

where we use $t_{min} = -100$ yr and $t_{max} = 0$ yr. Note that 100 yr is the free-fall time at a radius of ≈ 0.07 pc $\approx 1.8''$. We have chosen this particular time interval rather than one centered on $t = 0$ because it represents a period in which the angular momentum vector of the inner regions is relatively steady (see Figure 4.10). Such an interval more clearly elucidates many of the general properties of the simulation while minimizing the complications inherent in describing a flow that is not in a true steady-state.

Figure 4.11 shows the resulting radial profiles of the average electron number density, temperature, and radial velocity, while Figure 4.12 shows a radial profile of the average accretion rate, broken down into both inflow and outflow. We define the latter two quantities as

$$\begin{aligned} \dot{M}_{in} &\equiv -\langle 4\pi\rho \min(v_r, 0) r^2 \rangle \\ \dot{M}_{out} &\equiv \langle 4\pi\rho \max(v_r, 0) r^2 \rangle. \end{aligned} \tag{4.6}$$

Figures 4.11 and 4.12 show that the flow contains four distinct regions:

1. The outflow dominated region, $r \gtrsim 0.4$ pc, which falls outside the locations of the majority of the stars and where the flow is approaching the standard Parker wind solution with $\rho \propto r^{-2}$ and $\dot{M} \approx$ const. > 0.

2. The "feeding region" where the orbits of the stars mostly lie, 0.07 pc $\lesssim r \lesssim$ 0.4 pc, where $\dot{M}$ is both positive and increasing with radius due to the source term provided by the stellar winds.

3. The "stagnation region", 0.01 pc $\lesssim r \lesssim$ 0.07 pc, where the mass inflow and outflow rates approximately cancel and $\dot{M} \approx 0$.

4. The inflow dominated region, $r \lesssim$ 0.01 pc, where $\dot{M} \approx$ const. < 0.

The transition from region 3 to region 4 is marked by an increase of inflow relative to outflow, caused by the loss of pressure support at the inner boundary leading to an accelerated radial velocity that approaches Mach 1. The net effect of this is that, of the $\sim 7 \times 10^{-4} M_{\odot}/yr$ of material provided by the 30 stellar winds, only a small fraction of this, $\sim 7 \times 10^{-7} M_{\odot}/yr$, is accreting into the inner boundary; the rest fuels the outflow. However, the radius at which the flow transitions from regions 3 to 4, and hence, the constant accretion rate in the innermost radii, depends on the location of the inner boundary. Larger (smaller) r_{in} causes the transition to happen at larger (smaller) radii and thus results in larger (smaller) accretion across the inner boundary. This clear dependence of our simulation results on the location of the inner boundary is not necessarily a concern; in fact, we can use it to extrapolate down to the Schwarzchild radius of the black hole where a pressure-less boundary would be appropriate. We do this later in §4.5.3.

In Figure 4.12, the inflow rate at ~ 0.1 pc is ~ 2-3 10^{-5} $M_{\odot}$/yr, which is of order the canonical Bondi estimate for the rate at which gas should be gravitationally captured by the central black hole. However, only a small fraction of this mass actually accretes to smaller radii $\ll$ 0.1 pc (and the accretion rate at small radii decreases as we decrease the innermost radius of our simulation; see Figure 4.17). Thus the Bondi accretion rate estimate is not a good estimate of the accretion rate at small radii in our simulations. This is because, as we will show in more detail below, only the low angular momentum tail of the stellar wind material can accrete to small radii in our simulations.

For a flow in which radiative cooling is inefficient, the $T \propto r^{-1}$ scaling shown in Figure 4.11 is expected from conservation of energy, where $T \propto GM_{BH}/r$. If the flow were adiabatic this would imply a density power law of $r^{-3/2}$ for $\gamma = 5/3$, but instead we find $\rho \propto r^{-1}$. This is because the shocks generated by the accreting stellar wind material lead to an effective energy dissipation term that results in $p/\rho^{\gamma} \propto r^{-1/3}$, that is, an entropy profile that increases with decreasing radius. In Appendix 4.A we explain the precise shape of the density profile in terms of a model in which the stellar winds from only a small number of stars dominate the flow. An r^{-1} density profile in the inner region of the flow implies that the total amount of mass enclosed in a spherical shell of radius r, M_{enc}, scales as r^2 in this region. More precisely, we find that the enclosed mass at $t = 0$ is well approximated by

$$M_{enc} \approx 4 \times 10^{-5} M_{\odot} \left(\frac{r}{0.008\text{pc}} \right)^2, \tag{4.7}$$

which agrees with our simulations up to a factor of ~ few for $r > 2 \times 10^{-4}$ pc.

Figure 4.13 shows the mass-weighted average Bernoulli parameter and the relative contributions to the Bernoulli parameter from pressure and velocity. We find that the flow is, on average, unbound at all radii. For $r \gtrsim 0.04$ pc, the material is strongly unbound, that is, $\langle E \rangle \gg GM_{BH}/r$, and the Bernoulli parameter approaches a constant. This is expected from the fact that the majority of the stars are located between $0.05 - 0.4$ pc and fuel a Parker wind-type solution for $r > 0.4$ pc. By contrast, the gas in the inner $r < 0.05$ pc is only very slightly unbound, with the Bernoulli parameter closely mirroring the gravitational potential.

Radiative cooling can be important in localized regions for cooling of the shocked stellar winds at large radii ($r \gtrsim 0.07$ pc), but has a negligible effect on the inner regions of the flow ($r \lesssim 0.07$ pc). To quantify this, we note that there is only $\approx 10^{-3} M_\odot$ of gas with $T < 10^5$ K for $r \lesssim 0.07$ pc and no gas with $T \lesssim 10^6$ K by $r \lesssim 0.03$ pc. This can be understood using a simple time-scale analysis. At $r = 0.07$ pc, the ratio between the cooling time, $\langle t_{cool} \rangle \equiv \langle P/(\gamma - 1) \rangle / \langle Q_- \rangle$, and the local sound crossing time, $\langle t_{cs} \rangle \equiv r/\sqrt{\gamma \langle P \rangle / \langle \rho \rangle}$ is ~ 300, and increases rapidly with decreasing radius. For $r \gtrsim 0.07$ pc, however, this ratio is typically of order ~ 50 and can be as small as ~ 10. Note that this is an angle and time averaged quantity; localized regions at $r \gtrsim 0.07$ pc can have the ratio between t_{cool} and t_{cs} reach ~ 1.[4]

Figure 4.14 shows the average specific angular momentum of the accretion flow, weighted both by mass and mass flux, as well as the average direction vector of the mass weighted specific angular momentum. The bulk of the material falls into a sub-Keplerian rotation profile with $l \approx 0.5 l_{kep} = 0.5\sqrt{GM_{BH} r}$, while the angular momentum of the material that is accreting all the way through the inner boundary is constant with radius and equal to half the Keplerian value at the inner boundary, $l \approx 0.5 l_{kep}(r_{in})$. This indicates that only material with circularization radii $\lesssim r_{in}$ is able to truly accrete; the rest fuels outflow, as we shall show. The reason that both the mass-weighted specific angular momentum profile and the value of the specific angular momentum at the boundary are sub-Keplerian is that the flow is predominately pressure supported, as shown in Figure 4.13, where the rotational term comprises only $\sim 20\%$ of the Bernoulli parameter.

Furthermore, Figure 4.14 also shows that the direction of the angular momentum vector is $\approx$ const. for the inner $r \lesssim 0.4''$ and is essentially aligned with the normal vector of the clockwise disc of stars. We have shown previously in Figure 4.5 that five of the innermost six stars at the present day are classified as disc-stars, so it is not surprising that the resulting flow is also aligned with the disc if we consider that most of the material is provided by these nearby stars. The fact that this direction is $\approx$ constant with radius makes it convenient to define a new coordinate system in which the z-direction is aligned with the angular momentum. In this new coordinate system we can make 2D, φ-averaged contour maps to better study the disc structure.

In these new coordinates, Figure 4.15 shows contour maps of φ-averaged mass accretion rate overplotted with velocity streamlines, Bernoulli parameter, and density, in addition to φ-averaged θ profiles of density, angular velocity, temperature, and accretion rate at 0.04 pc $\approx 66 r_{in}$. Though we do find a disc-like structure with the density peaked in the midplane, the scale height of this disc is large, with only a factor of $\sim$ 2-3 contrast between the midplane density and the polar density. This is because the disc is hot and mostly pressure supported (see Figure 4.13), which causes the disc to puff up and reach a scale height, H, of $H \approx r$. Additionally, we find that accretion primarily occurs by bound material along the southern polar region, while the midplane and northern pole

---

[4] Since we include optically thin radiative cooling in the calculation, t_{cool}/t_{cs} is always $\gtrsim 1$; otherwise it would quickly evolve to $t_{cool}/t_{cs} \sim 1$.

are moderately unbound and generally outflowing. The asymmetry in θ is a direct result of the asymmetry in the distribution of non-disc stars at the present day (Figure 4.5), where a majority of the inner-most non-disc stars are located below the midplane of the stellar disc. The somewhat counter-intuitive result that the midplane is predominantly outflowing and not inflowing is caused by the stellar wind material having a wide range of angular momentum. The significant population of low angular momentum material would naturally accrete spherically, but the material with larger angular momentum can only reach a radius $\sim l^2/(GM_{BH})$, at which point it scatters off of the effective potential, preferentially towards the midplane. The presence of both of these components results in the accretion structure shown in Figure 4.15, where a combination of both high and low angular momentum material inflow along the southern pole until the circularization radii of the high angular momentum material is reached. At this point the unbound, high angular momentum material "turns aside" to the midplane and feeds outflow while the bound,low angular momentum material continues on until it either reaches the inner boundary or feeds the outflow along the northern pole.

These two very different components to the accretion flow are additionally seen in the fact that the midplane and the southern polar regions have very different dynamics. This is highlighted in Figure 4.16, where we show φ-averaged radial profiles of accretion rate, radial velocity, and angular velocity for $\theta = 90°$ and $\theta = 170°$. At $\theta = 170°$ (southern pole), the material is essentially in free-fall with an accretion rate that nicely matches the $\propto \sqrt{r}$ predicted from feeding by a few isolated stars (Appendix 4.A). At $\theta = 90°$ (midplane), on the other hand, $v_r \ll v_{ff}$ and the material is nearly Keplerian with velocity predominantly in the φ-direction.[5] This means that the flow can be roughly described as a superposition of a low angular momentum, spherical-Bondi type solution with a high angular momentum, Keplerian thick disc type solution. In our simulations, the former dominates the accretion rate while the latter dominates the mass.

Extrapolating Down To The Event Horizon

As discussed in the previous section, the amount of matter that accretes through the inner boundary depends on the value of r_{in}. This is for two reasons. First, the "absorbing" boundary condition that we use removes radial pressure support, leading to an increased inflow rate in the innermost region. Second, in order for material to accrete, it must have $l \lesssim 0.5 l_{in}$, where $l_{in} \equiv \sqrt{GM_{BH} r_{in}}$ is the Keplerian angular momentum at the inner boundary. Both of these effects would be physically reasonable if r_{in} represented the event horizon of the black hole, but unfortunately such a small r_{in} is too expensive for our current computational resources, which use $r_{in} \approx 300 r_G$. On the other hand, we have found that our simulation quantities roughly obey power laws over much of the inner domain, so we can reasonably extrapolate down to smaller radii.

The effect of the inner boundary is to force $v_r(r_{in})$ to be $\approx -c_{in} \sim -v_{ff}(r_{in}) \propto r_{in}^{-1/2}$, while we have shown that $\rho \propto r^{-1}$ (Figure 4.11). Thus, we expect $\dot{M} \propto \sqrt{r}$, which is the natural result of only handful of stars that have wind speeds comparable to their orbital speeds dominating the accretion supply (see Appendix 4.A). We have already shown that the accretion rate measured along the

---

[5] Note, however, that by comparing Figure 4.13 to Figure 4.16, $\langle v_r \rangle^2 \ll \langle v_r^2 \rangle$, meaning that there can exists large instantaneous radial flows that cancel out when averaged over time.

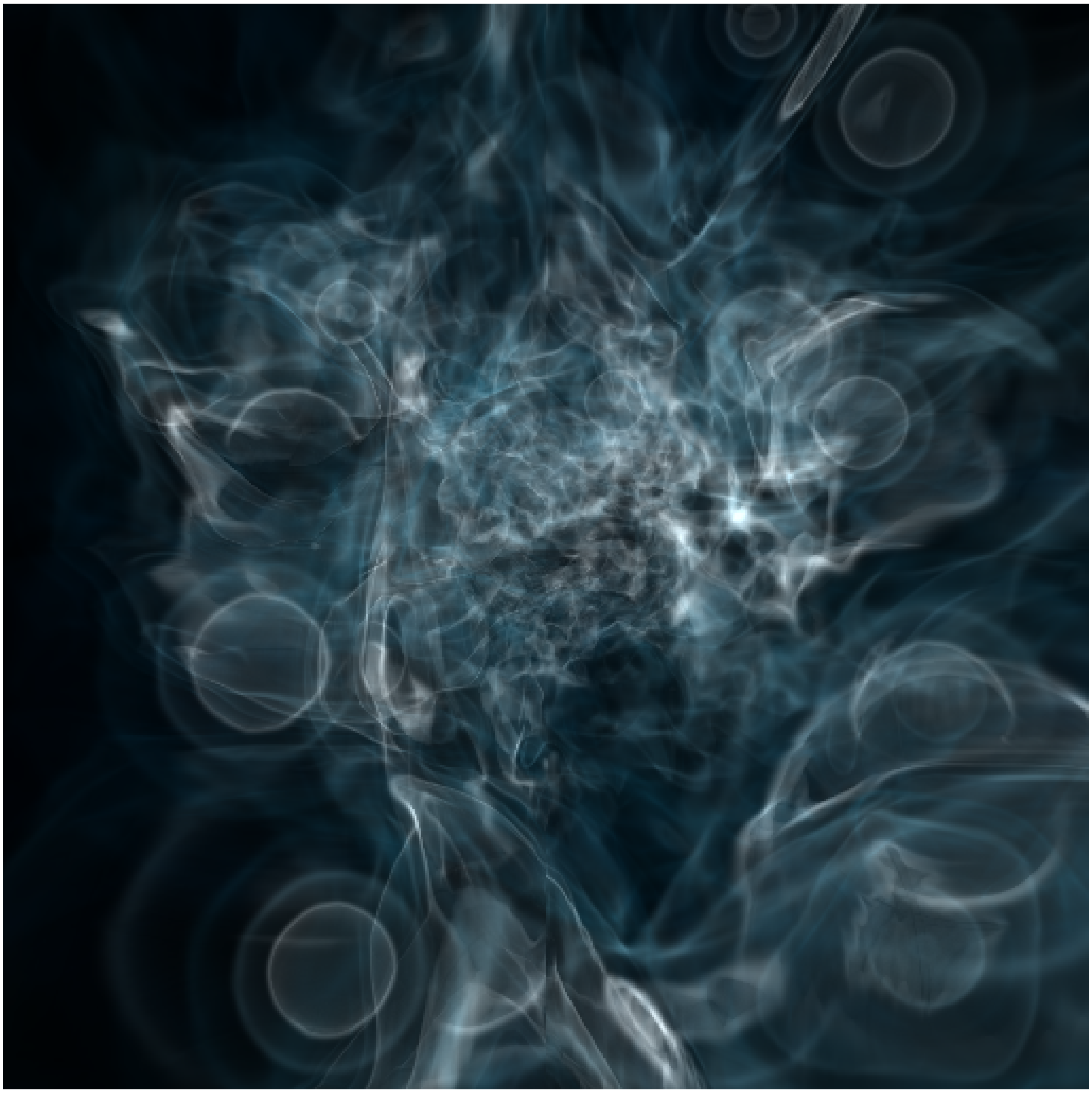

Figure 4.6: Three-dimensional rendering of our simulation on a 0.5 pc × 0.5 pc scale. This rendering was created with the `yt` code (Turk et al. 2011) using 8 'layers' evenly spaced logarithmically in mass density between 10^{-2} and $10^{0.5}$ $M_{\odot}/\mathrm{pc}^3$. As the stellar wind sources (which appear as circular, outlined rings) plow through the material, the winds themselves form bow shocks in the direction of motion. The interaction between these shocks causes a variety of fine scale structure to form in the flow. *An animation of this figure is available online.*

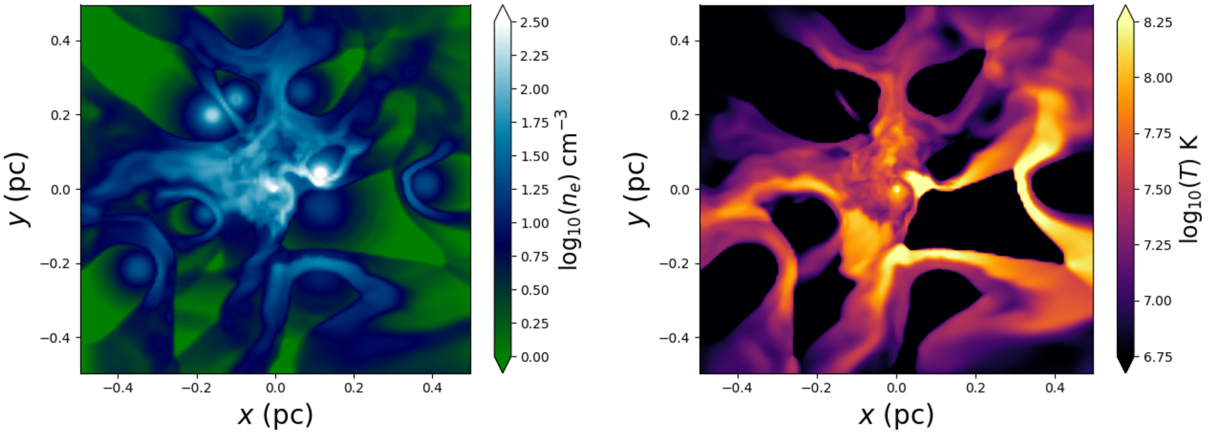

Figure 4.7: Plane-parallel slices in the plane of the sky ($z = 0$) of the electron number density, n_e, and Temperature, T, of our 3D hydrodynamic simulation, shown at the present day after running for 1.1 kyr from an initial vacuum state. The "stars" in our model are effectively point sources in mass, momentum, and energy (see §4.3) that travel on fixed Keplerian orbits constrained by observations. Here they appear as dense, cool, spherical regions. The winds emitted from the stars form bow shocks as they collide with the ambient material and heat to high temperatures ($\sim 2 \times 10^8$ K). On the scale of the image, most of the stellar wind material is unbound and outflowing due to high temperature and angular momentum (see Figures 4.12 and 4.13). *An animation of this figure is available online.*

southern pole that dominates the inflow nicely matches this scaling relation (Figure 4.16). For further confirmation of this result, in the top panel of Figure 4.17, we plot the accretion rate as function of radius for four different values of r_{in} compared to an $r^{-1/2}$ power law. The agreement is fairly good. By setting the constant of proportionality using the accretion rate in the $r_{in} \approx 300 r_G$ simulation, we find that

$$\dot{M} \approx 2.4 \times 10^{-8} M_\odot/\mathrm{yr} \sqrt{\frac{r_{in}}{r_G}}, \tag{4.8}$$

which is shown in the bottom panel of Figure 4.17 to be an excellent representation of our simulations. For a non-rotating black hole, the horizon is located at $2r_G$ and thus Equation 4.8 predicts an accretion rate of $\approx 3.4 \times 10^{-8} M_\odot$/yr. The Bondi rate that would be inferred from the density and temperature at $2''$ in our simulation is $2.4 \times 10^{-5} M_\odot$/y. Our estimated $\dot{M}$ at the horizon is a factor of ~ 700 lower due to the presence of rotationally-driven outflow. Remarkably, the prediction of Equation (4.8) is entirely consistent with the observational limits inferred from polarization measurements (Marrone et al. 2007) as well as previous estimates of the accretion rate based on models of the horizon-scale accretion flow (e.g., Shcherbakov & Baganoff 2010; Ressler et al. 2017). It is unclear if this result will hold in MHD simulations, however, since angular momentum transport in rotationally supported material may modify $\dot{M}$ from the value set by the low angular momentum tail in our hydrodynamic simulations.

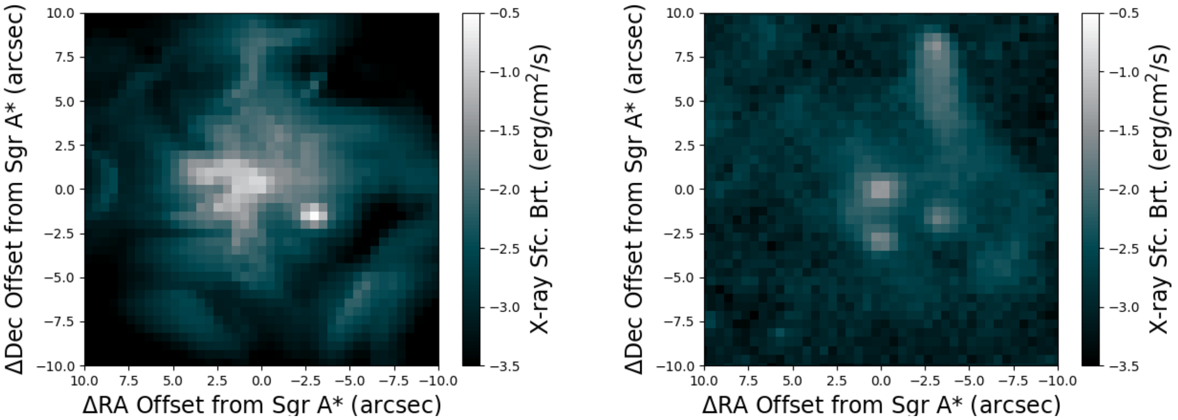

Figure 4.8: 2-8 keV surface brightness of the central 20″ × 20″ at the present day as calculated from our simulation (left) and as observed by *Chandra* (right) (Li et al. 2013). The surface brightness from the simulation has been coarsened to match the *Chandra* spatial resolution of ≈ 0.492″ per pixel, while the surface brightness from the observations is calculated assuming a mean photon energy of 5 keV and has not been corrected for absorption. Both images show several point sources corresponding to the stellar wind sources in addition to an increase in surface brightness at the position of the black hole. Note that, in our simulations, we do not the include the point source at (ΔRA, ΔDec) ≈ (-4.5″,8″) associated with the pulsar wind nebulae seen in the *Chandra* image. Integrated over the inner 1.5″ – 10″, the X-ray surface brightness from our simulation agrees well with the point-source-extracted luminosity calculated from observations (see Figure 4.19, Baganoff et al. 2003).

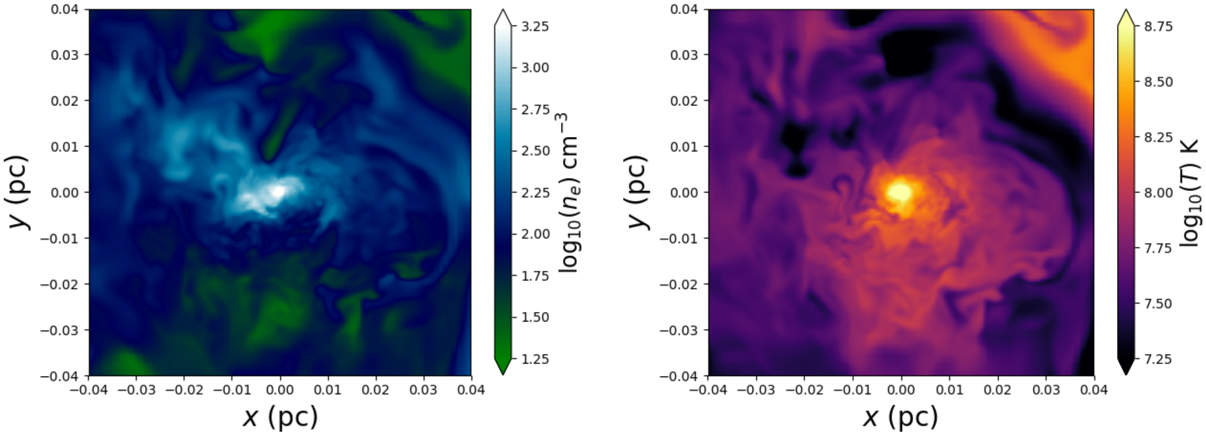

Figure 4.9: Same as Figure 4.7, except zoomed in to the inner 1”. At this scale, much of the kinetic energy provided by the stellar winds has been converted into thermal energy via the shocks seen in Figure 4.7, resulting in a relatively smooth, hot accretion flow. Note, however, the presence of a few relatively cold, high density clumps.

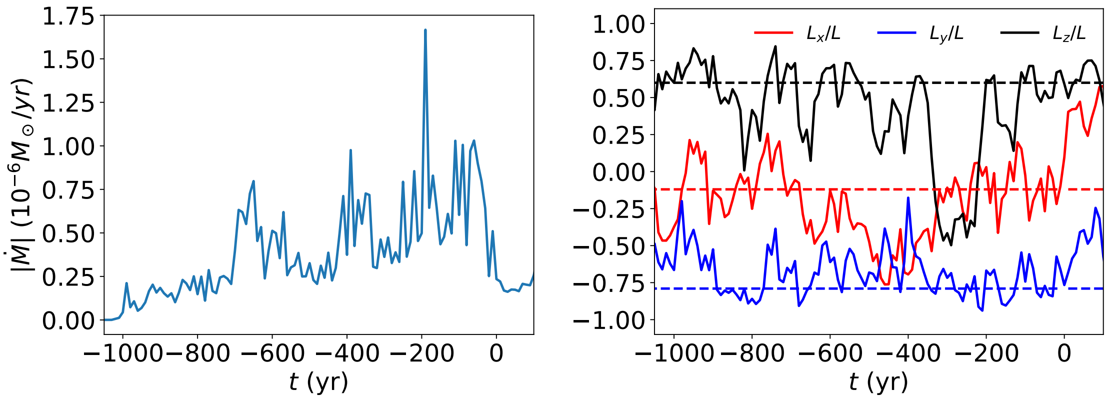

Figure 4.10: Top: Accretion rate as a function of time in our simulation, measured at $2.5r_{in} \approx 1.5 \times 10^{-4}$ pc $\approx 740r_g$. Bottom: Angular momentum direction vector averaged over the inner $10r_{in} \approx 6 \times 10^{-4}$ pc $< r < 0.03$ pc. Dashed lines represent the angular momentum vector of the stellar disc in which a majority of the innermost stars orbit. The largest spike in the accretion rate is associated with a rapid change in the angular momentum vector of the flow.

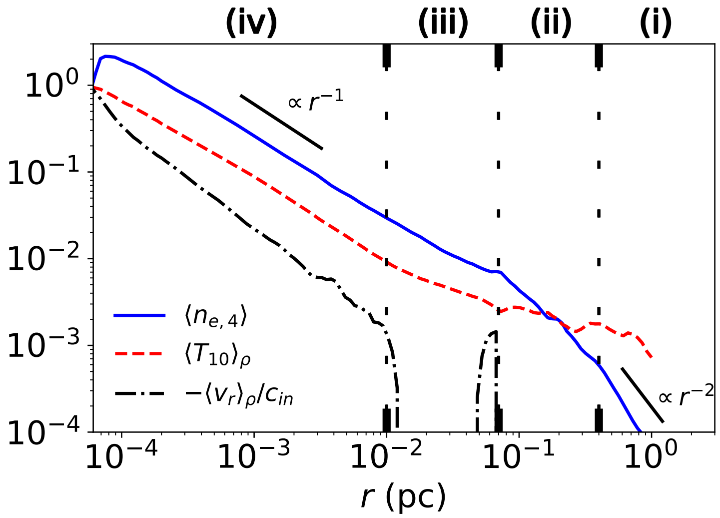

Figure 4.11: Time and angle averaged electron number density in units of 10^4 cm^{-3}, $\langle n_{e,4} \rangle$, temperature in units of 10^{10} K, $\langle T_{10} \rangle_\rho$, and radial velocity normalized to the average sound speed at the inner boundary, $\langle v_r \rangle_\rho / c_{in}$, where $c_{in} \equiv \langle c_s \rangle_\rho (r_{in})$. Vertical lines demarcate regions (i)-(iv) as defined in §4.5.3. In the inner accretion flow, $r \lesssim 0.07$ pc (regions iii and iv), all three variables follow power-laws in radius of $\propto r^{-1}$, while for $r \gtrsim 0.4$ pc (region i) the density follows an r^{-2} profile, as expected for a Parker wind-type solution.

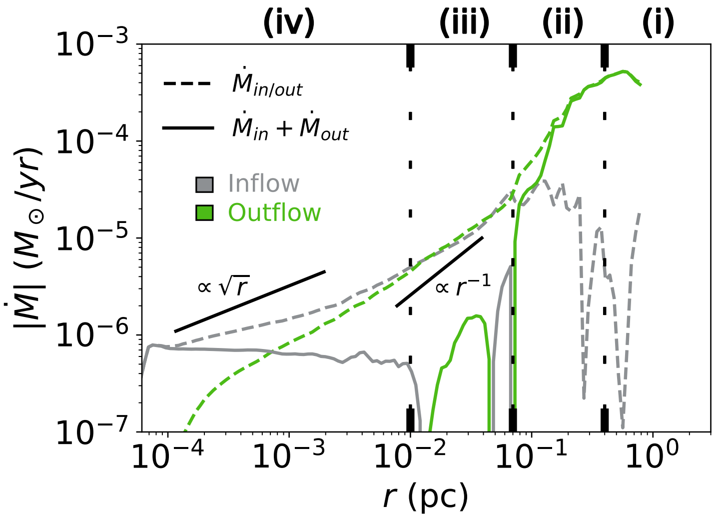

Figure 4.12: Time and angle averaged accretion rates as a function of radius, including the net accretion rate (solid) and inflow and outflow rates computed separately (dashed, Equation 4.6). Here Kelly green lines denote outflow while silver lines denote inflow. Vertical lines demarcate regions (i)-(iv) as defined in §4.5.3. Outflow dominates for $r \gtrsim 0.07$ pc (region i), where most of the stellar winds are located, while inflow dominates for $r \lesssim 0.01$ pc (region iv). In between, the rates are nearly equal in magnitude. Of the total $\approx 7 \times 10^{-4}$ $M_\odot$/yr added to the simulation from the stellar winds, only a small fraction, $\approx 6 \times 10^{-7}$ $M_\odot$/yr, flows into the inner boundary. In addition, the accretion rate at the inner boundary, r_{in}, decreases with smaller r_{in} (§4.5.3, Figure 4.17).

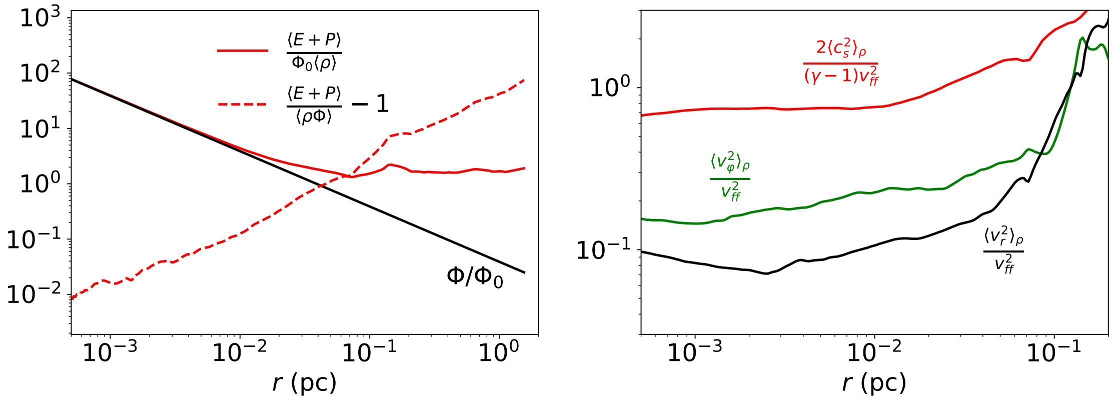

Figure 4.13: Left: Time and angle-averaged total specific energy (solid red), $(E+P)/\rho$, where $E \equiv 1/2\rho v^2 + P/(\gamma-1)$, gravitational potential (solid black), $\Phi \equiv GM_{BH}/r$, and the Bernoulli parameter (dashed red), $(E+P)/\rho - \Phi$. The latter quantity is normalized to the gravitational potential, while the former two are normalized to the gravitational potential at $r_0 = 0.04$ pc [i.e. $\Phi_0 = \Phi(r_0)$]. Right: Time and angle-averaged components of the Bernoulli parameter, including the pressure term (top line), the orbital kinetic energy term (middle line), and radial kinetic energy term (bottom line), all plotted as fractions of the gravitational potential, GM_{BH}/r. Here the azimuthal, φ direction is defined with respect to a coordinate system which has $\hat{z}$ aligned with the average density weighted angular momentum axis. The inner accretion flow is slightly unbound, with Bernoulli parameter $\gtrsim 0$, and predominantly pressure supported. Note that, comparing to Figure 4.11, $\langle v_r^2\rangle_\rho \propto r^{-1}$, while $\langle v_r\rangle_\rho \propto r^{-1}$, which is due to the cancellation of both inflow and outflow reducing the average of v_r.

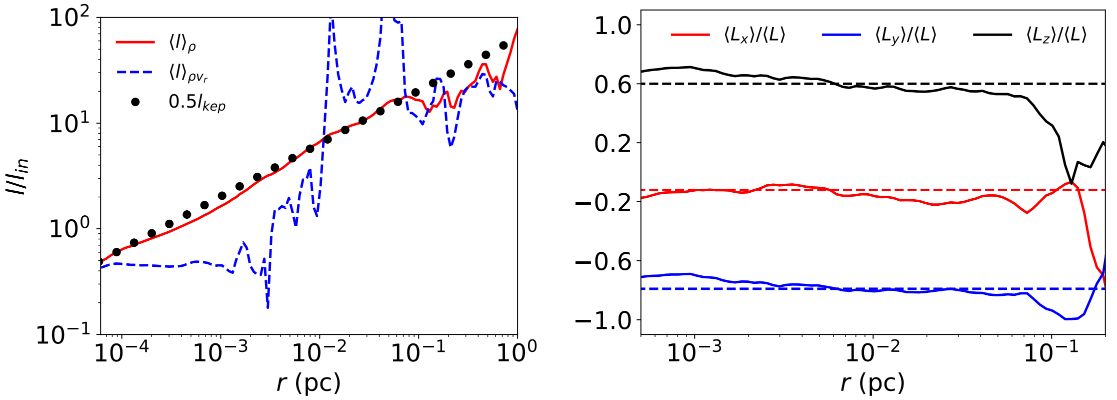

Figure 4.14: Left: Comparison between the density-weighted and the mass flux-weighted averages of the angular momentum, both normalized to the Keplerian value at the inner boundary, l_{in}. Right: Time and angle averaged angular momentum direction vector of the inner region of our simulation. Dashed lines represent the normal vector of the clockwise stellar disc taken from Paumard et al. (2006). Here we define $\langle L \rangle^2 \equiv \langle L_x \rangle^2 + \langle L_y \rangle^2 + \langle L_z \rangle^2$, where $L_i = \rho l_i$ is the angular momentum per unit volume in the ith direction. Most of the mass lies in a slightly sub Keplerian distribution with $l \approx 0.5 l_{kep}$ with a well-defined direction that is constant in the inner $r \lesssim 0.1$ pc and aligned with the clockwise disc of stars. The material flowing into the inner boundary, on the other hand, has a nearly constant angular momentum of $l \approx 0.5 l_{in}$ (left panel; dashed blue line), which shows that only material that has circularization radii $\lesssim r_{in}$ is able to accrete.

The Effect of Including S2

The star S2, which has an orbit that reaches $\sim$ 3000 r_g (or $\approx 0.01'' \approx 4$ mpc, Gillessen et al. 2017), is of particular interest for many studying the galactic center. Its exceptionally well-constrained orbit has been used to constrain the mass and distance to Sgr A*, and high-precision measurements of its next pericenter passage will be used to test the theory of General Relativity (Grould et al. 2017; Hees et al. 2017; Chu et al. 2018). Though S2 is much fainter and thus expected to have a much weaker stellar wind than the typical WR star surrounding Sgr A*, its proximity to the black hole could increase its potential effect on feeding and/or disrupting the accretion flow in the innermost radii (Loeb 2004; Nayakshin 2005; Giannios & Sironi 2013; Schartmann et al. 2018). This would be especially true at pericenter, which is expected to occur in the year 2018. To test this hypothesis, in this section we briefly consider the effect that the wind from this star could have on accretion onto Sgr A*. Note that S2 is among the most massive of the S stars (Habibi et al. 2017) and thus the most likely to have a strong wind.

For the observed properties of S2 (e.g. Habibi et al. 2017), the theoretical model of Vink et al. (2001) predicts a mass-loss rate of $\approx 2 \times 10^{-8}$ $M_\odot$/yr for a fiducial wind speed of 2000 km/s. Note that this mass-loss rate is $\sim$ 3 orders of magnitude less than the typical WR star in our simulation. Using said mass-loss rate and wind speed in addition to the precisely known orbit as given by Gillessen et al. (2017), we performed a second simulation that is identical to the the first except that it included S2 as an additional wind source term.

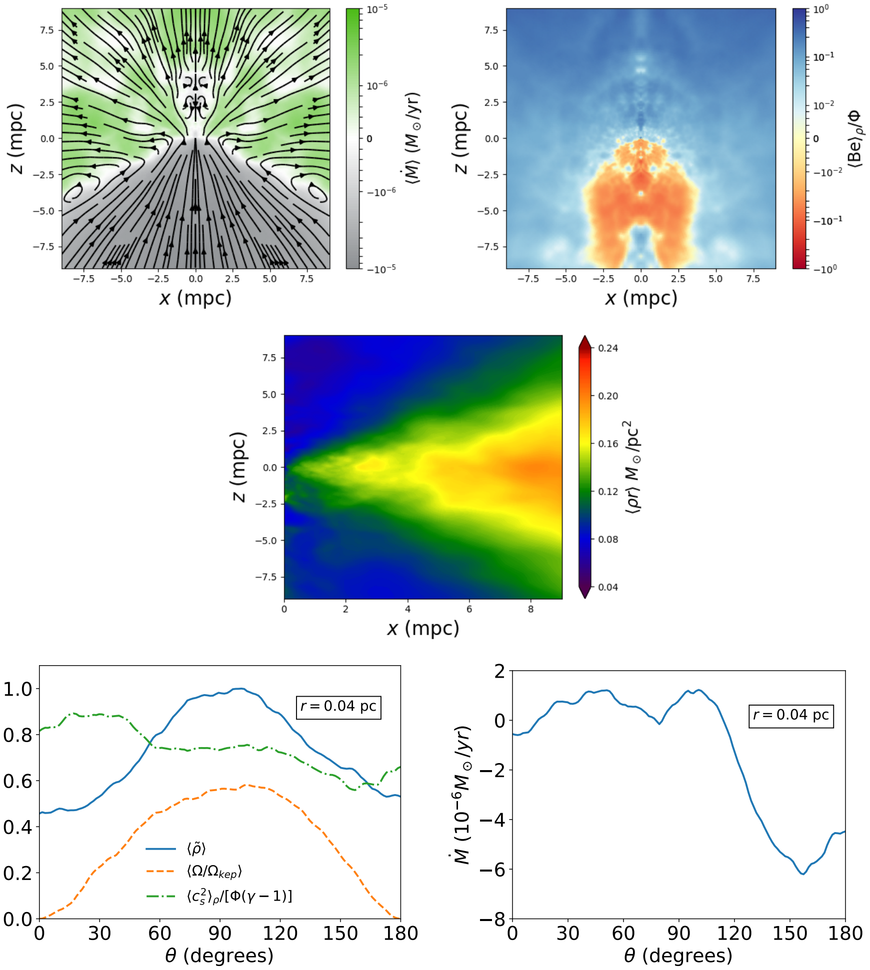

Figure 4.15: Top Left: Time and φ averaged mass accretion rate, $\dot{M} = 4\pi\rho v_r r^2$, where green denotes outflow and silver denotes inflow, overplotted with streamlines of velocity. Top Right: Time and φ averaged Bernoulli parameter relative to the gravitational potential, Be/Φ. Middle: Time and φ averaged mass density, multiplied by the spherical radius r to account for the $\rho \propto r^{-1}$ scaling we show in Figure 4.11. Bottom Left: Angular profiles at 0.04 pc $\approx 0.1''$ of the time and φ averaged mass density (normalized so that the peak density is 1), $\tilde{\rho}$, angular velocity in units of the Keplerian rate, Ω/Ω_{kep}, and the ratio between the thermal component of the Bernoulli parameter and the gravitational potential, $c_s^2/[\Phi(\gamma-1)]$. Here $\Omega \equiv v_\varphi/[r\sin(\theta)]$ and $\Omega_{kep} \equiv \sqrt{GM_{BH}/[r\sin(\theta)]^3}$ Bottom Right: Time and φ-averaged accretion rate as a function of polar angle at 0.04 pc. Here φ is defined as the azimuthal angle with respect to the angular momentum axis shown in the right panel of Figure 4.14. The disc that forms is very thick and pressure supported, with only a small contrast between the density in the midplane compared to the density at the poles (note the linear scale on the density contour and angular profile). Furthermore, accretion occurs primarily by bound material (Be<0) in the southern polar regions, while the midplane and northern pole are predominately composed of unbound(Be>0) outflow. This is caused by the asymmetry of the location of the non-disc stars (see Figure 4.5) and the fact that material can only inflow for $r > r_{circ}$, where r_{circ} is the circularizaiton radius, at which point it is preferentially "scattered" towards the midplane (defined with respect to the angular momentum axis).

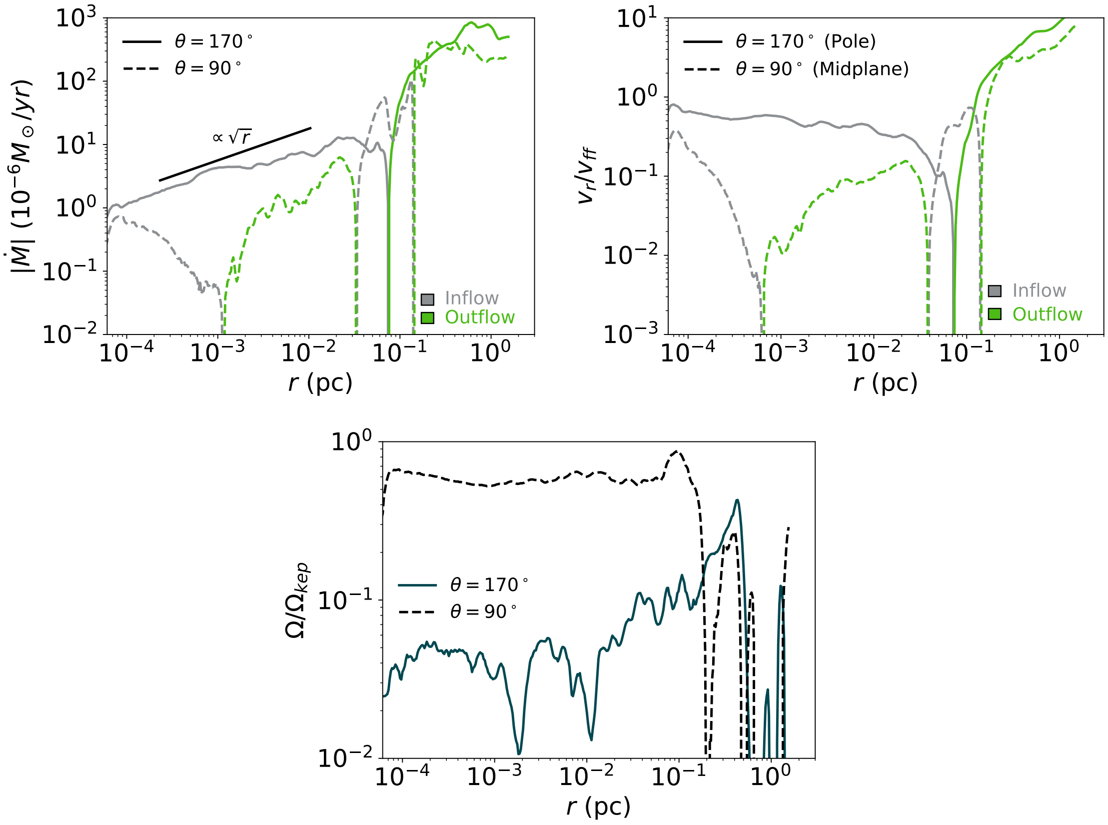

Figure 4.16: Time and φ-averaged radial profiles of accretion rate (top), radial velocity in units of the free fall speed (middle), and angular velocity in units of the Keplerian rate (bottom) along θ slices, where $\Omega \equiv v_\varphi/[r\sin(\theta)]$, $\Omega_{kep} \equiv \sqrt{GM_{BH}/[r\sin(\theta)]^3}$, and θ is defined with respect to the angular momentum axis shown in the right panel of Figure 4.14. Solid lines are profiles along the southern pole, dashed lines are profiles along the midplane (see Figure 4.15), while green denotes outflow and silver denotes inflow. The bound material in the southern pole is essentially in free-fall, with an accretion rate that nicely follows the $\sqrt{r}$ power-law predicted from isolated star accretion (Appendix 4.A). The material in the mid-plane, on the other hand, is dominated by pressure and rotational support with a much smaller radial velocity and inflow/outflow rates.

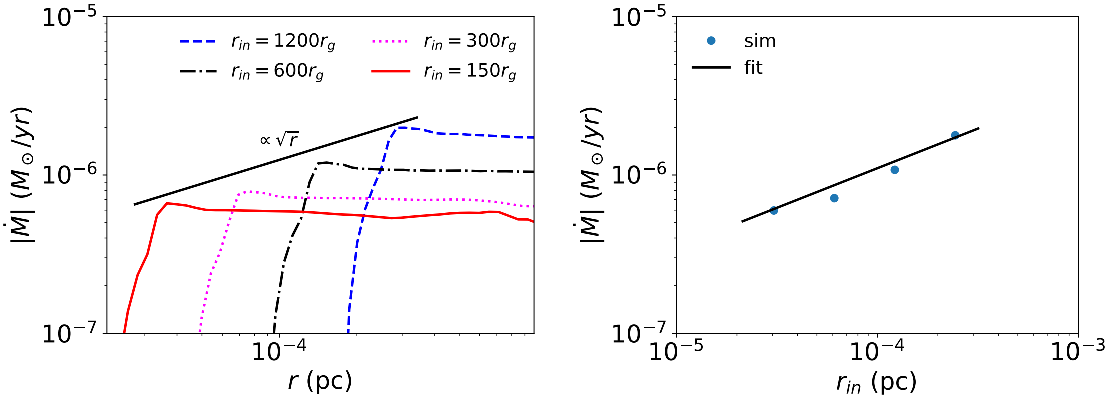

Figure 4.17: Dependence of the accretion rate on the inner boundary. Left: Time-averaged accretion rate as a function of radius for four different values of the inner boundary. Right: The fit presented in Equation 4.8 plotted vs. the time averaged accretion rate at $r = 2.5r_{in}$ for the same four values of the inner boundary radius. Using the $\sqrt{r}$ dependence of the accretion rate that holds well over this range of r_{in}, we estimate $\dot{M} \approx 3 \times 10^{-8}$ $M_\odot$/yr at the horizon of the black hole.

Figure 4.18 shows that including S2 has essentially no effect on the time and angle averaged flow properties. This is because, even at ~0.01”, the inflow and outflow rates shown in Figure 4.12 are still almost 2 orders of magnitude larger than the mass loss rate of S2. This is consistent with the results of Lützgendorf et al. (2016), who found that a simulation that included the winds of the S-stars alone could only provide significant accretion if their mass-loss rates were $\sim$ 10-100 times larger than those inferred from observations (e.g., the values quoted above for S2).

4.6 Constraining Stellar Wind Mass-loss Rates and Wind Speeds with X-ray Observations

The simulations presented in this paper used the mass-loss rates presented in Martins et al. (2007) that were obtained by fitting stellar wind models to infrared spectra. Their models included the effects of clumping, which reduce the inferred mass-loss rates for some of the stars (but not all) by a factor of $\sim$ 3. Estimates of the mass loss rates of the same stars derived from radio observations, however, are, on average, smaller by a factor of $\sim$ 2 (Yusef-Zadeh et al. 2015a). This is even without including the effects of clumping, which would reduce the radio-inferred mass-loss rates of some stars by another factor of $\sim$ 3. The infrared and radio data probe different spatial scales of the winds and use different modeling techniques so it is not clear which is a better representation of the true mass-loss rates.

To obtain an additional constraint, we turn to Baganoff et al. (2003), who presented spatially resolved X-ray observations of Sgr A* that measured the total 2-10 keV luminosity at two different scales, namely, between $1.5''$-$10''$ and also $< 1.5''$. As in previous work (Baganoff et al.

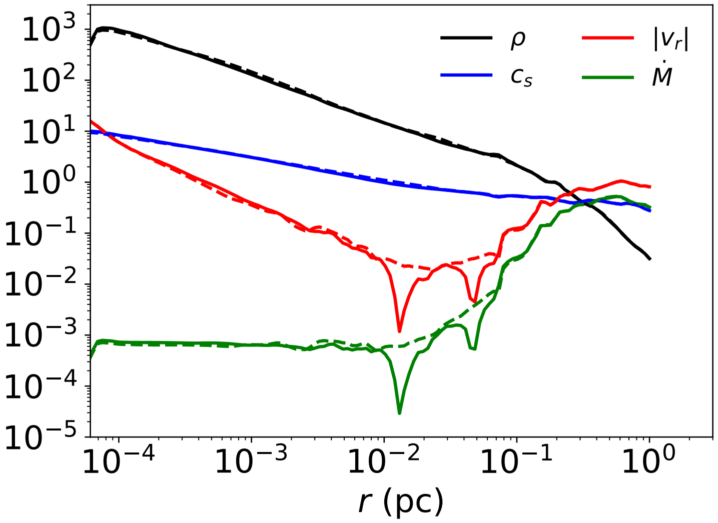

Figure 4.18: Comparison between the time and angle averaged radial profiles of mass density, sound speed, radial velocity, and accretion rate for simulations including the stellar wind provided by the star S2 (solid) and without S2 (dashed). The units of ρ, c_s (v_r), and $\dot{M}$ are $M_\odot/\mathrm{pc}^3$, pc/kyr, and $M_\odot$/kyr, respectively. Due to its low mass loss rate compared to the WR stars, including S2 has a negligible effect on the average radial profiles of the flow around Sgr A*.

2003; Quataert 2004; Rockefeller et al. 2004), we propose that the hot gas responsible for both of these emission components is provided by the stellar winds of the WR stars. In that case, these measurements of the X-ray luminosity help determine the stellar wind mass-loss rates, since the luminosity scales as $\propto n^2 \propto \dot{M}^2_{wind,tot}$ where $\dot{M}_{wind,tot}$ is the total mass-loss rate of all the stars. The constraint is even stronger when we consider that the two measurements probe regions in the flow with very different dynamics. $10''$ (0.4 pc) lies outside most of the stellar winds where the solution approaches a large scale Parker wind whose properties are primarily determined by the total mass-loss rate of the WR stars and the stellar wind velocities. $1.5''$ (0.06 pc), on the other hand, is inside most of the stellar winds and falls within the "stagnation region" described in §4.5.3. Here the hydrodynamic solution depends more strongly on the distribution of the stellar wind mass-loss rates with radius. For a fixed total mass-loss rate, a uniform distribution of mass-loss with radius results in a higher density at $1.5''$ than if most of the mass-loss is provided by stars at larger radii (Quataert 2004).

In order to compare our results to the *Chandra* observations, we again use SPEX (Kaastra et al. 1996) exactly as described in §4.3.2, except we consider only the contributions to Λ from photon frequencies corresponding to the 2-10 keV range, denoting this as Λ_X. The total X-ray luminosity of our simulation within a cylindrical radius s, $L_X(s)$, is then computed by integrating:

$$L_X(s) = \int_0^{2\pi} \int_{-z_{max}}^{z_{max}} \int_{r_{in}}^{s} \frac{\rho^2}{\mu_e \mu_{H,\odot}} \Lambda_X s ds dz d\varphi, \tag{4.9}$$

where z_{max} is half of the box length of our simulation and r_{in} is the radius of the inner boundary. Doing this, we find that at the present day, $L_X(10'') - L_X(1.5'') \approx 2.5 \times 10^{34}$erg/s and $L_X(1.5'') \approx 7.3 \times 10^{33}$ erg/s. These are to be compared with the *Chandra* measurements of 2.4 (1.8-3.2) $\times 10^{34}$ erg/s and 2.4 (1.8-5.4) $\times 10^{33}$ erg/s, respectively. The agreement between our models and the *Chandra* data is overall quite good, particularly accounting for uncertainties in massive star mass-loss rates (e.g. Smith 2014). In more detail, the X-ray luminosity between 1.5″ and 10″ is in excellent agreement with the *Chandra* data, but the X-ray luminosity of the inner 1.5″ of our simulation is overproduced by a factor of ~ few. As discussed above, this suggests that the overall mass-loss rate is roughly the right value but that the distribution of the mass-loss rates with radius (i.e. the location of the stars) is perhaps too spread out in radius such that there is an over-density at 1.5″ (see Quataert 2004). This is consistent with the fact the orbits of several of the 30 stars in our simulation are uncertain due to the lack of information about the line-of-sight position. Since the orbits directly determine the mass-loss distribution, we hypothesize that a better knowledge of the line of sight positions of the WR stars would bring our simulations into better agreement with observations.

The X-ray light curves shown in Figure 4.19 support this argument, which show that the X-ray luminosity between 1.5″ and 10″ has been relatively steady over the past ~ 400 years despite the fact that the stellar wind distribution has changed significantly (Figure 4.5). $L_X(1.5'')$ on the other hand, does display slightly more pronounced variation with time over the same interval, suggesting that is is more dependent on the instantaneous orbital configuration of the stars.

Even with the configurations of stellar winds adopted in our simulation, however, the discrepancy with the X-ray measurements is small enough that these results argue in favor of the Martins et al. (2007) mass-loss estimates as opposed to those of Yusef-Zadeh et al. (2015a), which would decrease L_X by a factor of $\gtrsim 4$.

Additionally, Baganoff et al. (2003) also provide a best fit temperature for the gas at ~ 10″, namely, 1.3 keV, which agrees very well with the value we find in our simulation ($\approx 1.5keV$, Figure 4.11). The temperature at this scale is predominately set by the stellar wind speeds (also taken from Martins et al. 2007), scaling roughly as v^2_{wind}. This agreement then implies a confirmation of the wind speeds to the ~ 10% level.

These two results together give us confidence that our simulation is capturing all of the hot gas observed by *Chandra* and that the resulting flow is a reasonable representation of observations.

4.7 Implications for Horizon-Scale Accretion Modeling

One of the goals of this work is to use the observationally constrained simulation of the accretion provided by WR stars to assess the "right" initial conditions for GRMHD simulations that

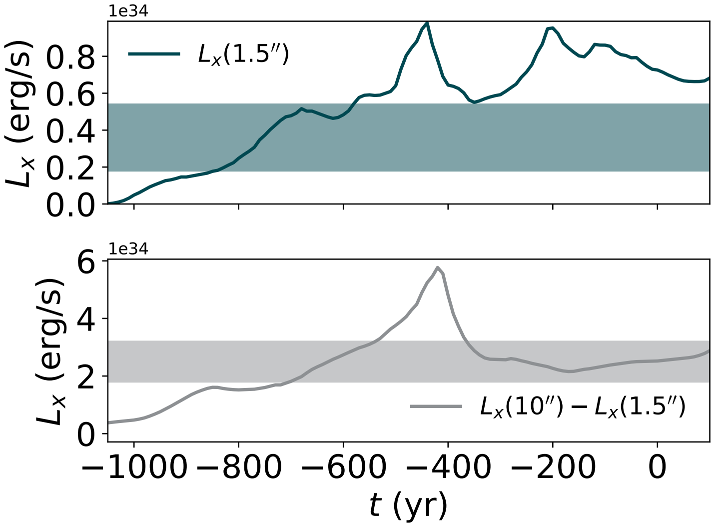

Figure 4.19: Total X-ray (2-10 keV) luminosity produced by our simulations as a function of time within a cylindrical radius of $1.5''$, $L_X(1.5'')$, and within cylindrical radii $1.5''$ and $10''$, $L_X(10'') - L_X(1.5'')$. The shaded regions represent the 90% confidence level intervals of *Chandra* observations of Sgr A*. At the present day, our simulation accurately reproduces the emission between $1.5''$ and $10''$ but has a luminosity within $1.5''$ that is a factor of 2-3 too large. This discrepancy is likely caused by the uncertainty in the stellar orbits or wind properties of the WR stars in our simulation leading to a moderate ($\sim$ 50%) over-density of gas at $\sim 1.5''$.

model Sgr A*. In this section we summarize the properties of the accretion flow presented in §4.5.3 by comparing and contrasting them to the standard initial torus structure used in past work.

Like the results of our simulation presented in §4.5.3, the typical initial torus used by many GRMHD simulations is thick and pressure supported. Unlike our results, however, this torus is usually well contained within some polar opening angle, beyond which there is a sharp cut-off in density. Here we have shown that the 'disc' is much less sharply defined, with a contrast of only a factor of $\sim$ a few between the midplane and the polar regions (Figure 4.15). Even more striking is the presence of a significant amount of low angular momentum inflow along the pole, which we estimate being as high as $3.4\times10^{-8}M_{\odot}/\mathrm{yr}$ when extrapolated to small radii (Figure 4.17), comparable to the accretion rate estimated at the horizon in Sgr A*. The presence of such an inflow could potentially inhibit the formation of jets, suppress outflow, and increase the net accretion rate onto the black hole in horizon-scale simulations.

This polar inflow also has the effect of driving a pressure supported outflow (Figure 4.15), so that the matter in the midplane of the disc is continually being recycled. In GRMHD simulations this could suppress the MRI if the growth rate is smaller than the inflow/outflow rate. That is, though the configuration is indeed unstable to the MRI with angular velocity decreasing with radius, it is possible that before the instability can grow significantly the fluid will be swept away and either accreted or propelled to large radii. Since our simulations produce a disc with root-mean-squared radial flow timescale that is comparable to (i.e., $\sim 1-2$ times longer than) the rotational period, a simple timescale analysis is inconclusive; a full treatment of MHD is required to determine the importance of the MRI on angular momentum transport in the disc.

Finally, we find that the angular momentum distribution follows a (sub) Keplerian profile of $\approx 0.5 l_{kep}$ as opposed to the constant angular momentum tori used by GRMHD simulations. This difference, however, is likely less important because the horizon-scale simulations quickly evolve to a similarly sub-Keplerian distribution after the onset of accretion.

Future work will seek to directly take the results of our simulations and implement them as initial and boundary conditions for a GRMHD simulation in order to determine the significance of these differences on the properties of the resulting flow.

4.8 Comparison to Previous Work

Several groups have studied the fueling of Sgr A* with 3D simulation using several different models for the stellar-wind emitting source terms (Rockefeller et al. 2004; Cuadra et al. 2005, 2006, 2008; Lützgendorf et al. 2016). Here we focus on the work of Cuadra et al. (2008) (C08), which is the most similar to ours in that they included the most up-to-date stellar mass-loss rates, stellar wind speeds, and current day star locations while also evolving the position the stellar wind sources with time. In particular, C08 focused on three different orientations of the accreting stars. The orientation of our stars at the present day is equivalent to their "1-disc" model with the exception of the star S97, whose orbit has been more precisely determined by Gillessen et al. (2017). The major differences between the two simulation are

- Computational methods: We use a conservative grid based hydrodynamic code while C08 used a smoothed-particle hydrodynamic (SPH) code. Conservative, finite-volume schemes excel in capturing shocks, an area in which SPH schemes can have trouble, particularly when the gas is diffuse and low temperature.

- The inner boundary radius.: The inner boundary of the C08 simulation was set at $0.05'' \approx 2$ mpc, while our inner boundary is $\approx$ 32 times smaller, at $\approx 1.6 \times 10^{-3}$ $''$ ≈ 0.06 mpc.

- The cooling function: C08 used a three-part piece wise cooling curve that approximates Sutherland & Dopita (1993) for a solar hydrogen abundance with $Z = 3Z_\odot$. We use a larger number of power law segments to approximate the cooling curve appropriate for stellar wind material of WR stars that are largely bereft of hydrogen (also with $Z = 3Z_\odot$). Furthermore, the `SPEX` code that we use to calculate the cooling function includes more lines than the Sutherland & Dopita (1993) calculation (see Schure et al. 2009), which enhances the peak of the curve at $\sim 10^5$ K. These differences, however, have a relatively small effect on the cooling curves, which are plotted in Figure 4.1. Except at the very highest ($T \gtrsim 10^9$ K) and lowest ($T \lesssim 3 \times 10^4$ K) temperatures, the cooling curves are within a factor of 2 of each other.

C08 focused on the effect of the different stellar orbital distributions on the accretion history and X-ray luminosity, while this work is primarily focused on modeling the structure of the innermost accretion flow at the present day. Thus much of the information presented here is not in C08 for comparison and vice-versa. We can, however, compare the mass accretion rate history and the radial profile of the angular momentum to C08, while noting that the radial profiles of density, temperature, and radial velocity of the C08 simulation are presented in a later work by the same group (Cuadra et al. 2015, C15) where it is labeled as the “control run.”

The level of variability seen in the accretion rate history is comparable in both simulations, with the average accretion rate in C08 being a factor of ~3-4 times higher as expected from the larger inner boundary radius used in their simulation. Also similar is the level of variability seen in the angular momentum vector as a function of time, which is primarily determined by the time-evolving configuration of the stellar winds. At the present day, however, our angular momentum vectors are in two different directions, forming an angle of $\sim 50°$ with each other. This is not necessarily surprising due to the high level of temporal variability in this vector (Figure 4.10) and the stochastic nature of the inner accretion flow. C08 also found that the stellar winds of only 3 stars contributed significantly to the accretion near the inner boundary which is consistent with the model we propose in Appendix 4.A to explain the $\dot{M} \propto \sqrt{r_{in}}$ dependence we find in our simulation.

While the accretion and angular momentum histories are broadly similar in the two simulations, there are striking differences seen in the radial profiles of fluid quantities, particularly in the inner region of the flow. These include:

- Temperature: we find $T \propto\approx r^{-1}$ with $T \approx 2 \times 10^8$ K at $0.1''$ (4 mpc) while C08 found $T \propto\approx r^{-0.4}$ with $T \approx 4\times10^7$ K at $0.1''$ (4 mpc), almost an order of magnitude lower. Note that part of the difference in magnitude is caused by our assumption that $X = 0$, corresponding to a larger mean molecular weight than that used by C08..

- Radial velocity: the radial Mach number of our simulation is $\approx 7 \times 10^{-2}$ ($v_r \approx 2 \times 10^8$ cm/s) at $0.1''$ (4 mpc), while in C08 at the same radius the radial flow is supersonic at ($v_r \gtrsim 10^8$ cm/s).
- Density: our density profile is much steeper, $\rho \propto\approx r^{-1}$, compared to C08, $\rho \propto\approx r^{-0.5}$.
- Angular momentum: we find $l \approx 0.5 l_{kep} \propto \sqrt{r}$, while C08 found $l \approx l_{kep}(0.05'' \approx 2 \text{ mpc}) =$ const.

What causes such large differences between the two simulations? We can only speculate. By varying the cooling function, we have found that our results are not strongly dependent on the particular choice of Λ, so it is not likely that this is the source of disagreement. On the other hand, we have found that the inner boundary condition can cause artificial effects out to $\sim$ a few r_{in}, namely, reducing pressure support and increasing radial velocity, so at $0.1''$ (4 mpc) C08's results may still be affected by their boundary at $0.05''$ (2 mpc). Also, as evidenced by their Figure 8, around $0.1''$ (4 mpc) they have only a handful of particles in their simulation meaning that the inner region of their simulation may be under-resolved.

We note that Cuadra et al. (2015) followed up on the work of C08 by including subgrid models to account for feedback from the black hole. Their models are motivated by the fact that, in reality,most of the material accreting at the radius corresponding to the inner boundary of their simulations may ultimately be ejected in an outflow. Indeed, our simulations that probe smaller radii generally support this expectation, though we find that the outflow proceeds in a direction *perpendicular* to the angular momentum axis (that is, in the orbital plane) of the gas, as opposed to their "instantaneous" feedback models that eject material either isotropically, in some fixed opening angle, or parallel to the angular momentum axis. With feedback, none of their models significantly improve the agreement between the flow properties in our simulations. Though the radial velocity and accretion rate are lower with feedback, their density and temperature profiles still have different scalings with radius than those seen in our simulations. In the same work, Cuadra et al. (2015) also present an "outburst" model where a large amount of mass is injected through the inner boundary over a 300 yr period some time in the past. Again, this model does not bring our simulations into any closer agreement, and, in fact, the density profile post-outburst is even flatter than their "control" run with no feedback.

4.9 Conclusions

We have presented the results of 3D hydrodynamic simulations that track the accretion of stellar winds in the galactic center from the stars at distances of $\sim$ 0.1 pc all the way down to $\sim$300 gravitational radii of Sgr A*, roughly 32 times further in than in previous work. These are also the first grid-based finite volume simulations of the fueling of Sgr A*. Our simulations include radiative cooling in collisional ionization equilibrium, and adopted the observationally constrained stellar orbits, mass loss rates, and wind speeds of the 30 WR stars that dominate the accretion budget. We find reasonable agreement between our predicted diffuse X-ray luminosity and *Chandra* X-ray observations (Figure 4.19). This demonstrates that the mass-loss rates and wind speeds from Martins et al. (2007) must be of order the true values (probably within a factor of 2). Our goal in this work is to detail the flow properties at the innermost radii in order to better motivate initial and boundary conditions for GRMHD simulations of Sgr A*. These will be used to interpret not only EHT and GRAVITY observations, but also the wealth of observational data that exists across the electromagnetic spectrum.

We find that the gas at small radii (well inside the orbits of the mass-losing stars, i.e., $r \lesssim 0.01$ pc) develops a 2-component structure. Most of the mass is moderately unbound in an equatorial rotation supported disc while most of the accretion proceeds by bound material along the poles via the low angular momentum tail of the stellar winds. Only a small fraction ($\lesssim 0.1\%$) of the stellar wind material is captured by the black hole, leading to a hot, pressure-supported, sub-Keplerian 'disc' of gas at small radii that is at most times (though not always) aligned with the clockwise stellar disc (Figure 4.10). The accretion rate at small radii is much less than the Bondi rate due to the finite angular momentum of the stellar wind material (Figure 4.12). While radiative cooling can be significant in the vicinity of the stellar winds, it has a negligible effect at smaller radii and thus cannot remove pressure support. Due to the pressure support and broad angular momentum distribution, there is only a mild contrast in density between the polar regions and the midplane (a factor of ~ a few), much more akin to spherical accretion than even very geometrically thick RIAF models (see Figure 4.15 and 4.17).

Accretion in our simulations is dominated by bound, low angular momentum material that flows in from the southern pole, feeding both accretion and outflow that is primarily directed along the midplane and northern pole (Figure 4.15). This structure is due to both the asymmetry of the distribution of non-disc stars about the midplane of the stellar disc at $t = 0$ (Figure 4.5) and also to the gas possessing a wide range of angular momentum, as expected when the stellar winds of only a few stars contribute to accretion and their wind speeds are comparable to their orbital velocities. Further evidence for this picture is that the accretion rate through the inner boundary scales as $\propto \sqrt{r_{in}}$, which is identical to the distribution of mass-loss rate vs. circularization radius produced by the wind of a single star (Appendix 4.A). Using this scaling relation to extrapolate down to the horizon of Sgr A* we find an accretion rate of $\approx 3.4 \times 10^{-8} M_{\odot}$/yr for a non-spinning black hole (Figure 4.17), consistent with observational limits on the horizon-scale accretion rate (Marrone et al. 2007; Shcherbakov & Baganoff 2010; Ressler et al. 2017).

We find that our results are not altered by including the star S2 as an additional wind source, despite its proximity to Sgr A* (Figure 4.18). This is because its mass-loss rate is ~ 3 orders of magnitude lower than most of the other stars in our simulation, so its effect on the time-averaged flow is negligible. Since S2 is the brightest of the 'S-stars' (Gillessen et al. 2017) and thus likely has the strongest wind of the S-stars, this result confirms that the $\lesssim 100$ other S-stars can safely be neglected in calculations of accretion in the galactic center.

The flow structure at the innermost radii that we have outlined here could have a significant impact on GRMHD simulations of accretion onto Sgr A* and their predicted observational properties. Polar inflow might directly oppose jet formation, while the outflow/inflow structure might be less susceptible to the build up of MRI turbulence if the inflow/outflow times are short compared to the MRI growth time. On the other hand, it is possible that the opposite will occur if an outflow from small radii disrupts the polar inflow we find in our simulations. Directly incorporating the flow properties found here as initial and boundary conditions in future horizon scale simulations will be a primary focus of future work.

A key possible limitation of our simulation is the neglect of magnetic fields, which can be a significant source of angular momentum transport in accretion discs and might alter the picture presented here. Magnetic fields might be important both by generating magnetic braking of the inflow and/or via the MRI. Furthermore, anisotropic conduction and viscosity along field lines may significantly alter the dynamics of the flow and suppress the accretion rate (e.g., Johnson & Quataert 2007; Shcherbakov & Baganoff 2010). MHD simulations of the problem studied here with and without conduction/viscosity will be carried out in the near future.

This is a particularly exciting time to be studying the galactic center, in which both observations and theory are rapidly pushing the boundary of what is feasible. In the not too distant future, as computational resources continue to improve, we may be able to simulate the entire dynamical range of accretion from the parsec scale of the WR stars all the way down to the event horizon of Sgr A*, even while including some of the non-ideal, collisionless physics important in this hot, low density plasma. Moreover, as the EHT and GRAVITY continue to take data, we will be able to compare directly to spatially resolved observations of the event horizon while self-consistently making predictions about the X-ray, infrared, and radio data at larger radii. Such a wealth of information combined with the computational and theoretical horsepower already being put in place will bring us that much closer to solving many of the outstanding questions related to the emission from the galactic center and inform our knowledge of low-luminosity AGN more generally.

Acknowledgments

We thank the anonymous referee for several helpful comments. We thank C. Gammie, J. Cuadra, J. R. Lu, R. Genzel, S. Gillessen, and K. El-Badry for useful discussions, as well as all the members of the horizon collaboration, http://horizon.astro.illinois.edu, for their advice and encouragement. We thank F. Baganoff for making the *Chandra* X-ray data available to us for use in comparison to our simulations. We thank D. Fielding for advice and help on plotting formats and give a double portion of thanks to C. J. White for his frequent aid in using the `Athena++` code. Finally, we thank N. M. Lemaster and P. F. Hopkins for freely providing the preliminary coding framework that we built upon to calculate the stellar wind source terms. This work was supported in part by NSF grants AST 13-33612, AST 1715054, AST-1715277, *Chandra* theory grant TM7-18006X from the Smithsonian Institution, a Simons Investigator award from the Simons Foundation, and by the NSF through an XSEDE computational time allocation TG-AST090038 on SDSC Comet. SMR is supported in part by the NASA Earth and Space Science Fellowship. This work was made possible by computing time granted by UCB on the Savio cluster.

Appendix

4.A Angular Momentum Distribution of a Single Accreting Star

In this Appendix we briefly describe a toy model of a single accreting star that can be used to qualitatively explain the scalings of $\dot{M}_{in}$ and ρ observed in our simulation.

Consider the case of a single wind-emitting star in a circular orbit around the black hole at a distance of r_{orbit}. Let the coordinate system be aligned such that the z-direction is aligned with the angular momentum of the orbit and consider the time at which the star is located at $(x, y) = (r_{orbit}, 0)$. By construction, the y-component of the specific angular momentum of the emitted gas is thus 0. We define a spherical polar coordinate system (r, θ, ϕ) centered on the star so that $\theta = 0$ corresponds to the y-direction, or equivalently the direction of the orbital velocity vector. For a given θ, assuming that pressure effects are negligible, stellar wind material that is emitted at some ϕ_0, with x-component of the angular momentum $l_x = \sin(\phi_0)\sin(\theta)v_{orbit}r_{orbit}$, will travel around the black hole and eventually collide with the material emitted at $-\phi_0$, with $l_x = -\sin(\phi_0)\sin(\theta)v_{orbit}r_{orbit}$. This collision results in a shock that converts the angular momentum in the x direction to internal energy. On the other hand, the z-component of the specific angular momentum of the stellar wind material can be written as

$$l_z = (v_{orbit} + \cos(\theta)v_{wind})\, r_{orbit}, \tag{4.10}$$

which is bounded by $l_{min} = (v_{orbit} - v_{wind})r_{orbit}$ and $l_{max} = (v_{orbit} + v_{wind})r_{orbit}$.

If we define the "distribution function," $f_x(x)$, of the mass ejected from the star per unit time with respect to some variable x as

$$\dot{M}_{wind} = \int_{x_{min}}^{x_{max}} f_x(x)dx, \tag{4.11}$$

then, using the relation $dl_z = -v_{wind}r_{orbit}\sin(\theta)d\theta$, we have:

$$f_{l_z}(l_z) = \frac{1}{2}\frac{\dot{M}_{wind}}{v_{wind}r_{orbit}} = \text{const.}, \tag{4.12}$$

with the limits $l_{min} < l_z < l_{max}$. This implies that the rate at which material with specific angular momentum l_z is emitted from the star is proportional to l_z. For the case of $v_{wind} > v_{orbit}$, some material will have $l_z < 0$ and will ultimately collide with an equal amount of material containing $-l_z$. Therefore, we define a "net" distribution function as

$$f_{l_{z,net}}(l_{z,net}) = \begin{cases} \frac{1}{2}\frac{\dot{M}_{wind}}{v_{wind} r_{orbit}} & |l_{min}| \leq l_{z,net} \leq l_{max} \\ \delta(l_{z,net}) \frac{1}{2}\frac{\dot{M}_{wind}}{v_{wind} r_{orbit}} (|l_{min}| - l_{min}) & \text{else,} \end{cases} \tag{4.13}$$

where $\delta(l_{z,net})$ is the Dirac-delta function. Equation (4.13) has three interesting extremes. First, when $v_{wind} \ll v_{orbit}$, the stellar wind material has angular momentum predominately equal to the orbital angular momentum of the star with very little scatter. This would result in the formation of a ring of material co-rotating with the star and almost no accretion. Second, when $v_{wind} \gg v_{orbit}$, the net z-component of the angular momentum is essentially 0, and Bondi-Hoyle-Lyttleton (Hoyle & Lyttleton 1939; Bondi & Hoyle 1944) type accretion is expected, with an accretion rate onto the black hole $\propto (v_{orbit}/v_{wind})^2 \dot{M}_{wind}$. Finally, the case of interest for this work is when $v_{wind} \sim v_{orbit}$, which results in an extended distribution of angular momentum with $0 < l_z < 2l_{orbit}$ (where we have dropped the "net" subscript because l_z is everywhere > 0). This wide range of angular momenta directly corresponds to a wide range in circularization radii, $r_{circ} = l_z^2/(GM_{BH})$, with distribution function

$$f_r(r_{circ}) = \frac{1}{4}\frac{v_{orbit}}{v_{wind}}\frac{\dot{M}_{wind}}{r_{orbit}}\sqrt{\frac{r_{orbit}}{r_{circ}}}, \tag{4.14}$$

over the range $0 < r < 4r_{orbit}$. If we assume that material can only accrete until it reaches $r = r_{circ}$, at which point it either settles into a disc or is converted into outflow, then we expect $\dot{M}_{in} \propto \sqrt{r}$. Finally, if the radial velocity of the in-falling matter is essentially free-fall, $v_r \propto r^{-1/2}$, we obtain a power law scaling for the mass density: $\rho \propto r^{-1}$.

Even when the stellar winds of multiple stars are contributing to the accretion flow, this picture should give a reasonable qualitative understanding as long as the stars are sufficiently isolated from one another. That is, for a given pair of stars, as long as the time for the two winds to collide is longer than the shortest free fall time, then the winds will not have a chance to shock and alter the angular momentum profile before plunging to smaller radii.

The true problem is, of course, more complicated, as, for example, the majority of the orbits are eccentric and pressure effects are non-negligible. However, this simple picture provides an intuitive understanding of our simulation results with a physical justification for the mass density and accretion rate scalings, directly relating them to the angular momentum distribution of a single star and the small number of accreting stars.

Chapter 5

Accretion of Magnetized Stellar Winds in the Galactic Centre: Implications for Sgr A* and PSR J1745-2900

An earlier version of this article was previously published as Ressler S. M., Quataert E., and Stone J. M., 2019, MNRAS, 482, L123

5.1 Abstract

The observed rotation measures (RMs) towards the galactic centre magnetar and towards Sagittarius A* provide a strong constraint on MHD models of the galactic centre accretion flow, probing distances from the black hole separated by many orders of magnitude. We show, using 3D simulations of accretion via magnetized stellar winds of the Wolf-Rayet stars orbiting the black hole, that the large, time-variable RM observed for the pulsar PSR J1745-2900 can be explained by magnetized wind-wind shocks of nearby stars in the clockwise stellar disc. In the same simulation, both the total X-ray luminosity integrated over 2-10″, the time variability of the magnetar's dispersion measure, and the RM towards Sagittarius A* are consistent with observations. We argue that (in order for the large RM of the pulsar to not be a priori unlikely) the pulsar should be on an orbit that keeps it near the clockwise disc of stars. We present a 2D RM map of the central 1/2 parsec of the galactic centre that can be used to test our models. Our simulations predict that Sgr A* is typically accreting a significantly ordered magnetic field that ultimately could result in a strongly magnetized flow with flux threading the horizon at $\sim 10\%$ of the magnetically arrested limit.

5.2 Introduction

The two largest rotation measures (RMs) observed in the galaxy are located within the central $\sim$ 0.1 pc of Sagittarius A* (Sgr A*). The largest is towards the radio source Sagittarius A* associated with the $\sim 4.3 \times 10^6$ $M_\odot$ black hole, which was measured in 2005 over a two-month time frame to be $\approx -5.6 \times 10^5$ rad/m^2 (Marrone et al. 2007). This value was roughly constant in time over that short interval and has had the same sign for at least ~ 5 years before then (Bower et al. 2002). The second largest RM is that observed towards the magnetar PSR J1745-2900 (Eatough et al. 2013) with a value of $\approx -6.6 \times 10^4$ rad/m^2. If, as is generally supposed, these large RMs are produced locally to the galactic centre, they offer the most direct probes of the magnetization of the accretion flow, a critical parameter for determining the state of the accreting plasma at Schwarzschild radii scales.

Both analytic modeling (Quataert 2004; Shcherbakov & Baganoff 2010) and three dimensional hydrodynamic simulations (Cuadra et al. 2008; Russell et al. 2017; Ressler et al. 2018), have shown that the winds of the ~ 30 Wolf-Rayet (WR) stars orbiting Sgr A* can account for the amount of hot gas observed by *Chandra* in X-rays at distances $\lesssim 10''$ from the central black hole (Baganoff et al. 2003). This hot gas has been invoked to explain the large RM observed in PSR J1745-2900 and even used as evidence that the galactic centre accretes strongly magnetized plasma (Eatough et al. 2013). If that is indeed the case, the winds of the stars themselves are the most likely source of magnetic field; any ambient field that may have been present would have been blown away by the winds. Unfortunately, though the mass-loss rates and wind speeds of the stars are reasonably well constrained observationally (Martins et al. 2007; Yusef-Zadeh et al. 2015a), nothing is known about the structure or the magnitude of the magnetic field in the winds. However, given that the orbital velocities and 2D positions of the stars are also known (Paumard et al. 2006; Lu et al. 2009; Gillessen et al. 2017), the problem of explaining the RM of Sgr A* and the magnetar is still fairly well posed.

In this chapter, we present the first three dimensional, magneto-hydrodynamic (MHD) simulations of the accretion flow around Sgr A* that include the winds of the WR stars. Our model extends that of Ressler et al. (2018) (Chapter 4 , hereafter R18) to include magnetized stellar winds, allowing for self-consistent modeling of the X-ray emission, the RMs towards PSR J1745-2900 and Sgr A*, and the inner accretion flow onto Sgr A*; we defer a detailed study of the latter to a future paper. §5.3 describes the physical model for the stellar winds employed in our simulation, §5.4 describes a simple toy model of isolated stellar winds useful for interpreting the RM towards the pulsar, §5.5 presents the results of the full 3D simulation of magnetized stellar wind accretion onto Sgr A*, focusing on the two RMs, and §5.6 concludes.

5.3 Magnetized Wind Model

The hydrodynamic stellar wind model described in R18 treats stellar winds as source terms in mass, momentum, and energy that move on fixed Keplerian orbits through the simulation domain. The sources are $r_w \approx 2\sqrt{3}\Delta x$ in radius, where Δx is the local grid spacing evaluated at the centre of the "star." This model was shown to accurately drive a wind possessing the desired mass loss rate, $\dot{M}_w$, and constant radial velocity, v_w, with negligible temperature. In order to make these winds magnetized, in this work we add two additional source terms to our `Athena++` simulations: one in the induction equation and one in the total energy equation.

We expect the magnetic fields of stellar winds at distances $r' \gg$ the Alfvén radius, r_A, the point at which the magnetic energy density of the wind equals its kinetic energy density, to be predominately in the φ' direction, where primes denote the frame of the star with the z'-axis aligned with its rotation axis. This is because flux conservation requires that the radial component of the field, $B_{r'}$, scales as $(r')^{-2}$, while the azimuthal component, $B_{\varphi'}$, scales as $(r')^{-1}$, so that at large radii $B_{\varphi'}$ will ultimately be the dominant component of the field (Weber & Davis 1967).

Here we parameterize the field by the ratio between the wind's ram pressure and magnetic pressure evaluated in the equatorial plane at $r' = r_A$, $\beta_w \equiv 8\pi\rho v_w^2/B_{\varphi'}^2\big|_{\theta'=\pi/2} = 2\dot{M}v_w/(B_A^2 r_A^2) =$ const., where B_A is the magnitude of the magnetic field at $r' = r_A$ and $\theta' = \pi/2$. For $r_A = R_\odot$, $M_w = 10^{-5}$ $M_\odot$/yr, and $v_w = 1000$ km/s, a given β_w corresponds to $B_A \approx 5.1$ kG$/\beta_w^{1/2}$. Though observational estimates of the magnetic fields in the winds of WR stars are sparse, ~ 10% of O-stars have been observed to have surface fields as high as ~ 100G-20kG (e.g. Donati & Landstreet 2009; Wade et al. 2016), so we expect this value of B_A to be reasonable for at least some of the galactic centre stars.

Adding a source term to the induction equation while maintaining $\nabla \cdot \mathbf{B} = 0$ requires precise consistency with the constrained transport algorithm used by `Athena++` to avoid numerical instability. Therefore, instead of adding a source term directly to the magnetic field, for each star we instead add a source term, $\mathbf{E_w}$, to the electric field with a curl only in the φ'-direction:

$$\mathbf{E_w} = -\frac{\pi B_A r_A v_w}{r_w^2}\cos(\theta)\sin\left(\frac{r'}{r_w}\pi\right)\mathbf{r'} \tag{5.1}$$

for $r' < r_w$ and 0 otherwise. This electric field corresponds to a source of magnetic field for $r' < r_w$

$$\nabla \times \mathbf{E_w} = \frac{\pi B_A r_A v_w}{r_w^2}\sin(\theta)\sin\left(\frac{r'}{r_w}\pi\right)\hat{\varphi}', \tag{5.2}$$

and 0 otherwise. The radial dependence of the electric field in Equation (5.1) was chosen to ensure that the field is continuous at the boundary of the source at $r' = r_w$, while the angular dependence was chosen to ensure that hoop stress doesn't diverge at the poles. This source of magnetic field also sources the total energy equation

$$\dot{E}_B = \frac{1}{4\pi}B_{\varphi'}\left(\nabla \times \mathbf{E_w}\right)\cdot\hat{\varphi}', \tag{5.3}$$

again for $r' < r_w$ and 0 otherwise. In each cell, $\dot{E}_B$ is volume-averaged while $\mathbf{E_w}$ is averaged over the appropriate cell edge (see Equations 22-24 of Stone et al. 2008). These source terms, in addition to the point source gravity of the black hole, optically thin radiative cooling due to line and bremsstrahlung emission, and the hydrodynamic wind source terms described in more detail in R18 are added to the conservative MHD equations.

For $\beta_w \gtrsim 5$, this model successfully drives a wind with the desired $\dot{M}_w$, v_w, and β_w while retaining the $\sin(\theta)$ dependence of the magnetic field. For $\beta_w \lesssim 5$, however, magnetic pressure serves to accelerate the wind in the radial direction. Thus, decreasing the parameter β_w beyond ~ 5 does not ultimately end up increasing $B_\varphi^2/(8\pi\rho v^2)\big|_{\theta'=\pi/2}$, which saturates at ~ 0.2. This is not just a limitation of our simple model but a physical limitation on the magnetization of winds at large radii (e.g. Lamers & Cassinelli 1999). Though a more sophisticated treatment of the angular dependence of $B_{\varphi'}$ might result in a slightly different saturation value, in general we expect $\beta_w \gtrsim 1$. Therefore, in what follows we consider only $\beta_w \geq 1$ in our analytic calculations and $\beta_w \geq 10$ in our simulations.

5.4 Analytic Model For The RM of PSR J1745-2900

Assuming a standard spherically symmetric wind with a toroidal magnetic field parameterized by β_w as in §2, the RM for a single stellar wind is given by

$$\begin{aligned} \mathrm{RM}_* \approx & \frac{15000 \text{ rad m}^{-2}}{\beta_w^{1/2}} \left(\frac{\dot{M}_w}{10^{-5} M_\odot/\mathrm{yr}}\right)^{3/2} \left(\frac{s}{10^{-2} \text{ pc}}\right)^{-2} \left(\frac{v_w}{10^3 \text{ km/s}}\right)^{-1/2} \\ & \times \int_{-\infty}^{z_p} \frac{s^2 \sin(\theta')\hat{\varphi}' \cdot \hat{z}}{(s^2+z^2)^{3/2}} dz, \end{aligned} \tag{5.4}$$

where the positive z-direction points away from Earth, while z_p and s are, respectively, the z-coordinate of and the projected distance to the pulsar. Since the dimensionless integral in Equation (5.4) can take on any value between $\pm\,\pi/2$,, we have

$$|\mathrm{RM}_*| \lesssim \frac{23000 \text{ rad m}^{-2}}{\beta_w^{1/2}} \left(\frac{\dot{M}_w}{10^{-5} M_\odot/\mathrm{yr}}\right)^{3/2} \left(\frac{s}{10^{-2} \text{ pc}}\right)^{-2} \left(\frac{v_w}{10^3 \text{ km/s}}\right)^{-1/2}. \tag{5.5}$$

Equation (5.4) shows that the RM for a given star is a rapidly decreasing function of projected distance, $\mathrm{RM}_* \mathrel{\tilde{\propto}} s^{-2}$, so that only the stars closest to the line of sight (LOS) will significantly contribute. Furthermore, it shows that in order for RM_* to be on the order of the observed -6.6×10^4 rad/m^2, there needs to be a star located $\lesssim 10^{-2}$ pc in projected distance from the pulsar assuming values typical of WR stars for $\dot{M}_w$ and v_w. The closest WR star (E32 aka 16SE1), however, has $s \sim 2.5 \times 10^{-2}$ pc and even with optimistic assumptions for other parameters would require a very large mass loss rate, $\dot{M}_w \approx 7 \times 10^{-5} M_\odot$/yr to reach $|\mathrm{RM}|_* \sim 6.6 \times 10^4$ rad/m^2.

Therefore, we conclude that it is unlikely that isolated stellar winds can produce a RM as large as that observed for the galactic centre magnetar. However, the RM near a star can be enhanced by a factor as much as ~ 16 or more by the presence of shocks with other winds or with the ambient medium. In fact, there are two other stars in the near vicinity of E32, namely, E23 (aka 16SW), and E40 (aka 16SE2), both located within ~ 0.01 pc in projected distance from E32. Since all three are disc stars, they are also clustered in 3D positions. As we now show, shocks between these stars are then expected and will affect the RM of the pulsar.

5.5 3D MHD Simulations

5.5.1 Parameter Choices and Computational Grid

The "stars" in our simulation are on fixed Keplerian orbits using the same prescription described in R18, where the z-coordinate of a star in the year $\sim$ 2005, z_*, is taken from Paumard et al. (2006) for stars within the stellar disc, while z_* for a non-disc star is set so as to minimize the eccentricity of its orbit. We use the mass loss rates and wind speeds of Cuadra et al. (2008) for all of the stars except for E23, E32, and E40, which we allow to vary within a range of uncertainty while fixing $\beta_w = 10$.

We ran a suite of simulations with different random choices for the spin axis directions of the stars and the mass loss rates and wind speeds of E23, E32, and E40. Here we present only one of these simulations, hereafter referred to as "the fiducial model;" out of the 7 random variations in wind properties we tried, this was the simulation that best reproduced the observed RM of the pulsar. We emphasize that this model is not unique and that our purpose is not to do a full parameter survey but to show that a reasonable choice of wind parameters can indeed reproduce the observed pulsar RM. Furthermore, some of our results depend on the choice of β_w, with the RM of the pulsar roughly scaling as $\sim \beta_w^{-1/2}$, while RM of Sgr A* and the net flux threading the inner boundary are only weakly dependent on β_w, perhaps because of magnetic field amplification at small radii. In a future paper we will explore other models.

The parameters of the three stellar winds closest to the magnetar (which sets its RM in our calculations) for this fiducial model are shown in Table 5.1, where we have denoted the spin axes of the stars (which determine the direction of the magnetic fields in the winds) as $\mathbf{n} = (n_x, n_y, n_z)$, defined in the same coordinate system as Paumard et al. (2006). Though the spin axes for the remaining stars are just as important for determining the RM of Sgr A*, there is not as direct a relationship between their values and the resulting RM compared to the case of the pulsar. The values of $\dot{M}_w$ and v_w shown in Table 5.1 are all within reasonable systematic observational uncertainties and do not significantly alter the total X-ray luminosity found in R18 that agrees well with *Chandra* observations, nor do they add any local X-ray excess that would have previously been observed near the pulsar.

Our computational grid is a 1 pc^3 box in Cartesian coordinates, with a base resolution of 128^3 in addition to 8 levels of nested static mesh refinement, emulating a grid with logarithmically spacing in radius. A region with radius of $\approx$ twice the smallest grid spacing at the centre of the grid, $r_{in} \approx 1.2 \times 10^{-4}$ pc is set to floors in density and pressure with zero velocity. The magnetic field is allowed to freely evolve in this region. In addition to the the floors and ceilings on density, temperature, pressure, and velocity described in R18, we add a density floor such that $B^2/(4\pi\rho) \leq \sqrt{2GM_{BH}/r_{in}}$, where $M_{BH} \approx 4.3 \times 10^6 M_\odot$ is the mass of Sgr A*. This condition is only activated at the innermost radii in magnetically dominated polar regions. As in R18, we run the simulation for 1.1 kyr up to what we refer to as the present day, $t = 0$, defined as January 1, 2017.

Table 5.1: Mass Loss Rates, Winds Speeds, and Spin Axes of the Three Stars Closest to PSR J1745-2900

Name	Alt. Name	$\dot{M}_w$	v_w	n_x	n_y	n_z
E23	16SW	0.8×10^{-5}	440	0.06	-0.70	0.71
E32	16SE1	2.7×10^{-5}	435	-0.08	-0.88	0.47
E40	16SE2	6.3×10^{-5}	1220	-0.22	0.95	-0.23

Notes– $\dot{M}_w$ is measured in $M_\odot$/yr and v_w is measured in km/s. Names are from Paumard et al. (2006).

5.5.2 Rotation Measure of PSR J1745-2900

The top panel of Figure 5.1 shows the RM as a function of time at the $t = 0$ location of the pulsar calculated from our fiducial simulation as z_p, the LOS position of the pulsar, $\rightarrow \infty$. Since neither the location nor velocity of the pulsar along the LOS is known, we fix its position to show how the RM varies at its current location. The bottom panel of Figure 5.1 shows how z_p affects the RM and its gradient in time. In this fiducial model, we find that we can roughly match the observed value of the pulsar RM and its gradient, if it is located within or behind the stellar disc. Although our predicted dispersion measure (DM) for the pulsar is of order $\sim$ 50 pc/cm^3, $\ll$ the observed value of $\sim$ 1700 pc/cm^3 (as expected for a DM dominated by a screen far from the pulsar), its gradient in time can be large enough ($\sim$ 2.5 pc/cm^3/yr) to plausibly account for the $\sim$ 0.06% change observed over a four year period (Desvignes et al. 2018).

Also shown in the top panel of Figure 5.1 is the RM for the pulsar calculated from the analytic isolated wind model as $z_p \rightarrow \infty$ (Equation 5.4 summed over all the stars), which neglects the effects of wind-wind interaction. Certain peaks in the RM (e.g., those at $\sim$ -0.5 kyr and $\sim$ -0.2 kyr) are well reproduced by the analytic model while others are seen only in the simulation (e.g., those at $\sim$ -0.7 kyr and the present day). The latter are caused by strong shocks between nearby winds, while the former are caused by winds located far from other stars. At the present day the RM is dominated by a radiative, magnetic pressure dominated shock between the winds of E32 and E40, with a post-shock region characterized by $|B_z| \approx 10$ mG, $n_e \approx 3000$ cm^{-3}, $T \approx 10^4$ K, and a LOS width of 0.01 pc. This shock is clearly seen in the 2D map of RM (Figure 5.2). We note that radiative cooling is not required for a large RM, which we have confirmed with a simulation that neglects cooling yet still has a comparable RM at the pulsar's LOS and across the domain.

Both Figure 5.1 and 5.2 show that the large RM at the $t = 0$ LOS of the pulsar is somewhat rare in both space and time. The typical value is closer to $\sim 1 \times 10^4$ rad/m^2. This is true for all of the variants we simulated (fixing $\beta_w \sim 10 - 100$; for $\beta_w \gg 100$ we found no simulation with a large enough RM) and suggests that the current high value of the observed RM is the result of a chance alignment of the pulsar with the region associated with three disc stars in close proximity. This result is not strongly affected by the $\sim$ 30-60% uncertainties on the $t = 0$ z-coordinates of these stars since the separations between them are predominantly perpendicular to the LOS. Bower et al. (2015b) found that the proper motion of the magnetar is consistent with an orbit in the clockwise stellar disc. Such an orbit might put the pulsar into more frequent alignment with closely interacting stellar winds and enhance the likelihood of observing a RM with the observed magnitude.

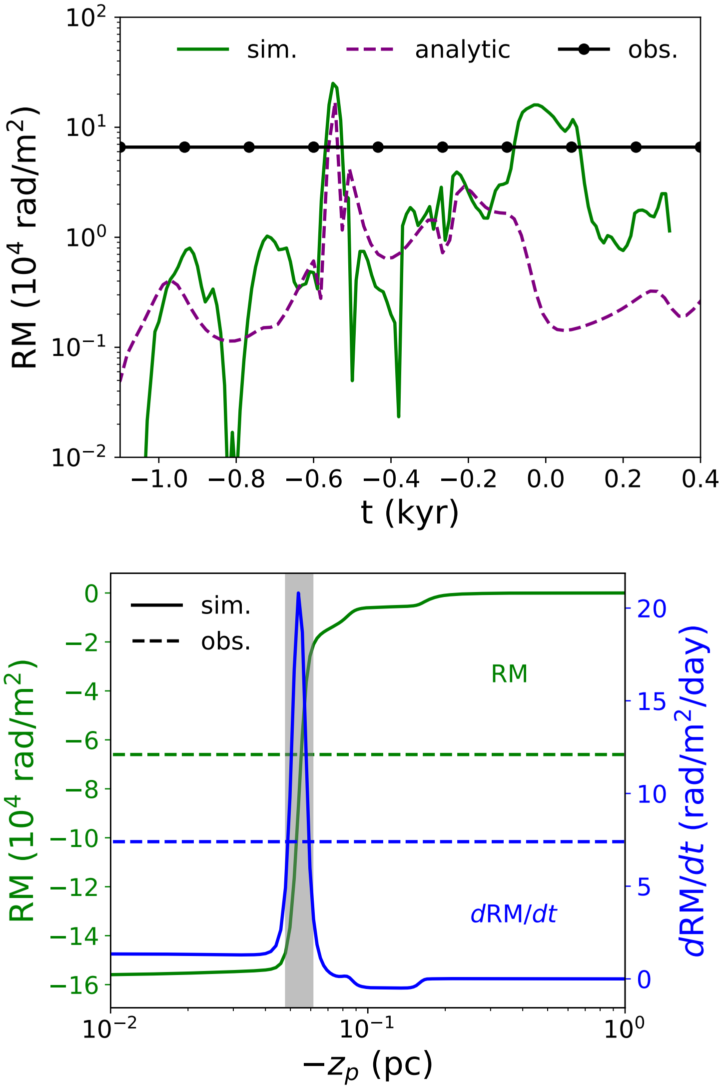

Figure 5.1: Top: Absolute value of the RM as a function of time at the pulsar's present day LOS calculated from our fiducial simulation (§5.5) compared to our analytic, isolated stellar wind model (§5.4). Also plotted is the present day magnitude of the pulsar's RM, $\approx 6.6\times10^4$ rad/m^2. Bottom: RM (solid green) and the time rate of change of the RM (solid blue) at $t = 0$ as a function of the z-coordinate of the pulsar, z_p, compared the observed RM (dashed green) and time variability (dashed blue, Desvignes et al. 2018). The shaded gray area represents the region in between the two disc stars, E32 and E40, where the two winds are shocking and enhancing the RM.

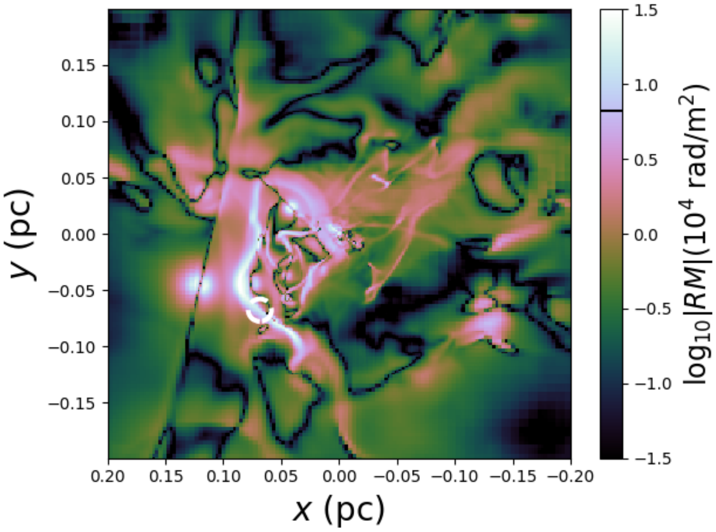

Figure 5.2: Absolute value of the RM calculated from infinity as a function of location in the plane of the sky for the galactic centre. The white circle represents the present day location of the magnetar, while the black line on the colorbar indicates the observed value of its RM. The origin is Sgr A*. Due to a shock between the winds of the stars E32 and E40 (aka 16SE1 and 16SE2), our fiducial model produces a RM large enough to explain the observed value at the pulsar's location. Such a large RM, however, is not ubiquitous to the central ~ 0.1 pc but occurs in only in a small portion of the domain, requiring a fortuitous alignment of the pulsar with either a wind or a shock. The probability of this occurring could be enhanced if the pulsar is on an orbit within or nearly within the clockwise stellar disc. Other pulsars detected in the future would likely have lower RMs.

5.5.3 Rotation Measure of Sgr A*

The top panel of Figure 5.3 shows the RM of Sgr A* as a function of time over a 700 year period. In contrast to the pulsar's RM, which at the present day can be directly traced to the parameters of only $\sim$ 3 of the winds, the precise behavior of the RM of Sgr A* near $t = 0$ is a complicated function of the spin axes, mass loss rates, and wind speeds of all 30 of the stellar winds. This is due to the fact that the RM of Sgr A* is set by the accreting material at the innermost region of our simulations at $r_{in} \approx 1.2 \times 10^{-4}$ pc, potentially a combination of gas from multiple winds. Because of this, we focus our analysis on the general statistical behavior of the RM of Sgr A* instead of its specific behavior at $t = 0$.

The RM in Figure 5.3 is a reasonable estimate even though our inner boundary does not extend all the way to the horizon. We expect the largest contribution to the RM to be set by the radius at which the electrons become relativistically hot, which is only slightly inside the inner boundary of our simulation. For the non-relativistic RM, $d(\mathrm{RM})/d\log(r) \propto r n_e B_{\parallel} \propto r^{-1}$, where we have used the radial dependencies of $n_e \propto r^{-1}$ and $|\mathbf{B}| \propto r^{-1}$ observed in our simulation. We have confirmed that this radial dependence of the RM is valid by running simulations with larger inner boundary radius. Once $k_b T_e \sim m_e c^2$, however, the RM becomes suppressed by factors of Θ_e^{-2}, where $\Theta_e \equiv k_b T_e/(m_e c^2)$. At the innermost boundary of our simulation, $\langle\Theta_e\rangle \approx 0.9$, and thus we would expect the RM to be set by the plasma properties at $r \sim 10^{-4}$ pc (i.e. $\approx$1.2 r_{in}). The magnitude of this RM is comparable for simulations with $\beta_w = 10$ and those with $\beta_w = 1000$, and is thus only weakly dependent on the magnetization of the stars.

A striking feature of the RM towards Sgr A* shown in Figure 5.3 is the timescale for sign changes, ranging from $\sim$ 3-100 years, much longer than the timescale of a few days for small amplitude fluctuations. Since the RM is dominated by scales $\sim r_{in} \approx 1.2 \times 10^{-4}$ pc, this means that the magnetic field is coherent in sign over $\sim 500 - 10{,}000$ Keplerian orbits and thus this sign is set by the dynamics at larger radii. We have confirmed this hypothesis by running simulations with different values of r_{in}, finding that although the magnitude of the RM scales as r_{in}^{-1}, the timescale for it to flip sign is roughly independent of r_{in}. Furthermore, this $\sim$ 3-100 year time scale is a robust result in simulations with a range of different wind parameters. We conclude that this is a generic prediction of our model due to the fact that the magnetic field is sourced by stellar winds at large radii. We expect that continual monitoring of the RM of Sgr A* over $\sim$ 10s of years would reveal a similar level of variability as seen in Figure 5.3 and, eventually, a sign change. Our simulations can plausibly explain the factor of $\sim$ 2 variability seen by ALMA over $\sim$ months between epochs in Bower et al. (2018) though not the much more rapid variability seen over $\sim$ hours within epochs. No sign reversal was yet seen.

Finally, we note that our simulations display a highly ordered magnetic field in the inner accretion flow with $|\langle\mathbf{B}\rangle|/\sqrt{\langle\mathbf{B}^2\rangle} \approx 0.3 - 0.4$, where $\langle\rangle$ denotes an average over all angles and radius for $r \lesssim 0.03$ pc. As shown in the bottom panel of Figure 5.3, this ordered field corresponds to a net

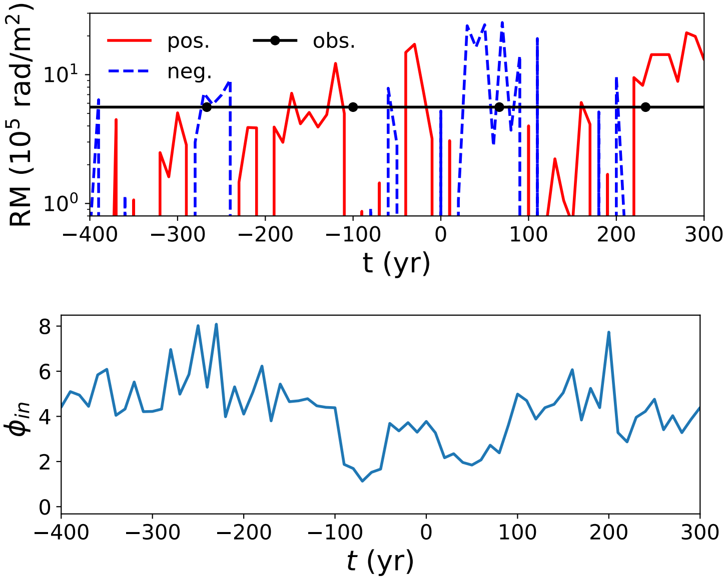

Figure 5.3: Top: RM as a function of time for Sgr A* in our fiducial 3D MHD simulation. Solid red lines are positive RMs, while blue dashed lines are negative RMs. Also plotted is the observed $t = 0$ magnitude of the RM, $\approx 5.6 \times 10^5$ rad/m^2. The RM of our simulation is typically of order the observed value and can remain the same sign for intervals as short as a few years or as long as $\sim$ 100 years. Though the RM and its smaller amplitude variability are set by the innermost region of the simulation ($r \sim 10^{-4}$ pc where the dynamical time is $\sim$ 3.5 days), the timescale for the RM to change sign is set by the dynamical time at much larger radii. Bottom: Dimensionless flux threading the inner boundary, ϕ_{in}, as a function of time (Equation 5.6). This ordered field leads to a strongly magnetized accretion flow, $\phi_{in} \sim 2 - 6$, where $\phi_{in} \sim 50$ roughly corresponds to the MAD limit.

magnetic flux threading one hemisphere of the inner boundary of

$$\phi_{in} \equiv \left. \frac{1/2 \int |B_r| r^2 d\Omega}{r\sqrt{|\dot{M}| v_{kep}}} \right|_{r=r_{in}} \approx 2 - 6, \tag{5.6}$$

where v_{kep} is the Keplerian velocity. We have found that this value is roughly independent of β_w, the orientation of the spin axes of the stars, and even r_{in}, so by extrapolating our simulations we robustly estimate $\phi_{in} \sim 2 - 6$ at the horizon. Considering that a magnetically arrested state (MAD) of accretion begins when $\phi_{in} \approx 50$ (Tchekhovskoy et al. 2011), this is a fairly significant amount of magnetic flux that could result in the formation of strong jets. As defined, ϕ_{in} is positive definite. The field responsible for this flux in the innermost regions of our simulation, however, reverses direction on roughly the same timescale as the RM in the top panel of Figure 5.3.

5.6 Discussion And Conclusions

We have shown that for a reasonable set of parameters, magnetized, 3D simulations of wind accretion onto Sgr A* reproduce the large RM observed towards the galactic centre magnetar, PSR J1745-2900, and can even account for its relatively large temporal gradient. Additionally, we find that for the same parameters the RM towards Sgr A* in our simulation is provided by an ordered magnetic field at $r \sim 10^{-4}$ pc ($\sim$ 250 Schwarzschild radii) and is roughly consistent with the observed value. Sgr A*'s RM retains its sign for $\sim 3-100$ year periods (depending on the exact simulation parameters), also consistent with polarization measurements. What's more, our predicted X-ray luminosity at scales of $2-10''$ from Sgr A* is consistent with *Chandra* observations, suggesting that the properties of the hot gas are being modeled faithfully.

In our models it is likely that the pulsar itself is within the clockwise stellar disc and that the RM is probing a shocked region between two WR stars in that disc. On the surface, such an explanation for the exceptionally large observed RM would seem like a fortuitous coincidence; regions with such large RMs are fairly rare in space and time at distances from the black hole comparable to that of the pulsar's LOS (Figures 5.1 and 5.2). On the other hand, if, as proposed by Bower et al. (2015b), the pulsar itself is on a bound, clockwise orbit in or near the disc, then proximity to regions of enhanced density and magnetic field would be more common.

Alternative models for the RM of the pulsar cannot be ruled out. Sicheneder & Dexter (2017) show that a chance alignment of the pulsar's LOS with an HII region much closer to Earth can reasonably explain both the observed DM and RM if the region is magnetized. Yusef-Zadeh et al. (2015b) argue that the RM could easily be provided by warm, ionized gas in Sgr A* west. Another possibility is that while the pulsar's RM is local to the galactic centre, it is not local to the inner parsec. This is suggested by the fact that two other pulsars in the galactic centre, J1746âĹŠ2849 and J1746âĹŠ2856, located 10-100 pc away from Sgr A* in projected distance, have RMs that are also fairly large, $\sim 10^4$ rad/m^2 (Schnitzeler et al. 2016).

In summation, we have presented a single numerical model that simultaneously explains the observed diffuse X-ray luminosity towards the galactic centre, the value and variability of the RM of the galactic centre magnetar, and the magnitude and constancy in sign of the RM of Sgr A*. Continual monitoring of the pulsar's motion and acceleration, follow-up observations of the RM of Sgr A*, improved constraints on the mass-loss rates and wind speeds of the stellar winds, and magnetic field strength estimates based on observations of Zeeman splitting of the absorption lines for the three winds closest to the pulsar (i.e. the winds of E23, E32, and E40) will be important for testing the validity of this picture. Our simulations predict a 2D RM map of the inner 0.5 pc of the Galaxy that can be used to test whether the RM is indeed produced local to Sgr A* using future pulsar detections. We also predict that Sgr A* is typically accreting significant magnetic flux (though below the MAD limit), enough to potentially power strong magnetic outflows.

ACKNOWLEDGEMENTS

We thank J. Dexter, C. Law, R. Genzel, F. Yusef-Zadeh, and D. Muñoz for useful discussions, as well as all the members of the horizon collaboration, http://horizon.astro.illinois.edut. We thank the referee for a positive report. This chapter was supported in part by NSF grants AST 13-33612, AST 1715054, AST-1715277, *Chandra* theory grant TM7-18006X from the Smithsonian Institution, a Simons Investigator award from the Simons Foundation, and by the NSF through an XSEDE computational time allocation TG-AST090038 on SDSC Comet. SMR is supported in part by the NASA Earth and Space Science Fellowship. This chapter was made possible by computing time granted by UCB on the Savio cluster.

Chapter 6

The Surprisingly Small Impact of Magnetic Fields On The Inner Accretion Flow of Sagittarius A* Fueled By Stellar Winds

An similar version of this article has been submitted to MNRAS as Ressler S. M., Quataert E., and Stone J. M.

6.1 Abstract

We study the flow structure found in 3D magnetohydrodynamic simulations of accretion onto Sagittarius A* via the magnetized winds of the orbiting Wolf-Rayet stars. These simulations cover over 4 orders of magnitude in radius to reach ≈ 300 gravitational radii, with only one poorly constrained parameter (the magnetic field in the stellar winds). Even for winds with relatively weak magnetic fields (e.g., plasma $\beta \sim 10^6$), flux freezing/compression in the inflowing gas amplifies the field to $\beta \sim$ few well before it reaches the event horizon. Overall, the dynamics, accretion rate, and spherically averaged flow profiles (e.g., density, velocity) in our magnetohydrodynamic simulations are remarkably similar to analogous hydrodynamic simulations. We attribute this to the broad distribution of angular momentum provided by the stellar winds, which sources accretion even absent much angular momentum transport. We find that the magneto-rotational instability is not important because i) of strong magnetic fields that are amplified by flux freezing/compression, and ii) the rapid inflow/outflow times of the gas and inefficient radiative cooling preclude circularization. The primary effect of magnetic fields is that they drive a polar outflow that is absent in hydrodynamics. Even in MHD, the angular momentum of the flow at small radii is typically aligned with the stellar disc of Wolf-Rayet stars. The dynamical state of the accretion flow found in our simulations is unlike the rotationally supported tori used as initial conditions in horizon scale simulations, which could have implications for models being used to interpret Event Horizon Telescope and GRAVITY observations of Sgr A*.

6.2 Introduction

The accretion system immediately surrounding Sagittarius A* (Sgr A*), the supermassive black hole in the center of The Milky Way, offers an unparalleled view of the diverse physical processes at play in galactic nuclei. Compared to other active galactic nuclei, the luminosity of the black hole is strikingly small, only $\sim 10^{-9}$ times the Eddington limit, this places it firmly into the regime of the well-studied Radiatively Inefficient Accretion Flow (RIAF) models. The proximity of the galactic centre allows for the environment immediately surrounding the black hole to be spatially resolved, including $\gtrsim$ 100s of stars in the central nuclear cluster (Paumard et al. 2006; Lu et al. 2009), the hot, X-ray emitting gas at the Bondi radius (Baganoff et al. 2003), and the ionized mini-spirals streaming inwards surrounded by the cold, molecular circumnuclear disc. Direct constraints on the near horizon environment are now possible with the detection of several localized infrared flares orbiting the black hole within $\sim$ 10 gravitational radii ($r_g \equiv GM/c^2$, where M is the mass of the black hole, G is the gravitational constant, and c is the speed of light) by GRAVITY (Gravity Collaboration et al. 2018) and the first resolved mm images by the Event Horizon Telescope (Doeleman et al. 2009; Event Horizon Telescope Collaboration et al. 2019a,b) soon to come. With such a wealth of observational data, Sgr A* can be used as a test-bed of accretion models in a way that no other system can.

It is generally believed that the black hole's gas supply is primarily set by the stellar winds of the $\sim$ 30 Wolf-Rayet (WR) stars orbiting at distances of $\sim$ 0.1–1 pc from Sgr A* (Paumard et al. 2006; Martins et al. 2007; Yusef-Zadeh et al. 2015a). The winds shock with each other to $\sim$ keV temperatures, producing X-rays around the Bondi radius that are well resolved by *Chandra* (Baganoff et al. 2003). However, a spherical Bondi estimate vastly over-predicts the observed Faraday rotation of the linearly polarized radio emission(Quataert & Gruzinov 2000a; Bower et al. 2003; Marrone et al. 2007). Instead, only a small fraction $\lesssim 10^{-3}$ of this gas reaches the horizon. It is this material that produces the X-ray and infrared flares as well as the 230 GHz emission targeted by EHT.

What exactly prevents most of the material at the Bondi radius from accreting is still an open debate. Several viable models have been proposed, including those that appeal to strong outflows (Blandford & Begelman 1999) and those that appeal to convective instabilities that trap gas in circulating eddies (Stone et al. 1999; Quataert & Gruzinov 2000b; Igumenshchev & Narayan 2002; Pen et al. 2003). The range of models corresponds to a dependence of density on radius between the two extremes of $r^{-3/2}$ and $r^{-1/2}$, with the combination of multiple observational estimates at $\sim$ 7 different radii supporting r^{-1} in the inner regions of the flow (Gillessen et al. 2018) with a potential break near the Bondi radius (Wang et al. 2013). Another key consideration is the angular momentum of the gas being fed at large radii. In the absence of magnetic fields or other processes, gas in axisymmetric flows can only accrete if it has a specific angular momentum (roughly) less than the Keplerian value at the event horizon. On the other hand the magnetorotational instability (MRI; Balbus & Hawley 1991a) can amplify an initially weak field causing gas to accrete while also driving strong magnetically dominated outflows in the polar regions.

Most simulations of accretion onto low luminosity AGN operate either explicitly or implicitly on the assumption that the MRI is the primary driver of accretion. For instance, GRMHD simulations used to model the horizon-scale accretion flow in the galactic center almost uniformly start from equilibrium tori seeded with weak magnetic fields that are unstable to the MRI. No low angular momentum gas is initially present. In this picture, understanding the physics of the MRI and how it depends on physical parameters like the net vertical flux in the disc or numerical parameters like resolution is essential for understanding accretion physics.

Sgr A* is unique among AGN in that we can plausibly expect to directly model the accretion of gas from large radii where it is originally sourced by the winds of the Wolf-Rayet stars. Since the hydrodynamic properties of these winds (Martins et al. 2007; Yusef-Zadeh et al. 2015a) as well as the orbits of the star themselves (Paumard et al. 2006; Lu et al. 2009) can be reasonably estimated from observations, the freedom in our modeling is limited mainly to the magnetic properties of the winds, which are less well known. In principle, a simulation covering a large enough dynamical range in radius could self consistently track the gas from the stellar winds as it falls into the black hole, determining the dominant physical processes responsible for accretion and directly connecting the accretion rate, density profile, and outflow properties of the system to the observations at parsec scales.

With this motivation, Cuadra et al. (2005, 2006, 2008) studied wind-fed accretion in the galactic centre with a realistic treatment of stellar winds and Cuadra et al. (2015); Russell et al. (2017) added a “subgrid” model to study how feedback from the black hole affects the X-ray emission. In Ressler et al. (2018) (Chapter 4, RQS18) we built on this key earlier work by treating the winds of the WR stars as source terms of mass, momentum, and energy in hydrodynamic simulations encompassing the radial range spanning from ~ 1 pc to $\sim 5 \times 10^{-5}$ pc ($\sim 300\ r_g$). One key result of RQS18 was that even in hydrodynamic simulations the accretion rate onto the black hole is significant and comparable to previous observational estimates (e.g., Marrone et al. 2007; Shcherbakov & Baganoff 2010; Ressler et al. 2017) due to the presence of low angular momentum gas. This is in part a consequence of a coincidence that the WR stars in the galactic centre have winds speeds comparable to their orbital speeds, so that there is a wide range of angular momentum in the frame of Sgr A*. Another key result was that the higher angular momentum gas that could not accrete did not build up into a steady torus but was continuously being recycled through the inner ~ 0.1 pc via inflows and outflows. Because of this complicated flow structure, it is not clear what effect magnetic fields would have. Would the rotating gas be unstable to the MRI? Would the MRI growth time be short enough compared to the inflow/outflow time in order to significantly effect the flow structure? If so, how is the net accretion rate altered? How significant are large scale magnetic torques in transporting angular momentum? These and more are the questions we address in this chapter.

Ressler et al. (2019) (Chapter 5, RQS19) presented a methodology for modeling the accretion of magnetized stellar winds by introducing additional source terms to account for the azimuthal field in each wind. In that work, we showed that a single simulation of fueling Sgr A* with magnetized winds can satisfy a number of observational constraints, providing a convincing argument that our model is a reasonable representation of the accretion flow in the galactic centre. First, our simulations reproduce the total X-ray luminosity observed by *Chandra* (Baganoff et al. 2003), meaning that we capture at least a majority of the hot, diffuse gas at large radii. Second, our simulations reproduce the r^{-1} density scaling inferred from observations that were taken over a large radial range (Gillessen et al. 2018), implying that we are capturing a majority of the gas at *all* radii and that our inflow/outflow rates have the right radial dependence. Third, our simulations can reproduce the magnitude of the RM of both the magnetar (produced at $r \gtrsim 0.1$ pc, Eatough et al. 2013) and Sgr A* (produced at $r \lesssim 10^{-4}$ pc, Marrone et al. 2007), demonstrating that our calculated magnetic field strengths are reasonable at both small and large scales. Fourth, our simulations can plausibly explain the time variability of the RM of Sgr A* (Bower et al. 2018), the time variability of the magnetar's RM, as well as the time variable part of its dispersion measure (Desvignes et al. 2018). In this chapter, we study the dynamics of this model in more detail, with the primary focus of determining the degree to which magnetic fields alter the flow structure seen in purely hydrodynamic simulations (e.g., Cuadra et al. 2008, RQS18).

This chapter is organized as follows. §6.3 reviews and summarizes the governing equations of the system including the magnetized wind source terms, §6.4 demonstrates in an isolated stellar wind test that our method produces the desired results, §6.5 presents the results of 3D MHD simulations of accretion onto Sgr A*, §6.6.1 compares and contrasts our results with previous work, §6.7 discusses the implications of our work for horizon scale modeling of the galactic centre, and §6.8 concludes.

6.3 Computational Methods

Our simulations use the conservative, grid-based code `Athena++`[1] coupled with the model for magnetized winds outlined in RQS19. This model is an extension of the purely hydrodynamic wind model presented in RQS18 and treats the winds of the WR stars as sources of mass, momentum, energy, and magnetic field that move on fixed Keplerian orbits. The hydrodynamic properties of the winds are parameterised by their mass loss rates, $\dot{M}_w$ and their wind speeds, v_w. The magnetic fields of the winds are purely toroidal as defined with respect to the spin axes of the stars and have magnitudes set by the parameter β_w, defined by the ratio between the ram pressure of the wind and its magnetic pressure at the equator (a ratio that is independent of radius in an ideal stellar wind).

---

[1] `Athena++` is rewrite of the widely used `Athena` code (Stone et al. 2008) in the c++ language. For the latest version of `Athena++`, see https://princetonuniversity.github.io/athena/.

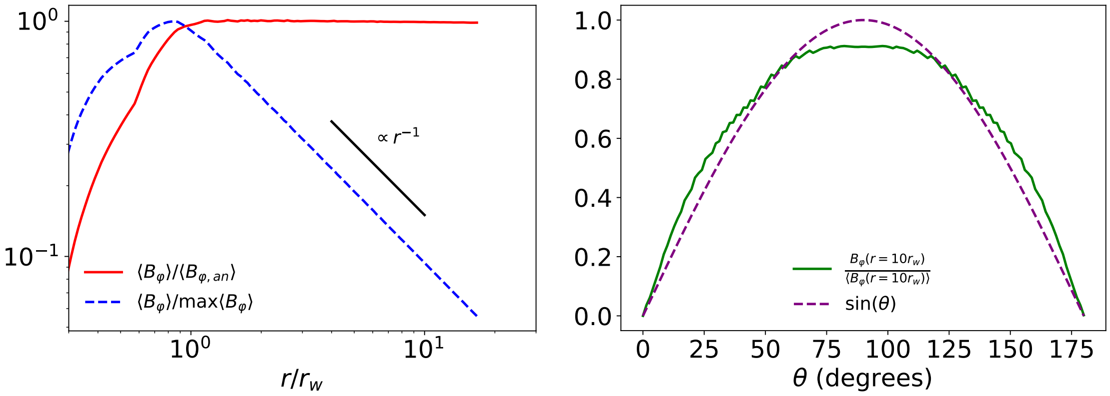

Figure 6.1: Left: Angle averaged azimuthal magnetic field, $\langle B_\varphi \rangle$, normalized to the $r \gtrsim r_w$ analytic expectation for $\beta_w = 10^2$ (solid red) and to its peak value (dashed blue). The agreement with the analytic solution is excellent. Right: θ dependence of B_φ at 10 wind radii (solid green) compared to $\sin(\theta)$ (dashed purple). The magnetic field is slightly more spread out in θ than $\sin(\theta)$ because the imbalanced magnetic pressure tends to push the gas towards the poles. This effect is more extreme for $\beta_w = 10$ (Figure 6.2).

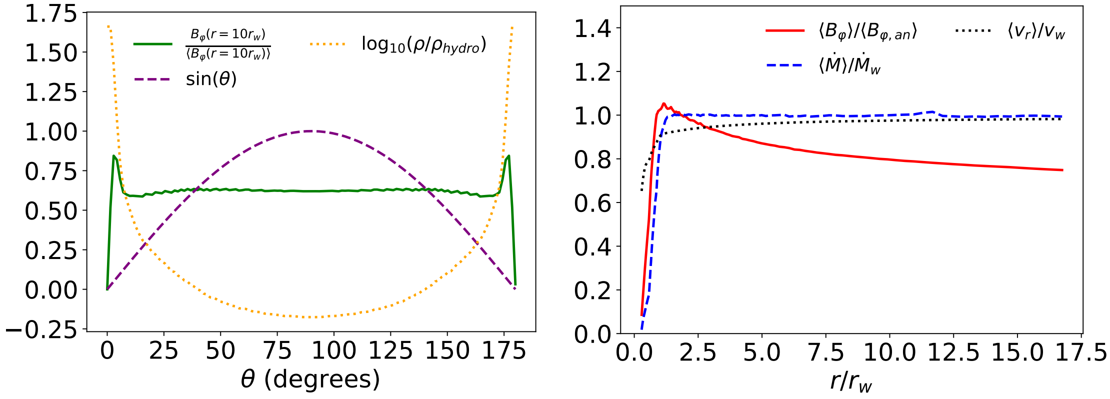

Figure 6.2: Left: θ dependence of the azimuthal magnetic field, B_φ (solid green), and the logarithm of the mass density divided by the purely hydrodynamic solution, $\log_{10}(\rho/\rho_{hydro})$ (dotted orange), both evaluated at 10 wind radii for $\beta_w = 10$ and compared with $\sin(\theta)$ (dashed purple). Right: angle averaged $\langle B_\varphi \rangle$ (solid red), accretion rate normalized to the expected value, $\langle \dot{M} \rangle/\dot{M}_w$ (dashed blue), and radial velocity normalized to the expected value, $\langle v_r \rangle / v_w$ (dotted black). Compared to the $\beta_w = 100$ case in Figure 6.1, the magnetic field is now strong enough to collimate the wind, enhancing the density by almost a factor of 100 at the poles. Despite this, the net accretion rate and wind speed are still consistent with the input parameters. Nonetheless, we focus on $\beta_w \geq 100$ for our simulations to avoid the collimating effect of magnetic fields on the stellar winds.

In brief, the equations solved in our simulations are

$$\begin{aligned}
\frac{\partial \rho}{\partial t} + \nabla \cdot (\rho \mathbf{v}) &= f\dot{\rho}_w \\
\frac{\partial (\rho \mathbf{v})}{\partial t} + \nabla \cdot \left(P_{tot}\mathbf{I} + \rho \mathbf{v}\mathbf{v} - \frac{\mathbf{B}\mathbf{B}}{4\pi} \right) &= -\frac{\rho G M_{BH}}{r^2}\hat{r} \\
&\quad + f\dot{\rho}_w \langle \mathbf{v}_{w,net} \rangle \\
\frac{\partial (E)}{\partial t} + \nabla \cdot \left[(E + P_{tot})\mathbf{v} - \mathbf{v} \cdot \mathbf{B}\mathbf{B} \right] &= -\frac{\rho G M_{BH}}{r}\mathbf{v} \cdot \hat{r} + \langle \dot{E}_B \rangle \\
&\quad + \frac{1}{2} f\dot{\rho}_w \langle |\mathbf{v}_{w,net}|^2 \rangle - Q_- \\
\frac{\partial \mathbf{B}}{\partial t} - \nabla \times (\mathbf{v} \times \mathbf{B}) &= \nabla \times \left(\tilde{E}_w \right),
\end{aligned} \tag{6.1}$$

where ρ is the mass density, $\mathbf{v}$ is the velocity vector, $\mathbf{B}$ is the magnetic field vector, $E = 1/2\rho v^2 + P/(\gamma - 1) + B^2/(8\pi)$ is the total energy, $\gamma = 5/3$ is the non-relativistic adiabatic index of the gas, $P_{tot} = P + B^2/(8\pi)$ is the total pressure including both thermal and magnetic contributions, Q_- is the cooling rate per unit volume due to radiative losses caused by optically thin bremsstrahlung and line cooling (using $Z = 3Z_\odot$ and $X = 0$), f is the fraction of the cell by volume contained in the wind, $\dot{\rho}_w = \dot{M}_w/V_w$, $V_w = 4\pi/3\ r_w^3$, $\mathbf{v}_{w,net}$ is the wind speed in the fixed frame of the grid, $\langle\rangle$ denotes a volume average over the cell, $\dot{E}_B$ is the magnetic energy source term provided by the winds, and $\tilde{E}_w$ is the average of the wind source electric field, $\mathbf{E_w}$, over the appropriate cell edge (see Equations 22-24 of Stone et al. 2008). Each 'wind' has a radius of $r_w \approx 2\sqrt{3}\,\Delta x$, where Δx is the edge length of the cell containing the center of the star.

6.4 Isolated, Magnetized Stellar Wind Test

To test that our implementation of the source terms drives a magnetized wind with the desired properties, we place a stationary wind in the center of a 3D, 1 pc^3 grid and run for 4 wind crossing times. The mass-loss rate of the wind is $\dot{M}_w = 10^{-5}\ M_\odot$/yr, the wind speed is $v_w = 1000$ km/s, and radiative cooling is disabled. We choose $\beta_w = 100$ to ensure that the magnetic field is non-negligible but relatively weak.

The left panel of Figure 6.1 shows that the angle-averaged φ component of the magnetic field matches the analytic expectation, scaling as r^{-1} as determined by flux conservation. The other components of the field are negligible. The right panel of Figure 6.1 shows the dependence of B_φ on polar angle θ at a distance of 10 times the wind radius. Since the φ source term in the induction equation is $\propto \sin(\theta)$, a dynamically unimportant magnetic field would also be $\propto \sin(\theta)$. For $\beta_w = 100$, however, corresponding to a magnetic pressure that is 1% of the ram pressure, the unbalanced $P_m \propto \sin(\theta)^2$ pushes the gas away from the midplane and towards the poles. This leads to the field being slightly lower than prescribed in the midplane and slightly higher near the poles, by a factor of $\lesssim 10\%$. We emphasize that this result is not an error in our model but a self-consistent consequence of magnetic stresses in the wind, which tend to collimate the flow (Sakurai

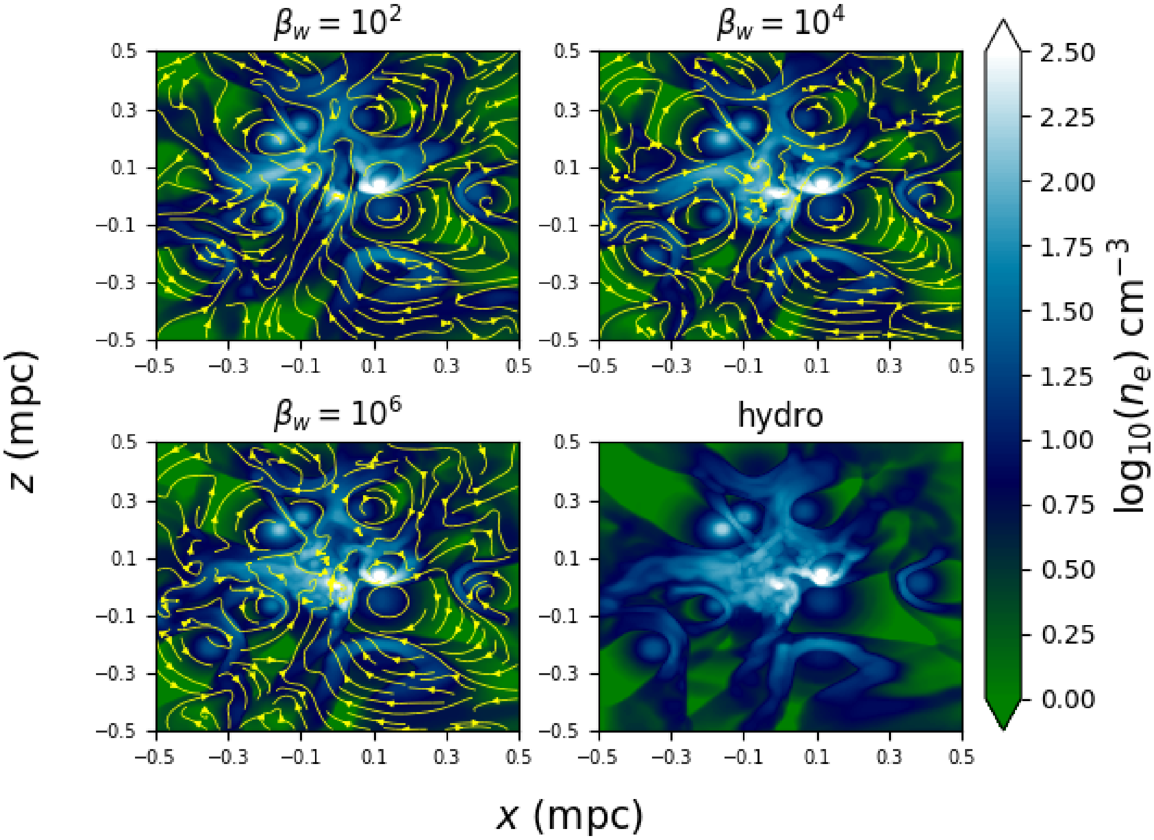

Figure 6.3: 2D slice in the plane of the sky of electron number density overplotted with projected magnetic field lines for the inner ~ 0.5 pc of our $\beta_w = 100$ (top left), $\beta_w = 10^4$ (top right), $\beta_w = 10^6$ (bottom left), and hydrodynamic (bottom right) simulations. Each 'star' in our simulation provides a purely toroidal magnetic field with direction determined by the random, independently chosen spin axes of the stars. No significant difference is seen in the simulations at this scale because the magnetic fields are relatively weak compared to the ram and thermal pressures of the gas.

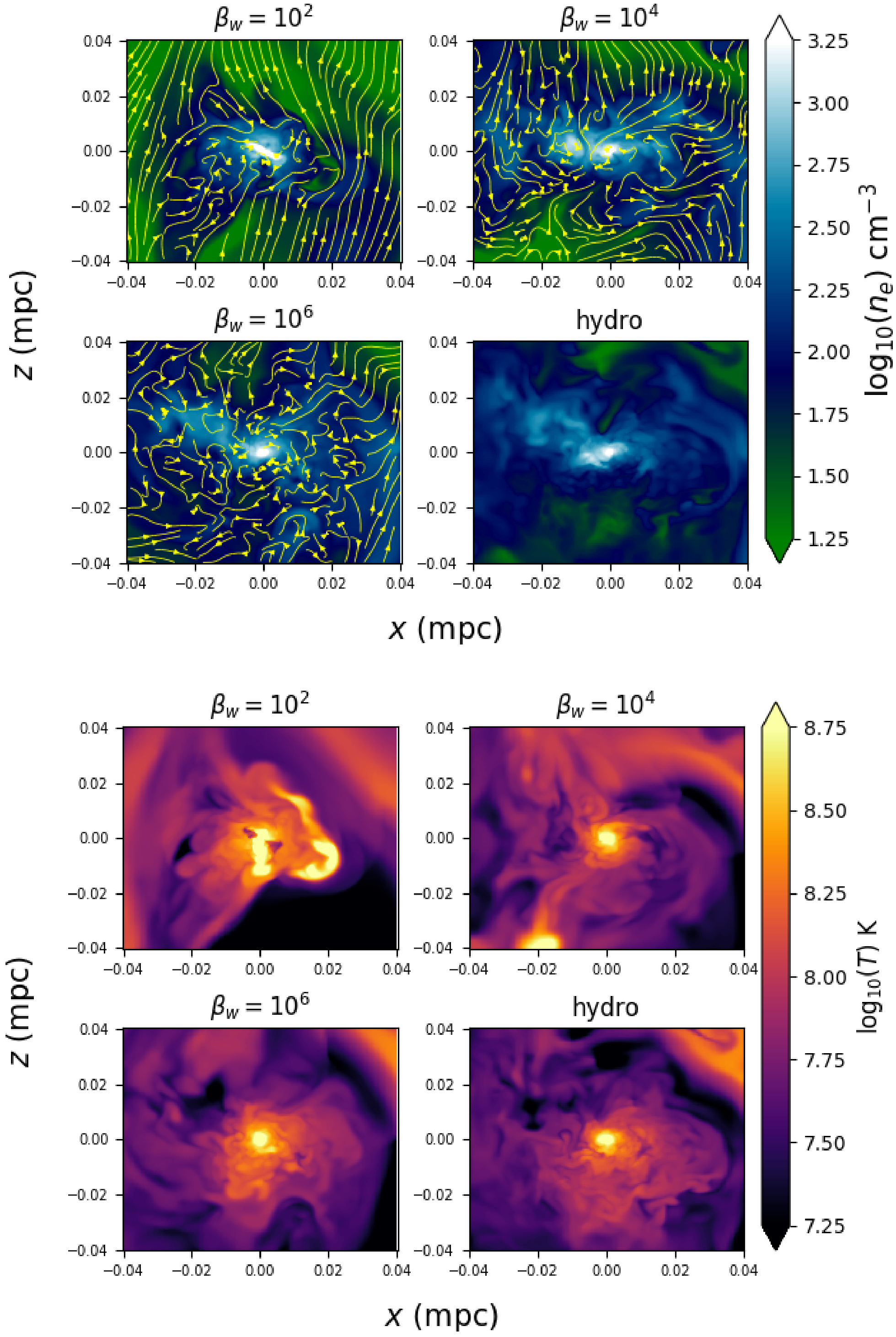

Figure 6.4: 2D slice in the plane of the sky of electron number density overplotted with projected magnetic field lines (top four panels) and temperature (bottom four panels) for the inner ~ 0.05 pc of our simulation. Compared to the 0.5 pc scale in Figure 6.3, the magnetic fields in the $\beta_w = 10^2$ and $\beta_w = 10^4$ simulations are more dynamically important and thus clear differences are seen in the density distribution compared to the hydrodynamic case. In addition, the larger the field strength in the winds, the larger the spatial scale over which the field lines are coherent.

1985). However, it is also important to note that the $\sin(\theta)$ dependence of the source term in the induction equation was chosen simply because it vanishes at 0 and π and not based on detailed modeling of the angular structure of MHD winds.

The angular structure of the wind seen in Figure 6.2 becomes even more pronounced for $\beta_w = 10$, where the magnetic pressure is now 10% of the ram pressure. Here the wind becomes highly collimated, as shown by the left panel of Figure 6.2, where the density is now concentrated at the poles and the magnetic field is roughly independent of polar angle. At the same time, the total mass outflow rate and angle averaged wind speeds are still in good agreement with the intended v_w and $\dot{M}_w$ as shown in the right panel of Figure 6.2.

As noted in RQS19, when β_w is further decreased to $\lesssim 5$ the magnetic pressure becomes large enough to accelerate the wind and make the solution inconsistent with the input parameters. Because of this we limit our studies to $\beta_w \gtrsim 10$ and focus primarily on $\beta_w \geq 10^2$. We show later that our results are insensitive to β_w for $\beta_w \sim 10^2 - 10^6$.

6.5 3D Simulation of MHD Wind Accretion Onto Sgr A*

6.5.1 Computational Grid and Boundary/Initial Conditions

We use a base grid in Cartesian coordinates of 128^3 covering a box size of 1 pc^3 with an additional 9 levels of nested static mesh refinement. This doubles the effective resolution every factor of ~ 2 decrease in radius and corresponds to an inner boundary radius of $r_{in} \approx 6 \times 10^{-5}$ pc$\approx 1.6 \times 10^{-3\prime\prime} \approx 300\ r_g$.

For the WR stars, we use the orbits, mass loss rates, and wind speeds exactly as described in RQS18, drawing primarily from Martins et al. (2007), Cuadra et al. (2008), Paumard et al. (2006), and Gillessen et al. (2017). These values differ slightly from those used in RQS19, where we modified the mass loss rates and wind speeds of four stars (within reasonable systematic observational uncertainties) to show that our simulations could reproduce the observed RM of the galactic centre magnetar. Each wind is given a randomly chosen direction for its spin axis that determines the azimuthal direction for the magnetic field; this random selection is made only once for each star so that each simulation we run has the same set of spin axes. Note that RQS19 used a different set of spin axes, but we have found our results insensitive to this choice. Here we also use a value of r_{in} that is a factor of 2 smaller than RQS19. We ran a total of 5 simulations; four in MHD with $\beta_w = 10, 10^2, 10^4$ and 10^6, and one in hydrodynamics (i.e., $\beta_w \to \infty$).

In §6.4 we showed that stellar winds with $\beta_w = 10$ in our model become highly collimated. We have found that this collimation has nontrivial effects on the resulting dynamics of the inner accretion flow (in particular, altering the angular momentum direction at small radii) in a way that makes separating the effects of large magnetic fields from this extra hydrodynamic consideration difficult. Furthermore, the precise nature of this collimation depends on our choice of angular dependence of $\tilde{E}_w$ in Equation (6.1), which was arbitrary. Thus we do not find it instructive to include $\beta_w = 10$ in our analysis. We do however, describe some of the main features of the $\beta_w = 10$ simulation that differ from those of higher β_w simulation in Appendix 6.A, though the main conclusions that we derive from our $\beta_w = 100 - 10^6$ simulations are consistent with the $\beta_w = 10$ simulation.

We initialize each simulation with floored density and pressure, zero velocity, and no magnetic field, starting at 1.1 kyr in the past. Here, for consistency with RQS18 January 1, 2017 is defined as the present day, i.e., $t = 0$.

Finally, we use floors on the density and pressure (see RQS18), and a ceiling on the Alfven speed (which is effectively an additional floor on density; see RQS19).

To ensure that our results are well converged, we ran an additional simulation that used a factor of 4 finer resolution within ~ 0.06 pc, though with a shorter total run time. As shown in Appendix 6.B, we find that our simulations show no significant dependence on resolution.

6.5.2 Overview

Figure 6.3 shows a 1 pc^2 2D slice in the plane of the sky (centered on the black hole) of the electron number density overplotted with magnetic field lines for $\beta_w = 100, 10^4$, and 10^6 compared to the hydrodynamic case. Magnetic fields do not significantly alter the dynamics at this scale because even for $\beta_w = 100$ the magnetic pressure in the winds is insignificant compared to their ram pressure. Thus, all panels are nearly identical. Slices of the temperatures show similarly small differences from the right panel of Figure 7 in RQS18 and are thus not included here. Figure 6.3 shows that, as desired, the magnetic fields lines wrap around the "stars," which show up as dense circles typically surrounded by bow shocks. Again, since the field is not dynamically important at this scale the field lines for different β_w's all have essentially the same geometry.

The top four panels of Figure 6.4 again show 2D slices of the electron number density overplotted with field lines but on a scale of ~ 0.08 pc, ten times smaller than Figure 6.3. The bottom four panels of the same figure show 2D slices of temperatures. While the $\beta_w = 10^6$ run still looks similar to the hydrodynamic simulation, the $\beta_w = 10^4$ and (particularly) $\beta_w = 100$ runs show significant differences. This is because, as we shall show, the field in the latter cases starts to become dynamically important at this scale. The field lines become increasingly ordered with decreasing β_w, going from mostly tangled for $\beta_w = 10^6$ (where the field is easily dragged along with the flow) to mostly coherent for $\beta_w = 100$ (where the field can resist the gas motion). This will have important implications for the field geometry at small radii in §6.5.6.

In the $\beta_w = 10^2$ simulation alone, a prominent large scale, hot, collimated outflow can be seen at particular times (at $t = 0$ in Figure 6.4 it is relatively weak, though can be seen reaching to $\sim$ 0.01 pc below the black hole in the top left temperature panel). Figure 6.5 presents a time series of the gas temperature, highlighting $T \geq 6 \times 10^7$ K and spanning $t = -600$ yr to $t = -450$ yr in 50 yr increments. In the initial frame, no clear outflow structure is seen, only strong shocks between winds. As time progresses, however, a thin $\geq 10^8$ K outflow appears coming out from the right side of the black hole, $\sim$ parallel to the angular momentum direction at this time. This outflow is magnetically driven and originates at small radii, as we shall show in the next section.

Figure 6.6 shows the angle-averaged root-mean-squared (rms) magnetic field strength and plasma $\beta \equiv P/P_m$, where P_m is the magnetic pressure, as a function of radius for different values of β_w. As expected, at large radii ($\gtrsim 0.1$ pc), the rms field and β scale simply as $\sqrt{1/\beta_w}$ and β_w,

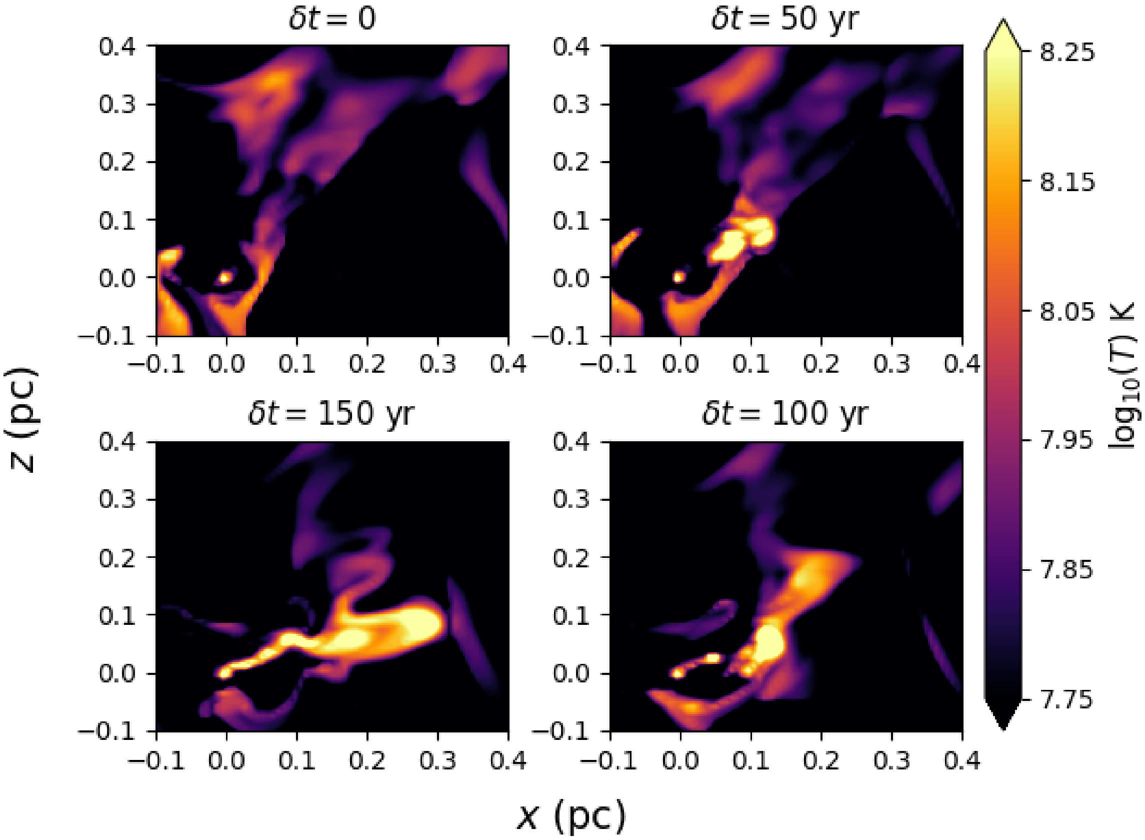

Figure 6.5: Time series of jet formation over the course of 150 years in the $\beta_w = 10^2$ simulation. Plotted are 2D gas temperature slices in the plane of the sky for the inner ~ 0.04 pc; note that we only show the upper right quadrant of the simulation to highlight the jet. Here δt is the time elapsed since the first snapshot. Time proceeds clockwise starting from the upper left panel. The color scale differs from that used in Figure 6.4 and was chosen to particularly highlight the highest temperatures. As time progresses, a collimated, high temperature outflow emerges asymmetrically from small radii until it reaches $r \sim 0.3$ pc. This 'jet' is present only sporadically during the course of the $\beta_w = 10^2$ simulation and not at all in the higher β_w simulations.

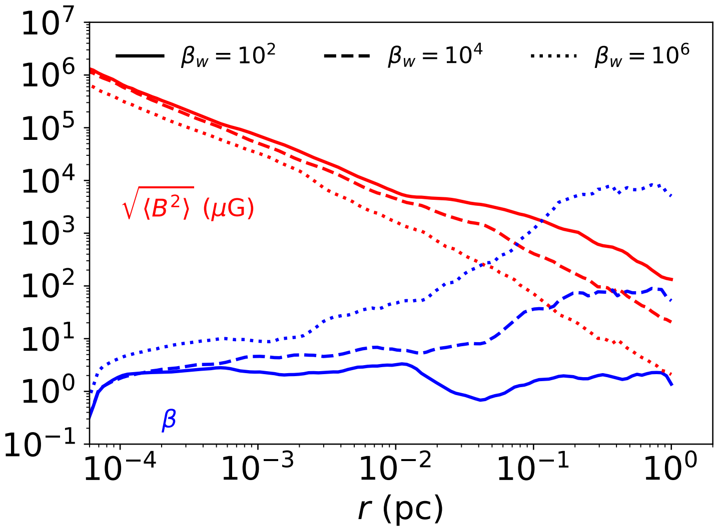

Figure 6.6: Comparison between the root-mean-squared magnetic field strength (red), $\sqrt{\langle B^2 \rangle}$, and plasma β (blue), $\langle P \rangle / \langle P_m \rangle$, for different values of β_w, which quantifies the magnetization of the WR stellar winds. Even though the field strength varies by 2 orders of magnitude at large radii (corresponding to a 4 orders of magnitude difference in β), the field strengths at small radii are all within a factor of $\lesssim 2$ (βs within a factor of $\lesssim 3$). This is because the field tends to be compressed and amplified by being dragged along with the gas motion until β reaches $\sim$ a few.

respectively. At small radii ($\lesssim 10^{-2}$ pc), however, there is a much weaker dependence of the rms field and β on β_w. In fact, both $\beta_w = 10^4$ and $\beta_w = 10^2$ reach $\beta \sim 2$ and ~ 1 G field strengths by 10^{-4} pc. Even in the $\beta_w = 10^6$ case, the field strength (β) at small radii is only a factor of ~ 2 less (3-4 larger) than in the $\beta_w = 10$ simulation. This is why RQS19 found that the rotation measure of Sgr A* and the net vertical flux threading the inner boundary of the simulation were roughly independent of β_w, since both quantities are set by the field at the innermost radii. Though this result might seem like a clear signature of a field regulated by the magnetorotational instability (MRI), we argue in §6.5.5 that this is not the case, and that instead the amplification is due to flux freezing in the inflow.

Despite the clear morphological differences at the ~ 0.08 pc scale in the density/temperature (Figure 6.4) and the fact that the flow can reach β of $\sim$ a few over orders of magnitude in radius (Figure 6.6), the radially averaged gas properties in the MHD simulations remain strikingly similar to the hydrodynamic results at all radii even for $\beta_w = 100$. This is shown in Figure 6.7, which shows the angle and time averaged density, sound speed, radial velocity, angular momentum, and accretion rate in addition to the accretion rate through the inner boundary as a function of time for both the $\beta_w = 100$ and the hydrodynamic run. Though there can be as large as a factor of three difference in accretion rate (corresponding to a difference in density at small radii) at specific times, on average, the accretion rate through the inner boundary is unchanged by the presence of the magnetic fields, falling between ~ 0.25 and 1.5 $M_{\odot}/yr$.[2] The differences in the average sound speed and radial velocity are negligible. We have tested that this result also holds for different values of the inner boundary radius.

6.5.3 Dynamics of The Inner Accretion Flow

To facilitate analysis of the accretion flow at small radii it is useful to define time intervals over which the angular momentum vector of the gas is relatively constant in time. Due to the stochastic nature of the simulations, this occurs at different times for each run, often not centered at $t = 0$. The purpose of this analysis, however, is to understand the general properties of the accretion disc, outflow, and magnetic field structure, not to make overly specific predictions for the present day. We expect that the intervals we choose are representative of the general accretion flow dynamics and structure.

Figure 6.8 shows the three components of the angle and radius-averaged (over the interval $r = 5 \times 10^{-4}$ pc and $r = 3 \times 10^{-2}$ pc) angular momentum direction vector as a function of time for our four simulations. We use this information to choose our particular choice of time intervals for averaging the flow structure: $[100, 200]$ yrs, $[0, 100]$ yrs, $[0, 100]$ yrs, and $[-100, 0]$ yrs for $\beta_w = 10^2, 10^4, 10^6$ and the hydrodynamic simulation, respectively. All of these intervals have angular momentum directions that are approximately constant in time and nearly aligned with the stellar disc containing about half of the WR stars. The angular momentum of the accretion flow is aligned with that of the stellar disc most of the time, though for the $\beta_w = 10^2$ simulation it has more frequent and larger deviations from the stellar disc than in the hydrodynamic simulation. The most significant of these is seen near $t = 0$, where the angular momentum of the gas in the $\beta_w = 10^2$ simulation is nearly anti-aligned with the stellar disk for a brief ~ 50 yr period. As shown in Appendix 6.A, the angular momentum of the gas in the $\beta_w = 10$ simulation is almost never aligned with the stellar disc due to the collimation of winds. Note that the *magnitude* of the angle and time-averaged angular momentum is similar for all simulations, being ~ 0.5 l_{kep} for $r \lesssim 0.1$ pc (see the left panel of Figure 14 in RQS18; the angle and time-averaged l in MHD differs at most by 20% from that in hydrodynamics as shown in Figure 6.7).

Defining a new 'z'' direction as the direction of the time averaged angular momentum vector, Figure 6.9 and Figure 6.10 show time series of the midplane ($\theta = \pi/2$) mass density on ~ 0.1 pc scales, weighted by radius (see Figure 6.7) in the hydrodynamic and $\beta_w = 10^2$ simulations, respectively. A time series for the $\beta_w = 10^4$ ($\beta_w = 10^6$) simulation is not shown but it looks qualitatively very similar to the $\beta_w = 10^2$ (hydrodynamic) case. Figure 6.11 shows the Bernoulli parameter, a measure of how bound the gas is to the black hole, in the same frame for all four simulations at a representative time. These figures show that the majority of the unbound, high angular momentum gas in the midplane at large radii is provided by the closest one or two stellar winds (namely, those of E23/IRS 16SW and E20/IRS 16C) as they orbit the black hole in all simulations. As this material streams inwards, however a clear difference is seen in the behavior at smaller radii in the different runs. In the hydrodynamic case, each fluid element largely conserves

---

[2] Due to the chaotic nature of our simulations, the instantaneous value of the accretion rate at $t = 0$ is not as robust as the time-averaged value.

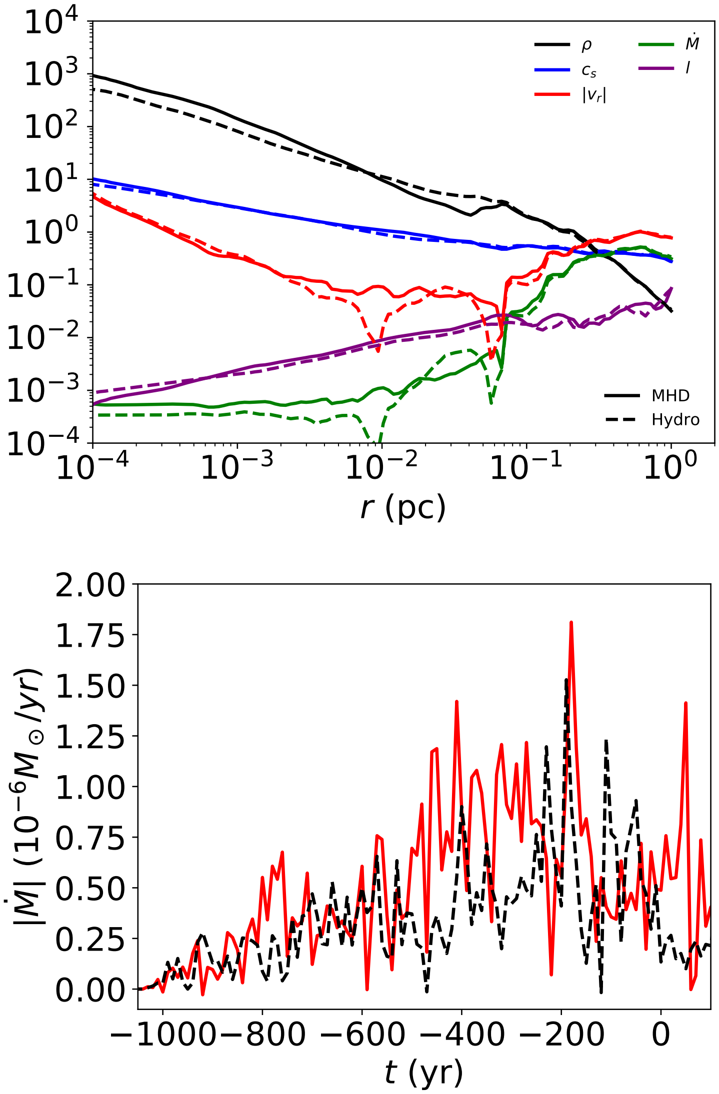

Figure 6.7: Comparison between the $\beta_w = 10^2$ MHD simulation (solid) and a purely hydrodynamic simulation (dashed). Top: present day angle-averaged mass density, ρ ($M_\odot/pc^3$), sound speed, c_s (pc/kyr), radial velocity, $|v_r|$ (pc/kyr), specific angular momentum, l (pc^2/kyr), and mass accretion rate, $|\dot{M}|$ ($M_\odot$/kyr), as a function of distance from the black hole. Bottom: Mass accretion rate as a function of time measured at $\approx$ 2 mpc $\approx$ 9700 r_g. Despite the relatively large magnetization of the stellar winds, the magnetic field has an almost negligible effect on the radial profiles. The small difference in density (and hence, accretion rate) is caused by the slightly different time dependence of the accretion rate leading to a different realization of the flow at $t = 0$ even though the statistics in time are similar. These conclusions are independent of β_w.

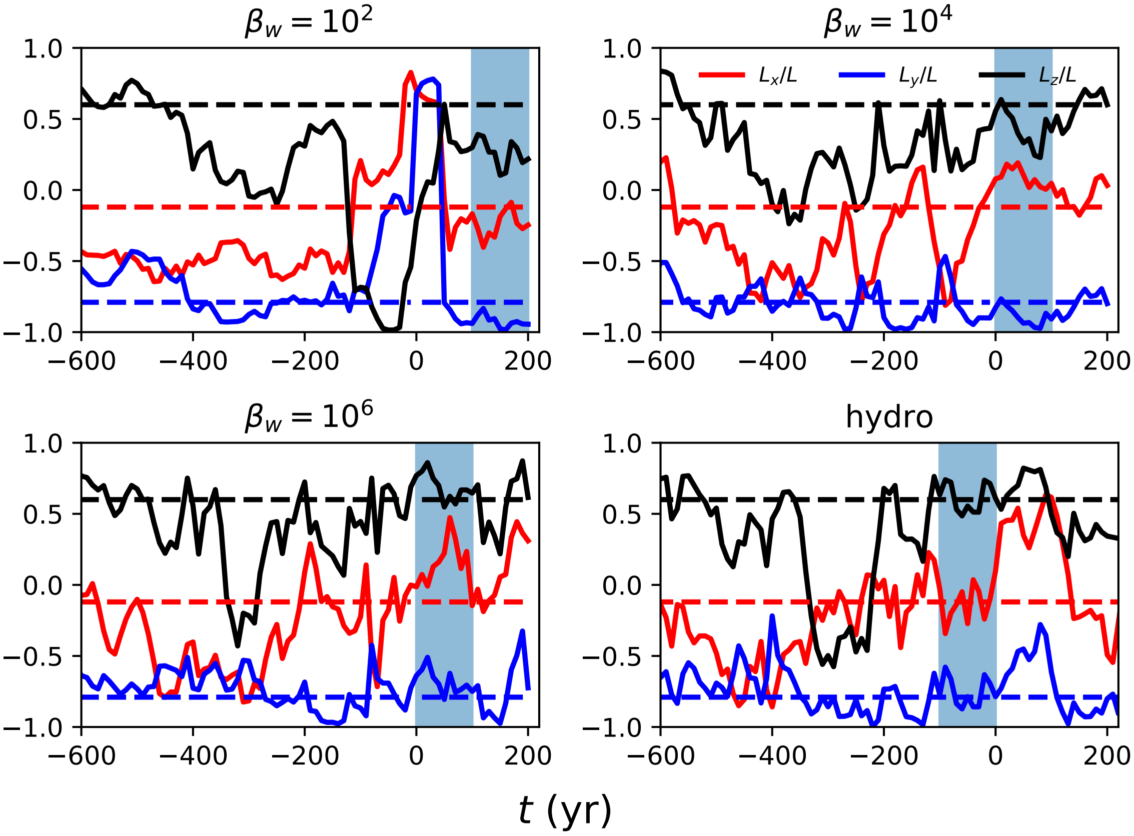

Figure 6.8: Angular momentum direction as a function of time for the gas in our $\beta_w = 10^2, 10^4, 10^6$ and hydrodynamic simulations, averaged in radius and angle over 5×10^{-4} pc to 3×10^{-2} pc. The blue shaded regions represent the time intervals that we choose to analyze the inner accretion flow, over which the angular momentum vector is relatively stable. Dashed lines represent the three components of the angular momentum direction vector of the clockwise stellar disc (Paumard et al. 2006; Lu et al. 2009).

its angular momentum and energy, thus remaining unbound. Gravity is only strong enough to bend the inflowing streams of gas around the black hole until they emerge on the other side as a spray of outflow that sends the gas out to larger radii without much accretion. The high angular momentum gas does not spend enough time at small radii to circularize or form a disc; instead the supply of matter at small radii is continually being lost and replenished. The same is true of weakly magnetized simulations (i.e., $\beta_w = 10^6$ and higher).

In MHD with strong magnetic fields (i.e., $\beta_w = 10^2$ and $\beta_w = 10^4$), however, this picture is different. Now the strong fields ($\beta \sim$ a few at small radii, Figure 6.6) are able to efficiently remove some angular momentum and energy from the gas via large-scale torques. This results in the originally unbound material becoming bound as it falls in so that its trajectory alters to form an inward spiral that ultimately accretes instead of spraying out the other side to large radii. The main difference, however, as we shall argue in §6.5.7, is that the outflow present in the midplane of the hydrodynamic simulation is now redirected to the polar regions. As in the hydrodynamic case, the gas with high angular momentum does not spend enough time at small radii to circularize or form a true disc. This is because it generally accretes (after being subjected to magnetic torques) or is dumped into an outflow before completing even a few orbits. Thus in both cases, the gas supply at small radii is continually being recycled and is set mostly by the hydrodynamic properties of the winds, in particular the wide range of angular momentum produced by the stellar winds.

Focusing now on the poloidal structure of the flow, Figure 6.12 shows the φ and time-averaged accretion rates for our four simulations while Figure 6.13 shows the same for the Bernoulli parameter. The hydrodynamic midplane structure described above results in a net outflow of high angular momentum, modestly unbound material in the midplane, while low angular momentum material freely falls in along the poles. The polar inflow also contains some higher angular momentum, unbound ($\mathrm{Be}/|\Phi| \lesssim 10^{-2}$ but ≥ 0) material that eventually hits a centrifugal barrier and turns aside and adds to the midplane outflow. For $\beta_w = 10^6$, where the field is relatively weak, the same structure is seen. However, for $\beta_w = 10^4$ and 10^2, the hydrodynamic accretion structure is completely reversed. For these more magnetized flows, not only is there net inflow of bound, $\mathrm{Be}/|\Phi| < 0$, material in the midplane, but the energy released from the gas as it loses angular momentum due to magnetic torques is deposited into an unbound, $\mathrm{Be}/|\Phi| \sim 10$ polar outflow. As evidenced by the fact that the net accretion rates are comparable in both cases, this outflow is similar to the one present in the hydrodynamic simulation but redirected from the midplane to the poles.

An additional consequence of the different poloidal dynamics is that the $\beta_w = 10^4$ and 10^2 simulations display a stronger density contrast between the midplane and polar regions compared to the $\beta_w = 10^6$ and hydrodynamic simulations. This is seen in Figure 6.14, which plots the time and φ-averaged density folded over the midplane at $r = 5$ mpc for the different simulations. Though the "disc" of gas is still quite thick, the equatorial to polar density contrast in the most magnetized case is now a factor of ~ 5 vs. only ~ 2 in the hydrodynamic and more weakly magnetized cases. This is, however, still a much lower density contrast than typical MHD and GRMHD simulations of MRI driven accretion in tori, which show outflows that are significantly more magnetically dominated, and in which the density at the poles is orders of magnitude less than the midplane.

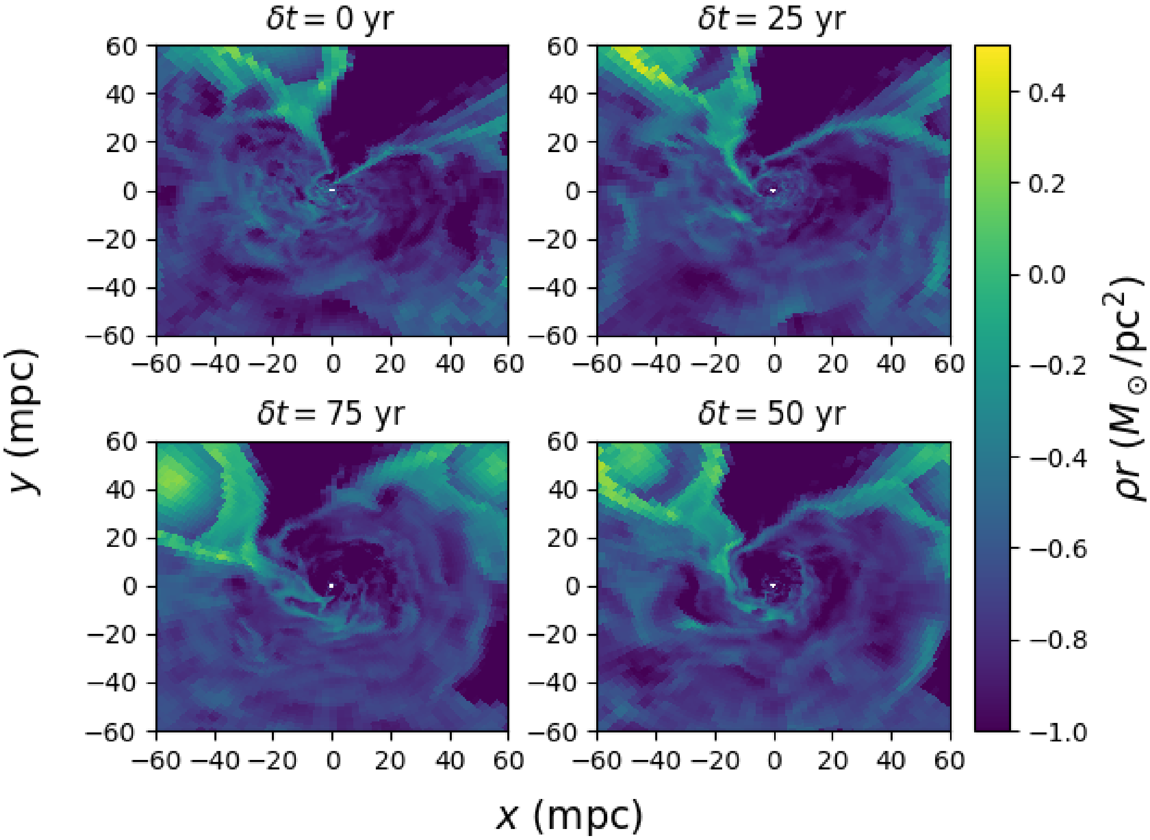

Figure 6.9: Sequence of midplane slices of the mass density weighted by radius separated by 25 year intervals for the hydrodynamic simulation. Here δt is the time elapsed since the first snapshot and time proceeds clockwise starting from the upper left. Material provided by the nearest two stellar winds (E20/IRS 16C in the upper left quadrant and E23/IRS 16SW in the upper right quadrant) streams inward but mostly has too much angular momentum to accrete without any redistribution of angular momentum. Instead, the streams of material ultimately hit a centrifugal boundary and then "spray" outwards on the opposite side of the black hole from which they approached. The bulk of the gas does not circularise nor form a steady disc.

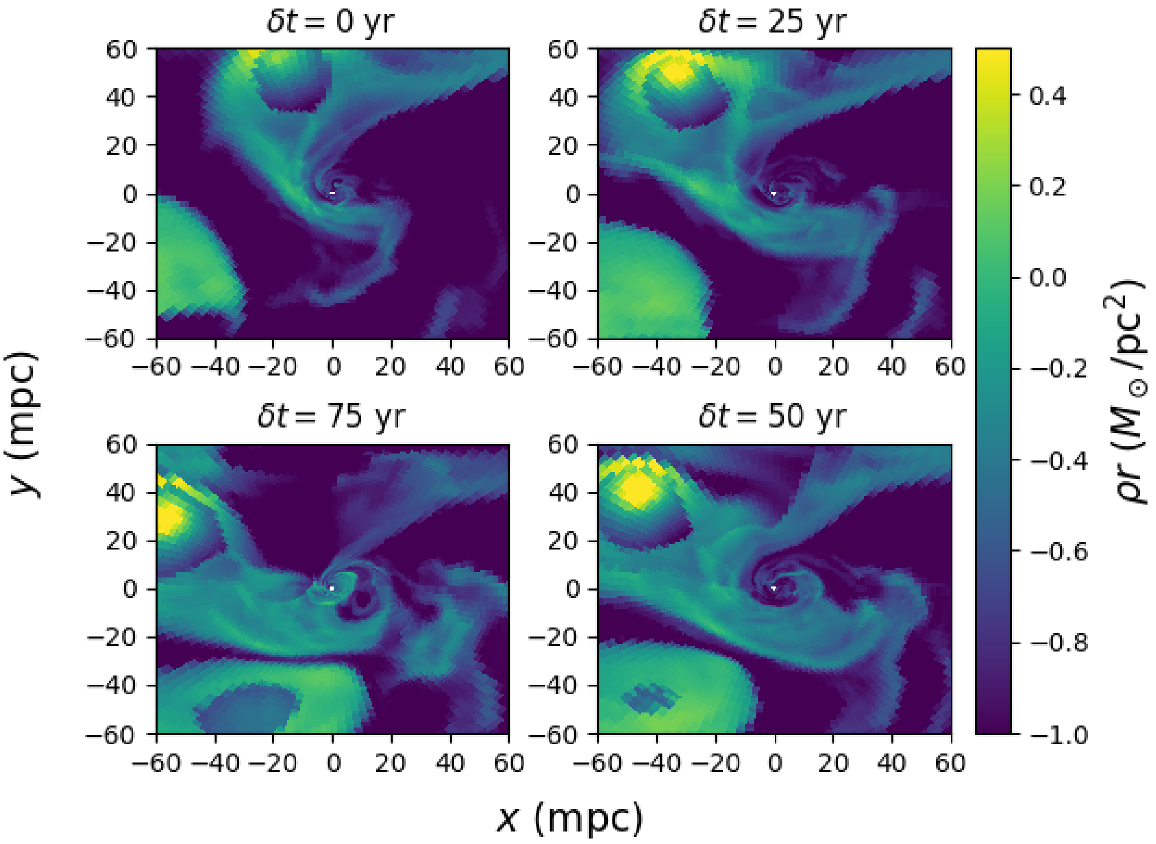

Figure 6.10: Sequence of midplane slices of the mass density weighted by radius separated by 25 year intervals for the $\beta_w = 10^2$ simulation. Time proceeds clockwise starting from the upper left panel. Note that $\delta t = 0$ is at a different absolute time relative to Figure 6.9. Instead of simply streaming in and "spraying" outwards as seen in the hydrodynamic case (Figure 6.9), strong magnetic fields are able to redirect the outflowing, high angular momentum gas towards the polar regions so that the midplane slice pictured here is mostly comprised of spiraling inflow. As in the hydrodynamic simulation, gas does not truly circularise into a disc but either accretes or outflows after only $\lesssim$ a few orbits around the black hole. While magnetic fields do provide a non-negligible torque that can remove angular momentum from the gas, this torque has limited time to operate and does not significantly modify the accretion rate, which is very similar in the hydrodynamic and MHD simulations (see Figure 6.7). The two stellar winds providing most of the material in this plot are E20/IRS 16C in bottom left quadrant and E23/IRS 16SW in the upper left quadrant.

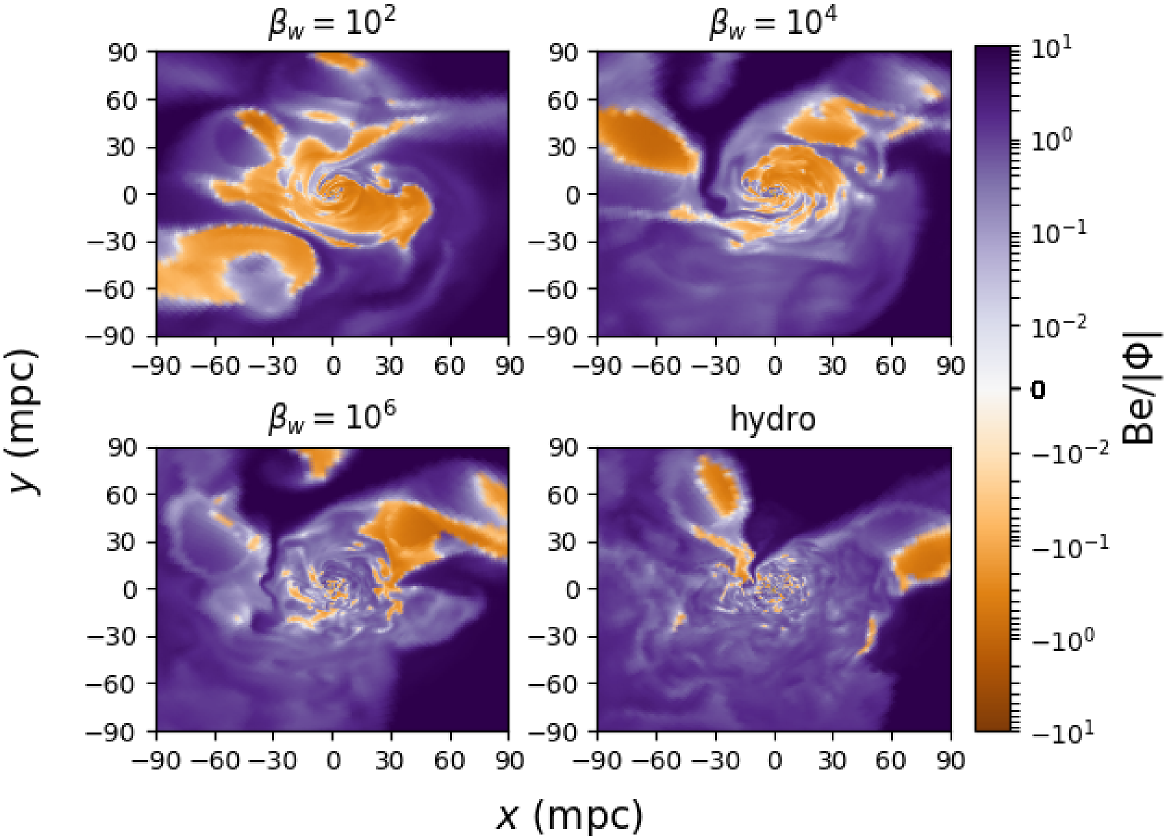

Figure 6.11: Midplane contours of the Bernoulli parameter, Be$\equiv |\mathbf{v}|^2/2 + \gamma/(\gamma-1)P/\rho - GM/r$, divided by the gravitational potential, $|\Phi| = GM/r$, in the four different simulations at representative times. Orange denotes bound material while purple denotes unbound material. Absent magnetic fields, the relatively high angular momentum gas provided by the nearby stellar winds is mostly unbound with too much angular momentum to accrete (see also Figure 6.9). Strong magnetic fields (as present in the $\beta_w = 10^2$ and 10^4 simulations), however, can torque the gas enough that it loses some angular momentum and becomes moderately bound to the black hole. The energy released by this process drives polar outflow.

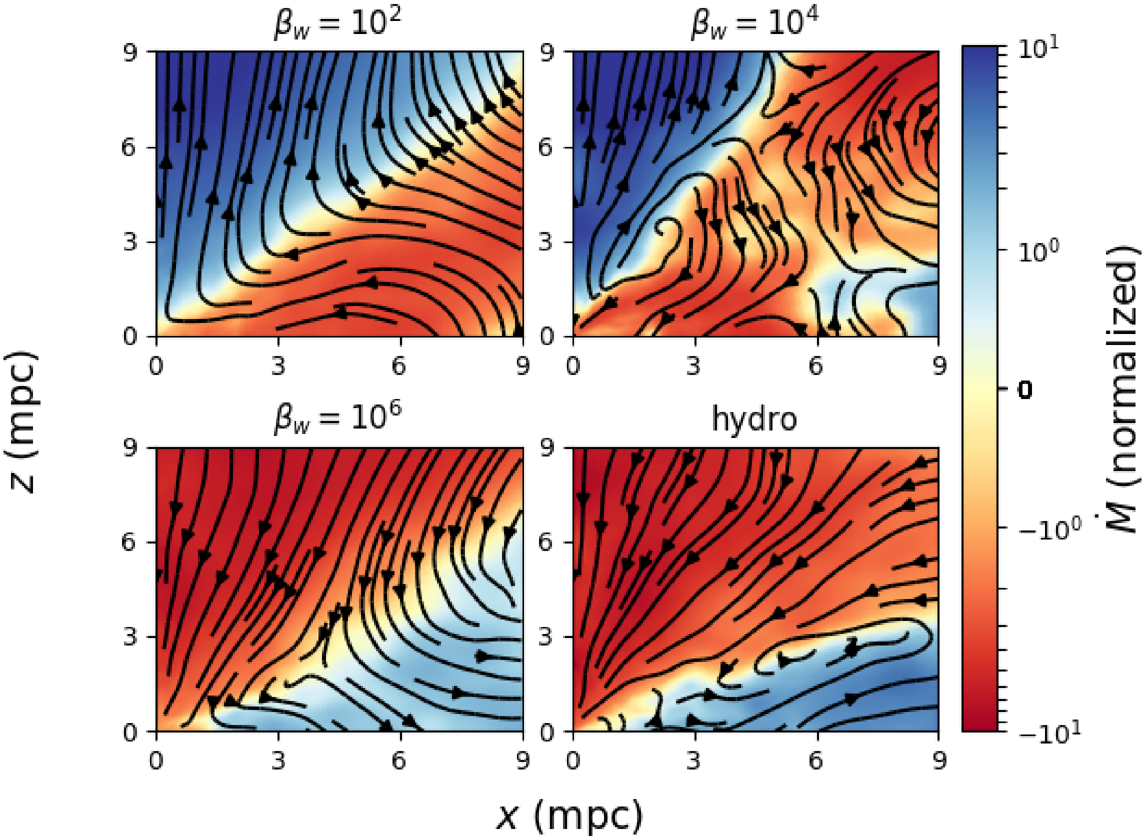

Figure 6.12: Time and φ-averaged accretion rate on mpc scales for each simulation, where the z direction is defined as the net angular momentum of the gas (Figure 6.8). Red represents inflow, blue represents outflow, and the accretion rate has been folded over the midplane and normalized such that the absolute value at 5 mpc is unity. For sufficiently large magnetic fields, the inflow/outflow structure seen in the hydrodynamic case is reversed, because the field is strong enough to redirect the outflow and confine it to the polar regions.

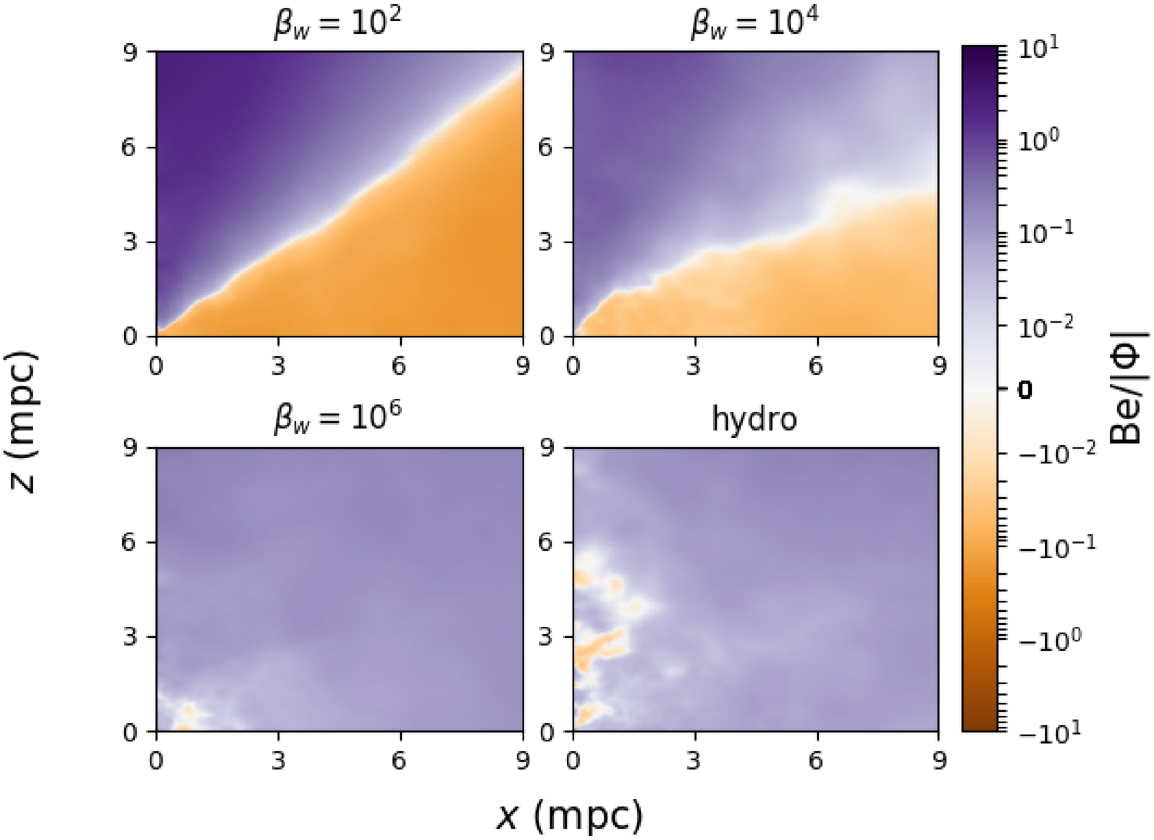

Figure 6.13: Time and φ-averaged Bernoulli parameter, Be, normalized to the gravitational potential, $|\Phi| = GM/r$ on mpc scales for each simulation, where the z direction is defined as the net angular momentum of the gas (Figure 6.8). Orange represents bound, purple represents unbound, and the Bernoulli parameter has been folded over the equator. Without magnetic fields, the material is slightly unbound throughout the domain except for some slightly bound material near the polar axis. Magnetic fields provide torque, releasing energy from the high angular momentum gas in the midplane and depositing it in the polar outflow (Figure 6.12).

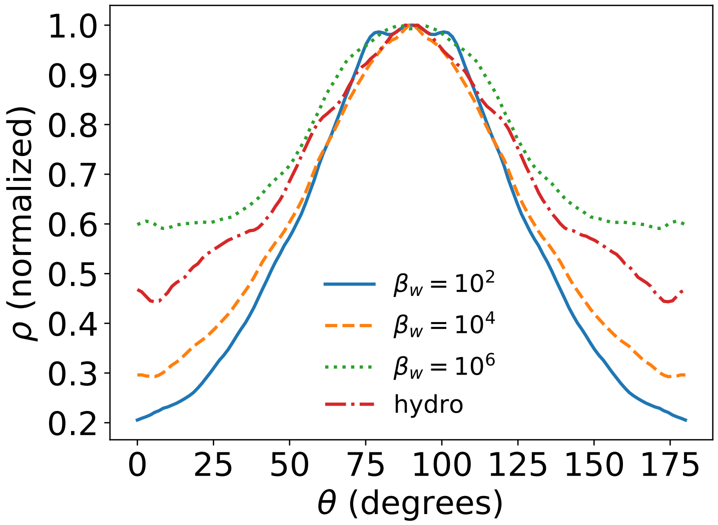

Figure 6.14: Time and φ averaged mass density at $r = 5$ mpc, normalized at $\theta = \pi/2$ and folded over the midplane. Strong magnetic fields lead to a larger contrast in density between the midplane and polar regions as compared to the hydrodynamic and more weakly magnetized flows.

6.5.4 Stresses

In order to quantify the relative contribution of the magnetic field to angular momentum transport, we calculate the Shakura & Sunyaev (1973) α-viscosity from our simulations. We do this in the same frames defined by the angular momentum direction during the time intervals shown in Figure 6.8 as described in the preceding subsection.

We follow Jiang et al. (2017) by defining the time and angle averaged Reynold's stress

$$S_h \equiv \langle \rho v_r v_\varphi \sin(\theta) \rangle - \langle \rho v_r \rangle \langle v_\varphi \sin(\theta) \rangle \tag{6.2}$$

and Maxwell stress

$$S_m \equiv \langle B_r B_\varphi \sin(\theta) \rangle. \tag{6.3}$$

Then the Shakura & Sunyaev (1973) α viscosities are simply $\alpha_h = S_h/P$ and $\alpha_m = S_m/P$, where we have chosen to use the thermal pressure instead of the total (thermal plus magnetic) pressure in the denominator for fair comparison between hydrodynamic and MHD simulations.

The resulting α's for each simulation are plotted in Figure 6.15. In both the hydrodynamic and $\beta = 10^6$ simulations, the stress is dominated by the Reynolds stress. This nonzero stress even without strong magnetic fields or other sources of viscosity can be understood by considering the inflow/outflow structure seen in Figure 6.12. Accretion occurs via low angular momentum (i.e., low v_φ) material in the polar regions where the φ-averaged v_r is large (i.e., close to free-fall) and negative while the midplane consists of high angular momentum (i.e., large v_φ) material with smaller in magnitude and positive φ-averaged v_r. Thus, $\langle \rho v_r v_\varphi \sin(\theta) \rangle$ is significantly different than $\langle \rho v_r \rangle \langle v_\varphi \sin(\theta) \rangle \propto \dot{M} l$, leading to a large α_h. Thus, α_h is not predominantly a turbulent viscosity but

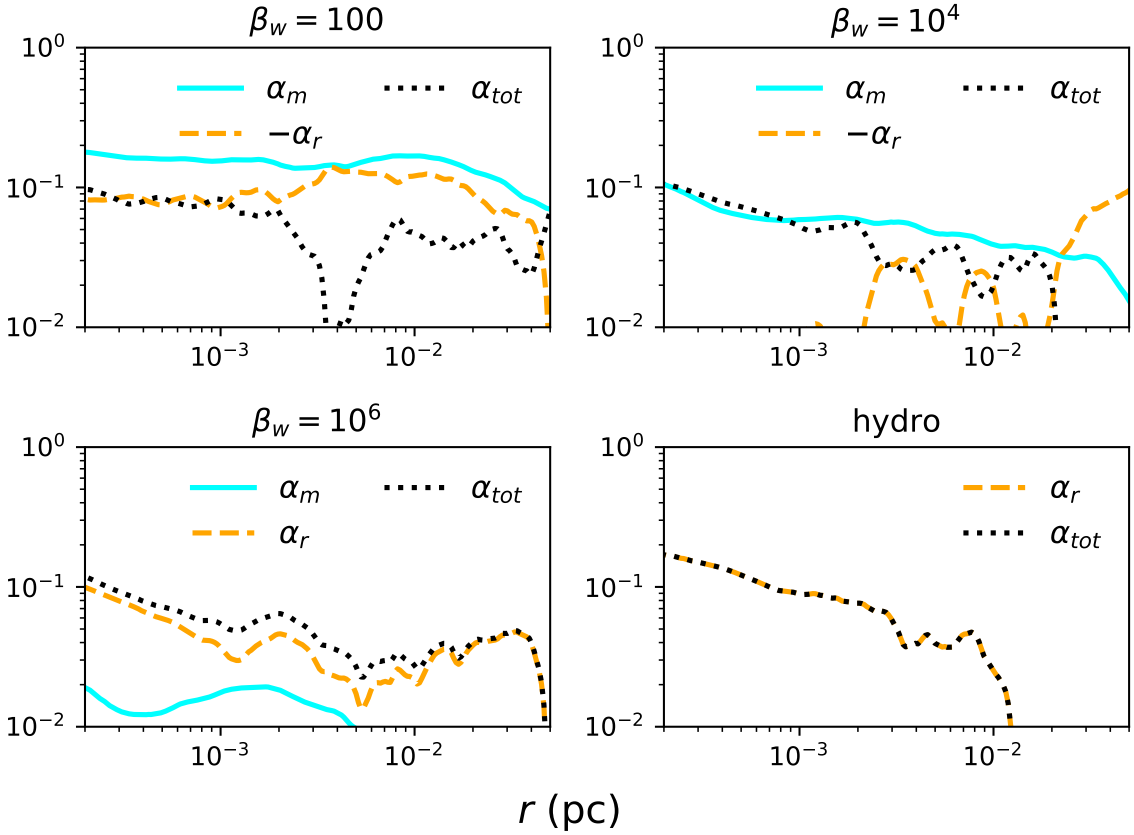

Figure 6.15: Comparison between the time averaged Maxwell (blue solid), Reynolds (dashed yellow), and total (dotted black) α viscosities as defined in §6.5.4 for each of our simulations. In the hydrodynamic case, non-axisymmetric structure and the presence of low angular momentum gas leads to a relatively large “stress”, and hence, accretion rate. For MHD simulations, while the total stress remains basically unchanged from the hydrodynamic case (see §6.5.4), the Maxwell stress can become larger than the total stress with $\alpha_m \approx 0.2$, with the Reynolds stress becoming negative to compensate.

a measure of the fact that you have a superposition of two types of flows: low angular momentum accretion and high angular momentum outflow. This picture is altered for $\beta_w = 10^4$, where the total stress is dominated by the Maxwell stress while the Reynolds stress is ~ 0, and for $\beta_w = 10^2$, where the total stress is a competition between a large Maxwell stress and a non-negligible, negative Reynolds stress (where a negative stress implies transport of angular momentum inwards). For these more magnetized flows, the magnetic field is strong enough to resist being wound up in the φ direction, providing non-negligible torque to rotating gas as it falls in.

In all cases, the total stress, $\alpha_{tot} = \alpha_h + \alpha_m$, is similar for $r \lesssim 10^{-2}$ pc, varying between $\sim 0.04 - 0.2$. This simply reflects the overall dynamical similarity of the flows independent of β_w. In a steady state accretion flow, the total stress can be written as (from equations 6.2 and 6.3)

$$\alpha_{tot} = \frac{F_J - \langle \dot{M} \rangle \langle l \rangle}{4\pi r^3 \langle P \rangle}, \tag{6.4}$$

where $F_J = \langle \rho v_r v_\varphi \sin(\theta) \rangle - \langle 4\pi r^3 B_r B_\varphi \sin(\theta) \rangle =$ is the constant flux of angular momentum and l is the specific angular momentum. The constant F_J is set by the accretion rate and angular momentum at the inner boundary and is generally small. Thus, since $\dot{M}$ and l are relatively unchanged in an angle averaged sense going from hydrodynamics to MHD, the total stress is unchanged.

6.5.5 MRI

We have shown (Figure 6.6) that the magnitude of the magnetic field at small radii is only weakly dependent on β_w, the parameter governing the strength of the magnetic field in the stellar winds. A natural mechanism to explain this is the magnetorotational instability, which can amplify an arbitrarily small magnetic field to reach $\beta \lesssim 10$ in differentially rotating flows, such as we have here. However, we have also shown that the gas in our simulations never circularizes and therefore does not spend many orbits at small radii. Consequently, there is not sufficient time in a Lagrangian sense for the MRI to grow.

We can further evaluate the role of the MRI by using an estimate of the fastest growing wavelength for perturbations given by

$$\lambda_{MRI,\theta} \approx \frac{2\pi |B_\theta|}{\sqrt{4\pi\rho}\Omega}, \tag{6.5}$$

where $\Omega \equiv v_\varphi/(r\sin(\theta))$ is the rotational frequency. At least two criteria need to be met in order for the MRI to operate in numerical simulations: 1) $\lambda_{MRI,\theta}$ needs to be resolved, that is, the cell length Δx needs to be $\ll \lambda_{MRI,\theta}$, and 2) $\lambda_{MRI,\theta}$ needs to be smaller than the scale height of the disc, otherwise the perturbations have no room to grow.

Figure 6.16 shows $\lambda_{MRI,\theta}$ in the midplane of the disc compared to the scale height of the disc, defined as $H \equiv r\langle \rho |\theta - \pi/2| \rangle / \langle \rho \rangle$, and the resolution of our grid. We find that $\lambda_{MRI,\theta}$ is sufficiently resolved at all radii but that it is larger than the scale height for all of our MHD simulations. This implies that even if the gas in our simulations were to circularize, which we reiterate does not in fact occur, the MRI would have no room to operate. Therefore, we conclude that the MRI is not an important source of magnetic field amplification or angular momentum transport in our

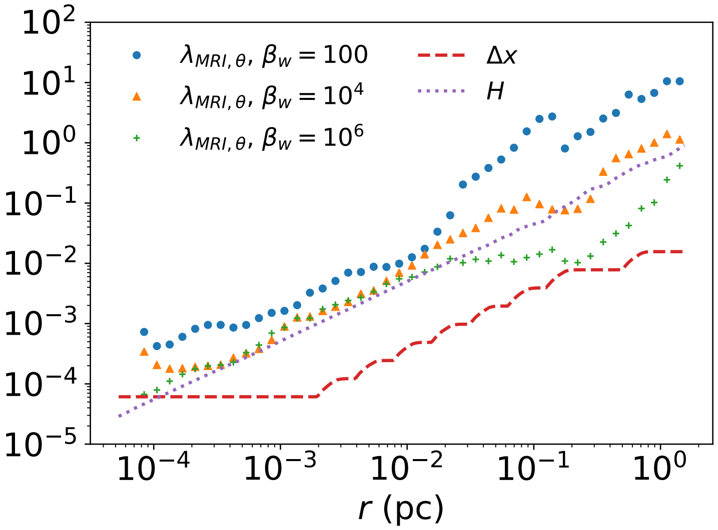

Figure 6.16: Wavelength of the most unstable mode for the MRI computed in the midplane for our three MHD simulations as compared to the scale height of the disc, H, and the resolution of our grid, Δx. $\lambda_{MRI,\theta}$ is well resolved but is larger than the scale height of the disc. The MRI is suppressed by the strong $\beta \sim$ few magnetic field (Figure 6.6) produced by compression as the gas flows in.

simulations. Instead, we explain the results of Figure 6.6 with simple compression/flux freezing. An initially weak field at large radii will be compressed as it is pulled inwards by the bulk motion of the gas. It will continue to do so until $\beta \sim$ a few, when the field becomes dynamically important and starts to resist the fluid motion. At this point, the field maintains $\beta \sim$ a few as it continues to accrete. For small β_w, this happens at large radii, while as β_w increases the field reaches $\beta \sim$ a few at progressively smaller radii. If we were able to reach even smaller radii with our simulations, we predict that even the $\beta_w = 10^6$ run will ultimately reach β of $\sim$ a few and the field would become dynamically important (see also §6.5.8).

6.5.6 Magnetic Field Structure

We now turn our attention to the structure of the magnetic field at small radii. RQS19 predicted that the amount of magnetic flux ultimately threading the inner radii of the domain, ϕ_{in}, is roughly insensitive to β_w and roughly constant in time, falling between $\approx 1-6$ in units such that the Magnetically Arrested Disc (MAD) limit is ≈ 50 (Tchekhovskoy et al. 2011). To demonstrate this result more clearly, Figure 6.17 plots ϕ_{in}, defined as

$$\phi_{in} \equiv \left. \frac{1/2 \int |B_r| r^2 d\Omega}{r\sqrt{|\dot{M}| v_{kep}}} \right|_{r=r_{in}}, \tag{6.6}$$

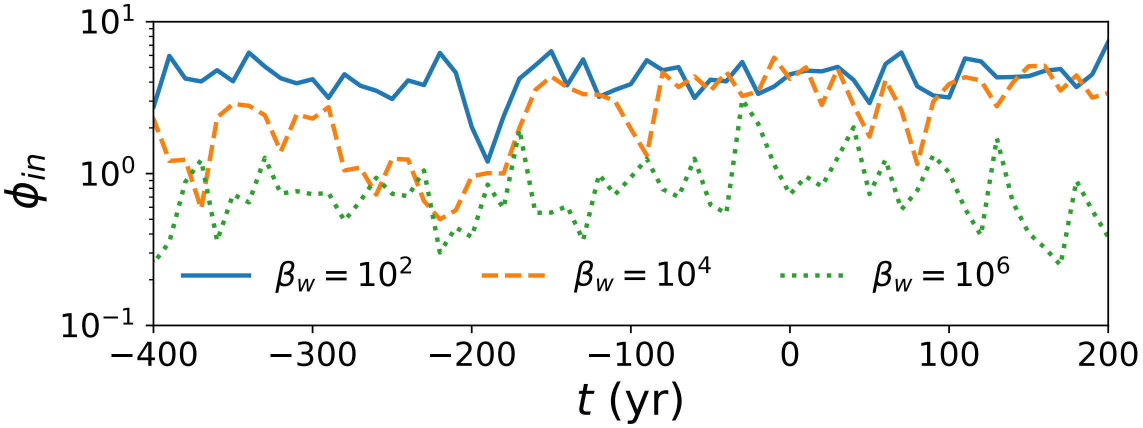

Figure 6.17: Magnetic flux threading the inner boundary as a function of time for our three MHD simulations, ϕ_{in}, in units such that the MAD value is ~ 50 (see Equation 6.6). Orders of magnitude difference β_w corresponds to only a factor of $\sim$ few difference in ϕ_{in} because the field strength at small radii is only weakly sensitive to β_w (Figure 6.6). In all cases ϕ_{in} is $\lesssim 10\%$ of the MAD limit. Magnetic reconnection regulates the value of ϕ_{in} so that it remains constant in time despite matter (and thus magnetic field) being continually accreted (bottom panel of Figure 6.7).

for our three MHD simulations. Across four orders of magnitude in β_w, ϕ_{in} varies by only a few, and for each run it is roughly constant in time. Averaged over the interval (-100 yr, 100 yr), the values are 4.4,3.5, and 1.1 for β_w of 10^2, 10^4, and 10^6, respectively, again in units where ~ 50 represents the MAD limit. These differences in ϕ_{in} are even smaller when extrapolated to smaller radii, which we do in §6.5.8. Briefly, we expect that for all reasonable β_w, ϕ_{in} at the horizon will be around the $\beta_w = 10^2$ value shown in Figure 6.17, independent of β_w. The result that ϕ_{in} becomes quasi-steady despite the fact that matter is continually being accreted (bottom panel of Figure 6.7) is noteworthy. This is likely a consequence of the magnetic field being accreted changing direction with time so that the incoming field reconnects with the field in the boundary in a way that regulates the value of ϕ_{in}. If instead the incoming field had the same orientation at all times, ϕ_{in} would show a continual rise until the field threading the boundary became strong enough to arrest accretion. Alternatively, it is possible that outflow preferentially removes magnetic fields, regulating the value of ϕ_{in}.

We quantify the relative strength of the vertical magnetic field by computing the ratio between the magnitude of the average magnetic field vector, $|\mathbf{B}|$, to the root-mean-squared field strength, $\sqrt{\langle B^2 \rangle}$. For a completely vertical field this quantity would be 1, while for a completely toroidal or random field it would be 0. Figure 6.18 plots $\langle|\mathbf{B}|\rangle/\sqrt{\langle B^2\rangle}$ averaged over angle and the inner 5×10^{-4} pc to 3×10^{-2} pc in radius for $\beta_w = 10^2, 10^4$, and 10^6, where we find that the relative strength of the ordered field increases with decreasing β_w. This same trend is seen in the poloidal field lines (Figure 6.19 where they are plotted on top of mass density), where the direction of the field goes from mostly random at $\beta_w = 10^6$, to nearly vertical at $\beta_w = 10^2$. The weaker the magnetic

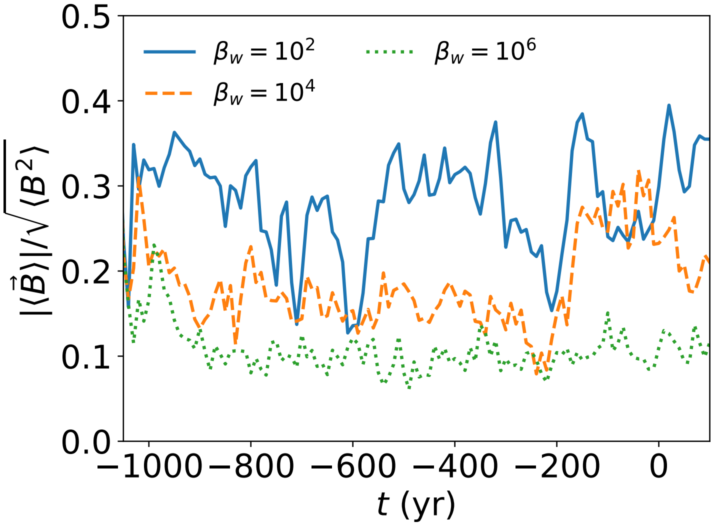

Figure 6.18: Magnitude of the time and angle-averaged magnetic field vector divided by the rms magnitude of the field for $\beta_w = 10^2$ (solid blue), $\beta_w = 10^4$ (dashed orange), and $\beta_w = 10^6$ (dotted green). This measures the degree to which the magnetic field is ordered, and increases with decreasing β_w because stronger fields are able to resist fluid motion and more effectively retain a coherent structure.

field, the more it is able to be twisted by the motion of the gas and lose its original structure.

The quantities plotted in Figures 6.18 and 6.19 do not effectively probe the φ component of the field, which in principle could be significant. To quantify this, we compare the relative strength of the mean B_φ to the mean B_r and B_θ field components. We define an 'antisymmetric' average of B_r as

$$\langle\tilde{B}_r\rangle = \int\limits_{t_1}^{t_2}\int\limits_{0}^{2\pi}\int\limits_{0}^{\pi/2} B_r d\theta d\varphi dt - \int\limits_{t_1}^{t_2}\int\limits_{0}^{2\pi}\int\limits_{\pi/2}^{\pi} B_r d\theta d\varphi dt, \tag{6.7}$$

where t_1 and t_2 are the endpoints of the time interval for averaging. The minus sign in Equation (6.7) prevents the radial field from averaging to zero over all angles. For $\beta_w = 10^6$, the toroidal field dominates with $\langle B_\varphi\rangle^2/\left(\langle\tilde{B}_r\rangle^2 + \langle B_\theta\rangle^2 + \langle B_\varphi\rangle^2\right) \approx 0.8 - 1$ for $r \lesssim 2\times10^{-2}$ pc because the field is weak enough to be completely stretched out by the orbital motion of gas. For $\beta_w = 10^4$, on the other hand, the field is able to resist the orbital motion (seen also in the torque that it exerts; Figure 6.15) and retain a predominantly poloidal structure, with $\langle B_\varphi\rangle/\left(\langle\tilde{B}_r\rangle^2 + \langle B_\theta\rangle^2 + \langle B_\varphi\rangle^2\right) \lesssim 0.2$ for $r \lesssim 3\times10^{-3}$ pc. This is even more true for $\beta_w = 10^2$, which has $\langle B_\varphi\rangle/\left(\langle\tilde{B}_r\rangle^2 + \langle B_\theta\rangle^2 + \langle B_\varphi\rangle^2\right) \lesssim 0.1$ for $r \lesssim 4\times10^{-3}$ pc.

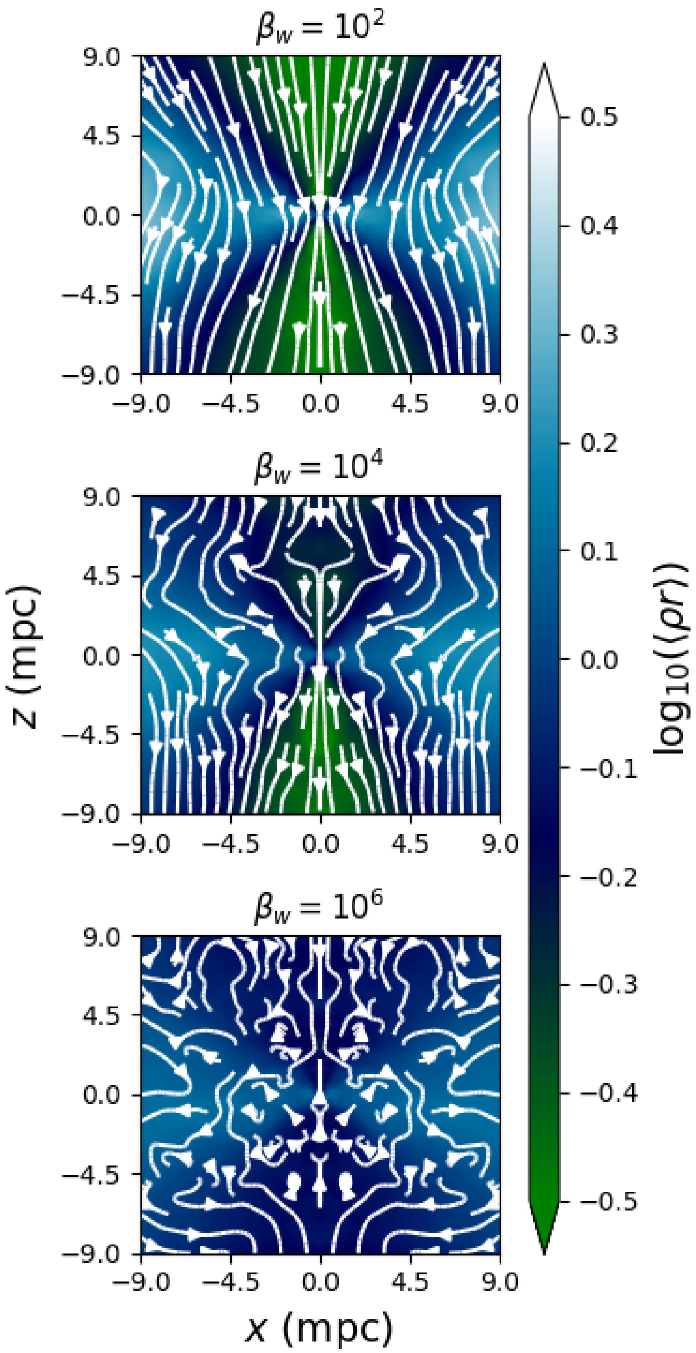

Figure 6.19: Time and φ-averaged mass density weighted by radius in a coordinate system such that the z-direction is aligned with the angular momentum of the gas (Figure 6.8), normalized, and overplotted with magnetic field lines for $\beta_w = 10^2$ (top), 10^4 (middle), and 10^6 (bottom). The stronger the field, the more it is able to resist being dragged along by the random motions of the flow and retain a coherent structure

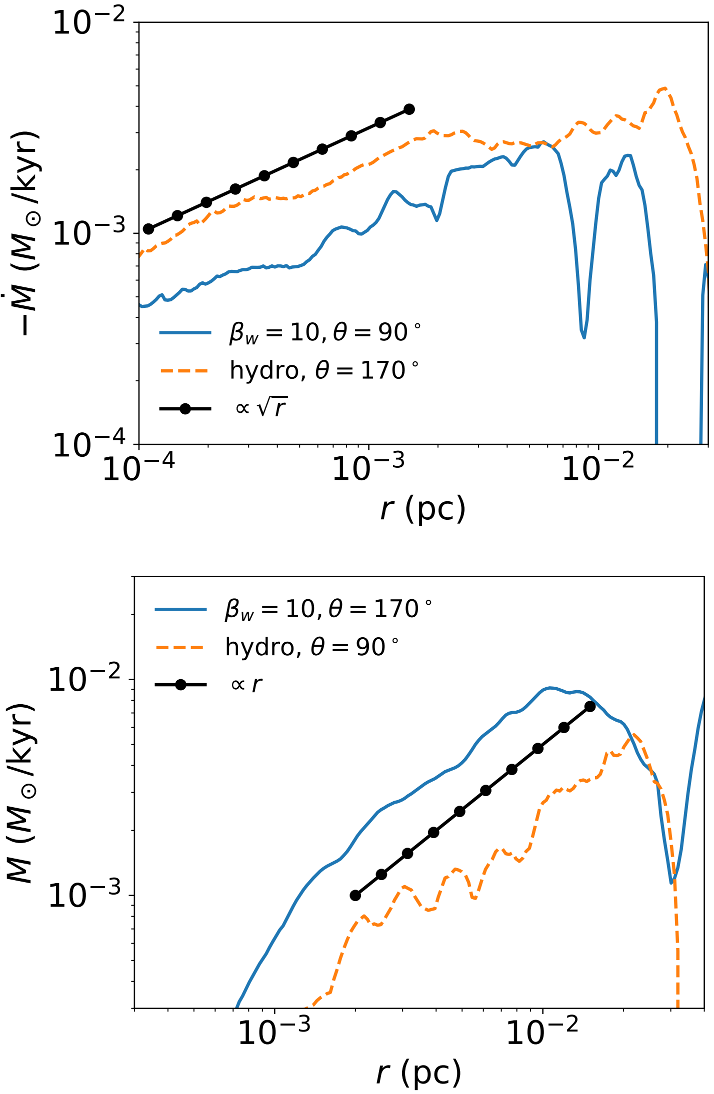

Figure 6.20: Top: Comparison between the time and φ-averaged accretion rate in the midplane for the $\beta_w = 10^2$ simulation (solid blue) vs. the pole for the hydrodynamic simulation (dashed orange). Both of these regions are dominated by inflow and show $\dot{M} \propto \sqrt{r}$ as expected for the $d\dot{M}/dl \approx$ const. distribution provided by the stellar winds. Bottom: Comparison between the time and φ-averaged accretion rate in the pole for the $\beta_w = 10^2$ simulation (solid blue) vs. the midplane for the hydrodynamic simulation (dashed orange). Both of these regions have a net outflow and show $\dot{M} \propto r$, implying a roughly constant velocity outflow since $\rho \propto r^{-1}$ (Figure 6.7).

6.5.7 Physical Interpretation of The Role of Magnetic Fields

Thus far we have presented seemingly paradoxical results. On one hand, for sufficiently magnetized stellar winds (e.g., $\beta_w = 10^2, 10^4$), the magnetic field at small radii reaches near equi-partition with the plasma, achieving $\beta \sim$ a few, reversing the polar inflow seen in hydrodynamic simulations, and driving accretion in the midplane. On the other hand, the net accretion rate through the inner boundary and the radially averaged fluid quantities are largely unaffected by the presence of magnetic fields. How can this be? In the conventional picture of MRI driven accretion from a rotationally supported torus, it would require an improbable cooincidence, where the midplane accretion driven by the MRI exactly equals the original hydrodynamic polar accretion despite the fact that they are governed by different physical considerations. As we have shown, however, our simulations do not fit this conventional picture. The gas with significant angular momentum clearly does *not* circularize into a configuration where the velocity is primarily in the azimuthal direction (e.g., Figures 6.9 and 6.10), but instead retains significant radial velocity of order free fall throughout the domain. Simply put, gas accreting from large radii is quick to either flow through the inner boundary or flow right back out. Magnetic fields are not strong enough to modify these flows by more than order unity even at $\beta \sim 1$. Moreover, even in the hydrodynamic simulation, inflow is not occurring only in the poles as Figure 6.12 would imply but at all polar angles. It is only in an azimuthally-averaged sense that v_r is positive and small in the midplane because there is also significant outflow present (at different φ). The primary role of magnetic fields, then, is not to drive accretion but to redirect the outflow from the midplane to the pole. This means that 1) the same physical processes govern accretion in the hydrodynamic and MHD simulations and 2) the net accretion rate is essentially determined by hydrodynamic considerations, namely, the distribution of angular momentum at large radii, a quantity set by the winds of the WR stars.

The lack of circularization in our simulations, the crucial factor in determining this accretion structure, is at least in part due to radiative cooling being inefficient at removing dissipated energy in the gas streamers seen in Figures 6.9 and 6.10. As the gas comes in along nearly parabolic orbits it heats up and (because it can't cool) expands outward, making it more difficult for it to circularize. This is analogous to the difficulty that simulations of tidal disruption events have in forming a circular accretion disc (for recent discussion, see, e.g., Stone et al. 2019; Lu & Bonnerot 2019).

6.5.8 Dependence On The Inner Boundary Radius

The simulations we have performed, while modeling a radial range of just over 4 orders of magnitude, are not able to penetrate all the way to the event horizon of Sgr A* but have inner boundary radii still a few hundred times farther out. Thus, it is important for us to understand how the artificially large inner boundary of our simulation (which acts as the black hole) affects the results. By varying the inner boundary, RQS18 showed that the predicted accretion rate through the inner boundary in our hydrodynamic simulations is $\dot{M} \approx 2.4 \times 10^{-8}$ $(r_{in}/r_G)^{1/2}$ $M_\odot$/yr, where the dependence on r_{in} is set by the distribution of accretion rate with angular momentum at large radii; for a smaller inner boundary radius, less material has angular momentum low enough to ultimately accrete. This predicted accretion rate is consistent with both observational constraints and emission models (see RQS18).

In MHD, we have shown that even for strong magnetic fields the radially averaged fluid variables are mostly unchanged going from hydrodynamics to MHD (Figure 6.7), including the accretion rate. Thus the above relation between $\dot{M}$ and r_{in} still holds. As we have argued in the preceding section, this counter-intuitive result is a consequence of the fact that the supply of infalling gas at small radii is still mostly set by the distribution of accretion rate with angular momentum at large radii. The gas provided by nearby stellar winds has a typical distribution of $d\dot{M}/dl \approx$ const. which results in $\dot{M}_{in} \propto \sqrt{r}$ (see Appendix A in RQS18). Note that since the winds emit at all angles, this is the distribution of infalling gas for both the poles and the midplane. Figure 6.20 confirms this expectation, showing that $\dot{M} \propto \sqrt{r}$ for the inflow in both hydrodynamics (in the polar region) and $\beta_w = 10^2$ MHD (in the midplane).

Figure 6.6 shows that β tends to decrease with decreasing radius until it reaches $\sim$ a few, at which point it becomes independent of radius. For $\beta_w = 10^2$ β is $\approx$ 1-2 and roughly constant throughout the domain, for $\beta_w = 10^4$ it decreases from $\beta \approx 200$ at large radii to $\beta \approx 2$ at $r \approx 6 \times 10^{-4}$ pc and remains constant for $r \lesssim 6 \times 10^{-4}$ pc, while for $\beta_w = 10^6$ it decreases from $\beta \approx 2 \times 10^4$ to $\beta \approx 4$ near the inner boundary. It is natural to suppose that if the inner boundary radius of the simulation was reduced then the $\beta_w = 10^6$ run would ultimately also reach $\beta \approx 2$. Regrettably this is not something we can test with our current computational resources; however, we can *increase* the size of the inner boundary and infer how β depends on r_{in} in the same way that we used to extrapolate $\dot{M}$ in RQS18. Doing so we estimate that all models with $\beta_w \leq 10^7$ will reach β of $\sim$ a few by 2 r_g (the event horizon radius of a non-rotating black hole). Thus $\beta_w \sim 10^7$ is a critical value that determines whether or not the horizon scale accretion flow will more closely resemble the hydrodynamic simulations ($\beta_w \gtrsim 10^7$) or the more magnetized wind simulations ($\beta_w \lesssim 10^7$).

Similar behavior is seen with the magnetic flux threading the inner boundary. Figure 6.21 shows the time-averaged ϕ_{in} for $\beta_w = 10^2$ and $\beta_w = 10^6$ and four values of the inner boundary radius. As was the case for β, ϕ_{in} is independent of r_{in} for $\beta_w = 10^2$. This is again because the $\beta_w = 10^2$ simulation has already reached $\beta \sim$ few at $r \gg r_{in}$. Since $\dot{M} \propto r_{in}^{1/2}\ v_{kep}(r_{in}) \propto r_{in}^{-1/2}$, Equation (6.6) gives $\phi_{in} \approx$ const. For $\beta_w = 10^6$ on the other hand, ϕ_{in} increases with decreasing r_{in}. Empirically, we find in Figure 6.21 that for $\beta_w = 10^6$, $\phi_{in} \propto r_{in}^{0.6}$, predicting that it will reach ≈ 5 by $r_{in} = 3 \times 10^{-6}$ pc $\approx 20\ r_g$. At that point, we expect ϕ_{in} to stop increasing in the same way that ϕ_{in} is independent of r_{in} for $\beta_w = 10^2$.

6.6 Comparison to Previous Work

In analyzing our simulations, we have found it instructive to compare and contrast our results with previous simulations in the literature that considered the problem of accretion onto Sgr A* and related systems via large scale feeding. In this section we do so for two key works.

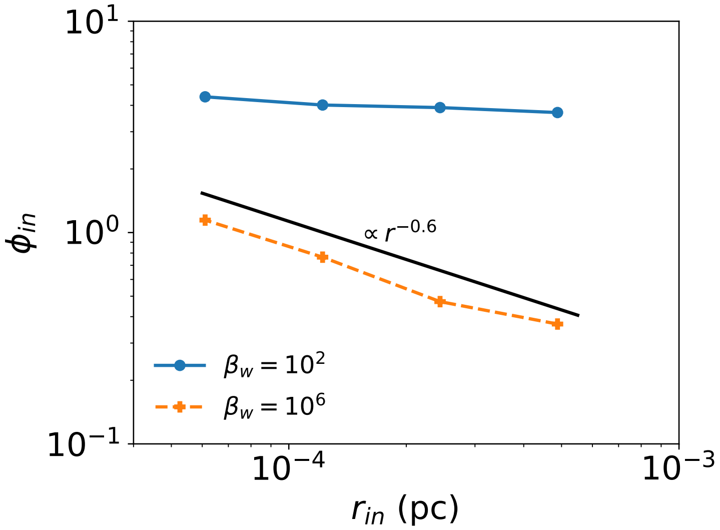

Figure 6.21: Magnetic flux threading the inner boundary of our simulation, ϕ_{in} (Equation 6.6), averaged over the time interval (-100 yr,100 yr) and plotted as a function of inner boundary radius for $\beta_w = 10^2$ (blue solid) and $\beta_w = 10^6$ (orange dashed). ϕ_{in} is independent of r_{in} for $\beta_w = 10^2$ where β has reached ~ few (Figure 6.6), while it increases with decreasing r_{in} for $\beta_w = 10^6$ because β is decreasing with decreasing r_{in}. For $\beta_w = 10^6$ we find $\phi_{in} \tilde{\propto} r^{0.6}$ and thus expect it to reach ~ 5 (the $\beta_w = 10^2$ value) for an inner boundary at the event horizon.

6.6.1 Proga & Begelman 2003

Proga & Begelman (2003a,b) (hereafter PB03A and PB03B) presented the results of 2D inviscid hydrodynamic (PB03A) and MHD (PB03B) simulations of accretion onto supermassive black holes as fed by gas with a θ-dependent distribution of angular momentum at large radii. This approach differs from the standard method of initializing simulations with equilibrium tori without any feeding at large radii and is perhaps a better approximation of the feeding of gas via stellar winds in the Galactic Centre. In fact, in many ways the results of PB03A and PB03B are strikingly similar to the results of RQS18 and those presented here. We both find that accretion in hydrodynamic simulations occurs via low angular momentum gas falling in mostly along the polar regions while the higher angular momentum midplane is (on average) outflowing. We both also find that this structure is reversed in MHD for sufficiently large magnetic fields, with the low angular momentum polar inflow getting quenched by magnetically driven polar outflow while gas in the midplane accretes. PB03B, however, found that the accretion rate in the MHD case was significantly reduced compared to the hydrodynamic case because the induced midplane accretion was not enough to compensate for the loss of polar inflow. In this work, on the other hand, the midplane accretion in MHD seems to roughly equal the original hydrodynamic polar inflow so that the net accretion rate is relatively the same in MHD and hydrodynamics.

The key difference lies in the structure of the high angular momentum gas in the midplane. PB03A found that this gas was able to circularise and build up into a nearly constant angular momentum torus that blocked the inward flow of gas for polar angles close to the equator. We find that the high angular momentum gas in our hydrodynamic simulation never circularises but mostly flows right back out after falling in to small radii. This is more easily accomplished in 3D where flow streams can avoid intersecting; in 2D axisymmetry (used in PB03A and PB03B), collisions between the infalling and outflowing high angular momentum gas are unavoidable and can dissipate radial kinetic energy and efficiently circularise the material. Because of this circularisation in PB03A, by adding even a weak magnetic field, the MRI is able to grow as the gas in the torus orbits and becomes the dominant driver of accretion. Thus, the accretion rate in PB03B is mostly set by completely different physical considerations (the properties of the MRI) than in PB03A (the availability of low/zero angular momentum gas). In our simulations, however, even in MHD the dominant source of accretion is still the supply of low angular momentum gas with an order unity correction for global torques provided by strong magnetic fields that have been compressed to β $\sim$ few at small radii. This means that the local supply of mass available to accrete is set mostly by hydrodynamic considerations (i.e., the distribution of angular momentum vs. accretion rate provided by the nearest stellar winds).

One of the main conclusions of PB03B was that the MRI driven accretion seen in their simulations was roughly independent of the angular momentum distribution of material sourced at large radii, ultimately resembling simulations that are initialized with an equilibrium torus seeded by a weak magnetic field. This served as partial motivation and justification for future work to mostly ignore large radii and instead focus on horizon scale ($\lesssim 100 - 1000 r_g$) simulations starting from equilibrium tori. Our results, however, suggest that when a more complicated treatment of accretion sourced by stellar winds in full 3D is considered, the properties of the accretion flow at small radii are very strongly influenced. We suspect that the major source of this difference is the non-axisymmetric nature of how the gas is fed by the winds, which inhibits circularization.

6.6.2 Pang et al. 2011

Pang et al. (2011) (P11) presented 3D MHD simulations in which gas is fed through the outer boundary with uniform magnetic field, spherically symmetric density and pressure, and purely rotational velocity such that the specific angular momentum l, varies as $\sin(\theta)$. This set up is quite similar to PB03B except for the field geometry (uniform vs. radial in PB03B), the field strength, and the addition of a third dimension. Unlike PB03B, however, P11 found that global magnetic torques and not the MRI were the governing physical mechanisms driving accretion in their simulations. This difference relative to PB03B is probably a consequence of the initial magnetic field in P11 being much stronger, with the initial β being $\sim 10^2$ in P11 compared to $\beta \sim 10^5 - 10^7$ in PB03B. This causes the magnetic field to become dynamically important before the gas can circularize (if it ever would have) and also suppresses the MRI. Dissipation of the field also leads to an unstable entropy profile, driving convection. A steady state is reached in which the gas is in near hydrostatic equilibrium, slowly falling inwards with magnetic pressure resisting the upward buoyancy force. Several aspects of the P11 simulations are similar to what we have found in ours. Both show a lack of circularization, both have the MRI suppressed by strong magnetic fields, and both find a density profile of $\sim r^{-1}$ with a corresponding $\dot{M} \propto \sqrt{r_{in}}$ relationship. At the same time, the accretion flow structures are very different in the two sets of calculations. Unlike P11, the gas in our simulations is not hydrostatic, because the ram pressure, ρv^2 is comparable to or larger than the magnetic and thermal pressures throughout the domain. We also find significant and coherent outflow, something absent in P11.

The root cause of these differences are related to the more complicated, asymmetric way that the winds of the WR stars supply gas (and magnetic field) to the black hole. While both sets of simulations can contain relatively large and coherent magnetic fields at large radii, the steady state of P11 is one in which the gas is being sourced in an approximately spherically symmetric way with rotation playing only a minor role. This is because after the initial transient in which the sourced gas first free falls and then transitions to a PB03A-like configuration, the build up of gas at small radii provides radial pressure support for the gas at large radii, significantly increasing the time it takes to accrete. At this point the magnetic torques have enough time to remove a large amount of the angular momentum at large radii, ultimately resulting in a quasi-spherical steady-state. In contrast, because the feeding in our simulations occurs in more of a stream-like manner (Figures 6.9 and 6.10), we have no build-up of gas to provide radial pressure support. Instead, radial velocities remain large and thus the effect of even significant ($\beta \sim$ few) magnetic torques are limited by the short inflow/outflow times. This means that rotation of gas is important throughout our simulations, with the distribution of angular momentum being the primary determinant of the accretion rate.

6.7 Implications for Horizon-Scale Modeling

The main properties of nearly all GRMHD simulations used to model the galactic center are governed by the evolution of the MRI. The supply of gas is determined by an initial rotating torus while low angular momentum material is absent. Our results suggest that for the galactic centre it may be critical to consider a more detailed model for how the gas is fed into the domain, particularly with respect to the distribution of angular momentum coming in from larger radii.

One large remaining uncertainty is how strong the outflows are from near the horizon and whether they significantly modify the dynamics at $\sim 1000\ r_g$ found here. Figure 6.5 shows that, at times, we do see strong outflows that can modify the gas out to ~ 0.3 pc scales. Since we find that $\dot{M} \propto \sqrt{r_{in}}$, the energy released in outflows should scale with the inner boundary as $\propto \dot{M} v_{kep}^2 \propto r_{in}^{-1/2}$, meaning that the strength of this outflow would be a factor of $\gtrsim \sqrt{150} \approx 10$ times higher if our simulation reached the event horizon. Additionally, if the black hole is rapidly rotating the magnetic field can extract a significant amount of energy from the black hole and further increase the energy in the outflow (Blandford & Znajek 1977b).

The time variability of the polarization vector observed in the GRAVITY flares (Gravity Collaboration et al. 2018) at $\sim 10\ r_g$ has been interpreted as the results of an orbitting "hot spot" embedded in a face-on rotating flow threaded by a magnetic field primarily in the vertical direction. Qualitatively, the geometry of the magnetic field at small radii in our $\beta_w = 10^2$ simulation agrees with this picture (Figures 6.19), with the poloidal field being larger than B_φ. On the other hand, the angular momentum direction of the inner accretion flow in Figure 6.8 is rarely as face-on as that of the best-fit orbit of the three flares ($L_z/L \approx 0.94 \pm 0.06$).

Psaltis et al. (2015) showed that preliminary EHT measurements of the size of the emitting region for Sgr A* 230 GHz are smaller than the expected "shadow" of the black hole: the distinct lack of emission caused by the presence of an innermost photon orbit. The authors use this measurement to constrain the angular momentum direction of the disc/black hole (which they assume to be aligned), and find that an inclination angle roughly aligned with the clockwise stellar disc is preferred. This is consistent with measurements of the position angle of the 86 GHz and X-ray emission performed by the VLBA on a scale of $\sim$ 10s of r_g (Bower et al. 2014) and by *Chandra* on a much larger scale of $\sim$ 1" (Wang et al. 2013), respectively. Our results are in good agreement with these observations, as the angular momentum of our innermost accretion flow is typically aligned with the stellar disc (Figure 6.8). Forthcoming higher sensitivity EHT measurements will be important for resolving the discrepancy with the leading interpretation of the GRAVITY data.

6.8 Conclusions

We have presented the results of 3D simulations of accretion onto the supermassive black hole in the galactic centre fueled by magnetized stellar winds. Our simulations span a large radial range, having an outer boundary of 1 pc and an inner boundary of $\sim 6 \times 10^{-6}$ pc ($\sim 300 r_g$), with approximately logarithmic resolution in between. The mass loss rates, wind speeds, and orbits of the stellar wind source terms that represent the $\sim$ 30 WR stars are largely constrained by observations while the relative strength of the magnetic field in each wind is parameterized by a single parameter β_w, defined as the ratio between the ram pressure and midplane magnetic pressure of the wind. In previous work, we have shown that our simulations naturally reproduce many of the observational properties of Sgr A* such as an accretion rate that is much less than the Bondi estimate, a density profile $\tilde{\propto} r^{-1}$, a total X-ray luminosity consistent with *Chandra* measurements, and the rotation measure of Sgr A*. In the present chapter we have focussed on the dynamics of accretion onto Sgr A* from magnetized stellar winds.

Our most significant and a priori surprising result is that the accretion rate onto the black hole, as well as the radial profiles of mass density, temperature, and velocity are set mostly by hydrodynamic considerations (Figure 6.7). This is true even when plasma β is as low as ≈ 2 over a large radial range (Figure 6.6). Without magnetic fields, the accretion rate and density profiles are set by the distribution of angular momentum with accretion rate provided by the stellar winds, a distribution which extends down to $l \approx 0$. This broad range of angular momentum is a consequence of the fact that the WR stellar wind speeds ($\sim$ 1000 km/s) are comparable to their orbital speeds. As a result, the stellar winds provide enough low angular momentum material to result in an extrapolated accretion rate that is in good agreement with previous estimates for Sgr A*. With magnetic fields, global torques provide only order unity corrections to this picture, with the accretion rate still mostly being determined by the supply of low angular momentum gas. This is a consequence of the fact that the high angular momentum material in our simulations does not circularize but mostly flows in and out with large enough radial velocity that the inflow/outflow times are short compared to the time scale for magnetic stresses to redistribute angular momentum.

Simulations with strong magnetic fields at small radii do however differ from hydrodynamic simulations in one important way. Hydrodynamic simulations are dominated by inflow along the poles, while the midplane is on average outflowing but composed of both inflow and outflow components at different θ and φ. By contrast, MHD simulations are dominated by inflow in the midplane, while the polar regions are on average outflowing but composed of both inflow and outflow components at different θ and φ. This is a consequence of the $\beta \sim$ few magnetic fields redirecting the high angular momentum outflow away from the midplane.

We find that the magnetic field increases rapidly with radius so that β tends to eventually saturate at small radii to a value of order unity independent of β_w (Figure 6.6). This growth of the field is caused by advection/compression as gas falls inwards and not by the MRI. There is neither sufficient time for the MRI to grow before gas is accreted or advected to larger radii, nor is there sufficient space for the instability to grow because flux freezing builds up a field for which the most unstable MRI wavelength is comparable to or larger than the disc scale height (Figure 6.16). Thus the conventional MRI-driven torus simulations that dominate the literature do not appear to have reasonable initial conditions for studying accretion in the galactic centre, at least on the scales that we can simulate here.

Elaborating on the result first presented RQS19, we have shown that our model predicts that the magnetic flux ultimately threading the event horizon, ϕ_{in}, will be $\sim$ 10% of the MAD limit, independent of β_w for $\beta_w \lesssim 10^7$ (Figure 6.21). Furthermore, we find that ϕ_{in} is relatively independent of time (Figure 6.17). An important caveat is that this prediction relies on extrapolation to smaller radii and assumes that the scaling between ϕ_{in} and the inner boundary radius that we found (Figure

6.21) holds at smaller radii than our simulations probe.

For sufficiently magnetized winds (i.e., $\beta_w = 10^2$ here), the magnetically driven, polar outflow can, at times, reach scales as large as ~ 0.3 pc (Figure 6.5). Since we expect the energy associated with this outflow to increase with decreasing inner boundary radius, it could potentially be a factor of > 10 times stronger in a simulation that reached the event horizon. This is even without considering the rotation of the black hole itself, which can also be an efficient mechanism for driving magnetized jets. Though there is no clear signature of a jet in the galactic centre, strong outflows from Sgr A* have been invoked as one possible explanation for the recent ALMA observations that show highly blue-shifted emission from unbound gas in a narrow cone (Royster et al. 2019).

The magnetic field structure at small radii depends on the parameter β_w (Figure 6.19). For smaller β_w (10^2 and to a lesser extent, 10^4) the field is strong enough to resist being wound up in the φ direction and remains mostly poloidal at small radii. For larger β_w ($\gtrsim 10^6$), the field is easily dragged along with the motion of the gas so that it becomes predominantly toroidal by the time β reaches order unity. The leading interpretation of the GRAVITY observations of astrometric motion of the IR emission during Sgr A* flares (Gravity Collaboration et al. 2018) requires that the horizon scale magnetic field be mostly perpendicular to the angular momentum of the gas. We find qualitative agreement with this result in our simulations that have more magnetized winds. A more quantitative comparison to the observations using full radiative transfer in GRMHD simulations using such a field as initial conditions will require additional work.

Cuadra et al. (2008) found that the winds of only 3 WR stars (E20/IRS 16C, E23/IRS 16SW, and E39/IRS 16NE) dominated the $t = 0$ accretion budget in their simulations that used the '`1DISC`' orbital configuration. This is both because of the proximity and relatively slow wind speeds (~ 600 km/s) of these winds. Since we adopted the '`1DISC`' configuration from Cuadra et al. (2008) with only slight changes, it is not surprising that the same three stellar winds seem to be the most important for determining the properties of the innermost accretion flow in our simulations[3] (e.g., Figures 6.9 and 6.10). Future observations that place stronger constraints on the mass-loss rates, wind speeds, and especially the magnetic field strengths of these stars would thus go a long way towards reducing the uncertainty in our calculation.

Several observations suggest that gas surrounding Sgr A* is aligned with the clockwise stellar disc both near the horizon and just inside the Bondi radius (Wang et al. 2013; Bower et al. 2014; Psaltis et al. 2015; though see also Gravity Collaboration et al. 2018). Our simulations are consistent with this result for $\beta_w \geq 10^2$ (Figure 6.8) but not for $\beta_w = 10$ due to wind collimation altering the distribution of angular momentum in the winds (Figure 6.A.2). If a large fraction of the accreting gas (and associated magnetic field) were sourced from material outside the region where the majority of the WR stars reside, then it would also be unlikely for its angular momentum to coincide with the stellar disc. In all of our simulations, the direction of the angular momentum of the inner accretion flow is not strictly constant in time over the ~ 1000 yr duration of our simulation (Figure 6.8). Therefore, the angular momentum of the gas sourcing the horizon scale accretion flow *must* be tilted with respect to the spin of the black hole at least moderately often since the

---

[3] Unlike the particle based calculation of Cuadra et al. (2008), we do not have a rigorous way to track the gas from each individual wind in our current implementation. We can only infer which stellar winds dominate the accretion budget from, e.g., the poloidal and toroidal animations.

time scale for the spin of the black hole to change is much longer than 1000 yr. Simulations of tilted accretion discs are thus likely necessary for horizon scale modeling of Sgr A*.

Our results could have a significant impact on current state of the art models of horizon scale accretion onto Sgr A*. GRMHD simulations to date almost universally rely on the MRI as the mechanism to drive accretion. It is not clear how much the results of these simulations and their observational consequences might change using the dynamically different flow structure found here. For instance, if the disc is less turbulent without the MRI, how does this effect the time-variability properties of the emission? Would nearly empty, magnetically dominated jets still be robustly present in GRMHD and does this depend on black hole spin and horizon-scale flux in the same way as in current simulations (e.g. Tchekhovskoy et al. 2011)? Such questions and more will be important to answer in order to further our understanding of the emission from Sgr A* and other low luminosity AGN.

Acknowledgments

We thank F. Yusef-Zadeh for useful discussions, as well as all the members of the horizon collaboration, http://horizon.astro.illinois.edu. EQ thanks the Princeton Astrophysical Sciences department and the theoretical astrophysics group and Moore Distinguished Scholar program at Caltech for their hospitality and support. This work was supported in part by NSF grants AST 13-33612, AST 1715054, AST-1715277, *Chandra* theory grant TM7-18006X from the Smithsonian Institution, a Simons Investigator award from the Simons Foundation, and by the NSF through an XSEDE computational time allocation TG-AST090038 on SDSC Comet. This chapter was made possible by computing time granted by UCB on the Savio cluster.

Appendix

6.A $\beta_w = 10$

In the main text we limited our analysis to $\beta_w \geq 10^2$ because smaller β_w leads to collimation of the stellar winds (Figure 6.2). This collimation, however, does not effect most of the main conclusions of this work, as we will now show.

The top panel of Figure 6.A.1 compares the time and angle-averaged hydrodynamic variables in the $\beta_w = 10$ simulation to those of the $\beta_w = 10^2$ simulation at times when the angular momentum direction at small radii is $\sim$ constant in time. The two simulations produce nearly identical mass density, sound speed, radial velocity, magnitude of angular momentum, and accretion rate when averaged over all angles. Thus our conclusion in the main text that magnetic fields do not play a leading role in determining the accretion rate still holds even with wind collimation. The bottom panel of Figure 6.A.1 shows the RMS magnetic field strength and β averaged over time and angle for the same two simulations. At large radii, the RMS field is only a factor of $\lesssim 2$ larger for $\beta_w = 10$ vs. $\beta_w = 10^2$, corresponding to a factor of $\sim$ 2-3 in β. This factor is smaller than 10 because the field is already $\beta \sim$ few in the $\beta_w = 10^2$ simulation, so even thought the magnetic pressure in the $\beta_w = 10$ winds are 10 times stronger, the gas saturates at $\beta \sim 1$. Conversely, at small radii, the field in the $\beta_w = 10$ simulation is actually *weaker* than the field in the $\beta_w = 10^2$ simulation by a factor of ~ 3.

Wind collimation has the most significant effect on the angular momentum direction of the inner accretion flow, as shown in Figure 6.A.2 which plots $\theta_{\rm disc}$, the angle between the accretion flow angular momentum and that of the stellar disc. For $\beta_w \geq 10^2$ (including the hydrodynamic run), the angular momentum of the gas is, for the most part, typically aligned with the stellar disc, with $\theta_{\rm disc} \sim 10^\circ - 40^\circ$. For $\beta_w = 10$ on the other hand, $\theta_{\rm disc}$ is much larger and even approaches 180°, where the gas rotates in the opposite direction of the stellar disc. This is because the collimation of the stellar winds has a non-trivial effect on the net angular momentum of the winds so that the angular momentum of the accretion flow depends more strongly on the spin axis of the stars (which determines where the winds collimate) than their orbital angular momentum.

6.B Resolution Study

We have argued in the main text in §6.5.5 that the MRI is not the governing mechanism for accretion in our simulations even though the most unstable wavelength is well resolved (Figure

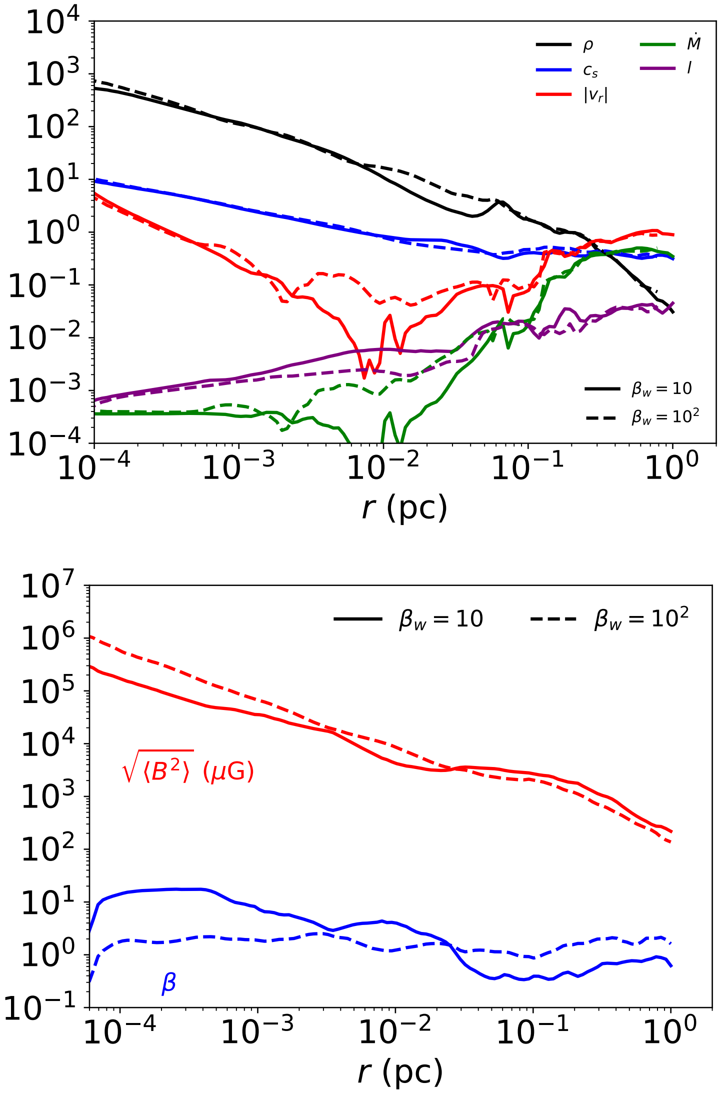

Figure 6.A.1: Comparison between time and angle-averaged quantities in the $\beta_w = 10$ (solid) and $\beta_w = 10^2$ (dashed) MHD simulations. Time intervals for averaging were chosen such that the angular momentum direction of the gas at small radii are relatively stable (0 ± 30 yr for $\beta_w = 10$ and 150 ± 30 yr for $\beta_w = 10^2$; see Figure 6.8 and top panel of Figure 6.A.2). Top: Mass density, ρ ($\mathrm{M}_\odot/\mathrm{pc}^3$), sound speed, c_s (pc/kyr), radial velocity, $|v_r|$ (pc/kyr), specific angular momentum, l, and mass accretion rate, $|\dot{M}|$ ($\mathrm{M}_\odot$/kyr), as a function of distance from the black hole. Bottom: RMS magnetic field strength, $\sqrt{\langle B^2 \rangle}$, and plasma β, $\langle P \rangle / \langle P_B \rangle$. The radial profiles of the hydrodynamic variables are essentially the same in two simulations, both of which are similar to the hydrodynamic simulation (Figure 6.7). Counter-intuitively, however, the $\beta_w = 10$ simulation has a weaker magnetic field at small radii (by a factor of ~ 3 for $r \lesssim 3 \times 10^{-3}$ pc) than the $\beta_w = 10^2$ simulation, despite having a stronger magnetic field at large radii (by a factor of $\lesssim 2$).

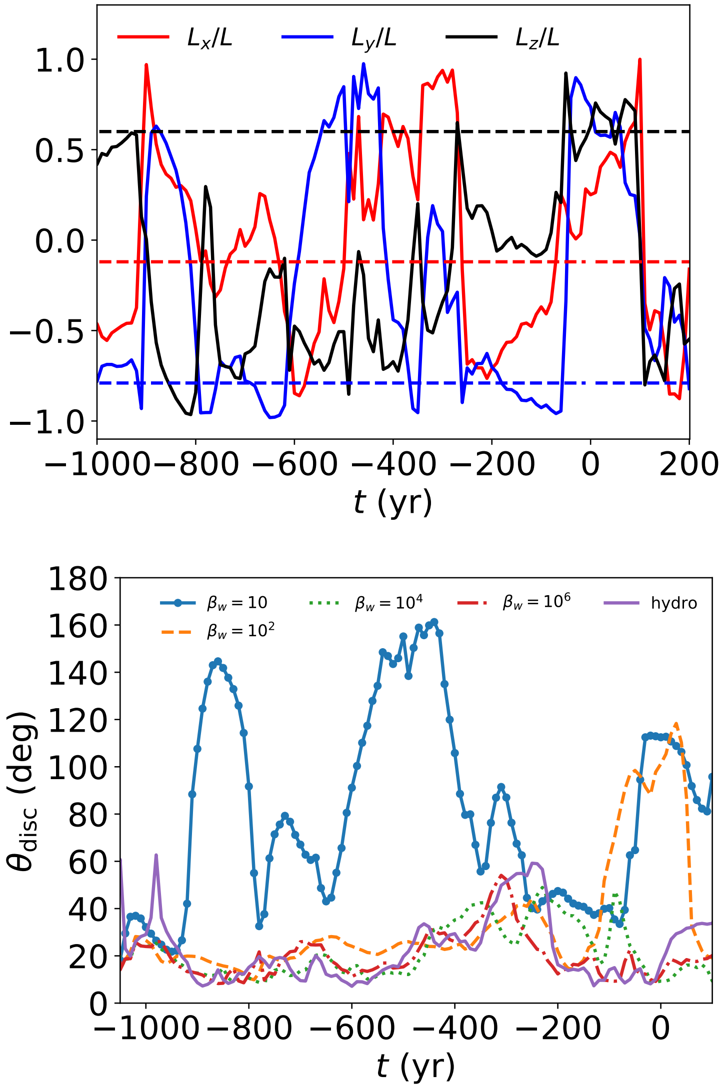

Figure 6.A.2: Top: Angular momentum direction as a function of time for the gas in our $\beta_w = 10$ simulation, averaged in radius and angle over 5×10^4 pc to 3×10^{-2} pc. Bottom: Angle that the net angular momentum of the inner accretion flow makes with the stellar disc for $\beta_w = 10$ (solid blue) compared with the rest of our simulations. The collimation of the stellar winds that is present in the $\beta_w = 10$ simulation (see §6.4) has a marked effect on the angular momentum of the resulting accretion flow which now shows much more significant and frequent deviations from the stellar disc and the time variability is of larger amplitude and higher frequency (cf. Figure 6.8).

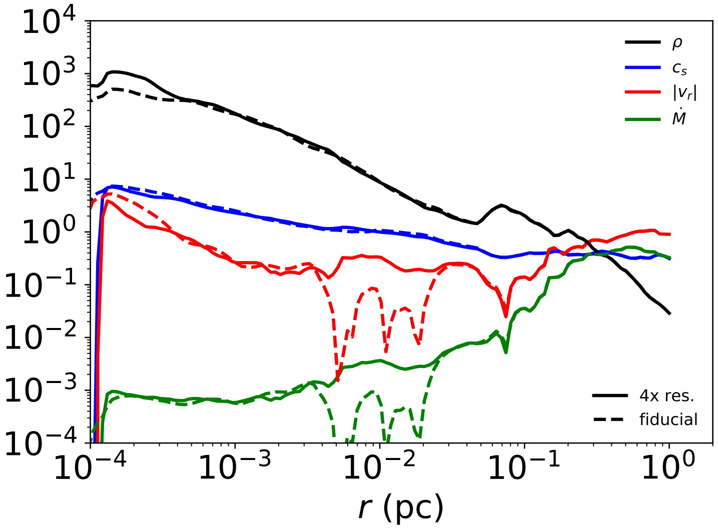

Figure 6.B.1: Demonstration of convergence for $\beta_w = 10$ simulations. Dashed lines are from a simulation at the fiducial resolution while solid lines are from a simulation with a factor of 4 higher resolution for $r \lesssim 0.06$ pc. The angle averaged mass density, ρ (black), sound speed, c_s (blue), radial velocity, v_r (red), and accretion rate, $\dot{M}$ (green), are essentially identical after being run for 25 yr (one orbital time at ≈ 0.02 pc) and thus converged at the fiducial resolution used throughout this work.

6.16). However, to be assured that resolution is not affecting our results, we performed two additional simulation with $\beta_w = 10$ and an inner boundary radius of $r_{in} \approx 1.2 \times 10^{-4}$ pc. The first simulation was run for 1.025 kyr until $t = -0.075$ kyr with our usual base resolution of 128^3 cells with 8 levels of mesh refinement that increase the resolution by a factor of 2 each time the radius decreases by a factor of 2. The second simulation increased the resolution by a factor of four within ~ 0.06 pc and ran for 25 yr after being restarted from the lower resolution simulation at -0.1 kyr. 25 yr is approximately an orbital time at 0.02 pc and thus spans many orbital times for the small radii of interest. Figure 6.B.1 shows that the resulting radial profiles of angle-averaged fluid quantities in the two simulations are nearly identical. Thus we are confident that the general properties of our simulations are well converged and not limited by resolution.

Bibliography

Aitken, D. K., Greaves, J., Chrysostomou, A., et al. 2000, ApJL, 534, L173
An, T., Goss, W. M., Zhao, J.-H., et al. 2005, ApJl, 634, L49
Anderson, J. L., & Witting, H. R. 1974, Physica, 74, 466
Andersson, N., & Lopez-Monsalvo, C. S. 2011, Classical and Quantum Gravity, 28, 195023
Antón, L., Zanotti, O., Miralles, J. A., et al. 2006, ApJ, 637, 296
Baganoff, F. K., Maeda, Y., Morris, M., et al. 2003, ApJ, 591, 891
Balbus, S. A., & Hawley, J. F. 1991a, ApJ, 376, 214
—. 1991b, ApJ, 376, 214
Ball, D., Özel, F., Psaltis, D., & Chan, C.-k. 2016, ApJ, 826, 77
Barrière, N. M., Tomsick, J. A., Baganoff, F. K., et al. 2014, ApJ, 786, 46
Bartko, H., Martins, F., Fritz, T. K., et al. 2009, ApJ, 697, 1741
Beloborodov, A. M., Levin, Y., Eisenhauer, F., et al. 2006, ApJ, 648, 405
Blandford, R. D., & Begelman, M. C. 1999, MNRAS, 303, L1
Blandford, R. D., & Königl, A. 1979, ApJ, 232, 34
Blandford, R. D., & Payne, D. G. 1982, MNRAS, 199, 883
Blandford, R. D., & Znajek, R. L. 1977a, MNRAS, 179, 433
—. 1977b, MNRAS, 179, 433
Bondi, H., & Hoyle, F. 1944, MNRAS, 104, 273
Bourouaine, S., Verscharen, D., Chandran, B. D. G., Maruca, B. A., & Kasper, J. C. 2013, ApjL, 777, L3
Bower, G. C., Falcke, H., Sault, R. J., & Backer, D. C. 2002, ApJ, 571, 843
Bower, G. C., Wright, M. C. H., Falcke, H., & Backer, D. C. 2003, ApJ, 588, 331
Bower, G. C., Markoff, S., Brunthaler, A., et al. 2014, ApJ, 790, 1
Bower, G. C., Markoff, S., Dexter, J., et al. 2015a, ApJ, 802, 69
Bower, G. C., Deller, A., Demorest, P., et al. 2015b, ApJ, 798, 120
Bower, G. C., Broderick, A., Dexter, J., et al. 2018, ApJ, 868, 101
Calderón, D., Ballone, A., Cuadra, J., et al. 2016, MNRAS, 455, 4388
Chael, A., Narayan, R., & Johnson, M. D. 2019, MNRAS, 486, 2873
Chael, A., Rowan, M. E., Narayan, R., Johnson, M. D., & Sironi, L. 2018, ArXiv e-prints, arXiv:1804.06416 [astro-ph.HE]
Chael, A. A., Narayan, R., & Saḑowski, A. 2017, MNRAS, 470, 2367
Chan, C.-K., Psaltis, D., Özel, F., et al. 2015a, ApJ, 812, 103

Chan, C.-K., Psaltis, D., Özel, F., Narayan, R., & Sadowski, A. 2015b, ApJ, 799, 1
Chandra, M., Foucart, F., & Gammie, C. F. 2015a, ApJ, in prep.
Chandra, M., Gammie, C. F., Foucart, F., & Quataert, E. 2015b, ApJ, 810, 162
Chandran, B. D. G., Dennis, T. J., Quataert, E., & Bale, S. D. 2011, ApJ, 743, 197
Chu, D. S., Do, T., Hees, A., et al. 2018, ApJ, 854, 12
Cotera, A., Morris, M., Ghez, A. M., et al. 1999, in Astronomical Society of the Pacific Conference Series, Vol. 186, The Central Parsecs of the Galaxy, ed. H. Falcke, A. Cotera, W. J. Duschl, F. Melia, & M. J. Rieke, 240
Cranmer, S. R., Matthaeus, W. H., Breech, B. A., & Kasper, J. C. 2009, ApJ, 702, 1604
Cuadra, J., Nayakshin, S., & Martins, F. 2008, MNRAS, 383, 458
Cuadra, J., Nayakshin, S., Springel, V., & Di Matteo, T. 2005, MNRAS, 360, L55
—. 2006, MNRAS, 366, 358
Cuadra, J., Nayakshin, S., & Wang, Q. D. 2015, MNRAS, 450, 277
Davis, S. W., Stone, J. M., & Pessah, M. E. 2010, ApJ, 713, 52
De Villiers, J.-P., & Hawley, J. F. 2003, ApJ, 589, 458
Desvignes, G., Eatough, R. P., Pen, U. L., et al. 2018, ApJL, 852, L12
Dexter, J. 2016, MNRAS, 462, 115
Dibi, S., Drappeau, S., Fragile, P. C., Markoff, S., & Dexter, J. 2012, MNRAS, 426, 1928
Do, T., Ghez, A. M., Morris, M. R., et al. 2009, ApJ, 691, 1021
Doeleman, S., Agol, E., Backer, D., et al. 2009, in Astronomy, Vol. 2010, astro2010: The Astronomy and Astrophysics Decadal Survey, 68
Doeleman, S. S., Weintroub, J., Rogers, A. E. E., et al. 2008, Nature, 455, 78
Dolence, J. C., Gammie, C. F., Mościbrodzka, M., & Leung, P. K. 2009, ApJs, 184, 387
Donati, J.-F., & Landstreet, J. D. 2009, ARA&A, 47, 333
Drappeau, S., Dibi, S., Dexter, J., Markoff, S., & Fragile, P. C. 2013, MNRAS, 431, 2872
Eatough, R. P., Falcke, H., Karuppusamy, R., et al. 2013, Nature, 501, 391
Eckart, A., García-Marín, M., Vogel, S. N., et al. 2012, A & A, 537, A52
Eckart, C. 1940, Phys. Rev., 58, 919
Event Horizon Telescope Collaboration, Akiyama, K., Alberdi, A., et al. 2019a, ApJL, 875, L1
—. 2019b, ApJL, 875, L2
—. 2019c, ApJL, 875, L3
—. 2019d, ApJL, 875, L4
—. 2019e, ApJL, 875, L5
—. 2019f, ApJL, 875, L6
Falcke, H., & Biermann, P. L. 1995, A&A, 293, 665
Falcke, H., Goss, W. M., Matsuo, H., et al. 1998, ApJ, 499, 731
Feldmeier-Krause, A., Zhu, L., Neumayer, N., et al. 2017, MNRAS, 466, 4040
Fishbone, L. G., & Moncrief, V. 1976, ApJ, 207, 962
Foucart, F., Chandra, M., Gammie, C. F., & Quataert, E. 2016, MNRAS, 456, 1332
Foucart, F., Chandra, M., Gammie, C. F., Quataert, E., & Tchekhovskoy, A. 2017, MNRAS, 470, 2240
Fragile, P. C., & Anninos, P. 2005, ApJ, 623, 347

Gammie, C. F., McKinney, J. C., & Tóth, G. 2003, ApJ, 589, 444

Gary, S. P., & Nishimura, K. 2003, Physics of Plasmas, 10, 3571

Gary, S. P., & Wang, J. 1996, JGR, 101, 10749

Genzel, R., & Eckart, A. 1999, in Astronomical Society of the Pacific Conference Series, Vol. 186, The Central Parsecs of the Galaxy, ed. H. Falcke, A. Cotera, W. J. Duschl, F. Melia, & M. J. Rieke, 3

Genzel, R., Schödel, R., Ott, T., et al. 2003a, Nature, 425, 934

—. 2003b, ApJ, 594, 812

Ghez, A. M., Salim, S., Weinberg, N. N., et al. 2008, ApJ, 689, 1044

Giannios, D., & Sironi, L. 2013, MNRAS, 433, L25

Gillessen, S., Eisenhauer, F., Trippe, S., et al. 2009, ApJ, 692, 1075

Gillessen, S., Eisenhauer, F., Perrin, G., et al. 2010, in Society of Photo-Optical Instrumentation Engineers (SPIE) Conference Series, Vol. 7734, Society of Photo-Optical Instrumentation Engineers (SPIE) Conference Series, 0

Gillessen, S., Plewa, P. M., Eisenhauer, F., et al. 2017, ApJ, 837, 30

Gillessen, S., Plewa, P. M., Widmann, F., et al. 2018, arXiv e-prints, arXiv:1812.01416

Gladd, N. T. 1983, Physics of Fluids, 26, 974

Gravity Collaboration, Abuter, R., Amorim, A., et al. 2018, A&A, 618, L10

Grould, M., Vincent, F. H., Paumard, T., & Perrin, G. 2017, A & A, 608, A60

Guan, X., & Gammie, C. F. 2008, ApJS, 174, 145

Guan, X., Gammie, C. F., Simon, J. B., & Johnson, B. M. 2009, ApJ, 694, 1010

Guo, X., Sironi, L., & Narayan, R. 2014, ApJ, 794, 153

Habibi, M., Gillessen, S., Martins, F., et al. 2017, ApJ, 847, 120

Hawley, J. F., Smarr, L. L., & Wilson, J. R. 1984, ApJ, 277, 296

Hees, A., Do, T., Ghez, A. M., et al. 2017, PRL, 118, 211101

Hiscock, W. A., & Lindblom, L. 1985, prd, 31, 725

Hornstein, S. D., Matthews, K., Ghez, A. M., et al. 2007, ApJ, 667, 900

Howes, G. G. 2010, MNRAS, 409, L104

—. 2011, ApJ, 738, 40

Hoyle, F., & Lyttleton, R. A. 1939, Proceedings of the Cambridge Philosophical Society, 35, 405

Ichimaru, S. 1977, ApJ, 214, 840

Igumenshchev, I. V., & Narayan, R. 2002, ApJ, 566, 137

Israel, S., & Stewart, J. M. 1979, Ann Phys, 118, 341

Jiang, Y.-F., Stone, J., & Davis, S. W. 2017, arXiv e-prints, arXiv:1709.02845

Jiménez-Rosales, A., & Dexter, J. 2018, MNRAS, 478, 1875

Johnson, B. M., & Quataert, E. 2007, ApJ, 660, 1273

Kaastra, J. S., Mewe, R., & Nieuwenhuijzen, H. 1996, in UV and X-ray Spectroscopy of Astrophysical and Laboratory Plasmas, ed. K. Yamashita & T. Watanabe, 411

Kempski, P., Quataert, E., Squire, J., & Kunz, M. W. 2019, MNRAS, 486, 4013

Koide, S. 2010, ApJ, 708, 1459

Komissarov, S. S. 1999, MNRAS, 303, 343

—. 2004, MNRAS, 350, 1431

Kunz, M. W., Stone, J. M., & Quataert, E. 2016, Phys. Rev. Lett., 117, 235101

Lamers, H. J. G. L. M., & Cassinelli, J. P. 1999, Introduction to Stellar Winds (Cambridge University Press), 452

Landau, L. D., & Lifshitz, E. M. 1975, The classical theory of fields (Course of theoretical physics - Pergamon International Library of Science, Technology, Engineering and Social Studies, Oxford: Pergamon Press, 1975, 4th rev.engl.ed.)

Lemaster, M. N., & Stone, J. M. 2009, ApJ, 691, 1092

Lemaster, M. N., Stone, J. M., & Gardiner, T. A. 2007, ApJ, 662, 582

Levin, Y., & Beloborodov, A. M. 2003, ApJL, 590, L33

Li, Z., Morris, M. R., & Baganoff, F. K. 2013, ApJ, 779, 154

Liska, M., Hesp, C., Tchekhovskoy, A., et al. 2017, ArXiv e-prints, arXiv:1707.06619 [astro-ph.HE]

Liu, H. B., Wright, M. C. H., Zhao, J.-H., et al. 2016a, A & A, 593, A107

—. 2016b, A & A, 593, A44

Lodders, K. 2003, ApJ, 591, 1220

Loeb, A. 2004, MNRAS, 350, 725

Lu, J. R., Ghez, A. M., Hornstein, S. D., et al. 2009, ApJ, 690, 1463

Lu, W., & Bonnerot, C. 2019, arXiv e-prints, arXiv:1904.12018

Lützgendorf, N., Helm, E. v. d., Pelupessy, F. I., & Portegies Zwart, S. 2016, MNRAS, 456, 3645

Lynden-Bell, D. 2003, MNRAS, 341, 1360

Lynn, J. W. 2014, PhD thesis, University of California, Berkeley

Mahadevan, R., & Quataert, E. 1997, ApJ, 490, 605

Mao, S. A., Dexter, J., & Quataert, E. 2017, MNRAS, 466, 4307

Marrone, D. P., Moran, J. M., Zhao, J.-H., & Rao, R. 2006, ApJ, 640, 308

—. 2007, ApJL, 654, L57

Martins, F., Genzel, R., Hillier, D. J., et al. 2007, A & A, 468, 233

McKinney, J. C., & Gammie, C. F. 2004, ApJ, 611, 977

McKinney, J. C., Tchekhovskoy, A., & Blandford, R. D. 2012, MNRAS, 423, 3083

Misner, C. W., Thorne, K. S., & Wheeler, J. A. 1973, Gravitation (W.H. Freeman and Co.)

Mościbrodzka, M., & Falcke, H. 2013, A&A, 559, L3

Mościbrodzka, M., Falcke, H., Shiokawa, H., & Gammie, C. F. 2014, A&A, 570, A7

Mościbrodzka, M., & Gammie, C. F. 2018, MNRAS, 475, 43

Mościbrodzka, M., Gammie, C. F., Dolence, J. C., Shiokawa, H., & Leung, P. K. 2009, ApJ, 706, 497

Narayan, R., Igumenshchev, I. V., & Abramowicz, M. A. 2003, PASJ, 55, L69

Narayan, R., Mahadevan, R., Grindlay, J. E., Popham, R. G., & Gammie, C. 1998, ApJ, 492, 554

Narayan, R., SÄ dowski, A., Penna, R. F., & Kulkarni, A. K. 2012, MNRAS, 426, 3241

Narayan, R., & Yi, I. 1994, ApJL, 428, L13

—. 1995, ApJ, 444, 231

Narayan, R., Zhu, Y., Psaltis, D., & SaáÿŚowski, A. 2016, MNRAS, 457, 608

Nayakshin, S. 2005, A& A, 429, L33

Neilsen, J., Nowak, M. A., Gammie, C., et al. 2013, ApJ, 774, 42

Noble, S. C., Gammie, C. F., McKinney, J. C., & Del Zanna, L. 2006, ApJ, 641, 626

Noble, S. C., Leung, P. K., Gammie, C. F., & Book, L. G. 2007, Classical and Quantum Gravity, 24, 259

Noh, W. F. 1987, Journal of Computational Physics, 72, 78

Novikov, I. D., & Thorne, K. S. 1973, in Black Holes (Les Astres Occlus), ed. C. Dewitt & B. S. Dewitt, 343

Numata, R., & Loureiro, N. F. 2015, Journal of Plasma Physics, 81, 023001

Özel, F., Psaltis, D., & Narayan, R. 2000, ApJ, 541, 234

Pang, B., Pen, U.-L., Matzner, C. D., Green, S. R., & Liebendörfer, M. 2011, MNRAS, 415, 1228

Paumard, T., Genzel, R., Martins, F., et al. 2006, ApJ, 643, 1011

Pen, U.-L., Matzner, C. D., & Wong, S. 2003, ApJ, 596, L207

Penna, R. F., Kulkarni, A., & Narayan, R. 2013, A& A, 559, A116

Porth, O., Chatterjee, K., Narayan, R., et al. 2019, arXiv e-prints, arXiv:1904.04923

Proga, D., & Begelman, M. C. 2003a, ApJ, 582, 69

—. 2003b, ApJ, 592, 767

Psaltis, D., Narayan, R., Fish, V. L., et al. 2015, ApJ, 798, 15

Quataert, E. 1998, Apj, 500, 978

Quataert, E. 2001, in Astronomical Society of the Pacific Conference Series, Vol. 224, Probing the Physics of Active Galactic Nuclei, ed. B. M. Peterson, R. W. Pogge, & R. S. Polidan, 71

—. 2004, ApJ, 613, 322

Quataert, E., & Gruzinov, A. 1999, ApJ, 520, 248

—. 2000a, ApJ, 545, 842

—. 2000b, ApJ, 539, 809

Rees, M. J., Begelman, M. C., Blandford, R. D., & Phinney, E. S. 1982, Nature, 295, 17

Remillard, R. A., & McClintock, J. E. 2006, ARA&A, 44, 49

Ressler, S. M., & Laskar, T. 2017, ApJ, 845, 150

Ressler, S. M., Quataert, E., & Stone, J. M. 2018, MNRAS, arXiv:1805.00474 [astro-ph.HE]

—. 2019, MNRAS, 482, L123

Ressler, S. M., Tchekhovskoy, A., Quataert, E., Chandra, M., & Gammie, C. F. 2015, MNRAS, 454, 1848

Ressler, S. M., Tchekhovskoy, A., Quataert, E., & Gammie, C. F. 2017, MNRAS, 467, 3604

Reynolds, C. S., Di Matteo, T., Fabian, A. C., Hwang, U., & Canizares, C. R. 1996, MNRAS, 283, L111

Riquelme, M. A., Quataert, E., Sharma, P., & Spitkovsky, A. 2012, ApJ, 755, 50

Rockefeller, G., Fryer, C. L., Melia, F., & Warren, M. S. 2004, ApJ, 604, 662

Royster, M. J., Yusef-Zadeh, F., Wardle, M., et al. 2019, ApJ, 872, 2

Russell, C. M. P., Wang, Q. D., & Cuadra, J. 2017, MNRAS, 464, 4958

Ryan, B. R., Dolence, J. C., & Gammie, C. F. 2015, ApJ, 807, 31

Ryan, B. R., Ressler, S. M., Dolence, J. C., Gammie, C., & Quataert, E. 2018, ApJ, 864, 126

Ryan, B. R., Ressler, S. M., Dolence, J. C., et al. 2017, ApJL, 844, L24

Sadowski, A., Wielgus, M., Narayan, R., et al. 2016, ArXiv e-prints, arXiv:1605.03184 [astro-ph.HE]

Sakurai, T. 1985, A&A, 152, 121
Sądowski, A., Narayan, R., Tchekhovskoy, A., & Zhu, Y. 2013, MNRAS, 429, 3533
Sądowski, A., Wielgus, M., Narayan, R., et al. 2017, MNRAS, 466, 705
Schartmann, M., Burkert, A., & Ballone, A. 2018, ArXiv e-prints, arXiv:1804.02860
Schnitzeler, D. H. F. M., Eatough, R. P., Ferrière, K., et al. 2016, MNRAS, 459, 3005
Schödel, R., Eckart, A., Mužić, K., et al. 2007, A&A, 462, L1
Schödel, R., Morris, M. R., Muzic, K., et al. 2011, A&A, 532, A83
Schure, K. M., Kosenko, D., Kaastra, J. S., Keppens, R., & Vink, J. 2009, A&A, 508, 751
Serabyn, E., Carlstrom, J., Lay, O., et al. 1997, ApjL, 490, L77
Shakura, N. I., & Sunyaev, R. A. 1973, A & A, 24, 337
Shapiro, S. L., Lightman, A. P., & Eardley, D. M. 1976, ApJ, 204, 187
Sharma, P., Quataert, E., Hammett, G. W., & Stone, J. M. 2007, ApJ, 667, 714
Shcherbakov, R. V., & Baganoff, F. K. 2010, ApJ, 716, 504
Shcherbakov, R. V., Penna, R. F., & McKinney, J. C. 2012, ApJ, 755, 133
Sicheneder, E., & Dexter, J. 2017, MNRAS, 467, 3642
Sironi, L. 2015, ApJ, 800, 89
Sironi, L., & Spitkovsky, A. 2014, ApJL, 783, L21
Sądowski, A., Narayan, R., Penna, R., & Zhu, Y. 2013, MNRAS, 436, 3856
Smith, N. 2014, ARA&A, 52, 487
Stone, J. M., Gardiner, T. A., Teuben, P., Hawley, J. F., & Simon, J. B. 2008, ApJS, 178, 137
Stone, J. M., Pringle, J. E., & Begelman, M. C. 1999, MNRAS, 310, 1002
Stone, N. C., Kesden, M., Cheng, R. M., & van Velzen, S. 2019, General Relativity and Gravitation, 51, 30
Sutherland, R. S., & Dopita, M. A. 1993, ApJS, 88, 253
Tchekhovskoy, A., McKinney, J. C., & Narayan, R. 2007, MNRAS, 379, 469
—. 2009, ApJ, 699, 1789
Tchekhovskoy, A., Narayan, R., & McKinney, J. C. 2010, ApJ, 711, 50
—. 2011, MNRAS, 418, L79
Telesco, C. M., Davidson, J. A., & Werner, M. W. 1996, ApJ, 456, 541
Toro, E. F. 2009, Riemann Solvers and Numerical Methods for Fluid Dynamics (Springer)
Townsend, R. H. D. 2009, ApJS, 181, 391
Trap, G., Goldwurm, A., Dodds-Eden, K., et al. 2011, A & A, 528, A140
Turk, M. J., Smith, B. D., Oishi, J. S., et al. 2011, ApJS, 192, 9
Vink, J. S., de Koter, A., & Lamers, H. J. G. L. M. 2001, A&A, 369, 574
Wade, G. A., Neiner, C., Alecian, E., et al. 2016, MNRAS, 456, 2
Wang, Q. D., Nowak, M. A., Markoff, S. B., et al. 2013, Science, 341, 981
Weber, E. J., & Davis, Jr., L. 1967, ApJ, 148, 217
White, C. J., Stone, J. M., & Gammie, C. F. 2016, ApJS, 225, 22
Witzany, V., & Jefremov, P. 2017, ArXiv e-prints, arXiv:1711.09241 [astro-ph.HE]
Wong, K.-W., Irwin, J. A., Shcherbakov, R. V., et al. 2014, ApJ, 780, 9
Yuan, F., Bu, D., & Wu, M. 2012, ApJ, 761, 130
Yuan, F., Gan, Z., Narayan, R., et al. 2015, ApJ, 804, 101

Yuan, F., Markoff, S., & Falcke, H. 2002, A&A, 383, 854
Yuan, F., & Narayan, R. 2014, ARA&A, 52, 529
Yuan, F., Quataert, E., & Narayan, R. 2003, ApJ, 598, 301
Yusef-Zadeh, F., Bushouse, H., Schödel, R., et al. 2015a, ApJ, 809, 10
Yusef-Zadeh, F., Diesing, R., Wardle, M., et al. 2015b, ApJL, 811, L35
Zhao, J.-H., Young, K. H., Herrnstein, R. M., et al. 2003, ApjL, 586, L29
Zhu, Y., Narayan, R., Sadowski, A., & Psaltis, D. 2015, MNRAS, 451, 1661